Synthesis, Characterization, and Functionalization of Bis-Thiosemicarbazones:

Applications in Metal Binding, Catalysis and As Single-Source Precursor

Inaugural-Dissertation

zur

Erlangung des Doktorgrades

der Mathematisch-Naturwissenschaftlichen Fakultät

der Universität zu Köln

vorgelegt von

Eric Tobechukwu Anthony

aus Nigeria

Diese Dissertation wurde am 25. April 2025 von der Mathematisch-Naturwissenschaftlichen Fakultät

der Universität zu Köln angenommen.

Köln 2025

TABLE OF CONTENTS

Chapter 3. Result and Discussion

Conclusion and Outlook

Experimental Section

Acknowledgement

Abstract

Synthesis, Characterization, and Functionalization of Bis-Thiosemicarbazones: Applications In Metal Binding, Catalysis and as Single-Source Precursor

Pentadentate Bis-thiosemicarbazones (BTSC) of class S^N^N^N^S binding sites have been known for their therapeutic activities. Thus, investigation of pentadentate BTSC in other fields besides biological activities is often scarce or lacking. Pentadentate BTSC ligand of type S^N^N^N^S comprises a dicarbonyl backbone, N^S core and a diamine tail. Pentadentate BTSC is appealing because the dicarbonyl backbone and the diamine tail can be derivatized, functionalized and conjugated with a nanoparticle (NP) or other molecules, thus potentially expanding the applications of pentadentate BTSC. Thus, the study commenced with the synthesis of various pentadentate BTSC ligands and their metal complexes to expand the library of BTSC. Single crystal XRD showed that Pd^{2+} and Zn^{2+} conform to a distorted square planar geometry. Pd^{2+} bind through S_{thiol}^N_{imine}^$N_{pyridinic}$^N_{amide}, exhibiting a thione/thiol character. Zn^{2+} is coordinated through S_{thiol}^N_{imine}^N_{imine}^S_{thiol} showing only thiol characters. Cu^{2+} coordinate through S_{thiol}^N_{imine}^$N_{pyridinic}$^N_{imine}^S_{thiol}, resulting in a bipyramidal geometry.

The reaction between pentadentate BTSC and the linkers (dopamine hydrochloride and (3-aminopropyl)-triethoxysilane) was first carried out and to establish a new route to conjugate BTSC with NPs. 1H NMR spectroscopy revealed the new amide bond, confirming the successful conjugation of BTSC with (3-aminopropyl)-triethoxysilane) or dopamine. Magnetic Fe_3O_4 conjugate of BTSC was first synthesized using the well-established NHS/EDC coupling route. The Fe_3O_4 was first coated with SiO_2, followed by the deposition of (3-aminopropyl)-triethoxysilane to afford amine functionalized Fe_3O_4 (Fe_3O_4@SiO_2–APTES) and subsequent conjugation with BTSC (Fe_3O_4@SiO_2–APTES–BTSC). The magnetic material (Fe_3O_4@SiO_2–APTES–BTSC) exhibit a high adsorption capacity for binding Pd^{2+}. The unusual high uptake of Pd^{2+} was attributed to different adsorbed species contributing to the uptake of Pd^{2+} ions, as revealed by different characterization techniques, including DFT calculations.

The newly developed route was employed to conjugate BTSC with different NP (SiO_2 and Fe_2O_3). SiO_2 was conjugated with BTSC at the dicarbonyl backbone, and Fe_2O_3 was conjugated with BTSC at the diamine tail part of the BTSC. SiO_2 was initially pre-functionalized with (3-aminopropyl)-triethoxysilane, and Fe_2O_3 was pre-functionalized with dopamine, and the subsequent reaction with BTSC at room temperature affords SiO_2@APTES–BTSC or Fe_2O_3–Dopamine–BTSC. SiO_2@APTES–BTSC was further coordinated with Pd^{2+} ions and employed as a heterogeneous catalyst in the

Suzuki-Miyaura cross-coupling reaction. X-ray Photoelectron Spectroscopy investigation of SiO$_2$@APTES–BTSC–Pd revealed that palladium is predominantly Pd^0, thus, an invaluable catalyst for coupling aryl compounds.

Metal complexes of pentadentate BTSC were also used as single-source precursors for synthesizing metal sulfides NPs. The metal sulfide NP particles were obtained by microwave-assisted decomposition of metal complexes of pentadentate BTSC. Thus, pure Cu$_{7.2}$S$_4$, Pd$_{16}$S$_7$, and ZnS metal sulfides NPs were synthesized.

1.1 Pentadentate Bis-thiosemicarbazones (BTSC)

Thiosemicarbazone (TSC) is a class of N^S ligands with primitive potential as biological agents (antiviral, antibiotic and antifungal).[1] The earliest report of TSC dates back to 1960s when TSC was employed as a probe for ketones.[2] Since their discovery, TSC compounds have been extended as probes for metal ions, as catalysts, and in precursor chemistry to synthesize metal sulfide NPs.[3–6] In recent decades, attention has been extended to bis-thiosemicarbazone (BTSC), focusing more on tetradentate BTSC. In fact, few tetradentate BTSC complexes, e.g., [^{64}Cu(ATSM)], have successfully reached clinical trials as anticancer agents and diagnostic probes for imaging cardiac hypoxia.[7] Pentadentate BTSC, such as 2,6–diacetylbenzene–bis(*N*-(4)–ethyl-thiosemicarbazone), have also been studied for their antitumor effects.[8]

In general, mono and bis-TSC are attractive because of the ease of derivatization of the ligand.[9] Therefore, TSC can bear different -R substituents (**Scheme 1**).[10] The derivatization of TSC can occur via the carbonyl or thiosemicarbazide moiety. Thus, there is a constant increase in the TSC library. The derivatization of TSC has also been extended to BTSC, where symmetrical and asymmetrical BTSC have been explored for their biological activities.[11] One of the benefits of derivatizing TSC is that the basic N^S donor atoms can be increased. Thus, while the basic TSC binds in bidentate coordination using the thiol/thione and imine pocket, a higher degree of TSC denticity has been reported.[12,13] The derivatization of TSC is also crucial because NP conjugate of TSC can be accessed in this manner.[14,15]
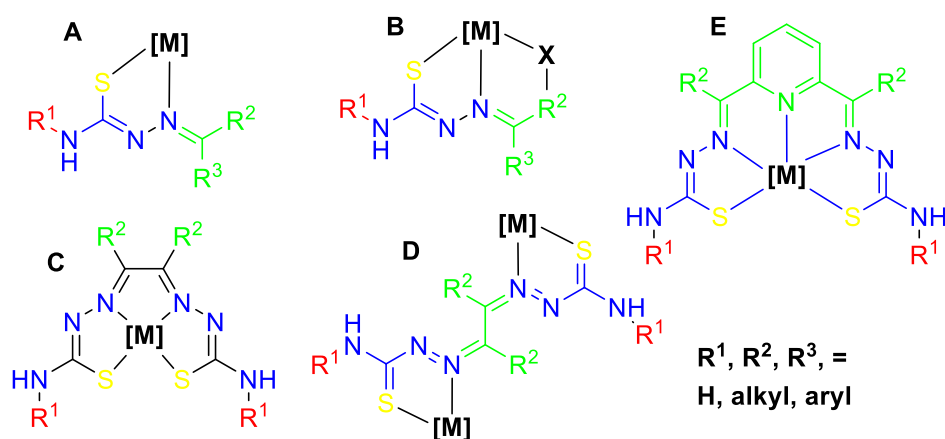
Scheme 1. Selected coordination modes of mono–TSC (**A**, **B**), tetradentate BTSC (**C**, **D**) and pentadentate BTSC modes (**E**).

Pentadentate BTSC can bind to metal ions in neutral and anionic forms through the lone pair from diimine N^S–core and the dicarbonyl donor atom (**Scheme 2**), i.e. pyridinic nitrogen and anionic

disulfur, giving rise to a highly conjugated system with pi-network consisting of alternating single and double bonds and bond length averaging between single and double bond. The coordination trend of the BTSC metal complex is vast because the metal centre influences the charge and coordination.[16]
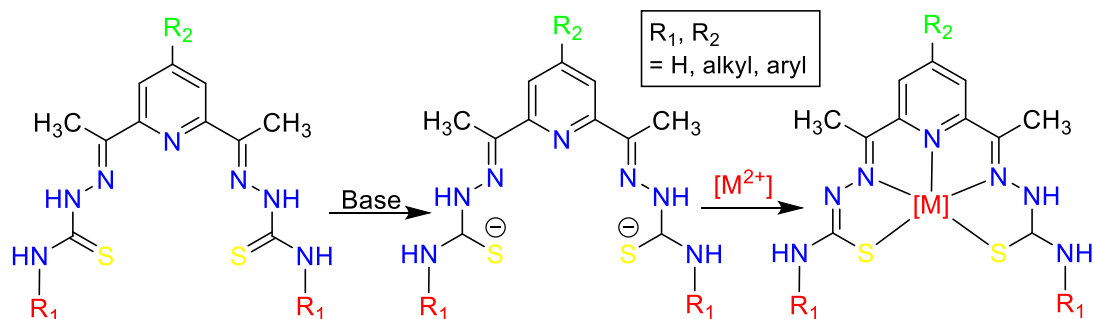
Scheme 2. Complexation of pentadentate BTSC with **M²⁺**.

TSC is also attractive because of their affinity for soft and hard metals.[17] Thus, TSCs have been used to recover metal ions from an aqueous solution, simultaneously as a sensor for metal poison in food and beverages.[18,19] In recovering metal ions from an aqueous solution, TSC is often anchored covalently on an NP (support) to ease the conjugate's recovery, thus limiting TSC leaching.[20] Consequently, graphene and cellulose have been conjugated with mono-TSC to recover metal ions from an aqueous solution.[21,22] The graphene/cellulose–TSC conjugate showed an affinity for soft metal, as indicated by its high adsorption capacity.[21,23]

The varieties of coordination modes adopted by mono-TSC complexes make mono-TSC complexes an invaluable homogenous catalyst for oxidation and reduction, hydrogenation, alcoholysis and condensation reaction.[5,6] Mono-TSC can adopt the pincer-type coordination effective in carbon–carbon coupling of aryls.[24] The inherent N^S donor atoms are also beneficial for many catalyst activities due to their air stability compared to traditional phosphine-based ligands.[25] Recently, studies have shifted towards heterogeneous catalysts due to the challenges associated with recovering spent homogeneous catalysts.[26] Therefore, mono-TSC complexes are conjugated with NPs. Many studies have utilized mono-TSC terminal amine as the binding site for the NP.[20] Polystyrene was covalently conjugated to TSC as a heterogeneous catalyst for the oxidation of alkenes and alcohol.[27] The carbonyl moiety of mono-TSC has also been explored as the anchoring site of NP.[28] Fe_3O_4 was conjugated with the mono-TSC copper complex via the carbonyl moiety and was employed as an Ullmann-type catalyst in the arylation of imidazole with iodo-benzene.

Mono-TSC is an invaluable source of sulfur atoms. Therefore, there is also a growing trend in using mono-TSC in precursor chemistry, especially as a single-source precursor in synthesizing metal sulfide NPs.[29,30] The inherent N^S TSC donor atoms have a varying affinity for metal ions; **S** have an affinity for soft metals, and N has an affinity for hard metals.[31] Therefore, the metal complexes of mono-TSC are not limited to the transition metals. Lanthanides, actinides and alkali metal complexes have all been reported.[32–34] Therefore, previously difficult-to-synthesize metal sulfides and bimetallic are now easily accessible in higher purity.[35–37]

Mono-TSCs are synthesized by condensing thiosemicarbazide with a carbonyl (aldehyde or ketones).[10] BTSC is synthesized similarly, except that thiosemicarbazides are condensed to two arms of dicarbonyl, thus opening the path for pentadentate BTSCs when the dicarbonyl backbone contains a donor atom, resulting in an S^N^R_4^N^S binding pockets.[38] In lieu, different binding pockets S^N^N^N^S, S^N^S^N^S and S^N^O^N^S have been reported for pentadentate BTSC (**Scheme 3**).[39,40] This thesis focuses on the S^N^N^N^S binding pocket obtained from the 2,6-diacetyl-pyridine derivatives.
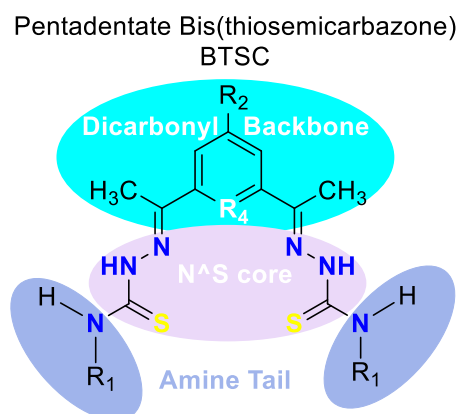
Scheme 3. General structure of BTSC showing the dicarbonyl backbone, N^S core, and diamine tails.

1.2 Thiosemicarbazones Nanoparticle Conjugate

TSC are attractive molecules, especially in their biological activities. However, for practical applications, TSC ligands are conjugated with support to ease the recovery of spent TSC or to target specific sites.[14,15] The structural flexibility of TSC is crucial in achieving the conjugation of TSC with support. The covalent anchoring of TSCs onto NPs is feasible via two approaches.

The first approach involved the reaction between thiosemicarbazide and carbonyl/ketone-bearing NPs. This is practical for carbon-based NPs. Ribose, galactose, glucose, and graphene-TSC NPs conjugates have been synthesized using this approach.[41–43] The reaction between the carboxylic acid

moiety of graphene oxide and TSC's terminal amine forms an amide bond. Similarly, the reaction between acryl-chloride moiety of carbon nanotubes and TSC's terminal amine has also been used to form an amide bond to anchor TSCs covalently.[20]

The second approach involves the covalent reaction of TSC with pre-functionalized NPs. This is the most common approach used to synthesize TSC-NP conjugates. The simplest form is to utilize TSC's terminal-NH to form a covalent bond between TSC and halogen pre-functionalized NPs. Alternatively, TSC may be derivatized with different functional groups to explore the affinity by relying on the chemistry of individual NP.[9]

1.3 Thiosemicarbazones in Suzuki-Miyaura Cross-Coupling Reaction

Thiosemicarbazone (TSC) and its metal complexes are widely known for their biological activities. However, their catalytic activities have also been gaining attention. Transition metal complexes of TSC are essential catalysts in various chemical reactions, including cross-coupling of aryls.[5,6] The enhanced catalytic activities of TSC metal complexes have been associated with the air stable N^S donor atoms. The donor atoms are responsible for the interesting stereochemical, electrochemical, and electronic properties important for catalytic activities.[44,45] The donor atoms are also responsible for the varieties of coordination modes adopted by TSC, including the pincer motif, which is vital for many catalytic reactions.[24,46] The chelate pocket of TSC, especially in multidentate coordinated TSC, is also essential for the stability of catalysts.[47]

Generally, the metal centre of a catalyst functions by acting as the binding site for the catalytic reaction, and the surrounding ligands and co-ligands offer the appropriate geometrical and electronic configuration toward the desired transition state for the required chemical reaction.[48] A homogenous catalytic system is attractive because the catalytic process can occur under a mild condition, offering high chemo- and regio-selectivity and catalytic activities.[46] However, since the catalyst phase is the same as the reactant and products, more energy and material are required to separate the desired products. This is a significant drawback for homogenous catalysts.[48] Thus, the quest to recover, regenerate, and reuse catalysts has led to a significant shift in the design of many catalysts. Recent catalyst designs have seen the use of insoluble NPs or the immobilization of traditional homogenous catalysts onto support such as NP.[28] However, the new interaction, e.g., the covalent bond between the support and metal complex, may negatively impact the electronic state of the metal centre, thus altering the catalytic activities.[48]

Pd-based complexes used in the Suzuki-Miyaura cross-coupling type reaction have received the most attention because of their industrial importance.[49] The reaction involves the coupling of organoboranes and organic electrophiles in the presence of a base.[50,51] Thus, reports that enhance the field continue to grow.[50] The mechanism that governs Pd-based cross-coupling has been extensively studied.[52] The catalytic cycle commences with the active Pd moiety, i.e., [**Pd⁰L₄**], which is succeeded by the oxidative addition of the aryl halide (Ar–X) to afford *trans*-ArPdXL₂ complex, this is followed by the nucleophilic attack on the *trans*-ArPdXL₂ complex, resulting in transmetallation, the product is finally obtained by reductive elimination (**Scheme 4**).[52]
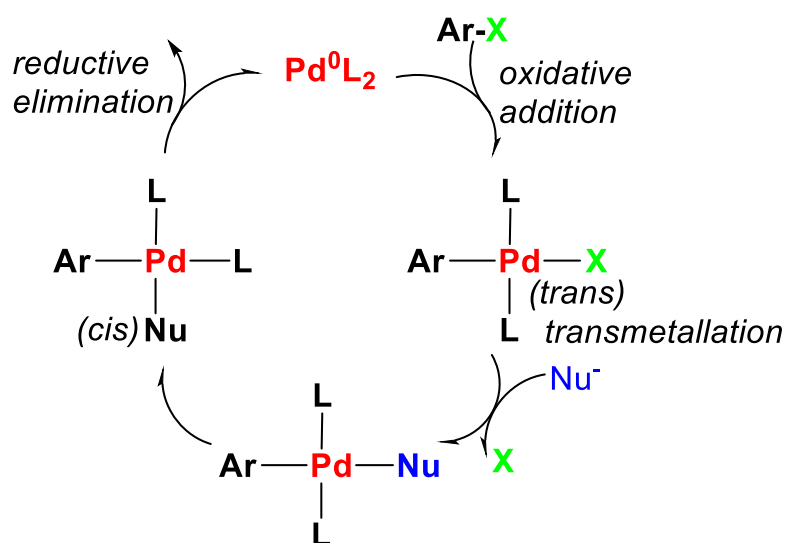
Scheme 4. Mechanism of Suzuki-Miyaura cross-coupling reaction

1.4. Homogenous Thiosemicarbazone Catalyst

In general, homogenous catalysts have received much attention due to their higher catalytic and selectivity rates. A phosphorus-based ligand characterized the traditional Pd catalysts used in the Suzuki-Miyaura reaction; the phosphorus ligand provides steric hindrance, essential during transmetallation and reductive elimination.[53,54] TSC Pd complex has been synthesized to include phosphorous ligands, enriching its composition alongside the intrinsic N^S donor atoms. This design enhanced the catalytic performance of TSC catalyst (**Scheme 5**).[55] The performance of phosphine-based TSC catalysts has also been enhanced by introducing additional ligands, highlighted by the effect of electron withdrawing and electron donating groups on the coupling of haloaryl with organoborane.[55] Among the tested ligands (-OCH₃, CH₃, H, Cl and NO₂), the electron-donating ligand was the most efficient catalyst for the Suzuki-Miyaura-type reaction.
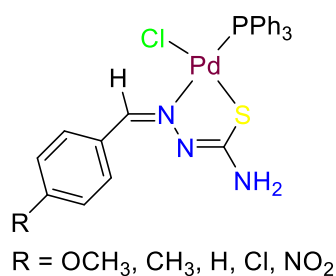
Scheme 5. Phosphine-based TSC Pd complex for Suzuki-Miyaura cross coupling reaction. Adopted from Ref.[55]

Investigating the impact of a more extensive ligand system is a practical tool in designing TSC catalysts for cross-coupling reactions. Thus, bis-diphenyl-phosphine ferrocene, bis-phenyl-phosphine and phenyl-phosphine TSC Pd complexes were compared in Suzuki-Miyaura-type reaction (**Scheme 6**). The catalytic performance of the bis-diphenyl-phosphine ferrocene-containing TSC Pd complex was superior to other catalysts, even in mild catalytic conditions. The high catalytic activities were attributed to the extensive ligand system.[56]
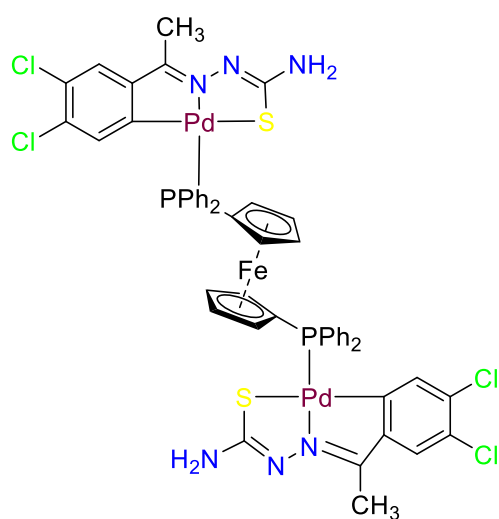
Scheme 6. Phosphine-based TSC Pd complex with extensive ligand system for Suzuki-Miyaura cross coupling reaction. Adopted from Ref.[56]

Nitroso-2-naphthol and quinoline-8-ol were also investigated as ancillary ligands as an alternative to the traditional phosphine-based ligand (**Scheme 7**).[57] The catalyst was adequate for coupling of wide range of haloaryl compounds with boronic acid, including the activation of C-F, C-I and C-Cl.[57] The reaction also proceed at room temperature, however at longer reaction time.[57]
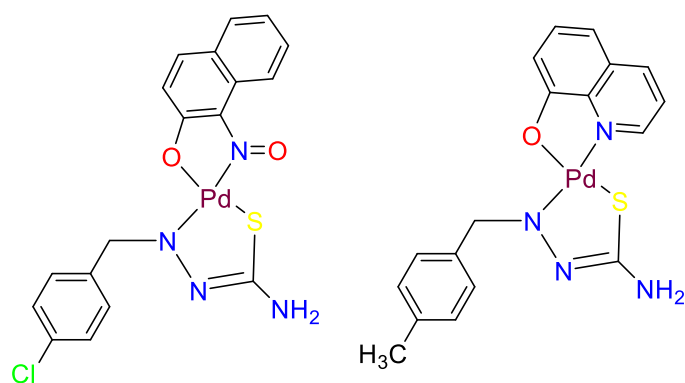
Scheme 7. TSC Pd complex with ancillary ligands for Suzuki-Miyaura cross-coupling reaction. Adopted from Ref.[57]

The pincer complexes are known for their excellent catalytic activities. This type of ligand is characterized as moisture, air and thermal-stable.[24] Tridentate TSC ligands usually conform to the pincer motif.[58] Salicylaldehyde TSC Pd complex was employed as an air and moisture-stable catalyst for coupling organoborane with aryl halides (**Scheme 8**).[59] The optimum catalytic condition was obtained in DMF solution at 100°C.[59] The coupling can also occur under a mild catalytic condition. However, activation of chloride substituent was low as compared to bromide substituent.[60]
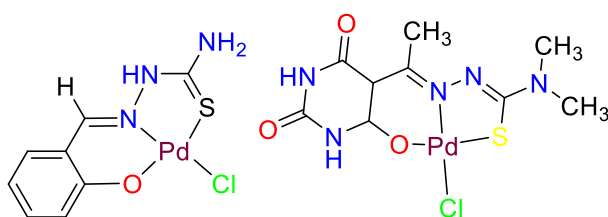
Scheme 8. Pincer conform TSC Pd complex for Suzuki-Miyaura cross coupling reaction. Adopted from Refs.[59,60]

1.5 Heterogenous Thiosemicarbazone catalyst

In the quest for a sustainable chemical process, relevance is given to the design of heterogeneous TSC catalysts. In lieu, Pd complexes TSC were conjugated with SiO_2 NPs. The covalent conjugation of TSC Pd complex and SiO_2 NP was achieved by reacting –NH pre-functionalized SiO_2 with carbonyl pre-functionalized TSC. The TSC–NP conjugate shows high catalytic activities and selectivity, and the spent catalyst can be recovered and regenerated for reuse (**Scheme 9**).[61] Carbohydrate was employed as the carbonyl constituent in the synthesis of TSC for the Suzuki-Miyaura type reaction. The

coupling reaction was achieved in high yield at 60 minutes reaction time. Substituted aryl chloride at the ortho position achieved the lowest coupling.[62]
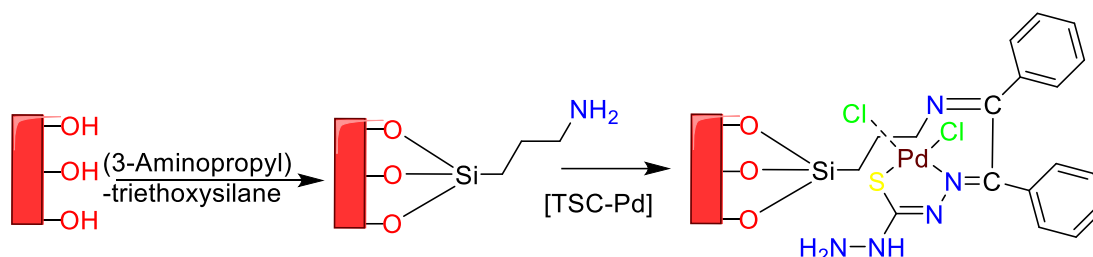
Scheme 9. TSC-Pd heterogenous catalyst for Suzuki-Miyaura cross coupling reaction. Adopted from Ref.[61]

1.6 Thiosemicarbazone Complexes as a Single-Source Precursor

TSCs are an important source of sulfur due to the inherent N^S donor atoms. Therefore, TSC metal complexes are ideal for the synthesis of metal sulfide.[63] Thus, several metal sulfide NPs have been reported, including transition metals and lanthanides.[37,63,64] Usually, the metal sulfide is obtained via the thermal decomposition of the TSC metal complex. The decomposition commences with eliminating alkene and rearrangement to form the metal sulfide NP (**Scheme 10**).[37]
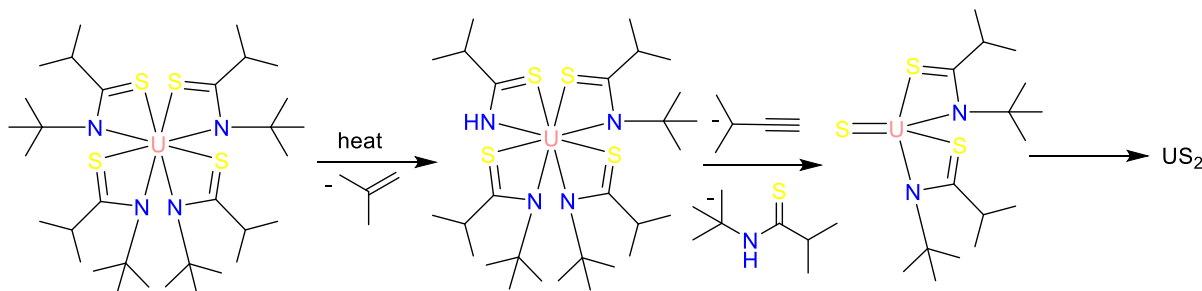
Scheme 10. Thermal decomposition of TSC complex for the synthesis of metal sulfide. Adopted from Ref.[37]

1.7 Thiosemicarbazone Nanoparticle Conjugate in Metal Binding

TSC are ideal for metal binding due to chelating properties. The inherent N^S donor atoms have different affinity for hard and soft acids.[65] TSC are anchored on a support (NP) during the binding and recovery of metal ions. In lieu, multiwall carbon nanotubes (MWCNs), carboxylate functionalized MWCNs and carboxylate functionalized MWCNs anchored with 1-isatin-3-TSCs was investigated for the adsorption of Pb^{2+} ions.[20] Increasing the solution pH value from 1 to 5.5 was favourable to all the adsorbents. Above the optimum pH (5.5), the surfaces of the carboxylate functionalized MWCNs and carboxylate functionalized MWCNs anchored with 1-isatin-3-TSC were characterized by the dissolution of the carboxylic group and protonation of amino groups, respectively. The adsorption

capacity of carboxylate functionalized MWCNs anchored with 1-isatin-3-TSC was superior (63.67 mg/g), when compared with the carboxylate functionalized MWCNs (7.36 mg/g). This showed that while the contribution of the carboxylate functional group ($^-$OH, a hard base) was lost, the thiol (SH) on the TSC retained its binding capacity, thereby contributing to its adsorption capacity.

Another study has also highlighted the impact of the N^S donor atoms by conjugating graphene oxide with TSC. Graphene oxide conjugated with TSC improved the affinity of the conjugate for Hg^{2+} ions.[43] The improved affinity for Hg^{2+} was caused by the reaction of the donor atoms (S and N) with Hg^{2+} ions, which results in a strong surface complexation reaction. Mesoporous silica conjugated with 5-*tert*-butyl-2-hydroxybenzaldehyde TSC. The resulting adsorbent was used for the removal of Pd^{2+}.[66] At the optimum pH (3.5), in the presence of 10 mg/L competing ions (Ca^{2+}, Fe^{3+}, Co^{2+}, Mg^{2+}, Zn^{2+}, Cu^{2+}, K^+, Na^+, Ag^+, Ru^{3+}, Al^{3+}, Ba^{2+} and Pt^{2+}), the SiO_2–TSC conjugate was selective for Pd^{2+} at 2 mg/L initial concentration, with slight loss of activities after the 9th cycle of the regeneration of the SiO_2–TSC conjugate.[67]

NP conjugate of TSC has also been used for preconcentration and detection of metal ions. Alumina–TSC conjugate was employed for the preconcentration and selective extraction of Cr oxyanions in the presence of competing metal ions.[68] The affinity of the Alumina–TSC towards Cr^{3+} oxyanion increased with increasing solution initial pH from 4 to 7, with adsorption capacity between the range 10 to 760 μmol/g. In contrast, the affinity for $C_2O_7^{2-}$ increased as the initial pH solution decreased from 4 to 1, with adsorption capacity between 100 to 400 μmol/g. Thus, it is viable to selectively extract chromium oxyanions by manipulating the initial solution pH. Polystyrene–1-phenyl-1,2-propanedione-2-oxime-TSC conjugate was employed to preconcentrate Cu^{2+} ions in aqueous solution, soil and food samples.[69] The polystyrene–TSC conjugate selectively complexed Cu^{2+} at initial solution pH 5. The adsorbed Cu^{2+} exhibits high stability in strong acid and alkaline mediums. However, competing ions such as Fe^{3+} and Hg^{2+} remain a challenge.[69]

Mesoporous SiO_2–TSC conjugate was employed to detect and remove Cu^{2+} from an aqueous solution.[67] The removal of Cu^{2+} ions was influenced by the solution pH, with the maximum adsorption capacity of 176.27 mg/g. The removal of optimum Cu^{2+} ions was observed at a neutral solution pH. Therefore, while TSC-based adsorbents show high adsorption capacity and can function in selective extraction and preconcentration, competing ions remain challenging. However, this shortcoming associated with competing ions can be overcome by manipulating the solution's initial pH since N^S donor atoms present in TSCs can function independently at opposing pH values.

1.8 Aim of this Work

The aim of this thesis is to synthesize a range of pentadentate BTSC and their NP conjugate (BTSC–NP). The BTSC–NP conjugate is used for the binding Pd^{2+}. The Pd^{2+} coordinated BTSC–NP is further employed as a catalyst in the Suzuki-Miyaura-type cross-coupling reactions. The conjugation of NP with BTSC was attempted via the dicarbonyl backbone and the diamine tail (**Scheme 11**). A further aim was to use BTSC metal complexes as a facile single-source precursor in the synthesis of metal sulfides.

The aim of the project was achieved by following these objectives:

- Synthesis of pentadentate BTSC and their complexes and derivatization of pentadentate BTSC to bear additional functional groups at the dicarbonyl backbone and the diamine tails.
- The synthesis of pentadentate BTSC functionalization with dopamine hydrochloride, (3–aminopropyl)–triethoxysilane or (3-chloropropyl)-trimethoxysilane. Covalent anchoring of pentadentate BTSC with Fe_3O_4, SiO_2 and Fe_2O_3.
- Adsorption of Pd^{2+} ions in aqueous solution with $Fe_3O_4@SiO_2$–APTES–BTSC conjugates and investigation of the adsorption isotherm and the effect of hydrochemistry
- Carbon–carbon coupling of aryl compounds in the Suzuki-Miyaura-type reaction using SiO_2–APTES–BTSC–Pd^{2+} as heterogenous catalyst
- Synthesis of metal sulfides using BTSC metal complexes of Cu, Pd and Zn.

X = TSC's functional group
Z = anchoring group
Y = shell's function group
R',R" = alkyl or aryl
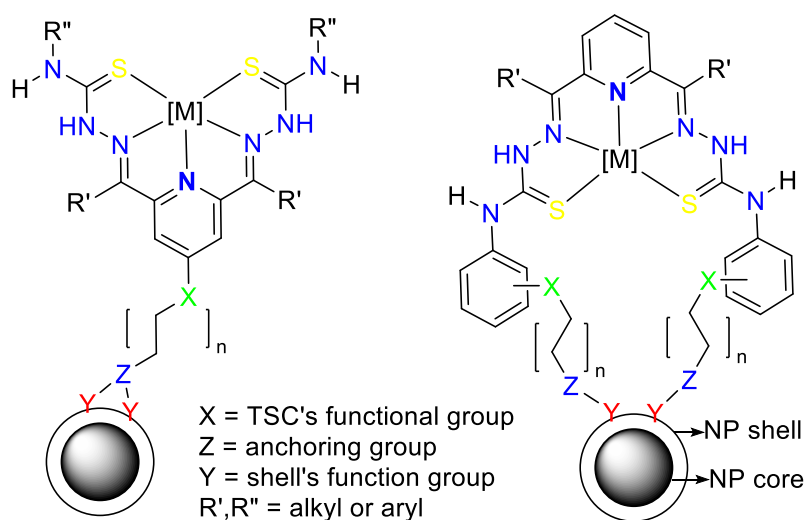
Scheme 11. NP conjugate of pentadentate BTSC anchored through dicarbonyl backbone or diamine tail.

Chapter 2. Results and Discussion

2.1 Synthesis of Pentadentate BTSC and their NP Conjugates

Pentadentate Bis-Thiosemicarbazones (BTSC) are an essential class of N^S donor ligands for synthesizing metal complexes with various applications.[8] BTSC ligands comprise a dicarbonyl backbone and a core N^S core.[70] Both the dicarbonyl backbone and N^S core can be derivatized to bear different constituents and functional groups, thus expanding the BTSC library.

The primary consideration of this study was to synthesize BTSC with different anchoring groups at the dicarbonyl backbone or at the amine tail, which can further react with dopamine hydrochloride, (3–aminopropyl)–triethoxysilane or (3-chloropropyl)-trimethoxysilane, to finally afford a BTSC that can covalently bond with NPs in the simplest chemical reaction. The four functional groups of interest are carboxylate, hydroxyl and halogen. This aim was achieved by first synthesizing a series of thiosemicarbazides, i.e., the N^S core, followed by the synthesis of the dicarbonyl (backbone) and finally, the condensing of the dicarbonyl with thiosemicarbazides to afford a series of pentadentate BTSC.

2.2 Results and Discussion

2.2.1 Synthesis of Thiosemicarbazides

Two methods have previously been described for the synthesis of thiosemicarbazides.[71] **1**) a two-step reaction involving the treatment of carbohydrazide with isothiocyanates or ammonium thiocyanate, **2**) a one-pot reaction involving the treatment of boiling dithiocarbamate salt with hydrazine.[71] The one-pot is ideal for water-soluble primary amine, gives a reasonable yield, and does not involve the highly toxic thiophosgene. After cooling, thiosemicarbazide is obtained as a colourless precipitate in an aqueous solution (**Scheme 12**). Possible contamination arises from the reaction of thiosemicarbazide terminal amine with common solvents such as acetone and ethyl acetate. The synthesized series of thiosemicarbazides are presented in **Scheme 13**. The hydrazine protons of the thiosemicarbazide appeared at the opposing end of the proton NMR spectrum (**Table 1**).
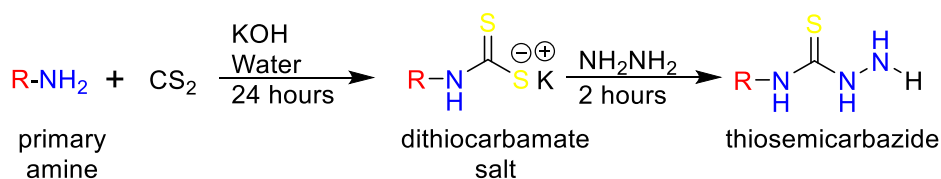
Scheme 12. General method for the synthesis of thiosemicarbazide
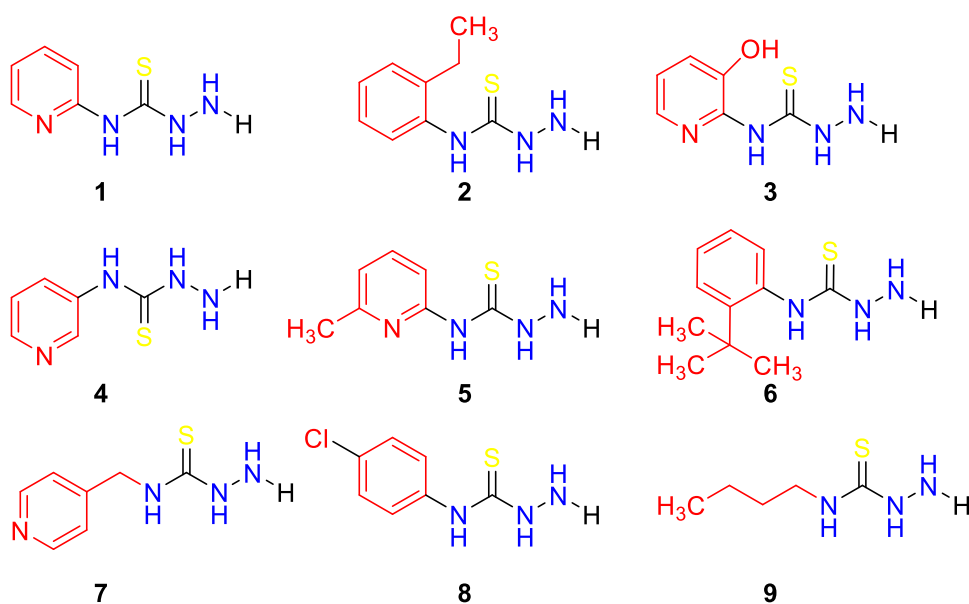
Scheme 13. Synthesized thiosemicarbazides in this study.

Table 1: 1H NMR data of thiosemicarbazide measured in DMSO–d_6

Comp	Aryl					Alkyl		Hydrazine	
1	7.07 – 6.97	7.13	7.76	8.22				5.23	12.59
2		7.28	7.61	8.22		2.67	1.25	4.03	9.04[a]
3	6.94	7.72	7.72	8.33				5.24	12.43
4	7.33	8.07	8.31 – 8.23	9.28				5.24	9.28
5		6.86	6.94	8.08			2.26	5.21	12.65
6	7.14 – 7.07	7.21	7.50	7.69			1.27	4.78	9.64[a]
7			7.31 – 7.21	8.53 – 8.39			4.64 – 4.45	4.74	8.84
8			7.38 – 7.27	7.67				4.86	9.17
9					3.63	1.48 – 1.32	0.96	3.80	7.78[a]

[a] Samples measured in CDCl3.

2.2.2 Synthesis of 2,6-diacetyl-pyridine (DAP) derivatives

With the successful synthesis of the thiosemicarbazide. The study proceeds to the synthesis of the dicarbonyl backbone and its derivatives. The dicarbonyl was synthesized by acetylation of substituted pyridine (**Scheme 14**).[72,73] First, substituted pyridine and pyruvic acids were dissolved in an aqueous acidic solution. The addition of ammonium thiosulfate salt in the presence of $AgNO_3$ caused the evolution of CO_2. Substituted 2,6–diacetyl–pyridine was purified via column chromatography using neat DCM. 4–chloro–pyridine and 4–bromo-pyridine were purchased as hydrochloride salts. The

hydrochloride salts were basified with saturated NaOH before acetylation to avoid generating silver chloride salts. In the case of 4–(diethyl–phosphite)–2,6–diacetyl–pyridine, substituted pyridine, i.e., 4–(diethyl–phosphite)–pyridine, was obtained via coupling of diethyl–phosphite with 4–bromo–pyridine in the presence of triethylamine using Pd-catalyst to eliminate triethylamine–hydrobromide. The product 4–(diethyl–phosphite)-pyridine was subsequently treated with pyruvic acid to obtain the 4–(diethyl–phosphite)–2,6–diacetyl-pyridine.
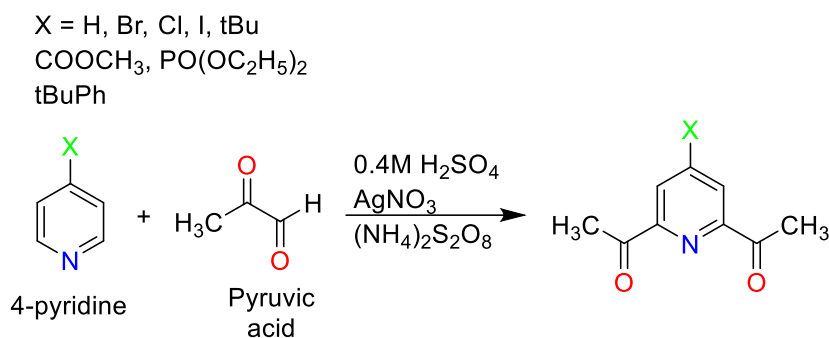
Scheme 14. General method for the synthesis of substituted 2,6-diacetyl-pyridine derivatives.

A series of DAP backbones were synthesized (**Scheme 15**), primarily focusing on synthesizing dicarbonyl with additional functional groups to allow functionalization with linkers and the subsequent covalent functionalization with NP. Another benefit of functionalizing the dicarbonyl backbone is to improve the solubility of the resulting BTSCs. The dicarbonyl is characterized by a relatively low isolated yield (< 12%). The lowest isolated yield of 2% was obtained 4–(diethyl–phosphite)-DAP.
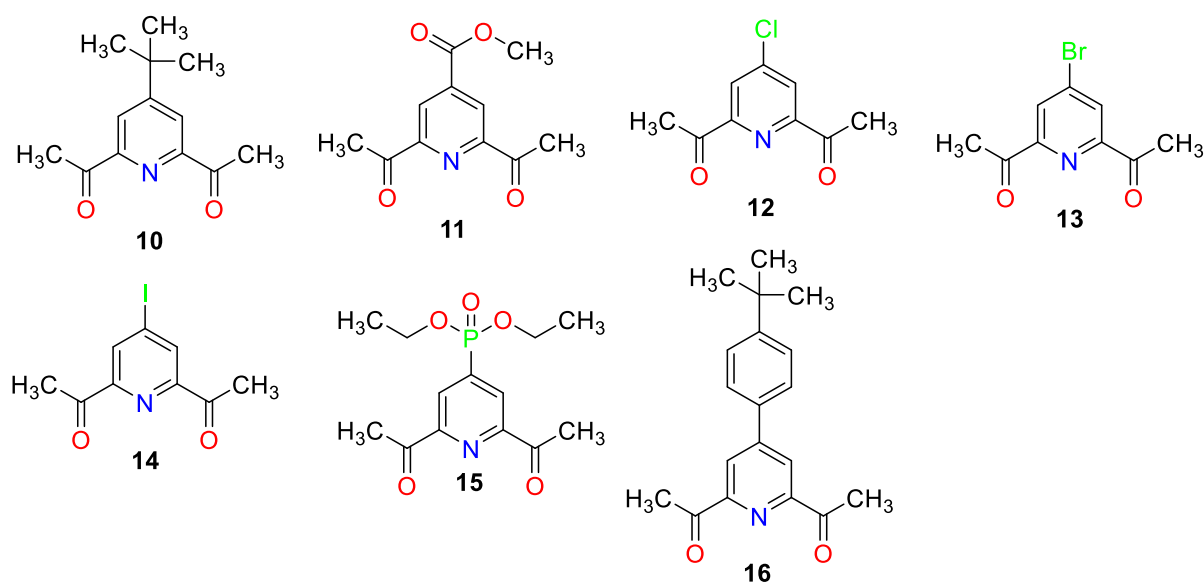
Scheme 15. Series of 2,6-diacetyl-pyridine derivatives synthesized in this study.

2.2.2.1 1H NMR of Dicarbonyl

The representative 1H NMR spectra of the dicarbonyl are presented in **Fig. 2** and **3** for 4-methyl-isonicotinate-2,6-DAP and 4–(diethyl–phosphite)-DAP**.** The most identifying peaks are the two symmetrical -CH$_3$ peaks associated with the diacetyl, which appeared at δ = 2.8 and 2.7 ppm. The additional -CH$_3$ of the ester moiety for compound **11** appeared at 4.03 ppm. The symmetric -CH$_2$ and -CH$_3$ parts of the phosphonic acids appeared at 4.28 and 1.38 ppm.
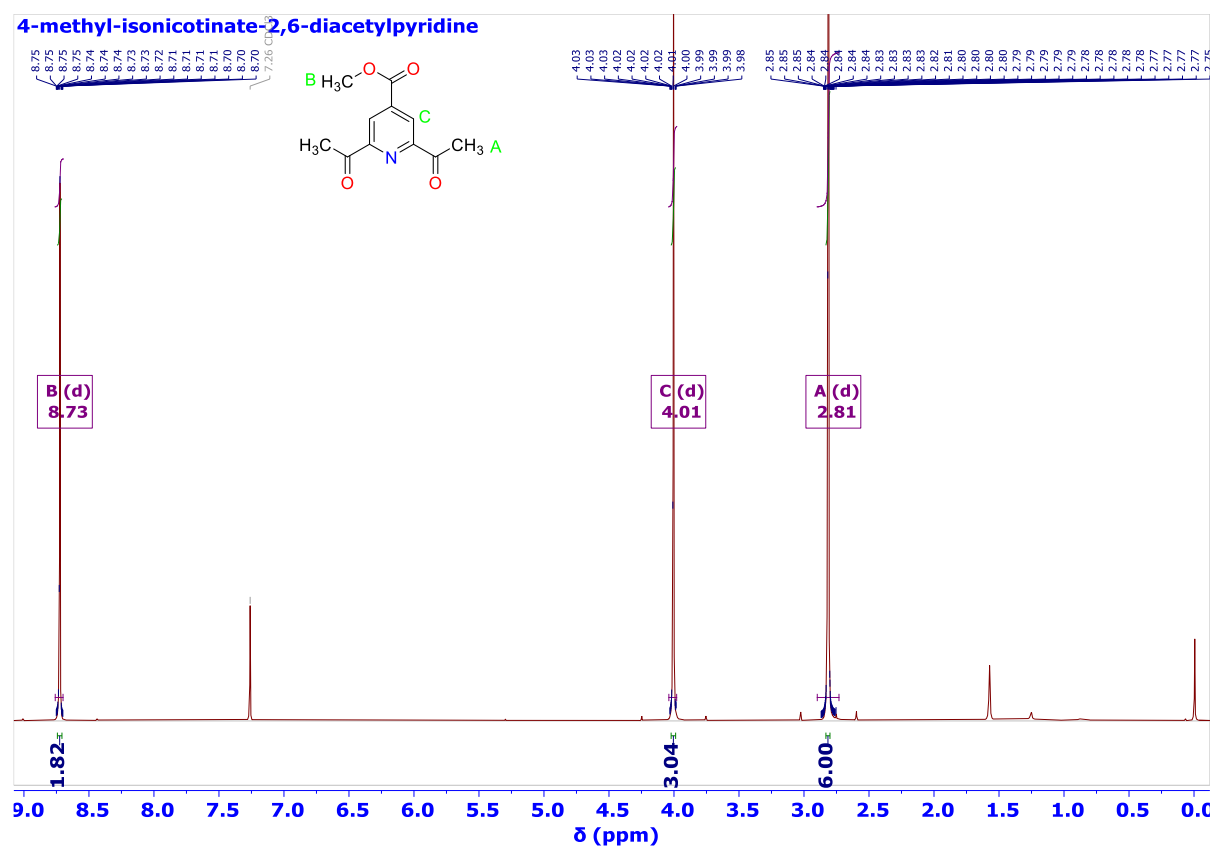
Fig. 2. 1H NMR spectrum of 4-methyl-isonicotinate-2,6-DAP measured in CDCl$_2$
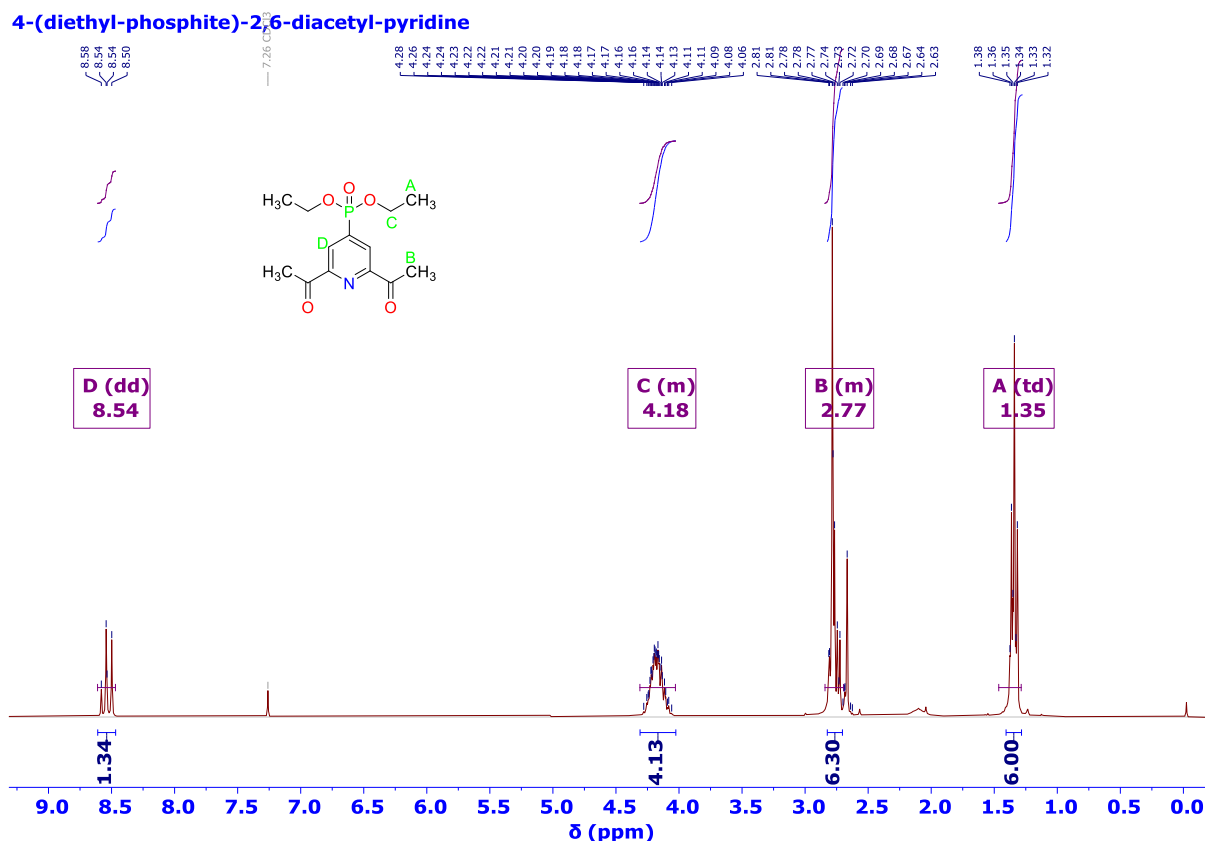
Fig. 3. 1H NMR spectrum of 4–(diethyl–phosphite)-DAP measured in CDCl$_2$

2.2.3 Synthesis of pentadentate Bis-Thiosemicarbazones

Having successfully obtained the substituted dicarbonyl, series of BTSC was obtained via a condensation reaction involving 2,6-diacetyl-pyridine or substituted 2,6-diacetyl-pyridine (ratio 1) with thiosemicarbazide (ratio 2) in acetic acid solution (**Scheme 16**). The reaction was catalyzed with 0.1 mL of CF$_3$COOH. BTSCs were obtained as yellow solids with reasonable yields (52 – 66%). Earlier attempts to synthesize BTSC in ethanol and methanol using acetic acid as a catalyst yielded impure products.[74,75] This is due to the solubility of the thiosemicarbazide precursors.
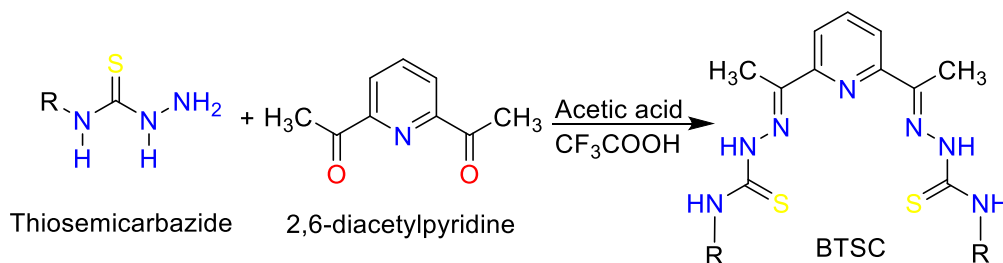
Scheme 16. General method for the synthesis of BTSC.

Using the method mentioned earlier, commercially available 2,6-diacetyl-pyridine was used to synthesise a series of BTSC presented in **Scheme 17**.
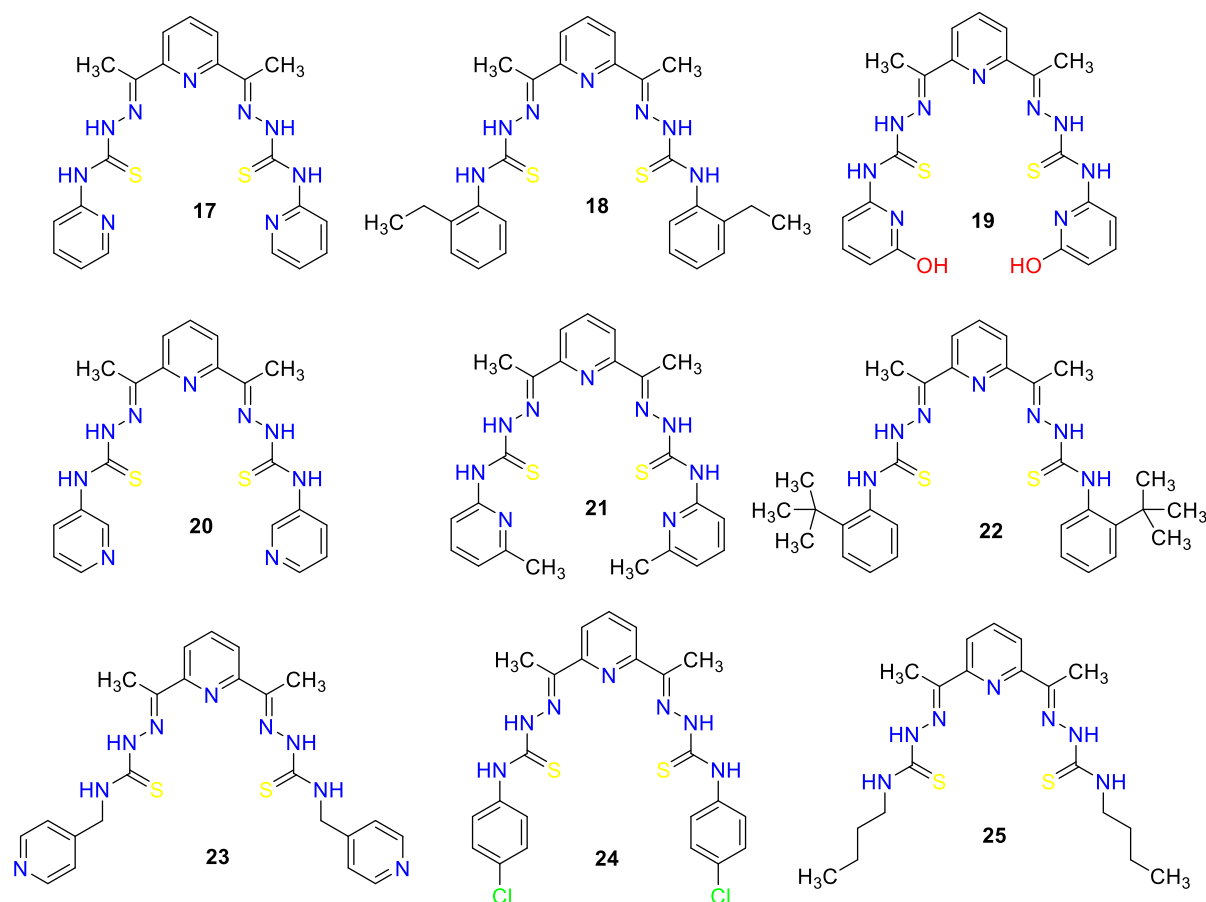
Scheme 17 A series of BTSC starting with 2,6–diacetyl–pyridine

2.2.3.1. 1H NMR of Bis-Thiosemicarbazones

The structural information of all the new compounds was elucidated using 1H NMR. Representative spectra are presented in Fig. **4** and **5**. The most identifying peaks are the two symmetrical -CH$_3$ at both arms of the dicarbonyl backbone, which appeared upfield at around 2.59 ppm, and the two characteristic hydrazine protons appearing downfield at around 15.08 and 11.18 ppm for 2,6-diacetylpyridine-bis-4-*N*-2-pyridyl BTSC (**Table 2**). One of these hydrazine protons appeared upfield in thiosemicarbazide; however, when BTSC was formed, the signal appeared downfield. The three aforementioned characteristic peaks have been reported at 2.45, 10.35 and 8.45 ppm, respectively.[76] A triplet dividing both arms of the BTSC appeared at 8.01 ppm. This triplet is absent with 4-substituted BTSC.
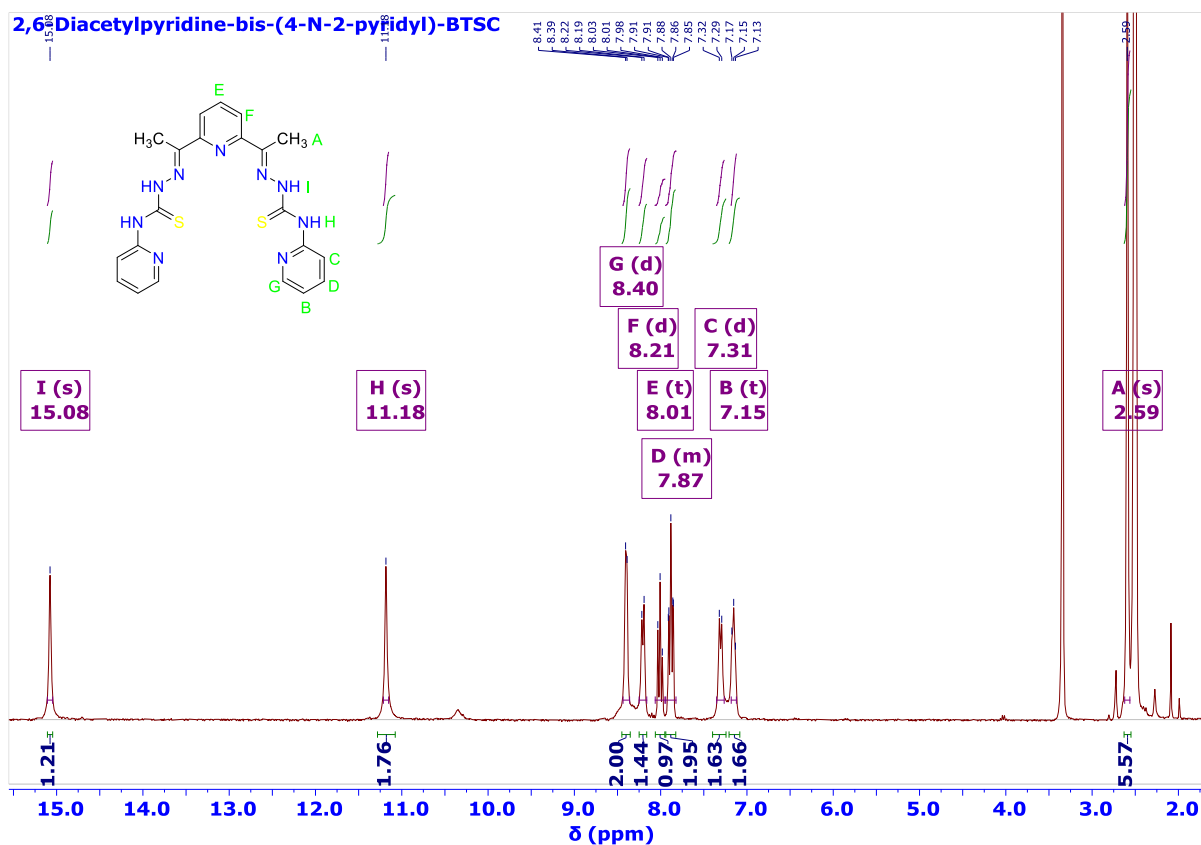
Fig. 4. 1H NMR spectrum of 2,6-diacetylpyridine-bis-4-*N*-2-pyridyl-BTSC measured in DMSO–d6
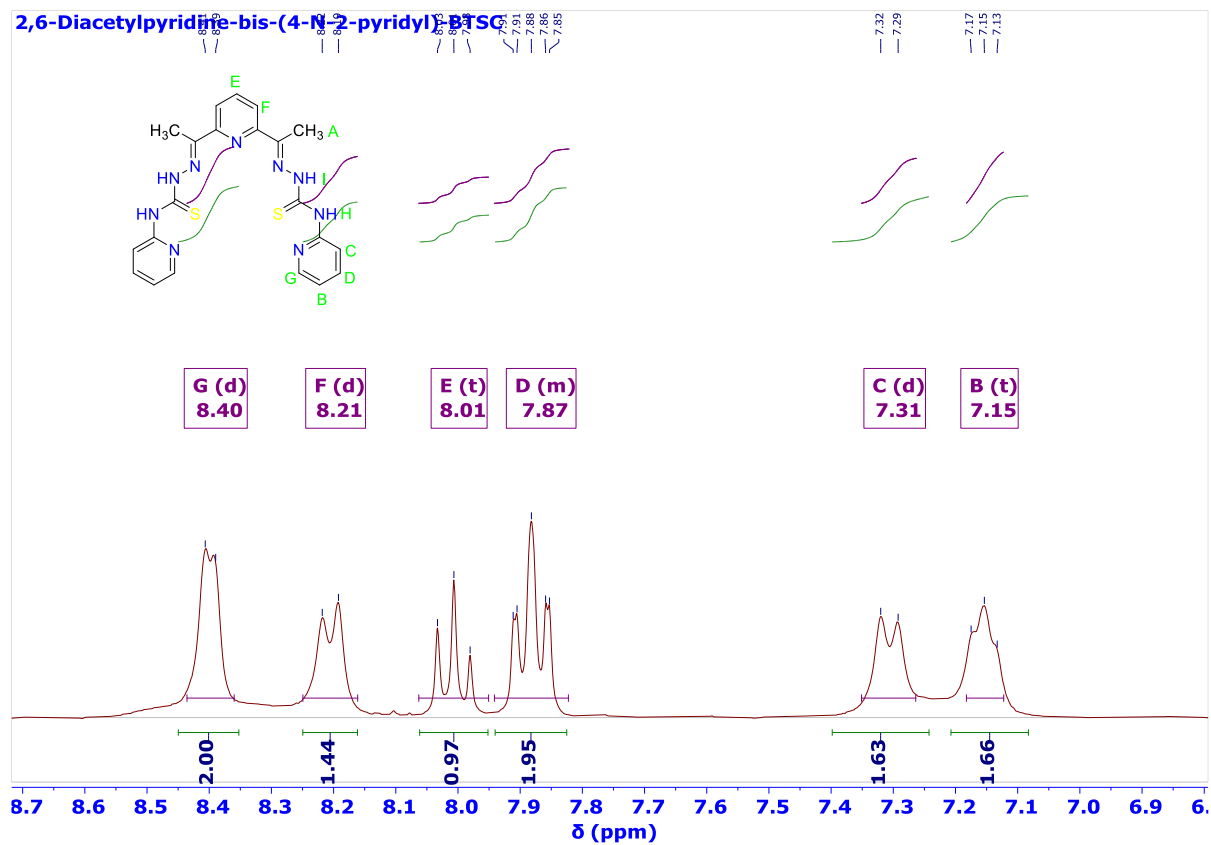
Fig. 6. 1H NMR spectrum of 4-bromo-2,6-diacetylpyridine-bis-4-*N*-2-pyridyl-BTSC measured in DMSO–d6, showing a magnified portion of the spectrum.

Table 2: 1H NMR data of thiosemicarbazide measured in DMSO–d6

Compound	Aryl				Alkyl			Hydrazine	
17	7.94	8.01	8.21	8.40	–	–	2.59	11.18	15.08
18	–	7.28	7.28	7.79	–	2.61	2.54	10.10	10.67
19	6.61	6.73	7.17	7.97	–	–	2.48	8.11	15.49
20	8.14	8.40	8.59	8.70	–	–	2.55	–	10.55
21	7.98	8.09	8.29	8.39	–	2.33	2.57	11.09	15.18
22	7.28	7.35	7.38	7.87	–	1.32	2.79	8.05	8.26
23	–	–	7.62	8.66	–	5.01	2.48	9.43	10.77
24	–	7.40	7.60	7.82	–	–	–	8.50	10.40
25	–	–	–	8.39	1.64	3.64	2.44	8.67	10.26[a]

[a] Samples measured in CDCl3.

2.2.3.2 Molecular Structure of Bis-Thiosemicarbazones

The crystal and molecular structures of 2,6-diacetylpyridine-bis-4-*N*-2-pyridyl-BTSC and its -bromo derivatives are presented in **Fig. 7 – 9** as the representative structure, and the crystallography data are presented in **Table 3**. Both compounds were recrystallized from hot DMSO. 2,6-diacetylpyridine-bis-4-*N*-2-pyridyl-BTSC was crystallized as a dimeric compound in the triclinic space group *P-1*, 4-bromo-2,6-diacetylpyridine-bis-4-*N*-2-pyridyl-BTSC was crystallized in the monoclinic space group *P* 2$_1$/*n*. The ligand arms showed open conformations; the conformations were obtained through an *E* configuration about the two hydrazone motifs.[77,78] The crystal arrangement of 2,6-diacetylpyridine-bis-4-*N*-2-pyridyl-BTSC is similar to a tilted edge-to-face herringbone arrangement with three co-crystallized DMSO. 4-bromo-2,6-diacetylpyridine-bis-4-*N*-2-pyridyl-BTSC unit cell also showed a flattened herringbone packing with translated related moieties co-crystallized with DMSO. The average bond distances between C=S (1.69) and C=N (1.29) are consistent with the literature. [77]
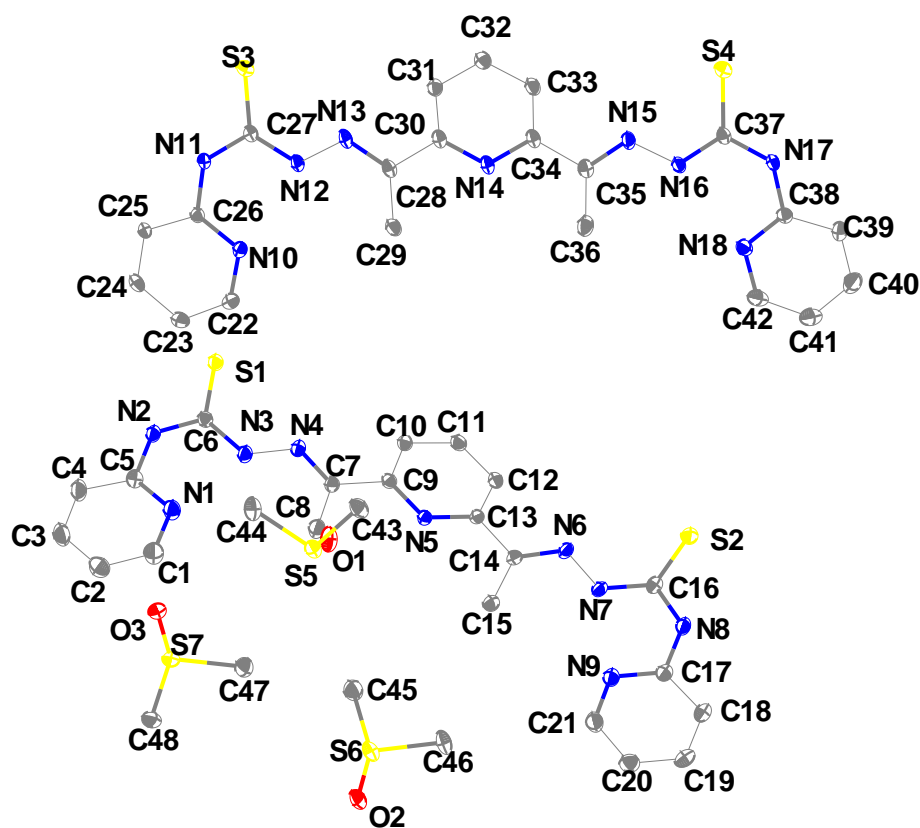
Fig. 7. Molecular structure of 2,6-diacetylpyridine-bis-4-*N*-2-pyridyl-BTSC showing two independent BTSC molecules with 3 co-crystallized DMSO in BTSC·3DMSO, ellipsoids drawn at the 50% probability level.
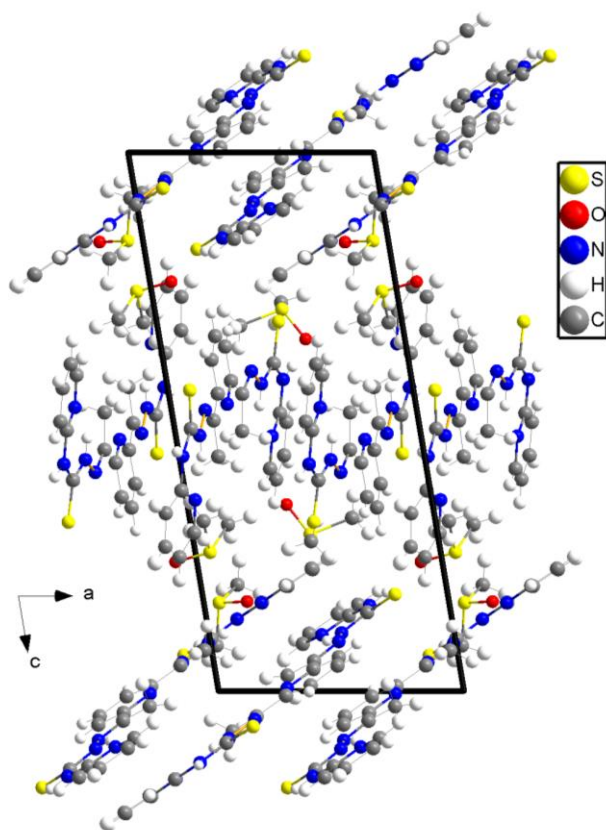
Fig. 8. Crystal structure of 2,6-diacetylpyridine-bis-4-*N*-2-pyridyl-BTSC viewed along the crystallographic *a*-axis with 3 co-crystallized DMSO
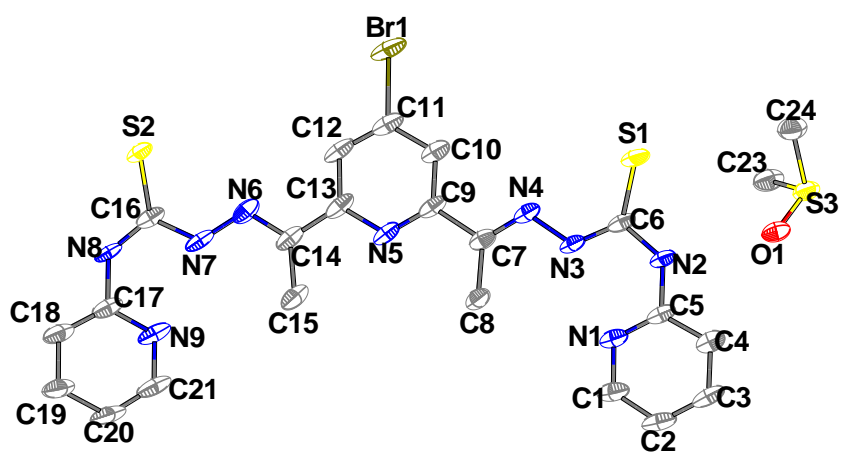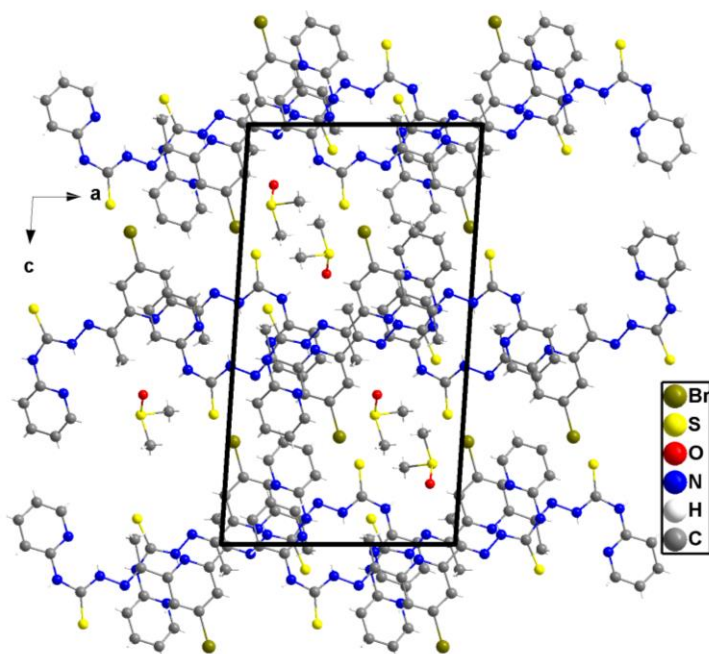
Fig. 9. Molecular structure of 4-bromo-2,6-diacetylpyridine-bis-4-*N*-2-pyridyl-BTSC with 2·EtOH, ellipsoids drawn at the 50% probability level; Crystal structure viewed along the crystallographic *b*-axis (**right**).

Table 3. Cell and refinement parameters of the crystal structures of 2,6-diacetylpyridine-bis-4-*N*-2-pyridyl-BTSC, its *tert*butyl and bromo derivatives.[a]

Compounds	**17**·3DMSO	**17-3**·2EtOH	**17-4**·DMSO
Empirical formula	$C_{24}H_{30}N_9S_{3.5}$	$C_{58}H_{76}N_{18}S_4O_6$	$C_{23}H_{26}BrN_9OS_3$
Formula weight (g/mol)	580.78	1249.62	620.62
Crystal system	Triclinic	Triclinic	Monoclinic
Space group	*P*-1	*P*-1	P2$_1$/n
a (Å)	10.4117(5)	11.0093(5)	11.9508(7)
b (Å)	13.4568(7)	12.1613(6)	10.6152(5)
c (Å)	21.8339(11)	12.2514(5)	21.5916(13)
α (°)	82.427(2)	108.019(2)	90
β (°)	78.435(2)	97.002(2)	93.680(2)
γ (°)	67.895(2)	102.782(2)	90
Volume (Å^3) / Z	2771.4(2) / 2	1488.8(1) / 2	2733.5(3) / 4
ϱ_{calc} (g/cm^{-3})	1.392	1.309	1.508
μ (mm^{-1})	0.344	0.219	1.769

Limiting indices	−14 < h < 14	−15 < h < 15	−14 < h < 14
	−19 < k < 19	−17 < k < 17	−19 < k < 19
	−31 < l < 31	−17 < l < 17	−31 < l < 31
Reflection collected	252789	140417	6797
Independent reflections / R_{int}	16944 / 0.0795	9112 / 0.0486	6797 / 0.0727
Data/restraints/parameters	16944/0/695	9112/ 0 / 376	6797 / 0 / 338
goof on F^2	1.067	1.073	1.087
R_1, wR_2 [$I > 2\sigma(I)$]	0.0530	0.0526	0.0703
R_1, wR_2 (all data)	0.1403	0.1516	0.1479
Residual electrons and holes (e Å^{-3})	1.163/−0.753	1.163/−0.753	0.1203/ 0.1644
CCDC	2181735	2181658	2183984

[a] From single crystal structure determination at 100 K using Mo-Kα radiation (λ = 0.71073 Å). Refinement by full–matrix least–squares methods on $F_0{}^2 \geq 2\sigma(F_0{}^2)$.

2.2.4 Anchoring Bis-Thiosemicarbazone with APTES

Having successfully synthesized BTSC, we proceed with the covalent anchoring of BTSC with different linkers. This is important because one of the goals of this thesis is the covalent anchoring of BTSC with NP. The linker can bind with BTSC and NP at opposite ends. Therefore, three linkers (3-aminopropyl)-triethoxysilane (**APTES**), 3-chloropropyl-trimethoxysilane (**CPTES**), and dopamine hydrochloride were chosen in this study. APTES was anchored with 2,6–diacetyl–pyridine–bis–(4–N–2–ethylaniline)–BTSC via the dicarbonyl backbone (**Scheme 18**), while CPTES and dopamine hydrochloride were anchored with 2,6-diacetylpyridine-bis-(4-N-3-hydroxyl-2pyridyl)-BTSC and 2,6-diacetylpyridine-bis-(4-N-chlorophenyl)-BTSC via the diamine tail (**Scheme 19**). The covalent conjugation of 2,6–diacetyl–pyridine–bis–(4–N–2–ethylaniline)–BTSC with (3-aminopropyl)-triethoxysilane was achieved in THF, while the covalent conjugation of 2,6-diacetylpyridine-bis-(4-N-3-hydroxyl-2pyridyl)-BTSC with 3-chloropropyl-trimethoxysilane and 2,6-diacetylpyridine-bis-(4-N-chlorophenyl)-BTSC with dopamine hydrochloride was achieved in DMF. APTES and CPTES are prone to hydrolysis in DMF. Thus, one arm of APTES and CPTES were isolated as hydrolyzed parts.
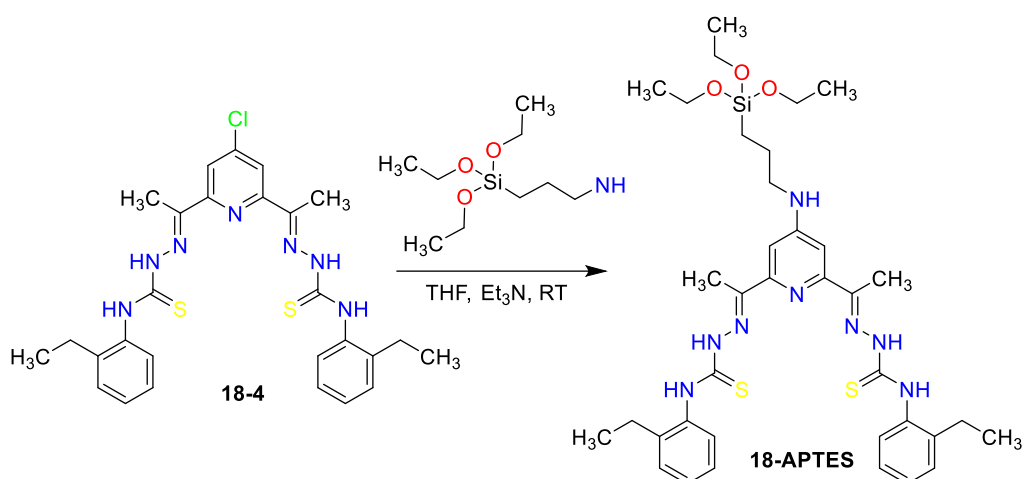
Scheme 18. Conjugation of 2,6–diacetyl–pyridine–bis–(4–*N*–2–ethylaniline)–BTSC with APTES

2.2.4.1 1H NMR of Bis-Thiosemicarbazones conjugate of APTES

The most identified peaks are the pairs of two symmetrical -CH₃, which appeared at 1.31 and 2.52 ppm as part of the parent BTSC. Additional protons in the upfield correspond to the APTES moiety, which includes the three -CH₃ at 1.58 ppm and the six -CH₂ appearing at 1.23, 2.73 and 3.83 ppm. The new amide bond was found at 5.66 ppm (**Fig. 10**). The symmetric hydrazine protons appeared downfield at 8.92 and 9.19 ppm, consistent with the parent BTSC described earlier (**Fig. 11**).
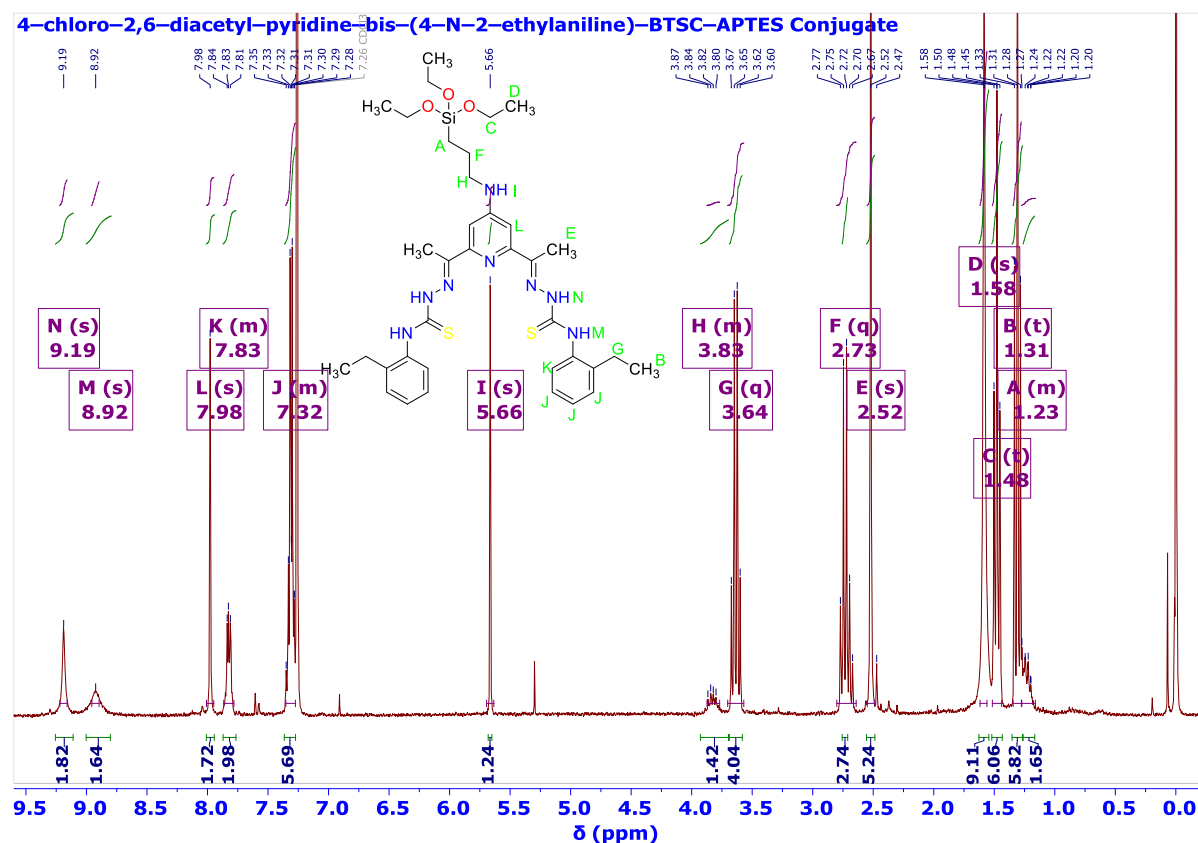
Fig. 10. 1H NMR spectrum of 4–chloro–2,6–diacetyl–pyridine–bis–(4–*N*–2–ethylaniline)–BTSC–APTES conjugate, sample measured in CDCl₃.
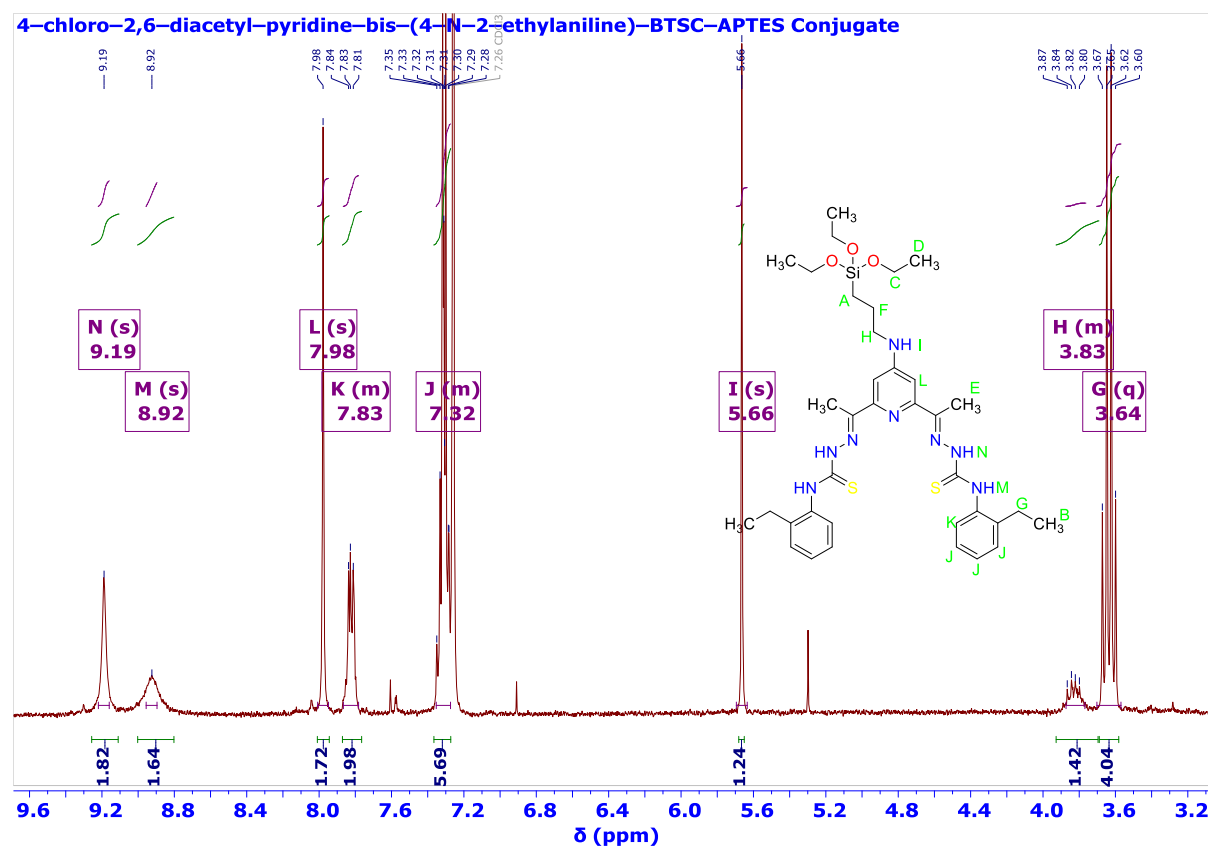
Fig. 11. 1H NMR spectrum of 4–chloro–2,6–diacetyl–pyridine–bis–(4–*N*–2–ethylaniline)–BTSC–APTES conjugate showing a magnified portion of the spectrum. Sample measured in CDCl₃.

2.2.5 Anchoring Bis-Thiosemicarbazone with Dopamine

Having conjugated BTSC with (3-aminopropyl)-triethoxysilane at the dicarbonyl site, we focus on conjugating BTSC with dopamine at the diamine tail. 2,6-diacetylpyridine-bis-(4-N-chlorophenyl)-TSCwas dissolved in DMF, and Et₃N was dopamine hydrochloride was added (**Scheme 19**).
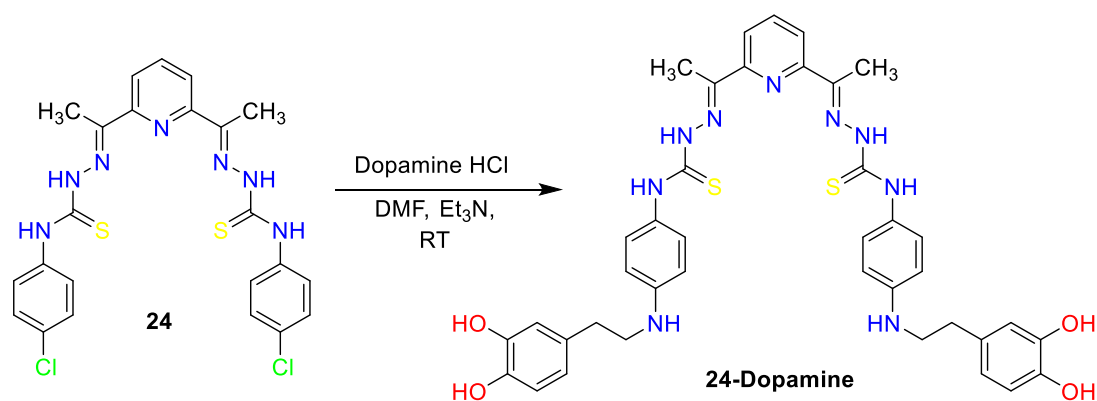
Scheme 19. Conjugation of Compound **24** with dopamine

2.2.5.1 1H NMR of Bis-Thiosemicarbazone with Dopamine

The 1H NMR spectra showed the symmetrical -CH$_3$ at 2.55 ppm, and the alkyl chain from the dopamine moiety appeared at 2.38 and 2.69 ppm (**Fig. 12**). The new amide bond appeared at 6.56 ppm. The aryl moiety of the dopamine appeared at 6.69, 7.35 and 8.81 ppm. The dicarbonyl signals appeared at 7.86 and 8.56 ppm. The hydrazine protons appeared downfield at 10.24 and 10.81 ppm (**Fig. 13**). Thiol-thione tautomeric character is visible in the 1H NMR spectrum of 2,6-diacetylpyridine-bis-(4-*N*-chlorophenyl)-BTSC–Dopamine conjugate. This character is also visible in the 1H NMR spectrum of unconjugated 2,6-diacetylpyridine-bis-(4-*N*-chlorophenyl)-BTSC (**Fig. 14**).
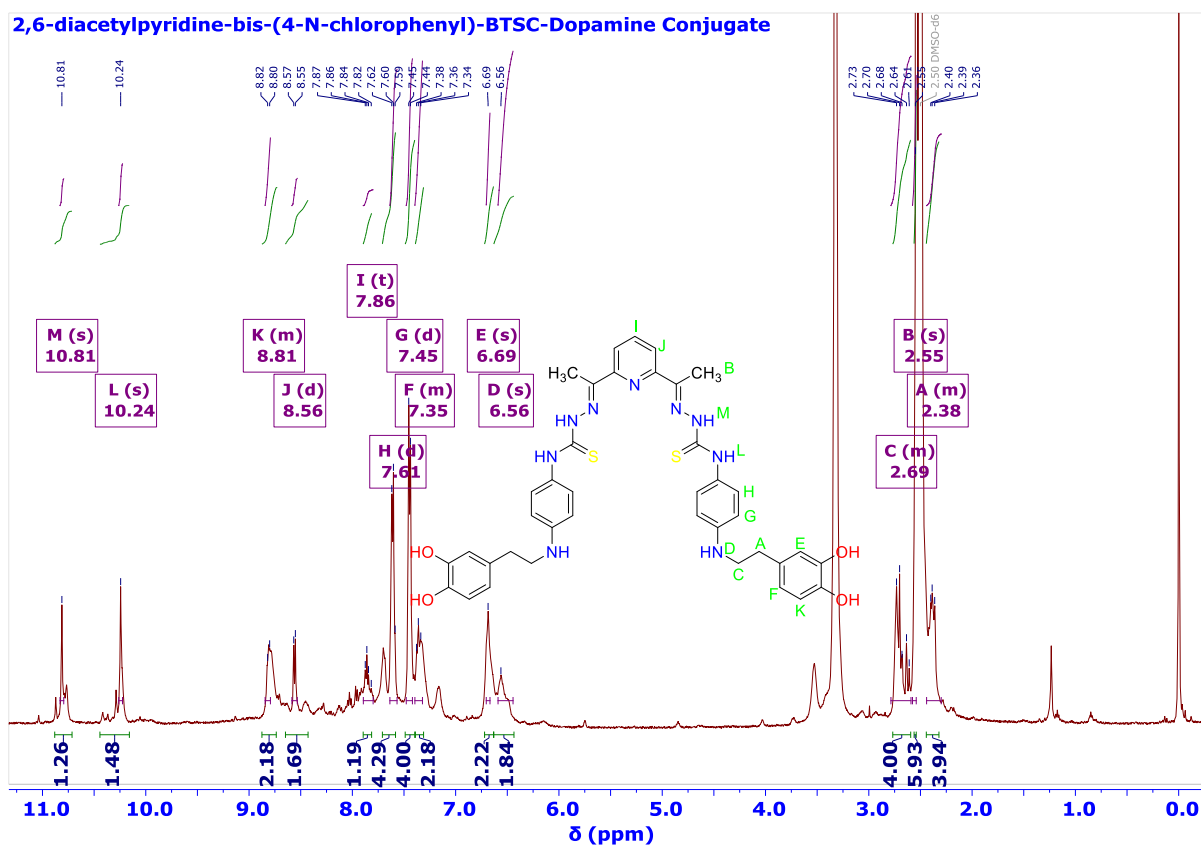
Fig. 12. 1H NMR spectrum of 2,6-diacetylpyridine-bis-(4-*N*-chlorophenyl)-BTSC measured in DMSO–d₆.
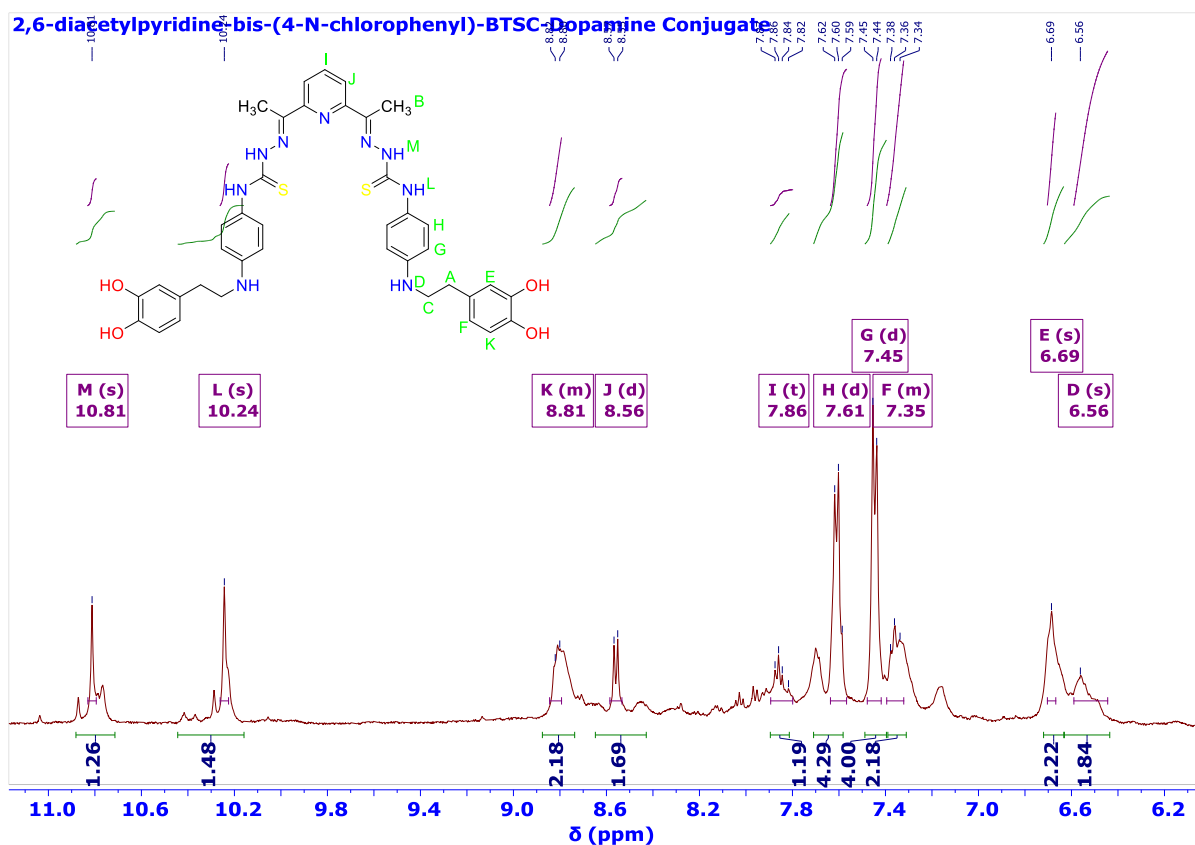
Fig. 13. 1H NMR spectrum of 2,6-diacetylpyridine-bis-(4-*N*-chlorophenyl)-BTSC–Dopamine conjugate. A magnified portion of the spectrum. Sample measured in DMSO–d₆.
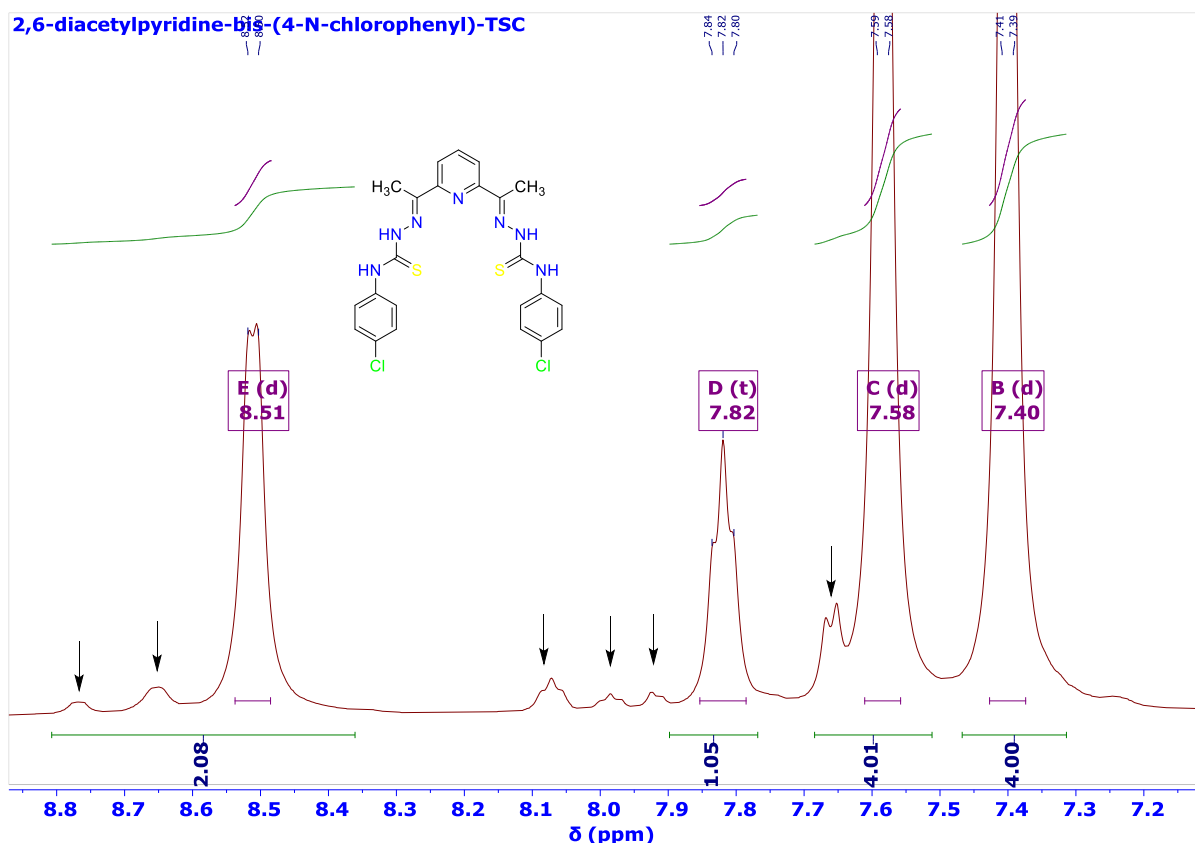
Fig. 14. Magnified 1H NMR spectrum of unconjugated 2,6-diacetylpyridine-bis-(4-*N*-chlorophenyl)-BTSC. Showing the minor tautomeric characters. Sample measured in DMSO–d₆.

2.2.6 Synthesis of Pentadentate Bis-Thiosemicarbazone Metal Complexes

The BTSC metal complexes were obtained by deprotonating BTSC with triethylamine, followed by coordination with metal ions. The metal complexes were obtained in good yield (55 – 90%).

2.2.6.1. 1H NMR of BTSC complexes.

The Pd complexes spectra showed the most interesting features due to the bonding. Several single protons were observed rather than the appearance of several two protons signals. The coordination of BTSC with Pd ions caused the BTSC Pd complex to lose its symmetry. A representative 1H NMR is presented in **Fig. 15**. The usual single protons of the free ligand associated with the two -CH₃ from the dicarbonyl backbone now appeared as two singlets upfield δ = 2.3 and 2.6 ppm, and the dicarbonyl aryl protons also appeared as two asymmetrical protons at δ = 7.9 and 7.88 ppm. The aryl protons at the ortho and meta position of the thiosemicarbazide moiety are also asymmetric, appearing at δ = 8.87 and 8.32 ppm and δ = 7.04 and 8.11 ppm, respectively. The uncoordinated hydrazine proton appeared as a singlet downfield (δ = 10.3 ppm) in contrast to the two hydrazine signals observed for the free ligand.
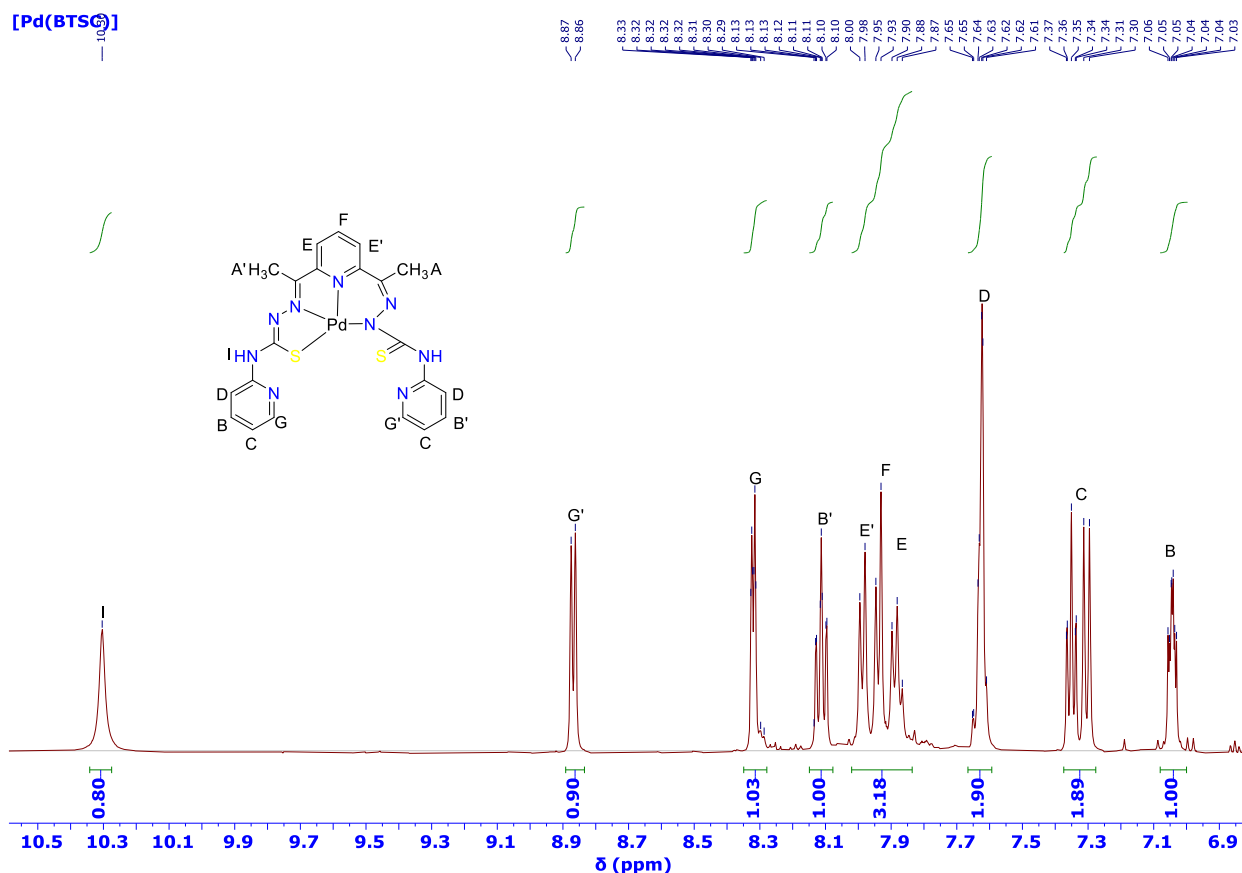
Fig. 15. Magnified portion of the 1H NMR spectrum of Pd complex of 2,6-diacetylpyridine-bis-(4-*N*-2-pyridyl)-BTSC measured in DMSO–d₆.

The representative 1H NMR of Zn complexes is presented in **Fig. 16**. The Zn complex has retained its symmetry. Thus, most signals appeared as two protons in the NMR spectra. The two symmetrical CH₃ protons appeared as a single at δ = 2.3 ppm, and the uncoordinated hydrazine protons appeared at δ = 9.0 ppm. The distinguishable proton which divides both arms appeared as a triplet at δ = 8.1 ppm, and the aryl protons from the thiosemicarbazide moiety appeared at δ = 7.05, 7.76, 7.87 and 8.28 ppm. Unlike Pd complex of BTSC, the Zn complex of the pentadentate BTSC has retained its symmetry.
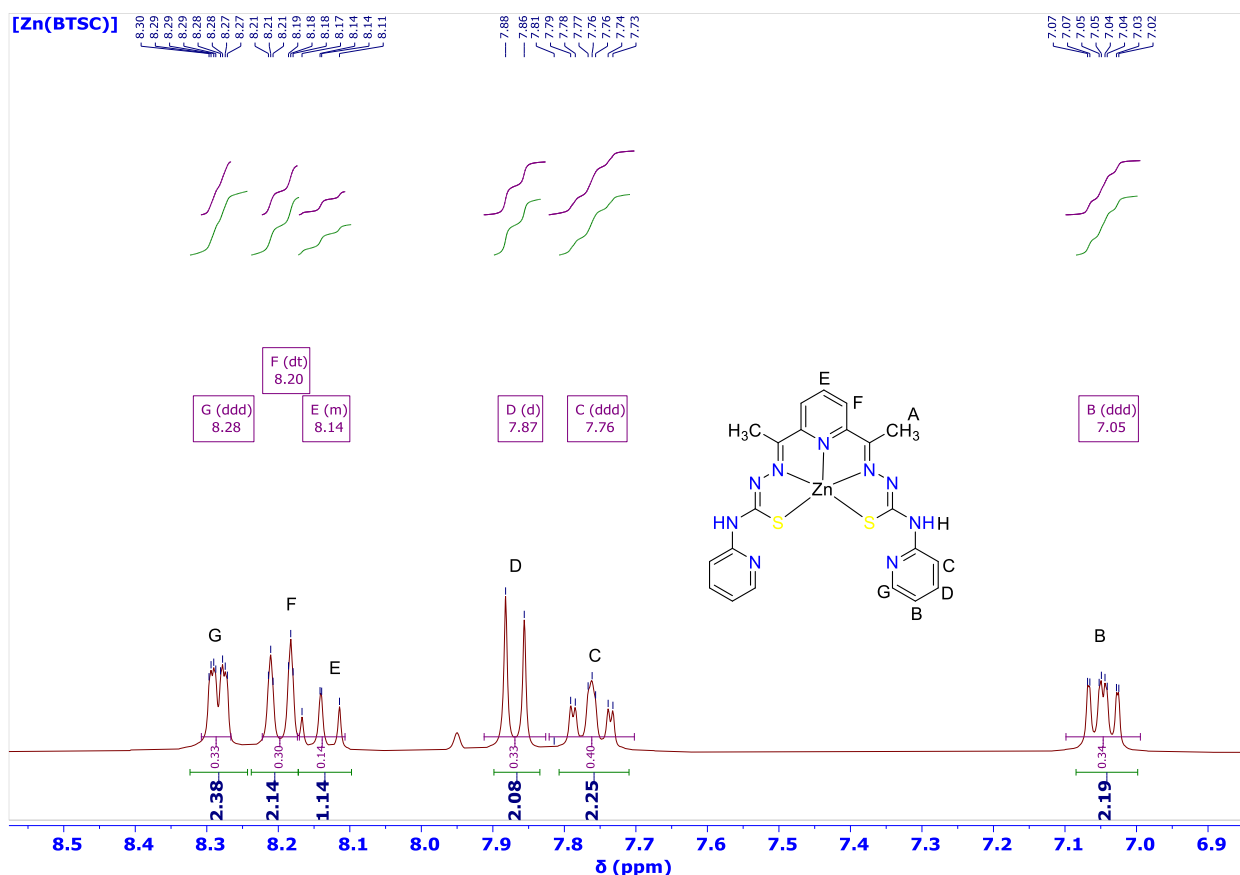
Fig. 16. Magnified portion of the 1H NMR spectrum of Zn complex of 2,6-diacetylpyridine-bis-(4-*N*-2-pyridyl)-BTSC measured in DMSO–d₆.

2.2.6.2 Molecular Structure of Bis-Thiosemicarbazone Metal Complexes

Single crystals, suitable for X-ray diffraction, were obtained for Pd and Zn complexes of 2,6–diacetyl–pyridine–bis–(4–*N*–2–ethylaniline)–BTSC; Cu complex of 2,6–diacetyl–pyridine–bis–(4–*N*–2–ethylaniline)–BTSC was also included as part of the synthesis of metal sulfide in future studies. Cu and Pd single crystals were obtained by slow evaporation in DCM, while Zn single crystal was obtained by the vapour diffusion of pentane over DCM. The crystal structure and molecular structures are shown in **Fig. 17**, and interatomic distances and angles are given in **Table 4** and **5**. [Cu(BTSC)] was isolated as a dimeric neutral compound exhibiting a trigonal bipyramidal geometry. Each Cu atom is coordinated as S^N^N^N^S, bridging through N–imine from either arm of the BTSC. [Cu(BTSC)] is predominantly a thiolate complex, with an average C–S bond distance of 1.73 [Å]. The distance (3.4 [Å]) between Cu–Cu suggests no metal-metal interaction. [Pd(BTSC)] is a neutral mononuclear complex exhibiting square-planar coordination with a slight distortion attached in a tetradentate binding through S^N^N^N (**Fig. 18**). The thione–thiol character of the complex is noticeable from the bond length between coordinated C–S (1.760 Å) and uncoordinated C=S (1.688 Å).

The bond distance between N–N (1.366 and 1.372 Å) and C–N (1.290, 1.311 and 1.307 Å) is intermediate between formal single and double bonds, indicative of delocalised electrons.[70,79] [Zn(BTSC)] was also isolated as a binuclear neutral compound, exhibiting a distorted square planar coordination. Each Zn atom is surrounded by two imines (N) and two thiols (S) atoms from both arms of the BTSC, forming two pairs of five-member rings (**Fig. 19**). Interestingly, the tetradentate coordination S^N^S^N does not include the pyridinic nitrogen. The average bond distance between M–N and M–S is comparable with reported complexes of BTSC.[80–82]
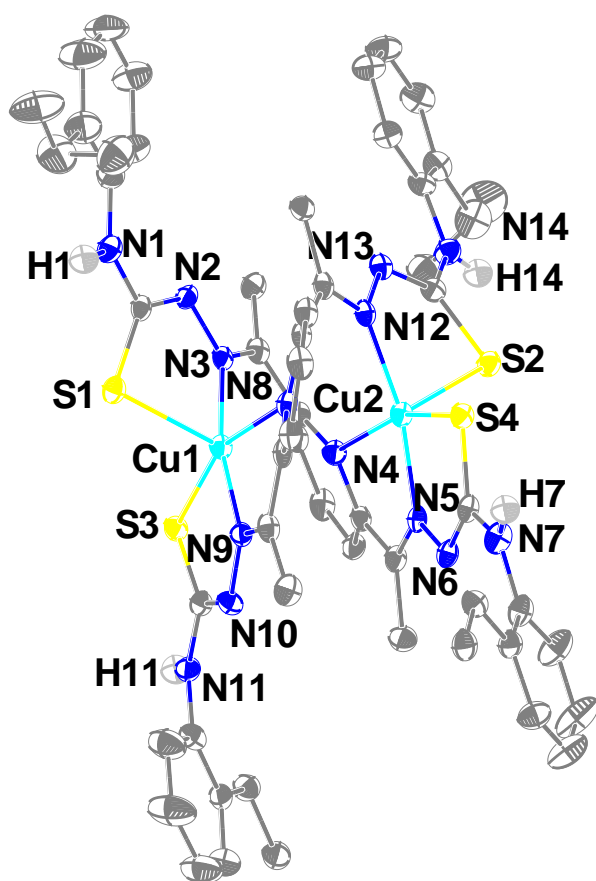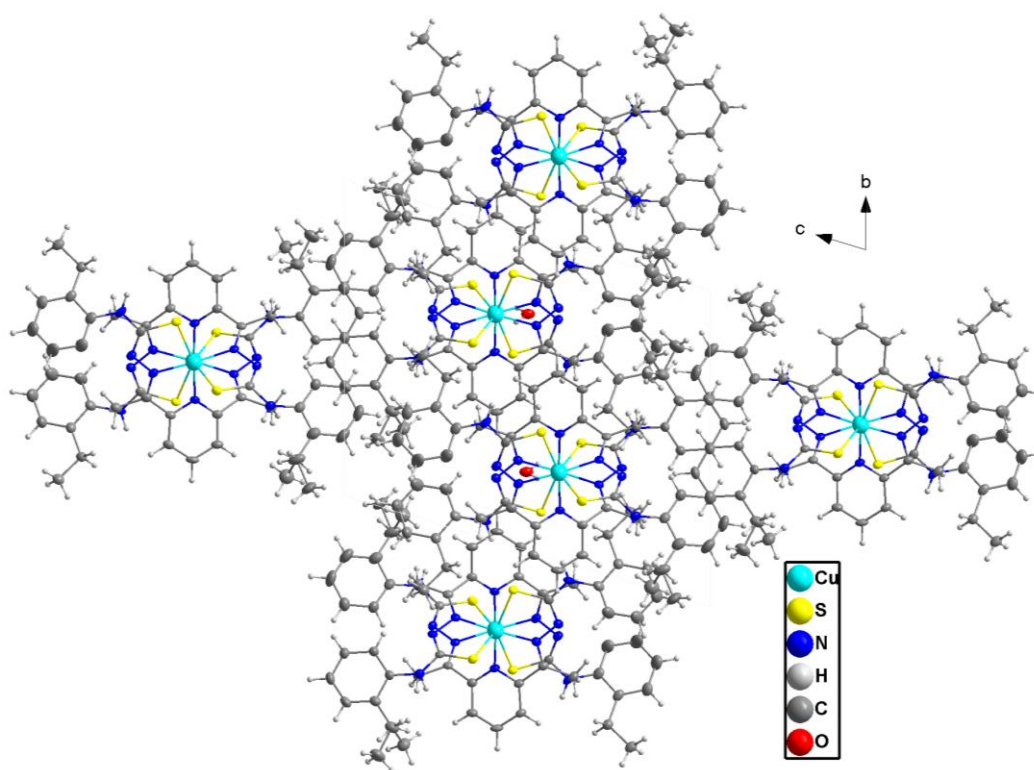
Fig. 17. Molecular structure and the molecular packing of Cu complex of 2,6–diacetyl–pyridine–bis–(4–*N*–2–ethylaniline)–BTSC, [Cu(BTSC)]·H₂O with a co-crystalized H₂O, projected along the *a*-axis.
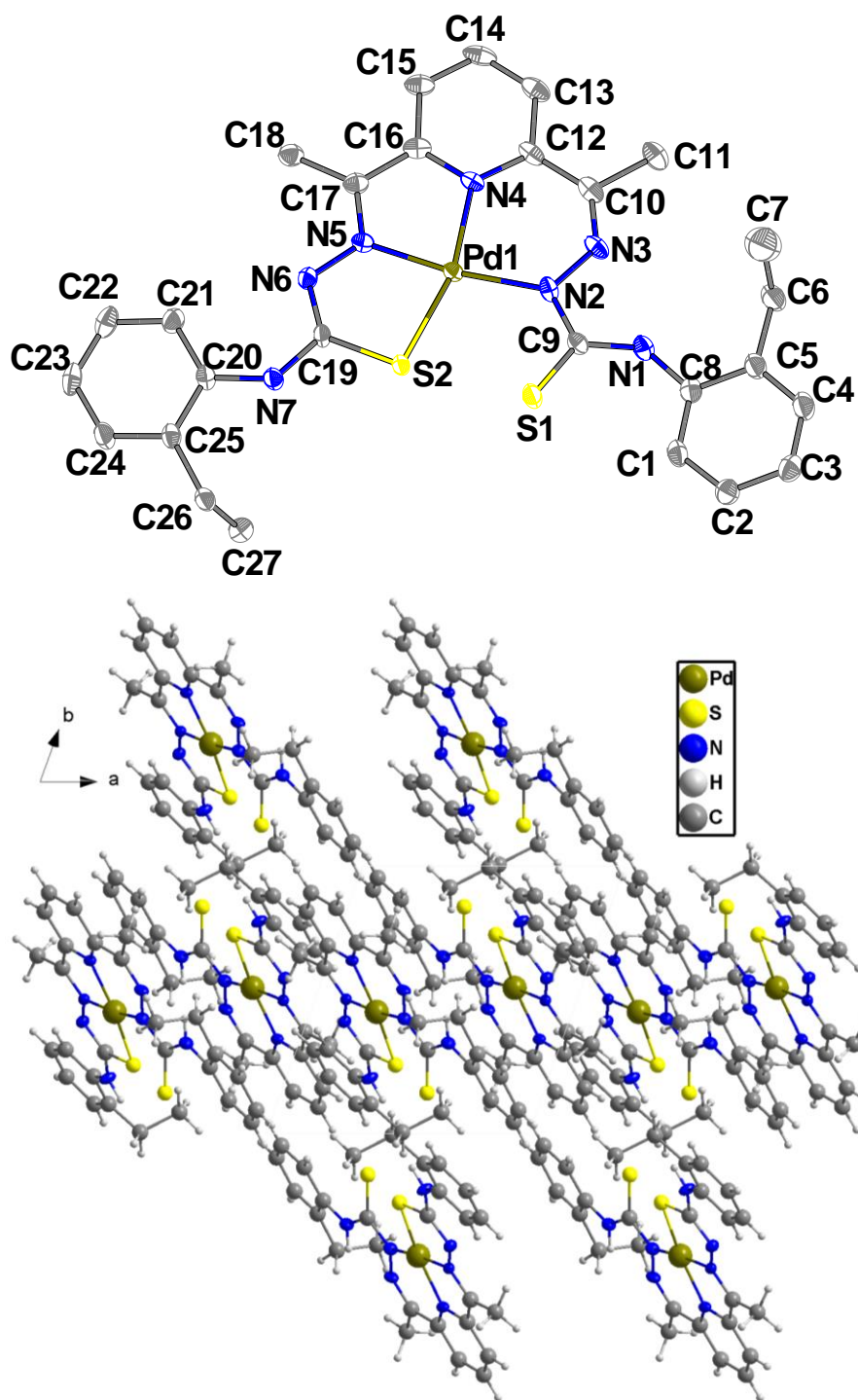
Fig. 18. Molecular structure and the molecular packing of Pd complex of 2,6–diacetyl–pyridine–bis–(4–N–2–ethylaniline)–BTSC, [Pd(BTSC)], projected along the *c*-axis.
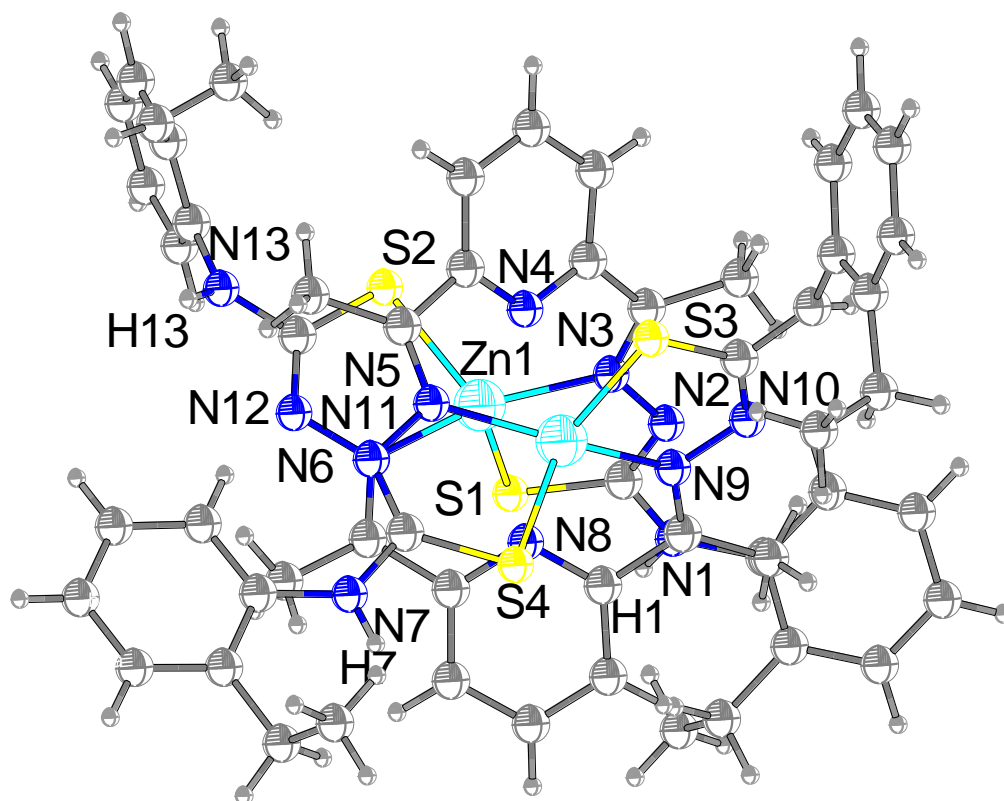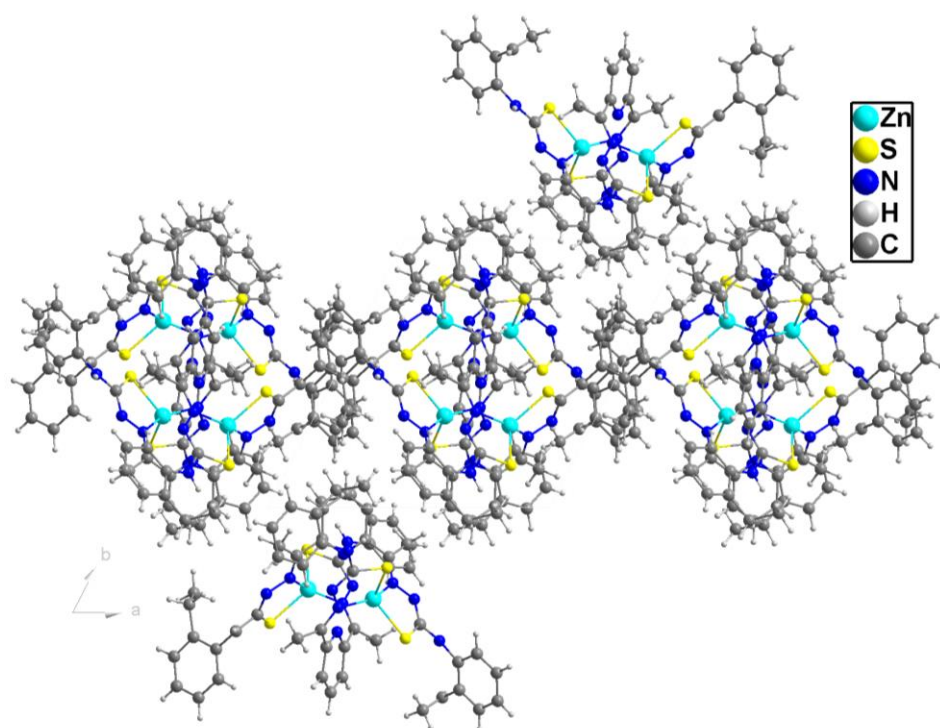
Fig. 19. Molecular structure and the molecular packing of Zn complex of 2,6–diacetyl–pyridine–bis–(4–*N*–2–ethylaniline)–BTSC, [(Zn(BTSC)], projected along the *c*-axis.

Table 4. Cell and refinement parameters of the crystal structures of Cu, Pd and Zn complexes of 2,6–diacetyl–pyridine–bis–(4–N–2–ethylaniline)–BTSC.[a]

	[Cu(BTSC)]·H_2O	[Pd(BTSC)]	[Zn(BTSC)]
Empirical formula	$C_{54}H_{59}N_{14}OS_4Cu_2$	$C_{27}H_{29}N_7S_2Pd$	$C_{55}H_{57}N_{13}S_4Zn_2$
Formula weight (g/mol)	1175.47	622.09	1159.209
Crystal system	Triclinic	Triclinic	Triclinic
Space group	P-1	P-1	P-1
a (Å)	11.153(2)	9.0446(10)	13.9789(9)
b (Å)	14.739(3)	10.0562(14)	14.1130(9)
c (Å)	18.201(3)	15.539(2)	16.6446(12)
α (°)	71.985(7)	75.797(5)	78.212(3)
β (°)	77.609(7)	86.605(5)	68.387(2)
γ (°)	81.240(7)	69.854(5)	60.583(2)
Volume (Å^3) / Z	2767.0(9) / 2	1285.8(3) / 2	2658.1(3) / 2
ϱ_{calc} (g/cm^{-3})	1.411	1.607	1.448
μ (mm^{-1})	0.972	0.916	1.112
Limiting indices	-14 ≤ h ≤ 14	-12 ≤ h ≤ 12	-19 ≤ h ≤ 19
	-19 ≤ k ≤ 19	-13 ≤ k ≤ 13	-20 ≤ k ≤ 20
	-24 ≤ l ≤ 24	-20 ≤ l ≤ 20	-23 ≤ l ≤ 23
Reflection collected	153669	61769	208553
Independent reflections / R_{int}	13897 / 0.0983	6413 / 0.0813	16261 / 0.0763
Data/restraints/parameters	13897/2/711	6413/0/338	16261/0/675
goof on F^2	1.046	1.105	1.047
R_1, wR_2 [$I > 2\sigma(I)$]	0.0721	0.0472	0.0504
R_1, wR_2 (all data)	0.0975	0.1224	0.0737
Residual electrons and holes (e Å^{-3})	2.47/-1.09	2.66/-0.67	1.40/-1.39
CCDC	2371292	2248575	2389147

[a] From single crystal structure determination at 100 K using Mo-Kα radiation (λ = 0.71073 Å). Refinement by complete–matrix least–squares methods on $F_0^2 \geq 2\sigma(F_0^2)$.

Table 5. Selected experimental metrics Cu, Pd and Zn complexes of 2,6–diacetyl–pyridine–bis–(4–N–2–ethylaniline)–BTSC.

	[Cu(TSC) [a]		[Pd(TSC) [a]		[Zn(TSC) [a]

	distances (Å)		distances (Å)		distances (Å)
Cu(1)–S(3)	2.3290(11)	Pd–S(2)	2.2946(10)	Zn(1)–S(1)	2.3630(8)
Cu(1)–S(1)	2.4379(12)	Pd–N(4)	2.042(3)	Zn(1)–S(2)	2.3500(7)
Cu(1)–N(9)	1.964(4)	Pd–N(5)	1.987(3)	Zn(1)–S(3)	2.3509(7)
Cu(1)–N(3)	1.998(3)	Pd–N(2)	2.032(3)	Zn(1)–S(4)	2.3487(8)
Cu(1)–N(8)	2.200(3)	S(2)–C(19)	1.760(4)	Zn(1)–N(3)	2.051(2)
Cu(2)–S(4)	2.3290(11)	S(1)–C(9)	1.688(4)	Zn(1)–N(11)	2.050(2)
Cu(2)–S(2)	2.4336(12)	N(4)–C(16)	1.356(5)	Zn(2)–N(5)	2.058(2)
Cu(2)–N(5)	1.967(4)	N(4)–C(12)	1.344(5)	Zn(2)–N(9)	2.051(2)
Cu(2)–N(12)	1.996(4)	N(5)–N(6)	1.366(4)	S(1)–C(19)	1.735(3)
Cu(2)–N(4)	2.204(3)	N(5)–C(17)	1.307(5)	S(2)–C(47)	1.732(3)
S(4)–C(20)	1.730(4)	N(2)–N(3)	1.372(4)	S(3)–C(37)	1.724(3)
S(3)–C(37)	1.743(4)	N(2)–C(9)	1.395(5)	S(4)–C(9)	1.745(3)
S(2)–C(47)	1.731(4)	N(6)–C(19)	1.311(5)	N(3)–N(2)	1.381(3)
S(1)–C(10)	1.730(4)	N(3)–C(10)	1.290(5)	N(9)–N(10)	1.370(3)
N(5)–N(6)	1.381(5)	N(1)–C(9)	1.355(5)	N(5)–N(6)	1.383(3)
N(9)–N(10)	1.378(5)	N(1)–C(8)	1.411(5)	N(11)–N(12)	1.372(3)
N(3)–N(2)	1.380(5)	N(7)–C(19)	1.365(5)	C(17)–N(3)	1.295(3)
N(12)–N(13)	1.390(5)	N(7)–C(20)	1.410(5)	C(10)–N(5)	1.292(3)
		angles (º)			
S(3)–Cu(1)–S(1)	104.00(4)	N(4)–Pd–S(2)	163.23(9)	S(1)–Zn(1)–S(2)	112.25(3)
N(9)–Cu(1)–S(3)	83.47(10)	N(5)–Pd–S(2)	82.92(9)	S(4)–Zn(1)–S(3)	116.72(3)
N(9)–Cu(1)–S(1)	108.37(10)	N(5)–Pd–N(4)	80.36(13)	N(3)–Zn(1)–S(2)	114.12(6)
N(9)–Cu(1)–N(3)	167.88(14)	N(5)–Pd–N(2)	172.54(13)	N(3)–Zn(1)–S(1)	83.58(6)
N(9)–Cu(1)–N(8)	78.10(13)	N(2)–Pd–S(2)	104.49(10)	N(11)–Zn(1)–S(1)	106.79(6)
N(3)–Cu(1)–S(3)	99.48(10)	N(2)–Pd–N(4)	92.24(13)	N(11)–Zn(1)–N(3)	153.47(9)
N(3)–Cu(1)–S(1)	82.45(10)	C(19)–S(2)–Pd	94.64(13	S(4)–Zn(2)–S(3)	116.72(3)
N(3)–Cu(1)–N(8)	96.72(13)	C(16)–N(4)–Pd	112.2(2)	N(5)–Zn(2)–S(3)	109.62(6)
N(8)–Cu(1)–S(3)	159.31(10)	C(12)–N(4)–Pd	120.8(3)	N(5)–Zn(2)–S(4)	84.13(6)
N(8)–Cu(1)–S(1)	90.79(9)	C(12)–N(4)–C(16)	120.8(3)	N(9)–Zn(2)–S(3)	85.23(6)
S(4)–Cu(2)–S(2)	104.31(4)	N(6)–N(5)–Pd	125.2(2)	N(9)–Zn(2)–S(4)	110.85(7)
N(5)–Cu(2)–S(4)	83.44(10)	C(17)–N(5)–Pd	117.0(3)	N(9)–Zn(2)–N(5)	152.07(9)

N(5)–Cu(2)–S(2)	108.14(10)	C(17)–N(5)–N(6)	117.7(3)	C(47)–S(2)–Zn(1)	92.38(9)
N(5)–Cu(2)–N(12)	167.97(13)	N(3)–N(2)–Pd	121.6(3)	C(37)–S(3)–Zn(2)	92.16(9)
N(5)–Cu(2)–N(4)	78.01(13)	N(3)–N(2)–C(9)	109.5(3)	C(9)–S(4)–Zn(2)	93.04(9)
N(12)–Cu(2)–S(4)	99.42(10)	C(9)–N(2)–Pd	128.9(2)	C(19)–S(1)–Zn(1)	91.84(9)
N(12)–Cu(2)–S(2)	82.6(1)	C(19)–N(6)–N(5)	128.9(2)	N(2)–N(3)–Zn(1)	120.03(16)
N(12)–Cu(2)–N(4)	96.85(13)	C(10)–N(3)–N(2)	128.9(4)	C(17)–N(3)–Zn(1)	123.47(18)

2.2.6.3 FT-IR Spectroscopy of Bis-Thiosemicarbazone Metal Complexes

2,6–diacetyl–pyridine–bis–(4–N–2–ethylaniline)–BTSC and its Cu^{2+}, Pd^{2+} and Zn^{2+} complexes will be selected as the representative vibration to give a specific overview of the vibration of BTSC complexes. Thus, the vibrational bands of the Cu^{2+}, Pd^{2+} and Zn^{2+} complexes of 2,6–diacetyl–pyridine–bis–(4–N–2–ethylaniline)–BTSC are compared with the uncoordinated ligand (**Fig. 20**). The free ligands is characterized by a distinct vibrations for N–H (1591, 2959 and 3295 cm^{-1}), C=S (755, 1156 and 1258 cm^{-1}) and C=N (1259 cm^{-1}), comparable with reported TSC.[83–86] The vibrational contribution from C–H, phenyl ring and C=C are noticeable around 530, 634, and 1318 cm^{-1}. For the BTSC metal coordinated system, a new vibration around 1720 cm^{-1} appeared, corresponding to C=N. The initial C=N vibration (1510 cm^{-1}) shifted or/and deformed (1408 cm^{-1} for Cu complex, 1453 cm^{-1} for Pd complex and 1445 cm^{-1} for Zn complex.[87,88] The coordinative contribution from C=S and N–H is noticeable by the deformation and shifting of bands. The N–H singlet vibration (2959 cm^{-1}) in the free ligand deformed into a doublet for all the complexes. Similarly, the N–H doublet vibration (3295 cm^{-1}) in the free ligand deformed into a narrow singlet for the Cu complex, a broad singlet for the zinc complex and a wide-broad singlet for the Pd complex. The changes in the vibrations are evidence of the successful coordination of BTSC with the metal ions.
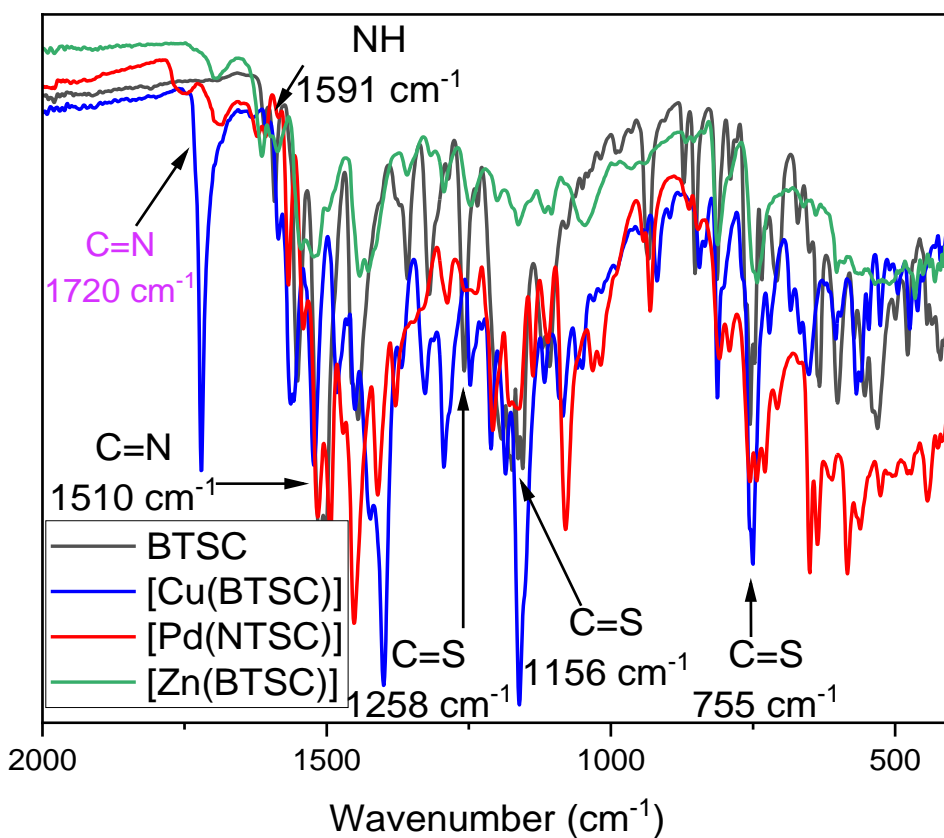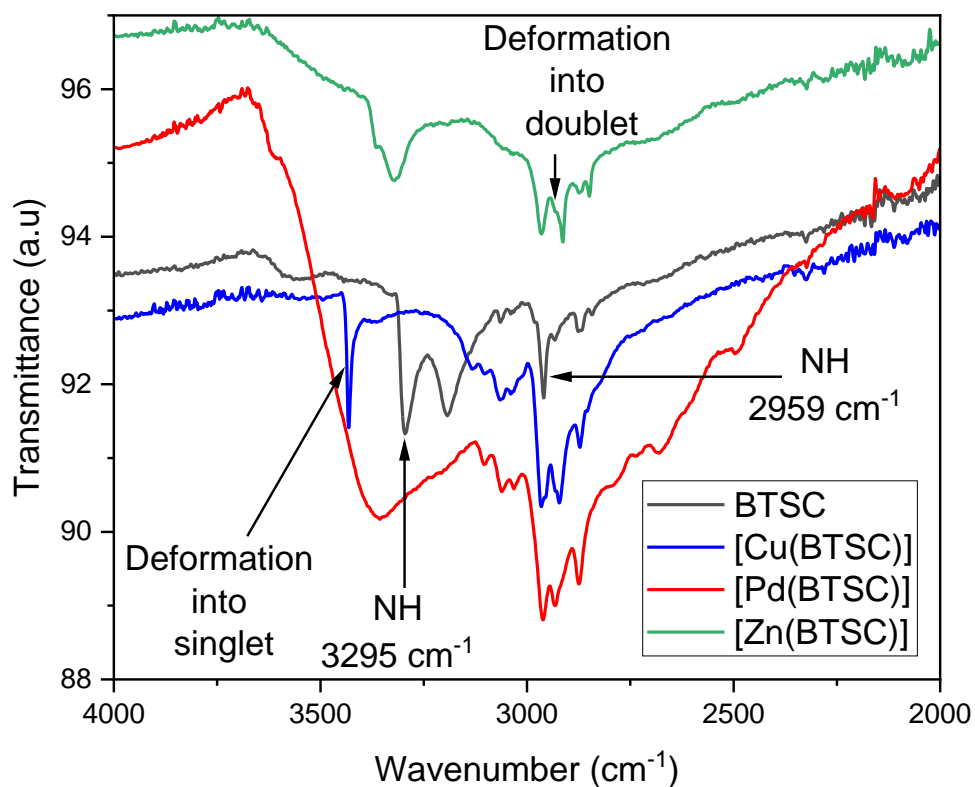
Fig. 20. FT-IR spectra of Cu²⁺, Pd²⁺ and Zn²⁺ complexes of 2,6–diacetyl–pyridine–bis–(4–*N*–2–ethylaniline)–BTSC ligands recorded between 400 – 4000 nm.

2.2.7 Synthesis of Bis-Thiosemicarbazone NP Conjugates.

Fe₃O₄, SiO₂ and Fe₂O₃ were the three NPs used in the thesis. Fe_3O_4 was chosen for its magnetic properties, and SiO_2 and Fe_2O_3 were selected for their biological relevance.

2.2.7.1 Synthesis of Fe₃O₄–APTES–BTSC Nanoparticle Conjugates

Fe_3O_4 NP was conjugated with BTSC (2,6-diacetylpyridine-bis-(4-*N*-2-pyridyl)-BTSC) via the well-established 1-ethyl-3-(3-dimethylaminopropyl)carbodiimide (EDC)/*N,N′*-dicyclohexylcarbodiimide (NHS) coupling route.[89,90] In the EDC/NHS coupling, an amide bond is formed from the reaction between carboxylate and amine functional groups (**Scheme 20**). In this case, ester-functionalized BTSC was synthesized by the condensation of Compound **1** (2–pyridyl-thiosemicarbazide) with Compound **11** (4–methyl–isonicotinate–2,6–diacetyl–pyridine). The hydrolysis of 4-methyl-isonicotinate 2,6-diacetylpyridine-bis-(4-*N*-2-pyridyl)-BTSC in DMF using saturated NaOH affords a carboxylic acid-functionalized BTSC (2,6-diacetylpyridine-4-carboxylic acid-bis-(4-*N*-2-pyridyl)-BTSC). Fe_3O_4 was obtained from a mixture of Fe^{2+} and Fe^{3+} salts via co-precipitation in a separate reaction. The obtained Fe_3O_4 NP was coated with triethoxy-(ethyl)silane (TOES) to obtain $Fe_3O_4@SiO_2$ and was conjugated with (3-aminopropyl)-triethoxysilane (APTES).[91] $Fe_3O_4@SiO_2$–APTES–BTSC was eventually obtained by reacting pre-functionalized $Fe_3O_4@SiO_2$–APTES with carboxylate functionalized BTSC. The covalent conjugation of $Fe_3O_4@SiO_2$–APTES with BTSC was achieved in DMF for 24 hours.
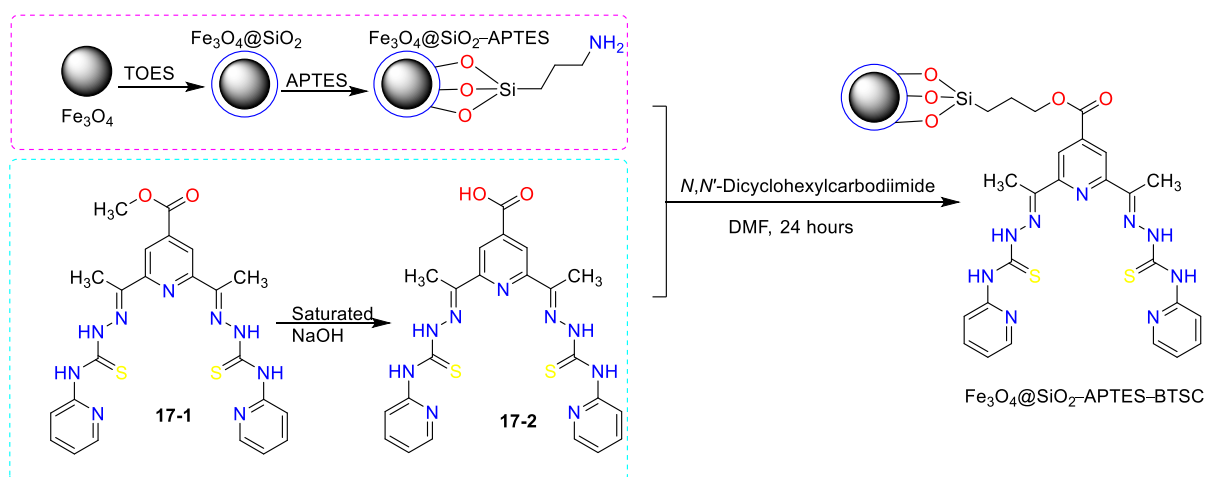
Scheme. 20. Hydrolysis of 4-methyl-isonicotinate 2,6-diacetylpyridine-bis-(4-*N*-2-pyridyl)-BTSC to afford the carboxylic functional group and conjugation of Fe_3O_4 with 2,6-diacetylpyridine-4-carboxylic acid-bis-(4-*N*-2-pyridyl)-BTSC .

2.2.7.2 1H NMR of Carboxylate Functionalized Bis-Thiosemicarbazone

The hydrazine protons for 4-methyl-isonicotinate 2,6-diacetylpyridine-bis-(4-*N*-2-pyridyl)-BTSC appeared at δ = 15.09 and 11.20 ppm (**Fig. 21**). The most identifying signals are the two symmetrical -CH₃ groups, 2.6 ppm. while the methyl group associated with the ester functional group appeared at δ = 3.9 ppm. The hydrazine protons for 2,6-diacetylpyridine-4-carboxylic acid-bis-(4-*N*-2-pyridyl)-TSC shifted downfield δ = 15.1 and 11.24 ppm on hydrolysis of the ester group (**Fig. 22**).
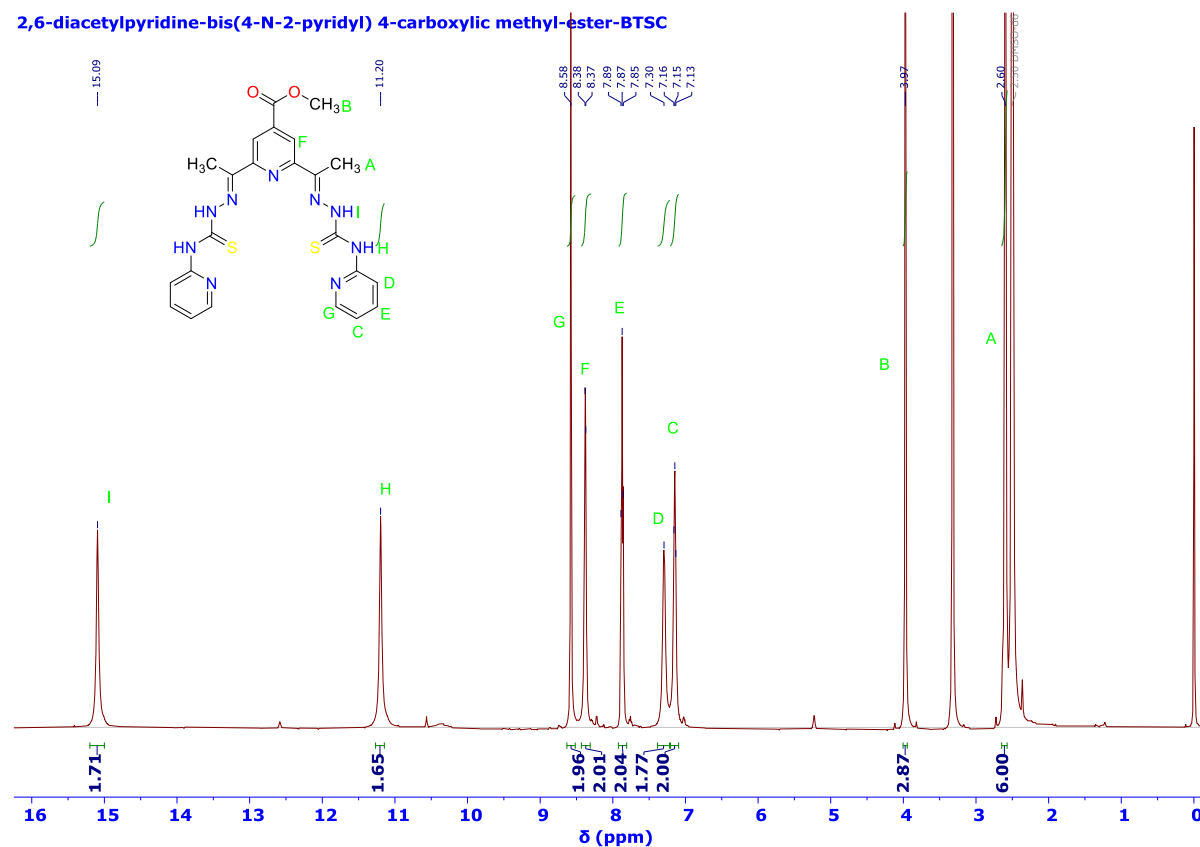
Fig. 21. 1H NMR spectrum of 4-methyl-isonicotinate 2,6-diacetylpyridine-bis-(4-*N*-2-pyridyl)-BTSC measured in DMSO–d₆.
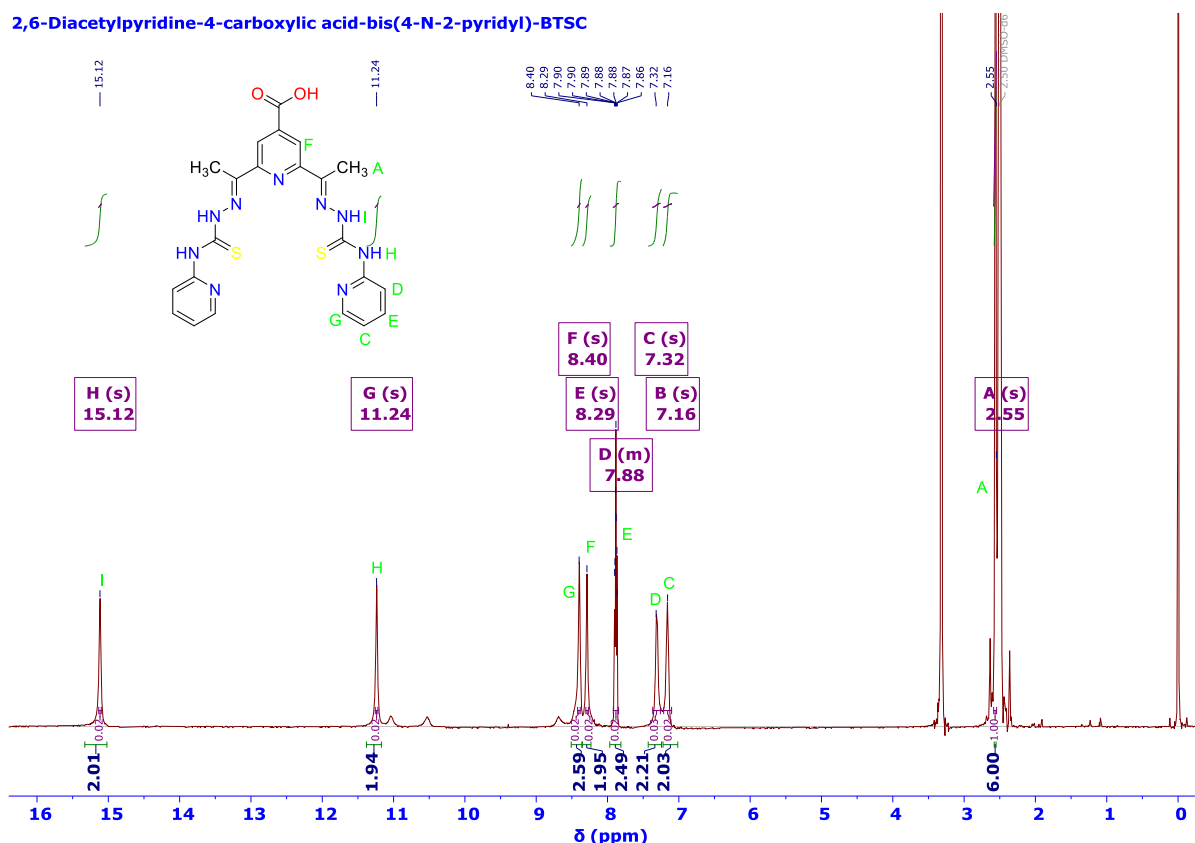
Fig. 22. 1H NMR spectrum of 2,6-diacetylpyridine-4-carboxylic acid-bis-(4-*N*-2-pyridyl)-BTSC measured in DMSO–d$_6$

2.2.7.3 FT-IR Spectroscopy of Fe$_3$O$_4$–APTES–BTSC Nanoparticles Conjugates

2,6-diacetylpyridine-bis-(4-*N*-2-pyridyl)-BTSC spectra showed several sharp and narrow bands at 516, 639, 767, 832, 1149, 1200, 1339, 1347, 1428, 1524 and 1603 cm^{-1}. The intense band at 767, 1149, 1524 and 1603 cm^{-1} correspond to out-of-plane bending of N-H, C=N stretching, N-H bending, and C=C bond stretching, based on comparison with 3,5-dimethyl-1*H*-pyrrole-2-carboxylate-4-thiosemicarbazone.[92,93] The C=S stretching was assigned to the band at 832 and 1428 cm^{-1}, and the aromatic ring associated C=N bond was observed at 1339 cm^{-1}. The weak broadband at 2882 and 3194 cm^{-1} suggests a symmetric N-H stretching since the asymmetric N-H band produces a strong band.[92,93] These sets of bands appeared for 4-methyl-isonicotinate 2,6-diacetylpyridine-bis-(4-*N*-2-pyridyl)-BTSC and 2,6-diacetylpyridine-4-carboxylic acid-bis-(4-*N*-2-pyridyl)-BTSC. The ester group and the corresponding OH vibration for 2,6-diacetylpyridine-4-carboxylic acid-bis-(4-*N*-2-pyridyl)-BTSC were observed as an intense band at 1727 cm^{-1} and 3247 cm^{-1}, respectively, with the appearance of a carboxylate signal at 1646 cm^{-1} (**Fig. 23**).
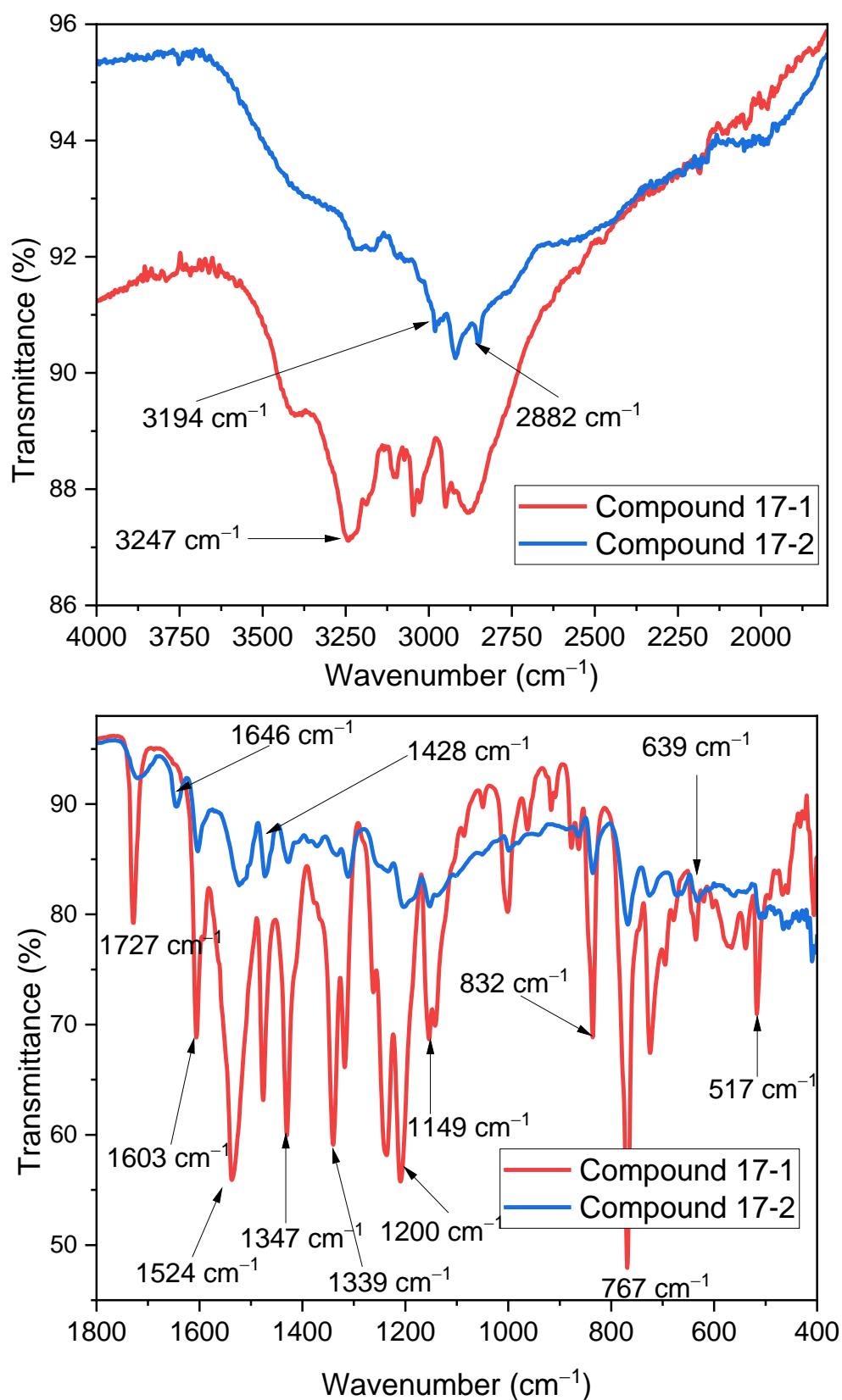
Fig. 23. FT-IR spectra of 4-methyl-isonicotinate 2,6-diacetylpyridine-bis-(4-*N*-2-pyridyl)-BTSC (**17-1**) and 2,6-diacetylpyridine-4-carboxylic acid-bis-(4-*N*-2-pyridyl)-BTSC (**17-2**) recorded between 400 – 4000 nm.

The pristine Fe_3O_4 exhibits two characteristic bands at 547 cm^{-1} and 3357 cm^{-1}, corresponding to Fe–O–Fe bond deformation and the O–H stretching (**Fig. 24**).[94] On coating Fe_3O_4 with TEOS, the band corresponding to the asymmetric stretching vibration of Si–O–Si bond and C–H bending appeared as an intense peak at 1067 cm^{-1} and a broad signal at 1638 cm^{-1}, respectively.[95] On pre-functionalization with APTES, a band for the symmetric N–H bending mode appeared at 2982 cm^{-1} confirming the presence of –NH functional group.[55] The covalent bonding of 2,6-diacetylpyridine-4-carboxylic acid-bis-(4-*N*-2-pyridyl)-BTSC with $Fe_3O_4@SiO_2$–APTES forming $Fe_3O_4@SiO_2$–APTES–BTSC caused the appearance of additional bands at 1477 cm^{-1} (C=C and C–C stretching), 1532 cm^{-1} (C=N stretching), 1591 cm^{-1} (C=S stretching) and 1606 cm^{-1} (N–H scissoring).[22,96]
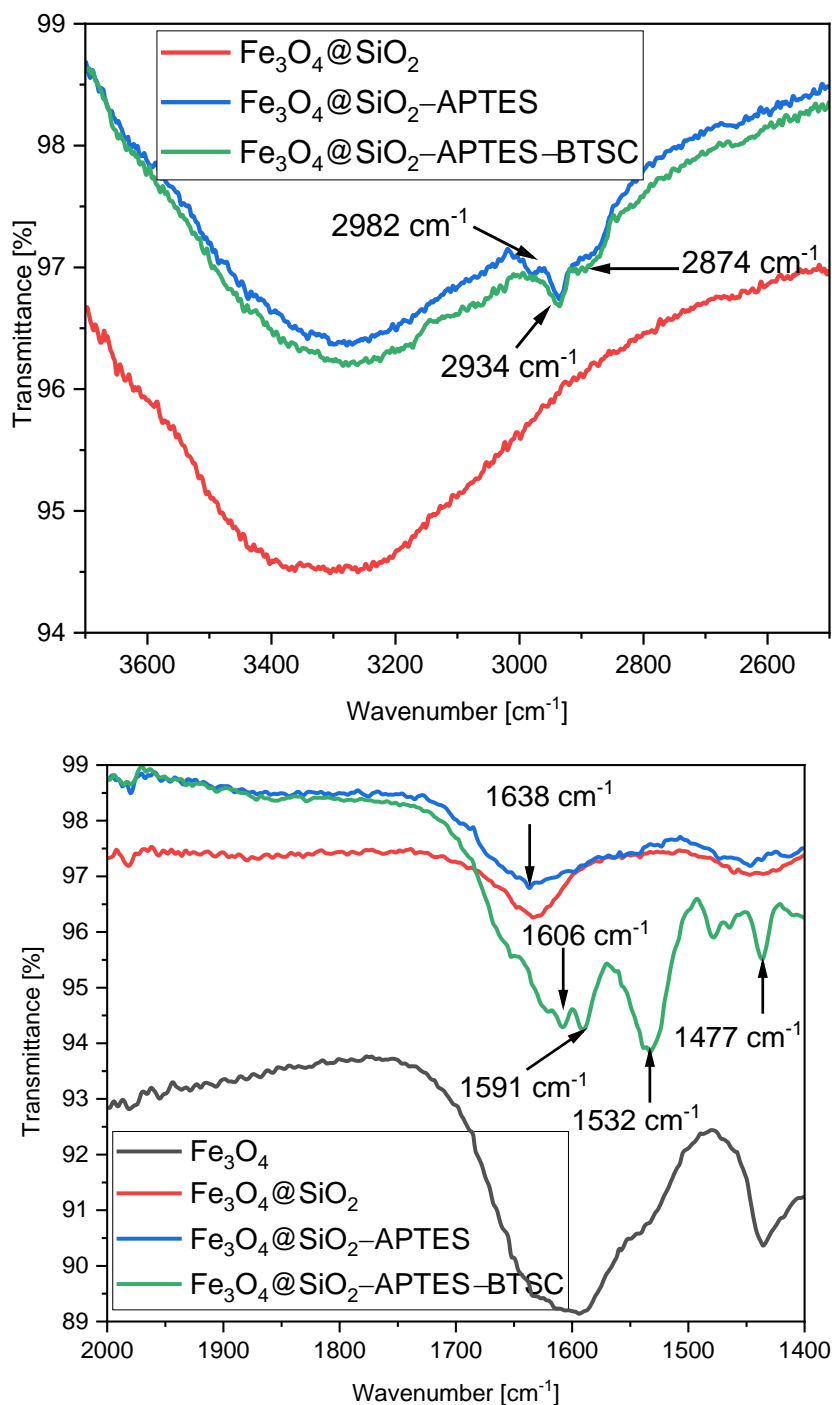
Fig. 24. FT-IR spectra of Fe_3O_4, $Fe_3O_4@SiO_2$, $Fe_3O_4@SiO_2–APTES$ and $Fe_3O_4@SiO_2–APTES–BTSC$ recorded between 400 – 4000 nm.

2.2.7.4 Powder XRD Patterns of $Fe_3O_4–APTES–BTSC$

The powder X-ray diffraction (PXRD) patterns of the Fe_3O_4, $Fe_3O_4@SiO_2–APTES$ and $Fe_3O_4@SiO_2–APTES–BTSC$ NPs are shown in **Fig. 25**. The Miller indices (202, 311, 400, 422, 511, 404, 533 and 731) observed from the PXRD patterns of the Fe_3O_4 NPs were comparable with spinel magnetite phase

(JCPDS: 19-0629). The crystallite size was calculated using the Debye–Scherrer equation D = $0.89\lambda/\beta\cos(\theta)$, where $\lambda = 0.7093$ (wavelength), β is the Full Width at Half Maxima (FWHM) of the most substantial peak (311). The sharp peaks align with the nanocrystalline character (crystallinity index = 78% and crystallite size = 72 nm) of the Fe_3O_4 sample. Coating the Fe_3O_4 NPs with the silane derivatives (Triethoxy(ethyl)silane (TOES) and (3-aminopropyl)-triethoxysilane (APTES)) caused a reduction in the crystallinity index to 48% and an increase in the crystallite size (84 nm). Finally, covalent functionalization with 2,6-diacetylpyridine-4-carboxylic acid-bis-(4-*N*-2-pyridyl)-BTSC further reduced the crystallinity index to 35% and a slight increase in the crystallite size (86 nm), in keeping with the surface functionalization through non-crystalline molecular entities.
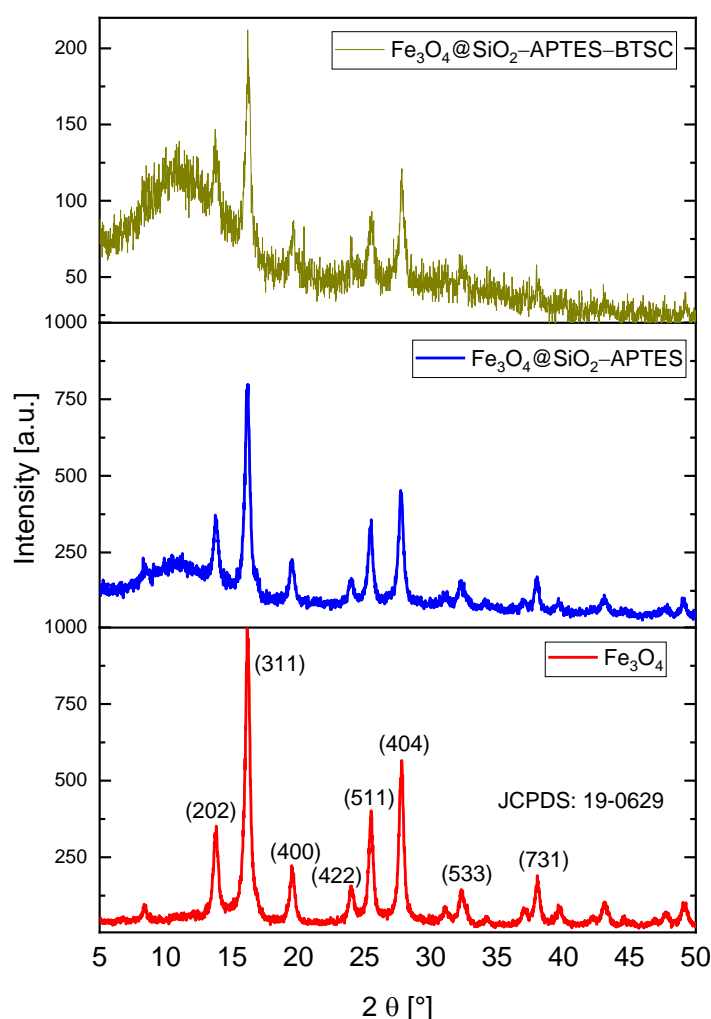
Fig. 25. PXRD patterns of Fe₃O₄, Fe₃O₄@SiO₂–APTES and Fe₃O₄@SiO₂–APTES–BTSC. JCPDS 19-0629 represents magnetite Fe₃O₄.

2.2.7.5 SEM and EDX Investigation of Fe₃O₄@SiO₂–APTES–BTSC Nanoparticles

Scanning electron microscopy (SEM) images of the Fe$_3$O$_4$@SiO$_2$–APTES–BTSC showed non-defined nanoparticles with some agglomeration (**Fig. 2.14**). The Energy Dispersive X-ray (EDX) analysis showed the presence of Fe, O, Si, C, N and S (**Fig. 2.15**).
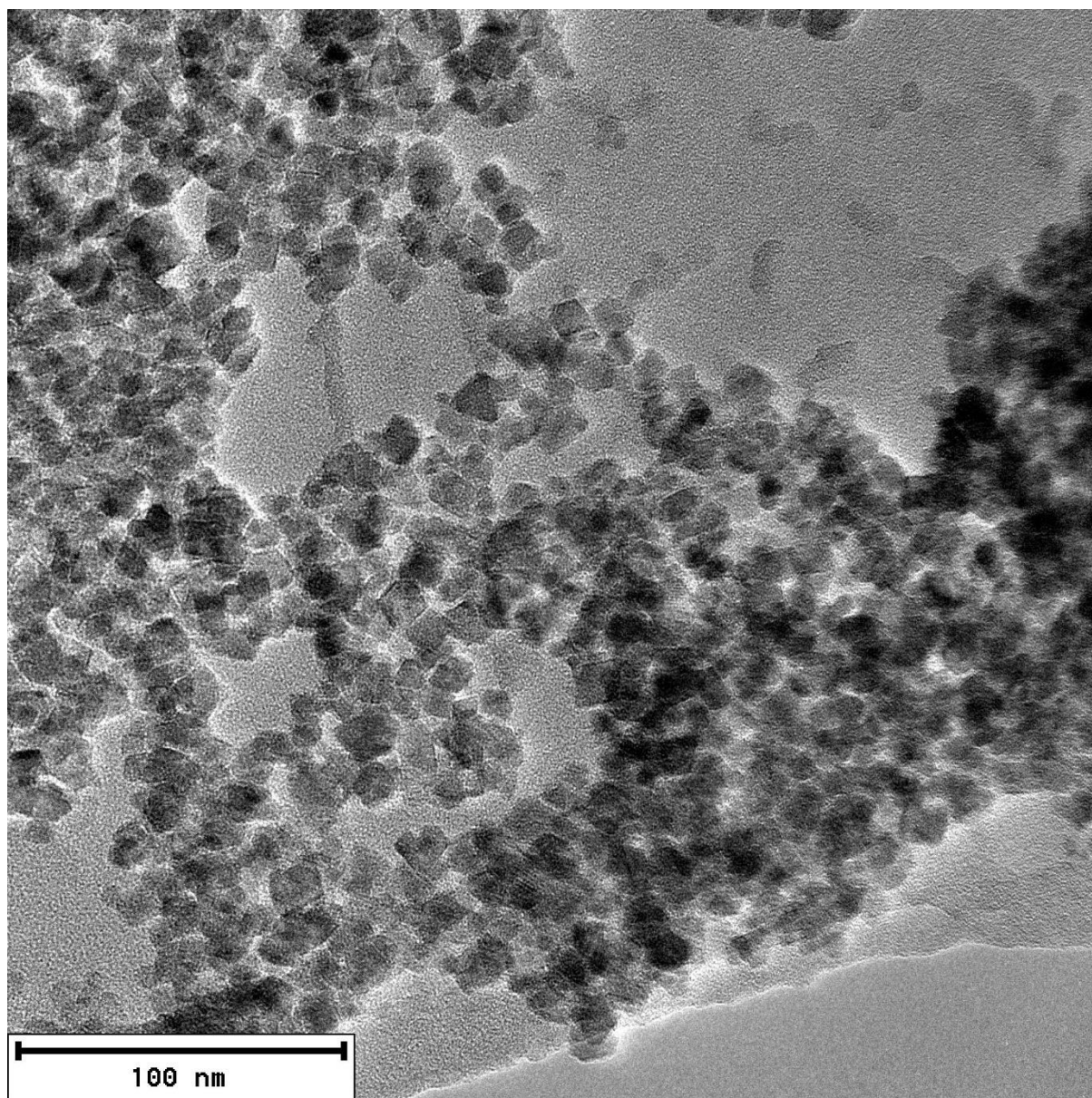
Fig. 26. SEM image of Fe$_3$O$_4$@SiO$_2$–APTES–BTSC NPs
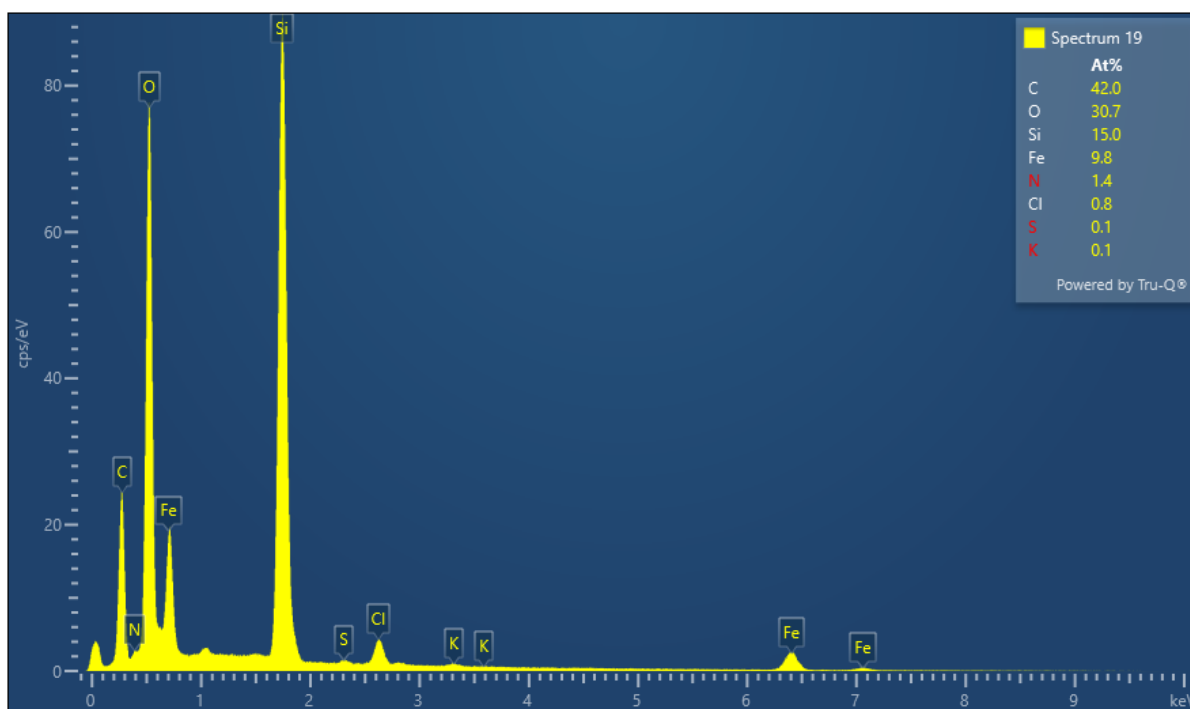
Fig. 27. EDX analysis of Fe$_3$O$_4$@SiO$_2$–APTES–BTSC

2.2.7.6 Thermogravimetry Analysis.

The thermal behaviour of the NPs (Fe$_3$O$_4$, Fe$_3$O$_4$@SiO$_2$–APTES and Fe$_3$O$_4$@SiO$_2$–APTES–BTSC) were examined using thermogravimetric analysis (TGA) under an inert (N$_2$) atmosphere (**Fig. 2.16**). Minimal weight loss was observed for the non-functionalized Fe$_3$O$_4$ NPs compared to Fe$_3$O$_4$@SiO$_2$–APTES and Fe$_3$O$_4$@SiO$_2$–APTES–BTSC. The Fe$_3$O$_4$ NPs was characterized by a two-step weight loss corresponding to adsorbed solvents (0.74%) and the release of surface functional groups or residual organic entities of Fe$_3$O$_4$ NPs (9.2%), respectively.[97] The amino-functionalized Fe$_3$O$_4$@SiO$_2$–APTES NPs are characterized by three-step weight losses (14.4%). The Fe$_3$O$_4$@SiO$_2$–APTES–BTSC adsorbent was also characterized by three-step weight losses, however, with a total weight loss of 16.8%. The additional weight loss compared to Fe$_3$O$_4$@SiO$_2$–APTES is attributed to the covalently bonded BTSCs.
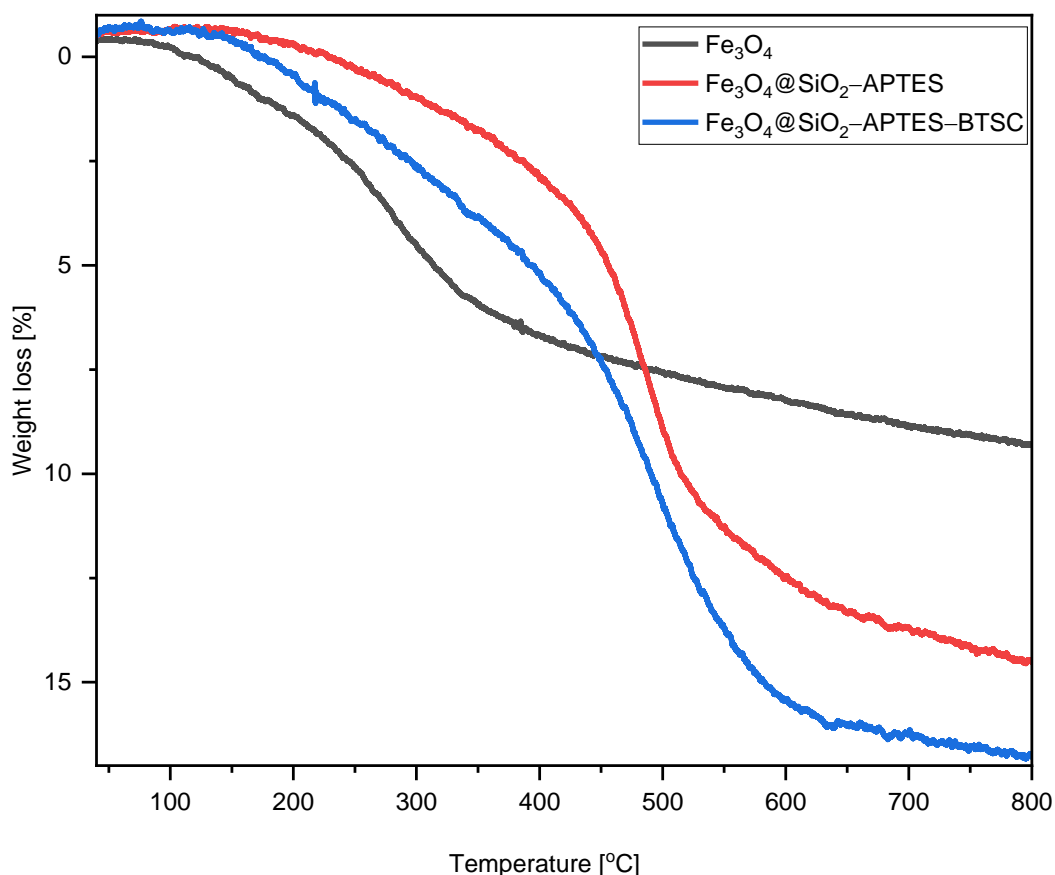
Fig. 28. TGA curve of Fe₃O₄, Fe₃O₄@SiO₂–APTES and Fe₃O₄@SiO₂–APTES–BTSC.

2.2.7.7 X-ray Photoelectron Spectroscopy of Fe₃O₄@SiO₂–APTES–BTSC NPs.

The XPS survey spectrum of the Fe₃O₄@SiO₂–APTES–BTSC NP showed signals for Fe, O, Si, N, C, and S at binding energies of 711.39, 532.39, 399.39, 338.72, 284.89, 228.22, and 103.39 eV, respectively (**Fig. 29**).[98] High-resolution XPS of the C 1s signals shows signals at 284.80, 286.30, 287.80, and 288.80 eV corresponding to different chemical environments such as C–C, C–OH, C=O, O–C=O, respectively.[99] The small peaks (%Area = 1.38 and 9.31) at 295.32 and 292.00 eV are impurities stemming from CF₃COOH. The N 1s signals of Fe₃O₄@SiO₂–APTES–BTSC at 399.2, 400.6 and 402.8 eV (**Fig. 29**) are related to pyridine N,[100,101] amide N,[102] and imine N atoms.[103]
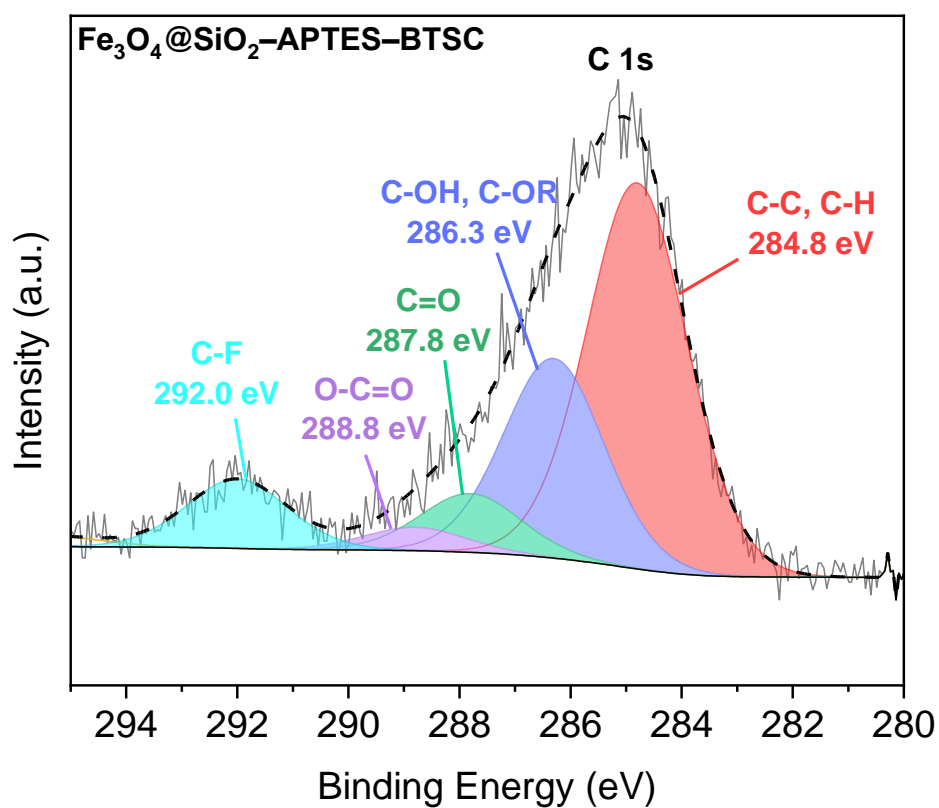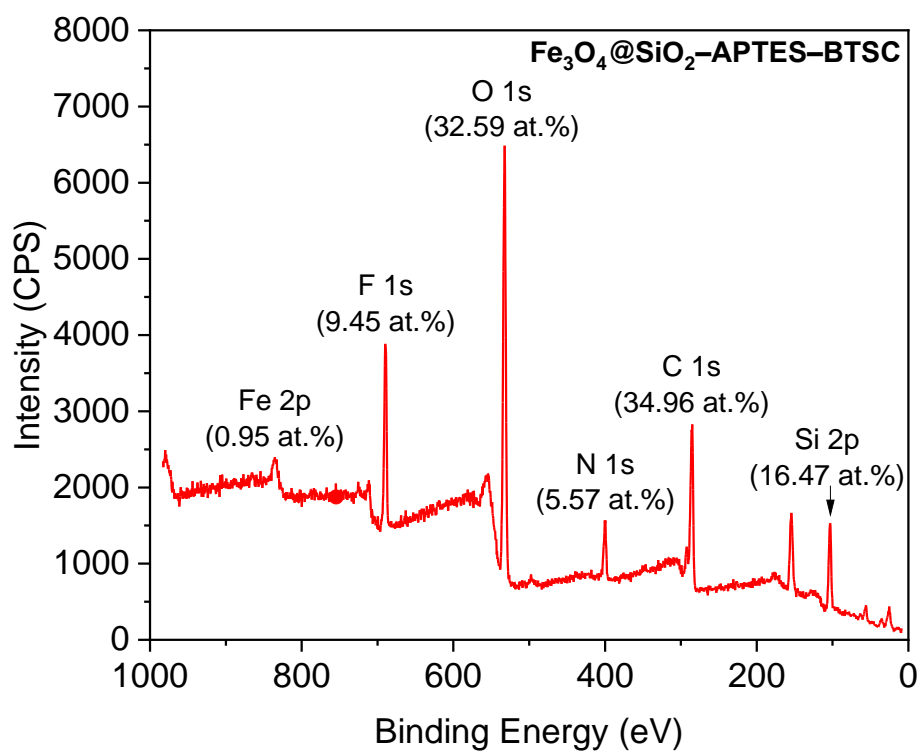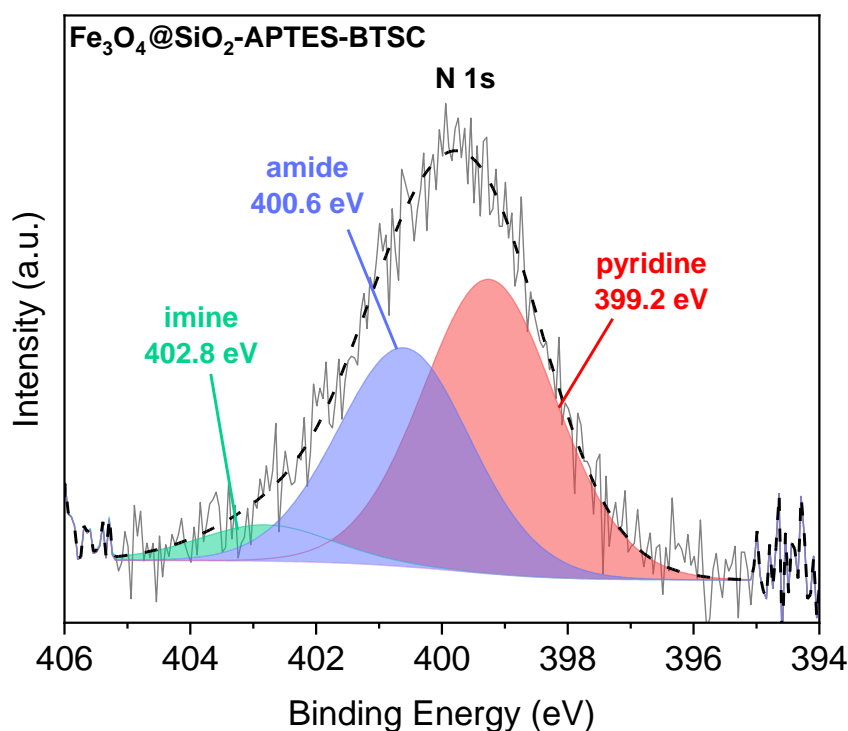
Fig. 29. XPS survey spectra of Fe₃O₄@SiO₂–APTES–BTSC.

2.2.8 Synthesis of SiO₂–APTES–BTSC

N-4–(2–ethylaniline)–thiosemicarbazide was reacted with 4-chloro-isonicotinate–2,6–diacetylpyridine to obtain compound 4–chloro–2,6–diacetyl–pyridine–bis–(4–*N*–2–ethylaniline)–BTSC in 29% yield. The reaction between 4–chloro–2,6–diacetyl–pyridine–bis–(4–*N*–2–ethylaniline)–TSC with APTES pre-functionalized SiO₂ afford SiO₂–APTES–BTSC. SiO₂–APTES–BTSC was subsequently coordinated with Pd²⁺ ions (**Scheme 21**).
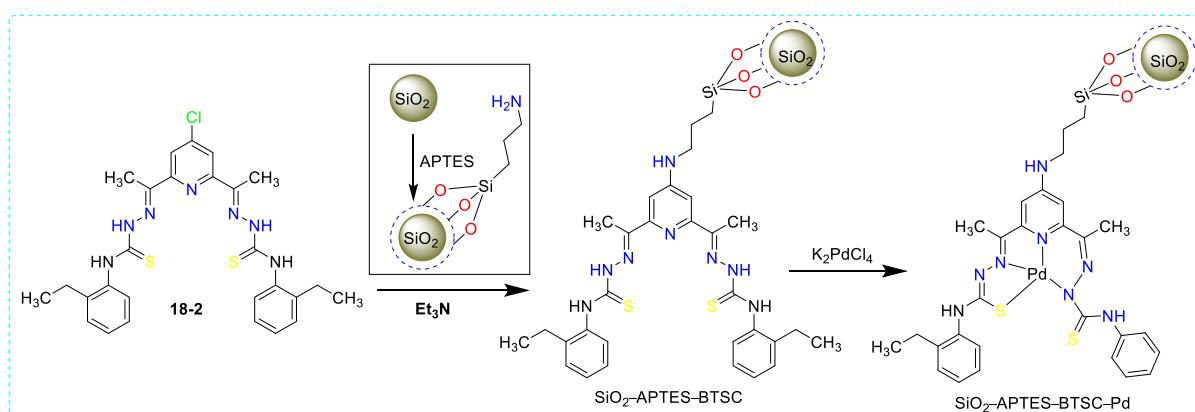
Scheme 21. Covalent conjugation of 4–chloro–2,6–diacetyl–pyridine–bis–(4–*N*–2–ethylaniline)–BTSC with SiO₂–APTES.

2.2.8.1 FT-IR Spectroscopy of SiO$_2$–APTES–BTSC

4–chloro–2,6–diacetyl–pyridine–bis–(4–N–2–ethylaniline)–BTSC shows intense peaks at 748 and 864 cm^{-1}, corresponding to C–Cl and C=S vibration, and the strong band between 1515 – 1588 cm^{-1} corresponds to C=N stretching based on comparison with 9–undecenal–TSC (**Fig. 30**).[96] The bands at 2956 and 3330 cm^{-1} are assigned to asymmetrical stretching of N–H based on comparison with coumarin–thiosemicarbazone and benzaldehyde–TSC.[104,105] On the bare SiO$_2$, the intense bands (450 and 1076 cm^{-1}) correspond to the bending and stretching of Si–OH and the asymmetric stretching of the Si–O–Si bond, respectively.[106] On coating SiO$_2$ with APTES, two additional bands appeared at 1863 and 2982 cm^{-1} corresponding to C–H and N–H vibration and the deformation of the band at 1634 cm^{-1} corresponding to Si–O. Additional bands were observed at 1494, 1561 and 2885 cm^{-1} on covalent functionalization with BTSC; the bands were assigned to N–H bending, C=S vibration, and N–H stretching, compared with ethyl–pyrrole–thiosemicarbazone.[93] New bands were observed after the coordination of Pd^{2+} at 668 and 1384 cm^{-1} assigned to Pd–N and Pd–S stretching.[107]
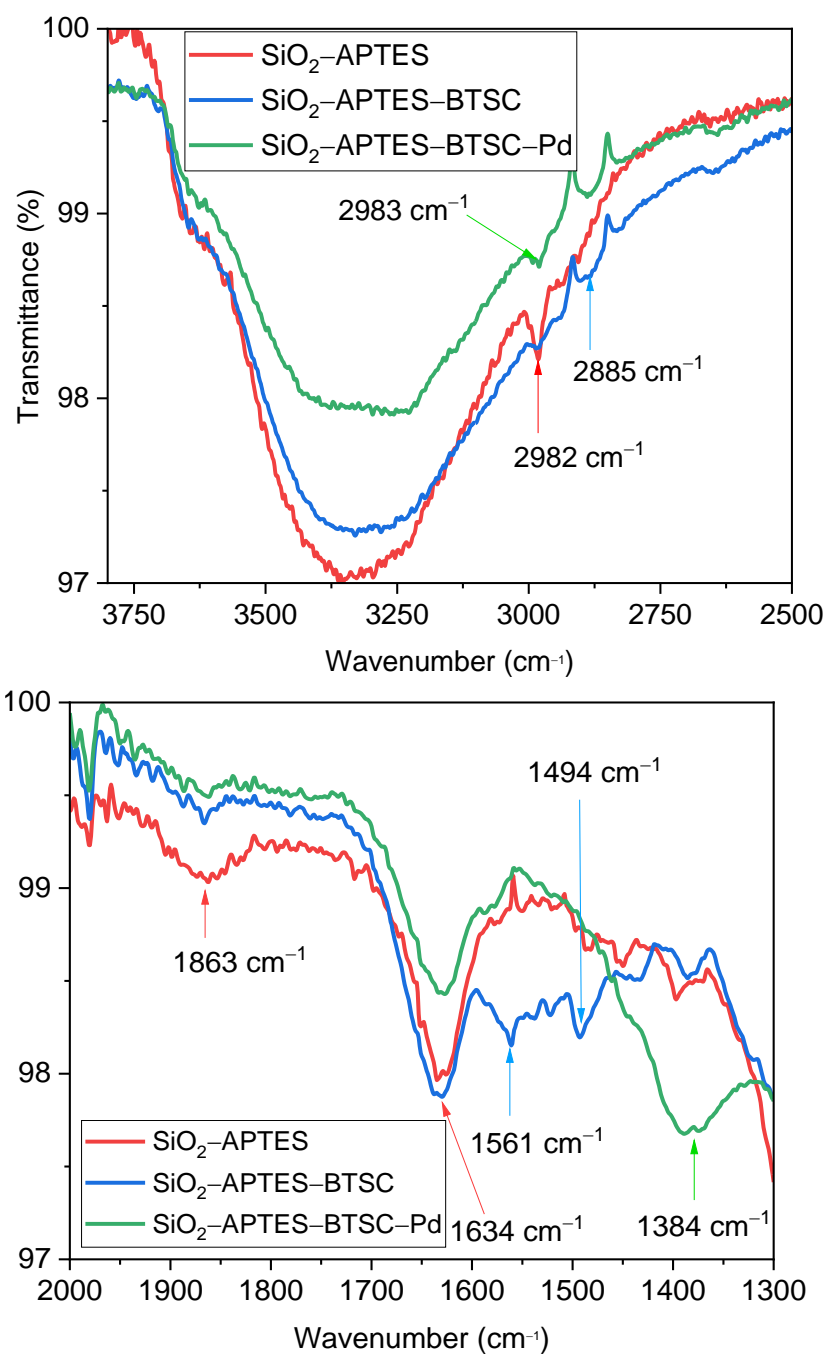
Fig. 30. FT-IR spectra of SiO₂–APTES, SiO₂–APTES–BTSC and SiO₂–APTES–BTSC–Pd Conjugate

2.2.8.2 X-ray Photoelectron Spectroscopy of SiO₂–APTES–BTSC–Pd Nanoparticles

The main peaks observed in the survey scan for SiO₂–APTES–BTSC NPs are Si 2p, Si 2s, Cl 2p, C 1s, N 1s and O 1s centred at 103, 153, 284, 400 and 532 eV (**Fig. 31**). For the survey scan of SiO₂–APTES–BTSC–Pd NPs, additional peaks appeared for Cl 2p and Pd 3d centered at 198 and 338 eV (**Fig. 31**). The absence of Cl 2p in the survey scan of SiO₂–APTES–BTSC is a strong indication that the covalent anchoring of BTSC to SiO₂ NPs was successful.
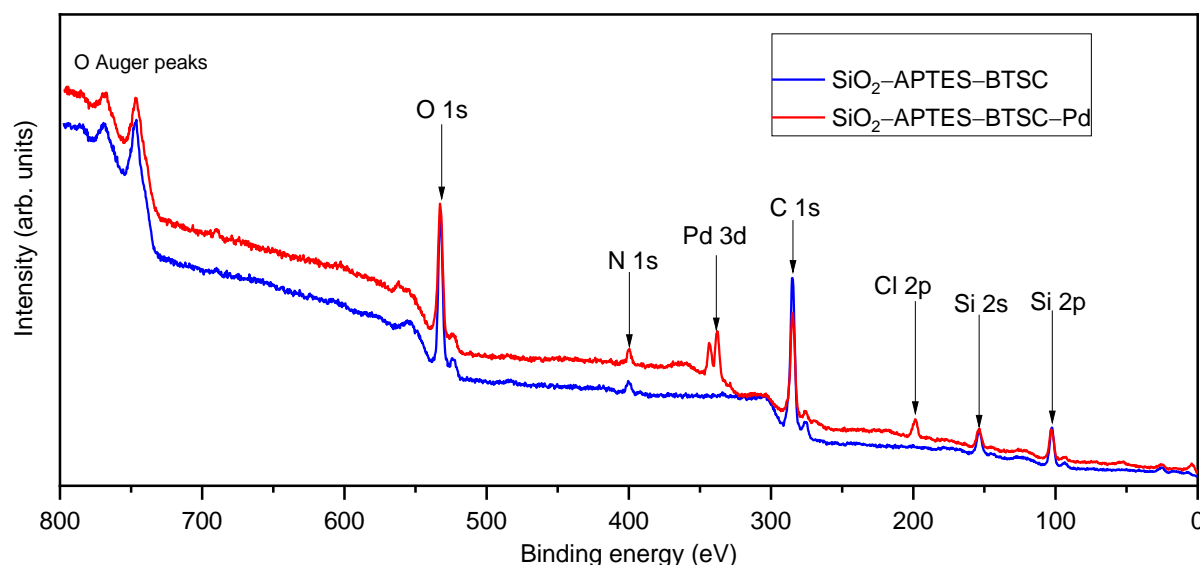
Fig. 31. XPS survey scan of SiO$_2$–APTES–H^{2}L and SiO$_2$–APTES–BTSC–Pd NPs.

The high-resolution XPS analysis of uncoordinated SiO$_2$–APTES–BTSC for C 1s spectra are deconvoluted into three peaks: C–C (284.5 eV), C–N (286.2 eV), and C=N (288.3 eV) (**Fig. 32**).[108,109] On coordination with Pd^{2+}, C–N (285.9 eV) and C=N (287.9 eV) shifted to a lower binding energies, suggesting that C=N was responsible for binding with Pd^{2+} ions (**Fig. 32**).[110] However, the binding energy of C–C (284.6 eV) remains unchanged because C–C was not involved in coordinating Pd^{2+}. N 1s spectra are deconvoluted into two peaks: pyridinic N (401.1 eV) and amine (399.6 eV).[111] On coordination, N 1s spectra are deconvoluted into three peaks, the binding energy of pyridinic N (400 eV) and imine (399.1 eV) shifted to a lower binding energy by 1.1 eV and 0.5 eV. The third peak (401.1 eV) is assigned to Pd–N. S 2p peak was located at 163.5 eV and shifted slightly to a lower binding energy (162.8 eV) by 0.7 eV on coordination with Pd^{2+} (**Fig. 33**).[112] Si 2p spectra are deconvoluted into two peaks: SiO$_2$ (103.1 eV) and Si–O–Si (101.9 eV).[113] SiO$_2$ shifted slightly to a higher binding energy by 0.2 eV; this may be associated with the interaction of Si atoms with Cl$^-$ ions from the K$_2$PdCl$_4$ precursor. The Pd 3d spectra are composed of two asymmetric peaks Pd 3d$_{3/2}$ (343.2 and 341.6 eV) and Pd 3d$_{5/2}$ (337.9 and 336.3 eV). These binding energies agree with the expected values of Pd^{2+} (343.2 and 337.9) and Pd^0 (341.6 and 336.3 eV). Similar binding energies have been reported for Pd^{2+} complexes of dithiocarbamates and [poly(styryl)phenanthroline] complexes.[114,115] The binding energy for Pd(^{0}) oxidation states is comparable with Pd metals.[116–118]
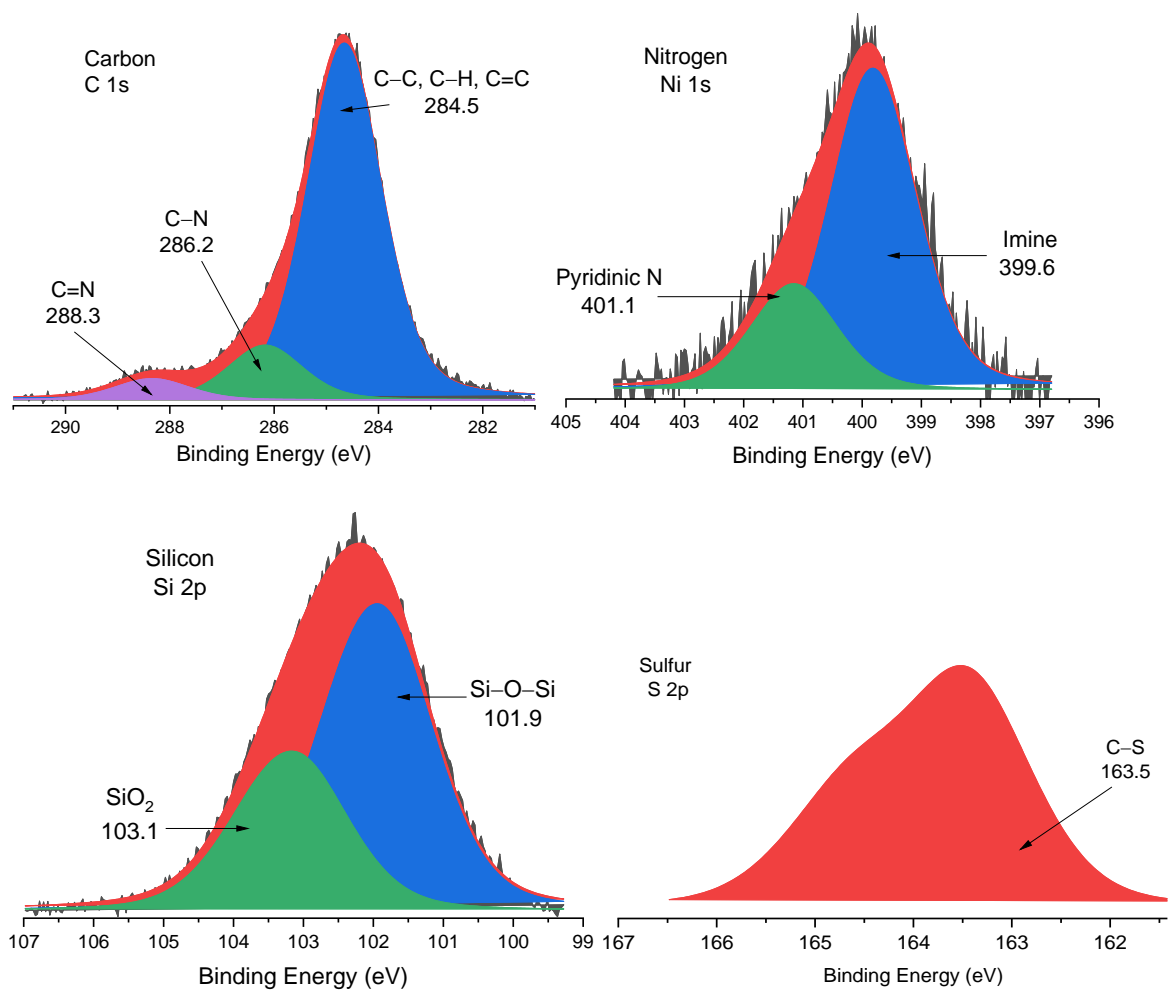
Fig. 32. XPS high-resolution spectrum of SiO₂–APTES–BTSC NPs.
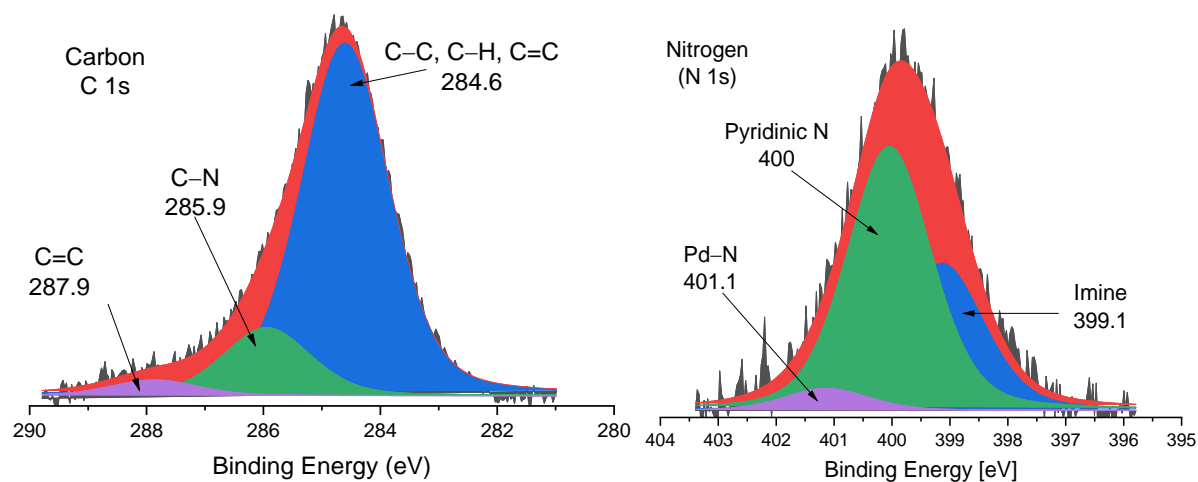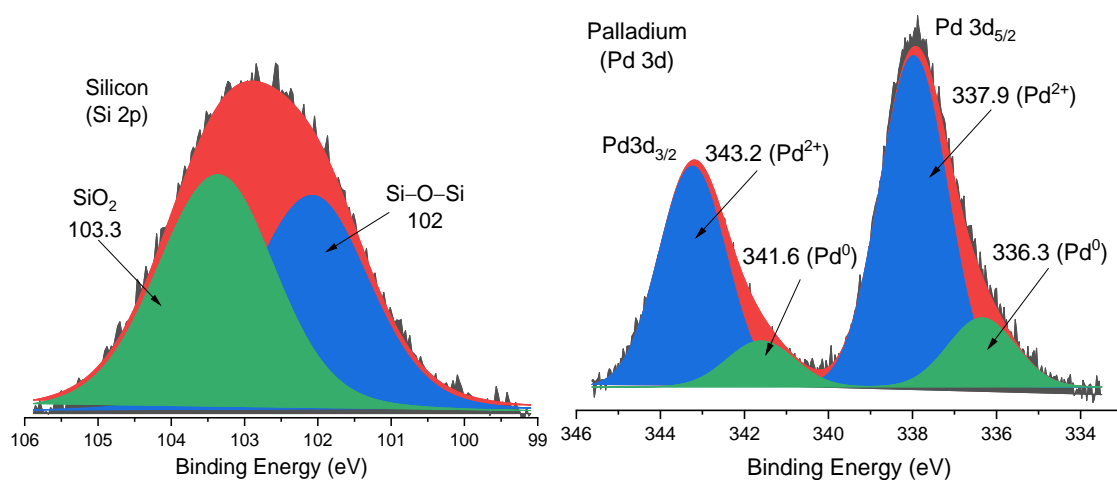
Fig. 33. High-resolution XPS spectrum of SiO₂–APTES–BTSC–Pd NPs.

2.2.8.3 UV-vis Absorption Spectroscopy of SiO₂–APTES–BTSC Nanoparticles

The UV-Vis absorption spectrum of SiO₂–APTES is characterized by a shoulder at 285 nm (**Fig. 34**).[119] 4–chloro–2,6–diacetyl–pyridine–bis–(4–N–2–ethylaniline)–BTSC is characterized by an intense absorption band at $\lambda_1 = 344$ nm, corresponding to a $\pi \rightarrow \pi^*$ transition. On covalent anchoring of 4–chloro–2,6–diacetyl–pyridine–bis–(4–N–2–ethylaniline)–TSC with SiO₂–APTES, the broad intense absorption band at 344 nm was deformed and shifted to 339 nm (hypsochromic shift).
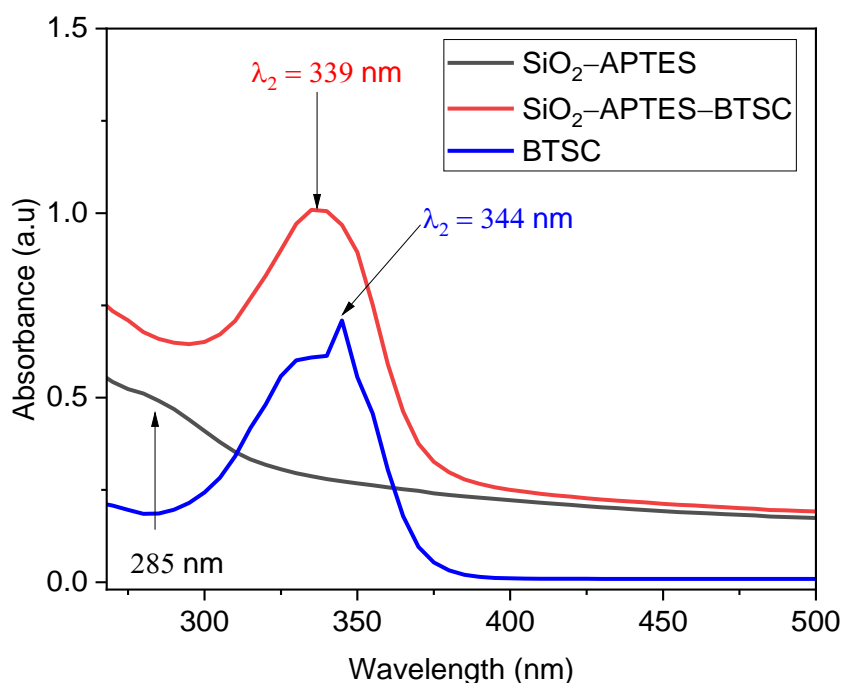
Fig. 34. UV–vis absorption spectra of SiO₂–APTES NPs, SiO₂–APTES–BTSC NPs and 4–chloro–2,6–diacetyl–pyridine–bis–(4–N–2–ethylaniline)–BTSC ligand.

2.2.8.4 Thermographimetry Analysis of SiO$_2$–APTES–BTSC

The thermal behaviour of SiO$_2$, SiO$_2$-APTES and SiO$_2$–APTES–BTSC were investigated under N$_2$ atmosphere over a temperature range between 30 – 800°C (**Fig. 35**). A 10%, 15% and 28% weight loss was observed for SiO$_2$, SiO$_2$-APTES and SiO$_2$–APTES–BTSC NPs, respectively.[120] The initial weight loss of 10% at temperatures between 30°C and 300°C is attributed to sorbed solvents. The additional 5% and 13% at temperatures between 400°C and 800°C were attributed to the decomposition of APTES and BTSC.
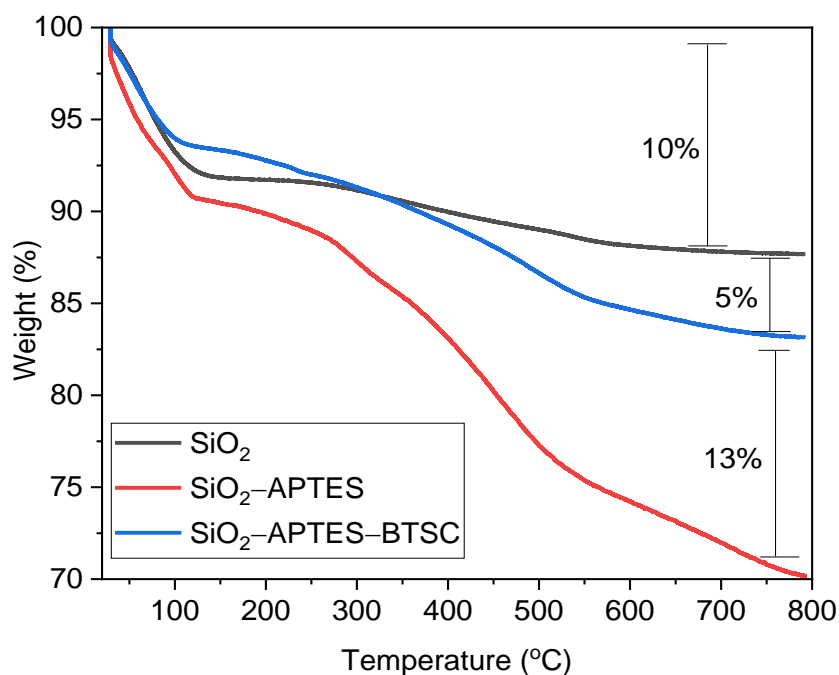
Fig. 35. TGA analysis of SiO$_2$, SiO$_2$–APTES and SiO$_2$–APTES–BTSC

2.2.8.5 Powder XRD Pattern of SiO$_2$–APTES–BTSC–Pd

All sample patterns appeared amorphous (**Fig. 36**), with a single broad peak,[121] similar to Stöber's results.[122,123] The non-crystalline nature of the particles is preserved (2θ = 21.18) after functionalizing with APTES and covalently bonding with the TSC ligand.[124]
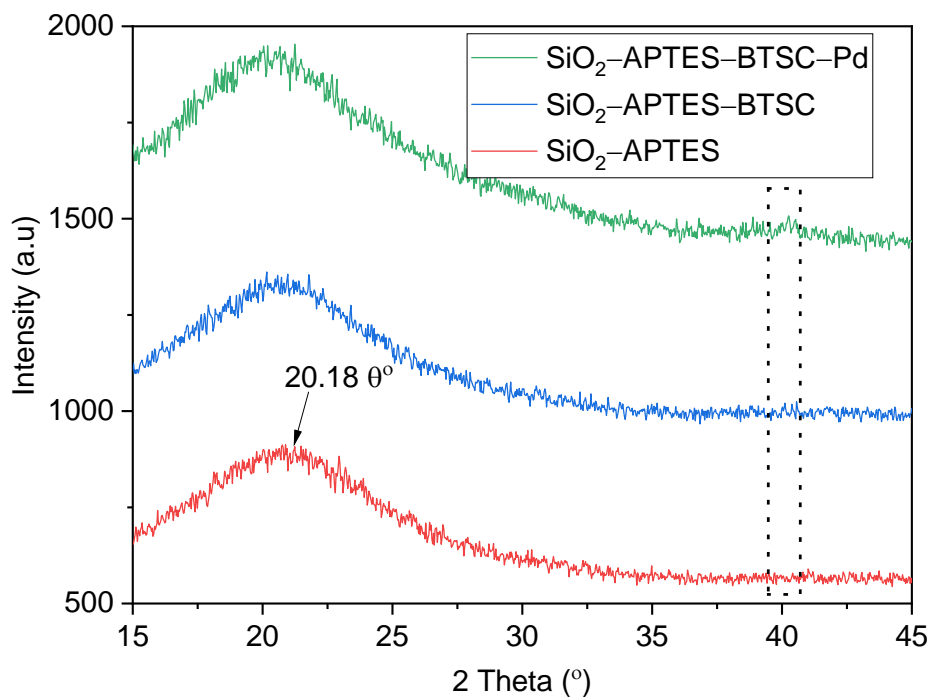
Fig. 36. PXRD patterns of SiO₂–APTES, SiO₂–APTES–BTSC and SiO₂–APTES–BTSC–Pd NPs.

2.2.8.6 SEM and EDX Investigation of SiO₂–APTES–BTSC–Pd

SEM images showed that the SiO₂–APTES NPs are monodispersed nanospheres with a mean diameter of 207 nm (**Fig. 37**). The diameter of individual particles was calculated using Image J software.[125] The EDX analysis shows Si and O as the main elemental composition, highlighting the purity of the NPs. On covalent conjugation of SiO₂–APTES NPs with 4–chloro–2,6–diacetyl–pyridine–bis–(4–N–2–ethylaniline)–BTSC and coordination with Pd²⁺, the SEM image showed the non-uniform distribution of Pd²⁺ particles on the surface of the SiO₂ NPs (**Fig. 38**).
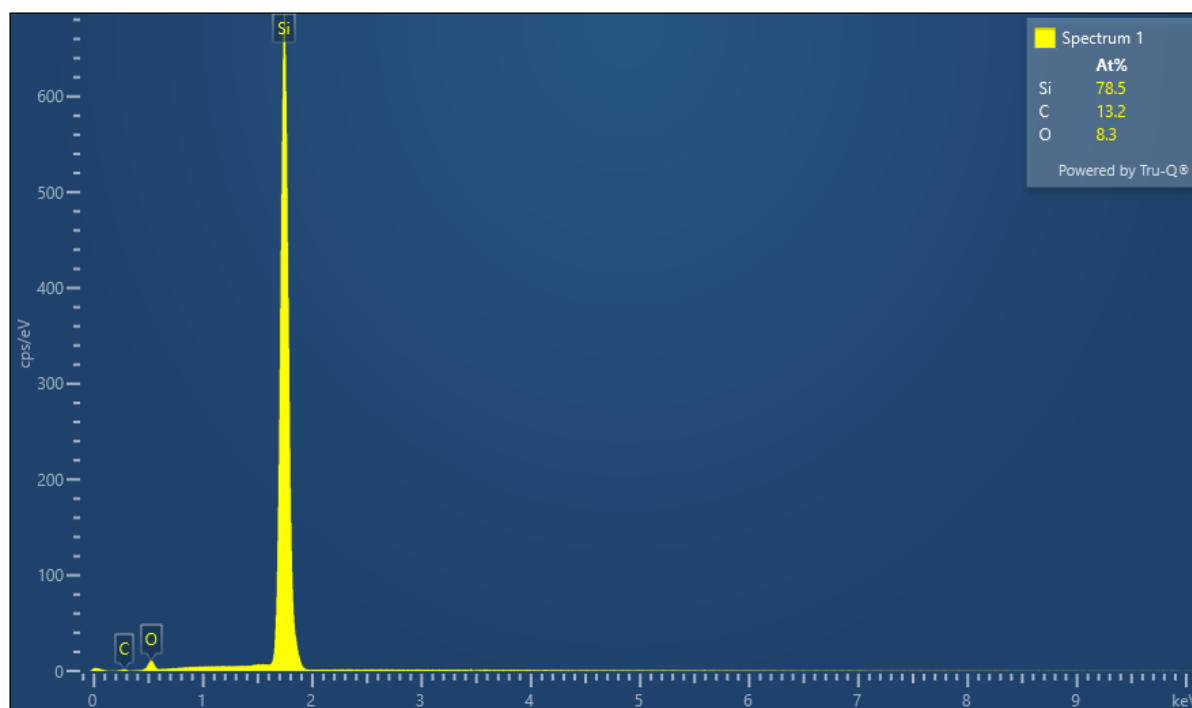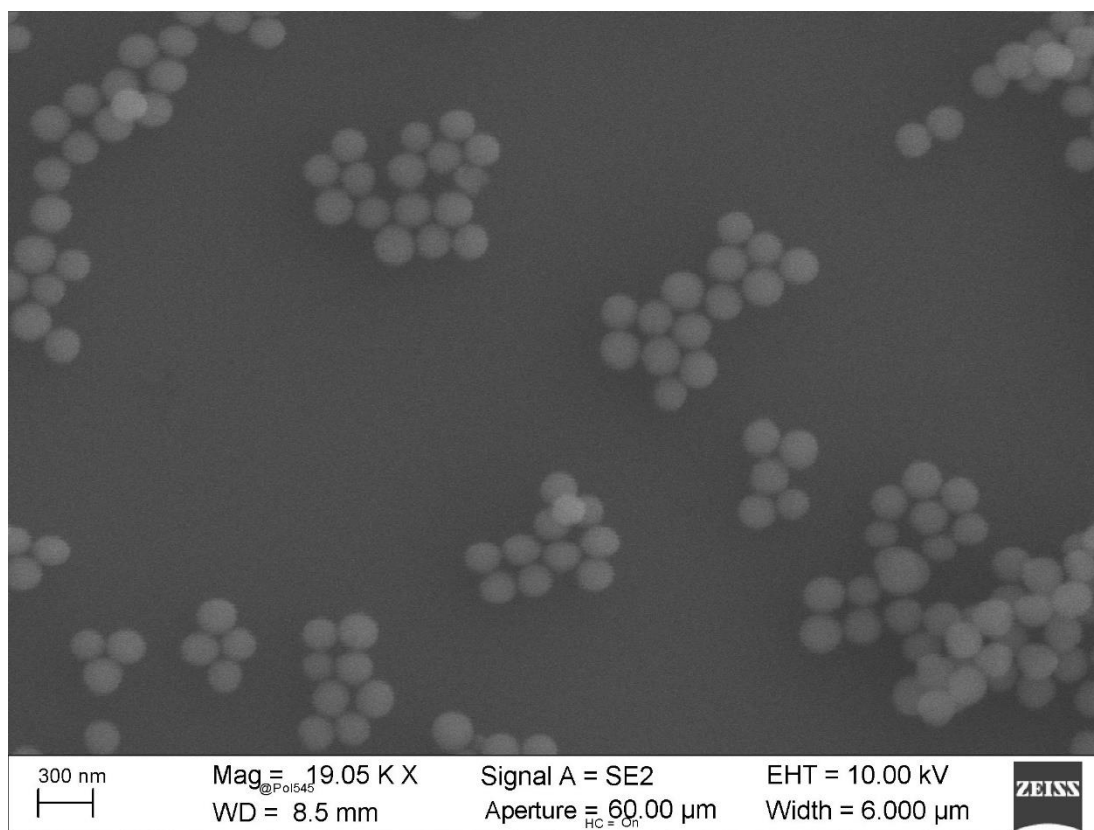
Fig. 37. SEM image and EDX analysis of SiO₂ NPs.
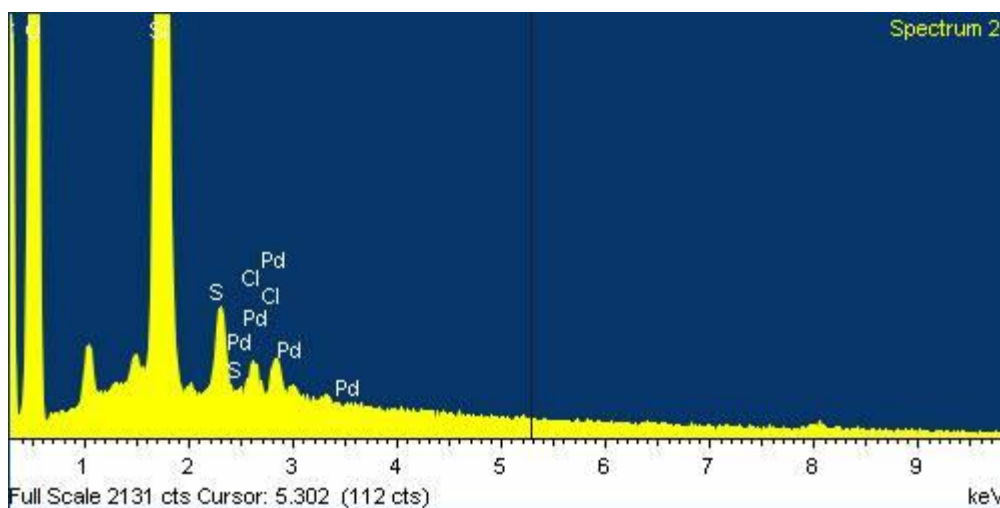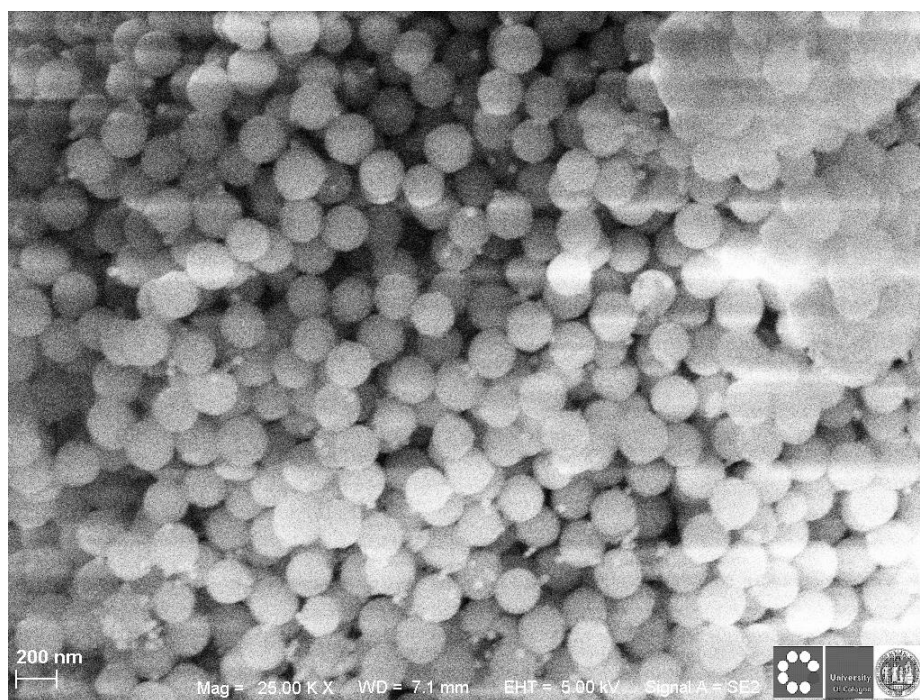
Fig. 38. EDX analysis of SiO$_2$–APTES–BTSC–Pd NPs.

2.2.9 Synthesis of Fe$_2$O$_3$–Dopamine–BTSC

2,6-diacetylpyridine-bis-(4-*N*-chlorophenyl)-TSC was conjugated with Fe$_2$O$_3$ (**Scheme 22**) This was achieved by reacting Dopamine pre-functionalized Fe$_2$O$_3$ with compound 24 in DMF for 4 days in the presence of Et$_3$N. The black Fe$_2$O$_3$–Dop–BTSC conjugate was recovered via vacuum filtration.
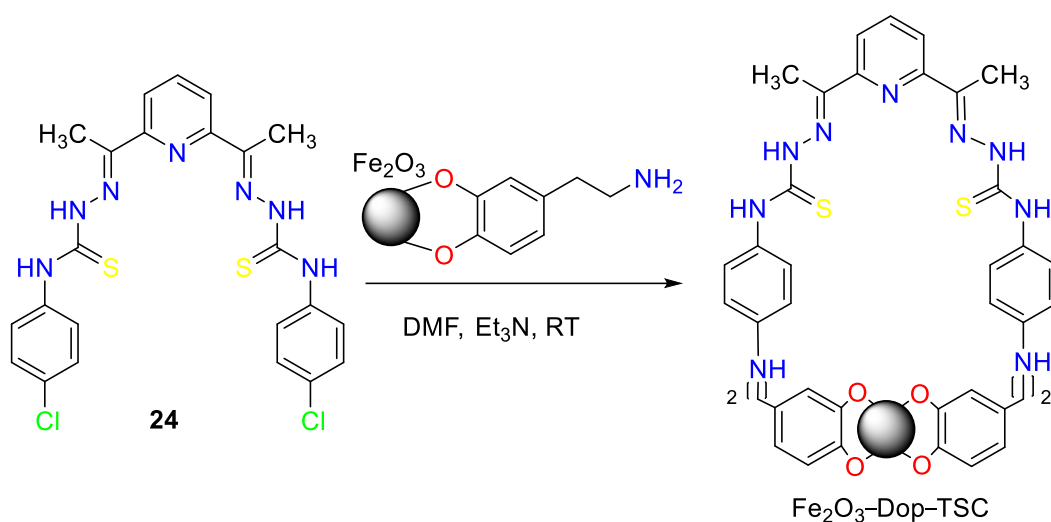
Scheme 22. Conjugation of 2,6-diacetylpyridine-bis-(4-*N*-chlorophenyl)-BTSC ligand with Dopamine pre-functionalized Fe₂O₃ NPs.

2.2.9.1 Powder-XRD Pattern of Fe₂O₃–Dop–BTSC

The PXRD pattern for Fe₂O₃ and Fe₂O₃–Dop–BTSC NP is presented in **Fig 39**. The powder XRD pattern is similar to α-Fe₂O₃ [126]. The sharp patterns implied that Fe₂O₃ is more crystalline compared with Fe₂O₃-Dop. On covalent functionalisation with BTSC, Fe₂O₃–Dop–BTSC displayed a significant reduction in the sharp edges, indicating successful covalent functionalisation. The amorphous nature of Fe₂O₃–Dop–BTSC is due to the covalent anchoring of BTSC on the surface of Fe₂O₃.
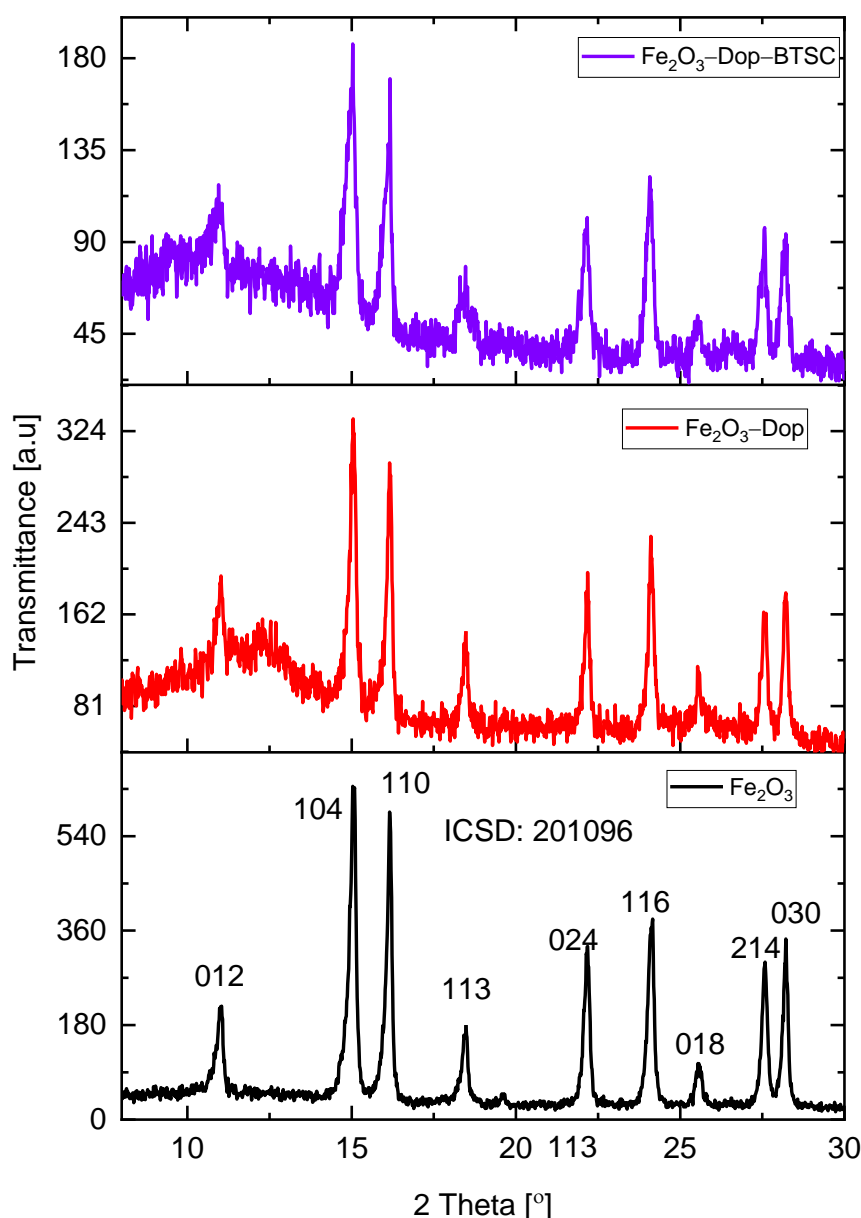
Fig. 39. Powder XRD pattern of α-Fe₂O₃, Fe₂O₃–Dop and Fe₂O₃–Dop–BTSC NPs

2.2.9.2 FT-IR Spectroscopy of Fe₂O₃–APTES–BTSC

The FT–IR spectra of pristine Fe₂O₃ (**Fig. 40**) are characterized by prominent bands at 452 and 527 cm⁻¹ corresponding to Fe–O bending vibrational modes, while N–H and O–H bending and stretching appeared at 1106 and 3089 cm⁻¹, respectively, due to residual organic content from DMF, PVP and hydrazine. BTSC–Dop is characterized by prominent bands at 1507, 3114 and 817 cm⁻¹ corresponding to N–H, O–H and C=S.[127–129] On conjugating dopamine pre-functionalized Fe₂O₃ with BTSC, an additional band was observed for N–H at 2930 cm⁻¹, and other prominent bands were observed at 798, 1081 and 3380 cm⁻¹, corresponding to C=S, N–H bending, and O–H stretching.[130]
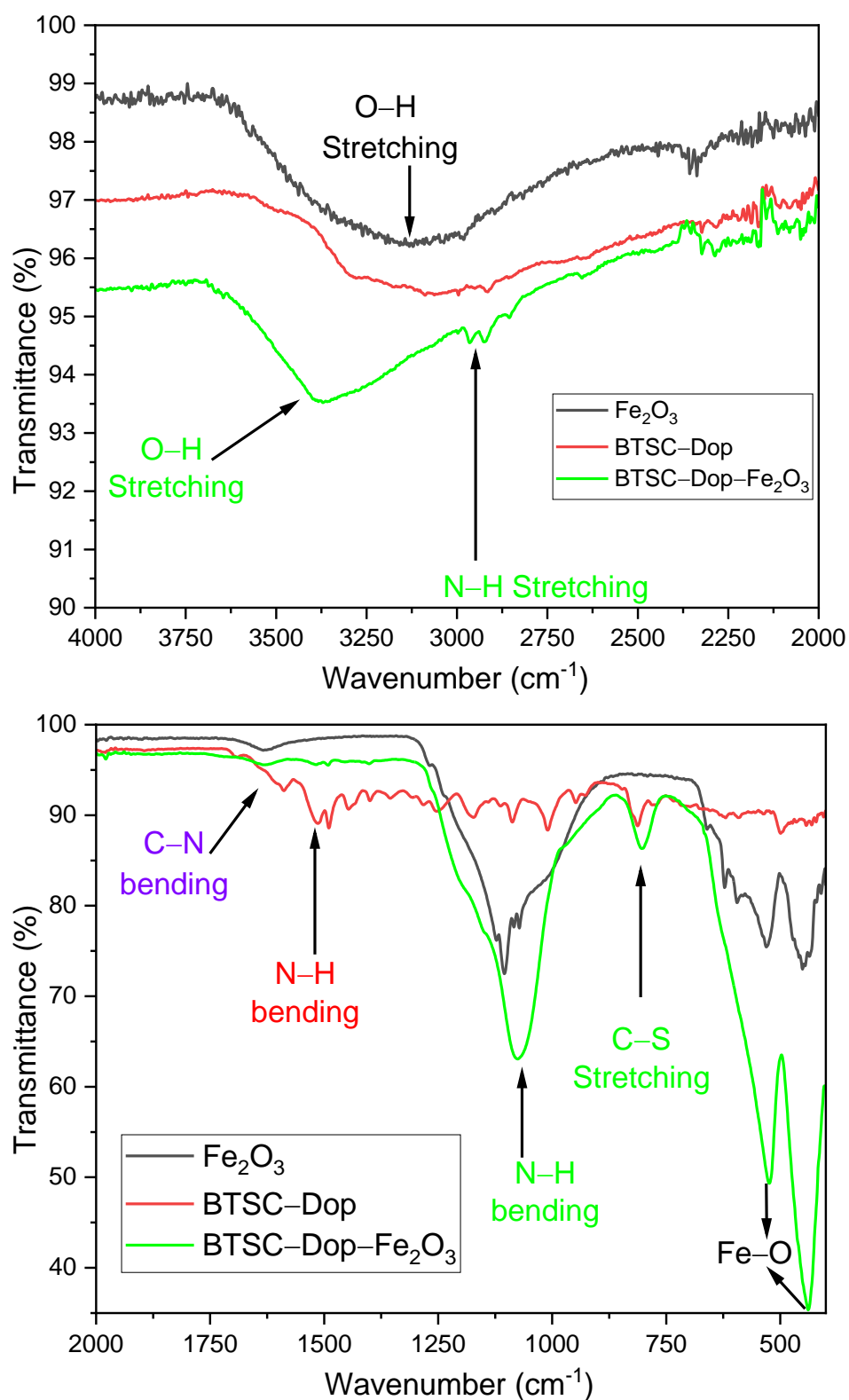
Fig. 40. FT–IR spectra of Fe_2O_3, Fe_2O_3–Dop and Fe_2O_3–Dop–BTSC NPs.

2.2.9.3 Thermal Analysis of Fe_2O_3–Dopamine–BTSC Nanoparticles

The thermogravimetry analysis of the NPs (Fe_2O_3, Fe_2O_3–Dop and Fe_2O_3–Dop–BTSC) between 30 and

800°C (**Fig. 41**), provides an insight into the thermal stability of the NPs. Fe_2O_3 showed two stages of

weight loss: 6.79% between 200 – 250°C and 15.49% between 300 and 550°C, corresponding to the elimination of water molecules and decomposition of organic solvents present in the Fe_2O_3 NPs, respectively.[131] Additional weight loss (17.70%) between 450 and 800°C corresponding to the decomposition of dopamine molecules was observed for Fe_2O_3–Dop. The final steep weight loss (28.54%) in Fe_2O_3–Dop–BTSC NPs corresponds to the decomposition of BTSC between 600 – 800°C. This is an indication that the covalent functionalisation was successful. The decomposition of the covalently attached BTSC at a high temperature indicates that Fe_2O_3–Dop–BTSC NPs have high thermal tolerance.
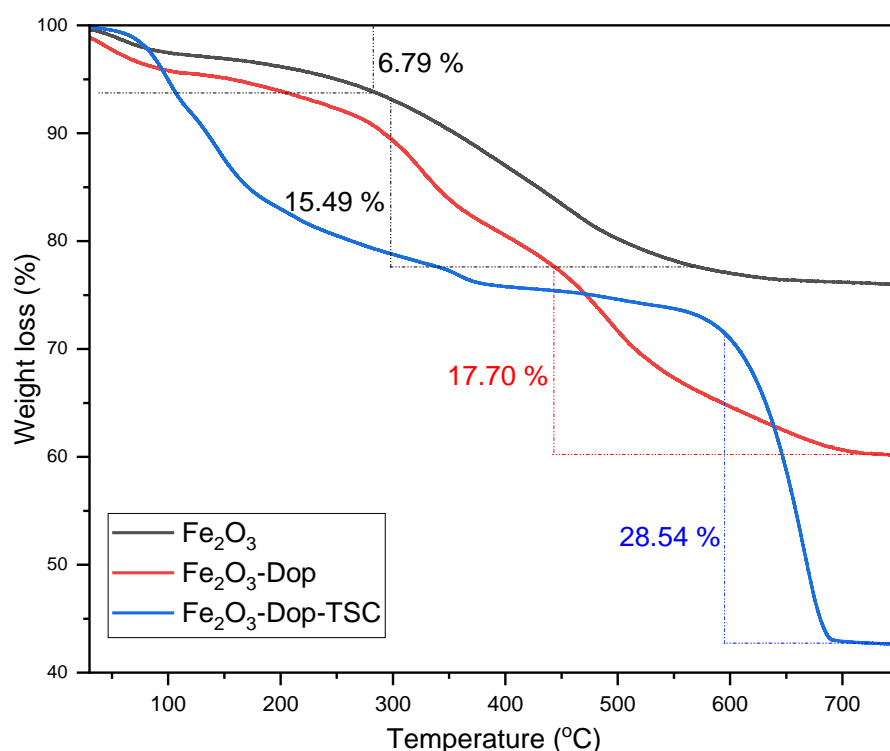
Fig. 41. TGA analysis of Fe_2O_3, Fe_2O_3-Dop, Fe_2O_3-Dop-BTSC nanoparticles.

2.2.10 Synthesis of Metal Sulfide Nanoparticles

Metal complexes (Cu, Pd, Zn) of 2,6–diacetyl–pyridine–bis–(4–*N*–2–ethylaniline)–BTSC were used for synthesizing metal sulfides NP. The complexes were dissolved in *N*–methyl–2–pyrrolidione solution. Metal sulfide NP was obtained after 10 minutes of decomposition in the microwave (**Scheme 23**). An attempt to synthesize PdSn bimetallic NP was unsuccessful because all the protons in the 1H NMR spectra could not be assigned. Therefore, the study of the synthesis of bimetallic NP was not explored further.
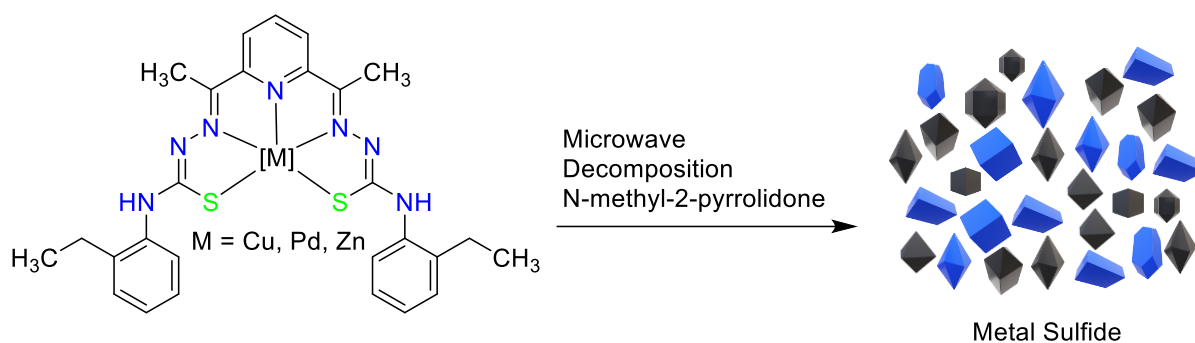
Scheme 23. Microwave-assisted decomposition of metal complexes of BTSC

2.2.10.1 Thermal Decomposition of Metal Complex of Bis-Thiosemicarbazone

The TGA and DSC thermogram of Cu, Pd and Zn complexes of 2,6–diacetyl–pyridine–bis–(4–*N*–2–ethylaniline)–BTSC were recorded between 30°C and 600°C. The first stage of weight loss, between 30 – 38%, which occurred at 130, 170, and 164°C for Cu, Pd, and Zn complexes, suggests that the complexes do not contain superficial water molecules, and the weight loss is attributed to the degradation of the complexes (**Fig. 42**). This is consistent with the DSC profile. The melting of the complexes commences at 191, 198, and 210°C, respectively. This is followed by the thermal decomposition to form the metal sulfides between 300 and 350°C for all the metal complexes. This is also consistent with the microwave-assisted synthesis of the metal sulfides. Further heating caused the decomposition of the metal sulfides, which corresponded with the final weight loss.
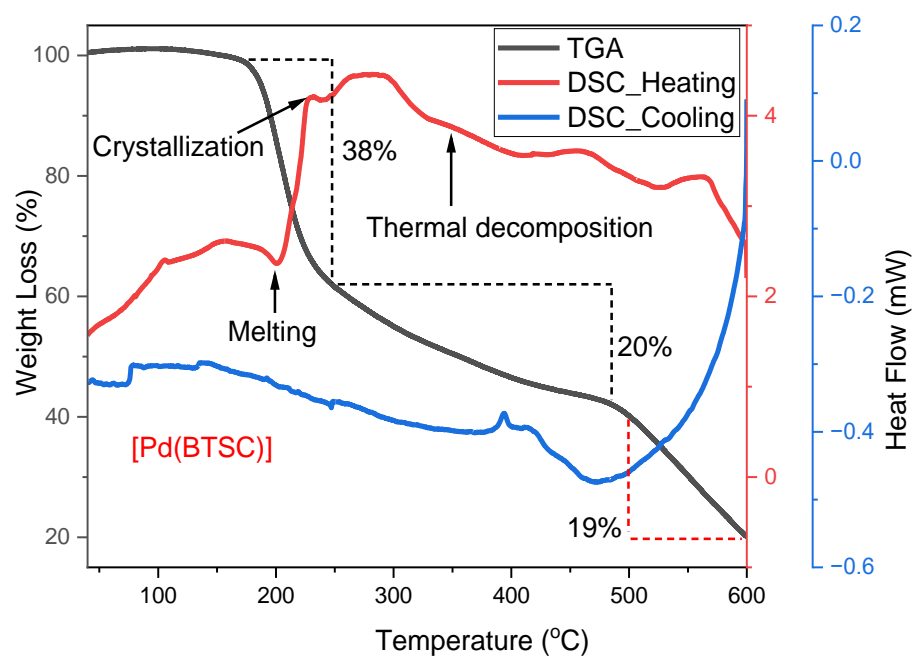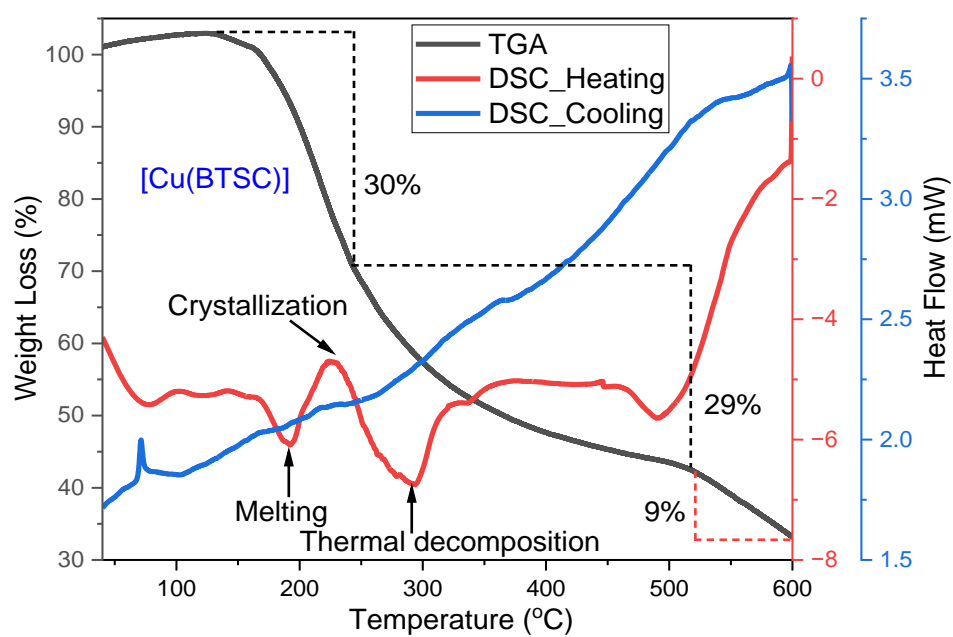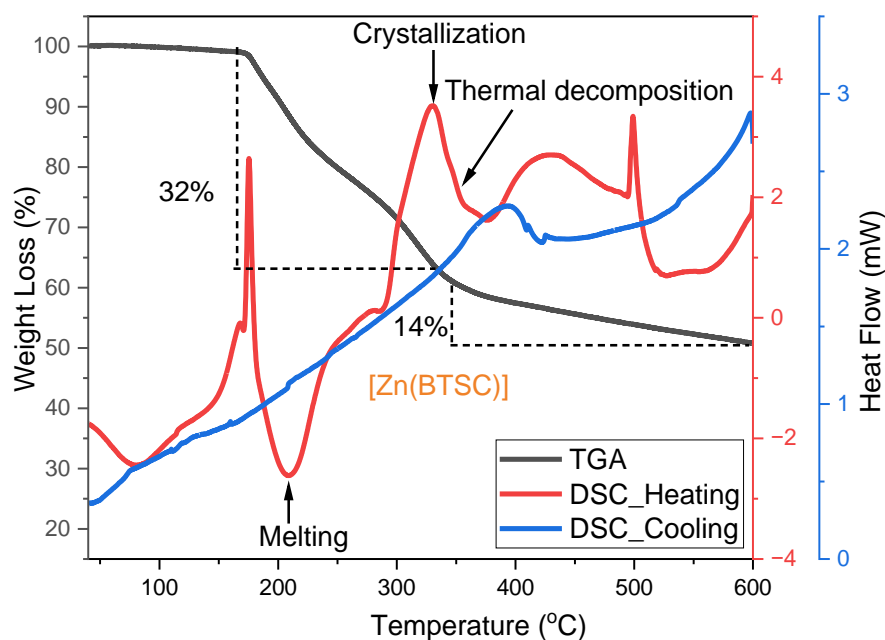
Fig. 42. Thermogravimetry analysis of Cu^{2+}, Pd^{2+} and Zn^{2+} complexes of 2,6–diacetyl–pyridine–bis–(4–*N*–2–ethylaniline)–BTSC. TGA in black and DSC heating (red) and cooling (blue) lines.

2.2.10.2 Powder–XRD Pattern of Metal Sulfide NPs

The diffraction patterns of copper sulfide can be indexed to cubic Cu$_{7.2}$S$_4$ (digenite, PDF no. 01-072-1966) and the space group *Fm–3m*. The significant diffraction peaks are at 2θ = 14.6 (020), 20.7 (220) and 24.3 (311). Palladium sulfide can be indexed to cubic Pd$_{16}$S$_7$ (PDF no. 01-073-9923) and the space group *I–43m*. The prominent diffraction peaks are 2θ = 11.1 (211), 17.0 (123), 18.2 (040) and 19.3 (411). ZnS can be indexed to the cubic ZnS (sphalerite, PDF no: 01-071-5976) and the space group *F- 4 3 m*. All the NPs appeared amorphous. No impurity pattern was noticeable in all the synthesized NPs (**Fig. 43**).
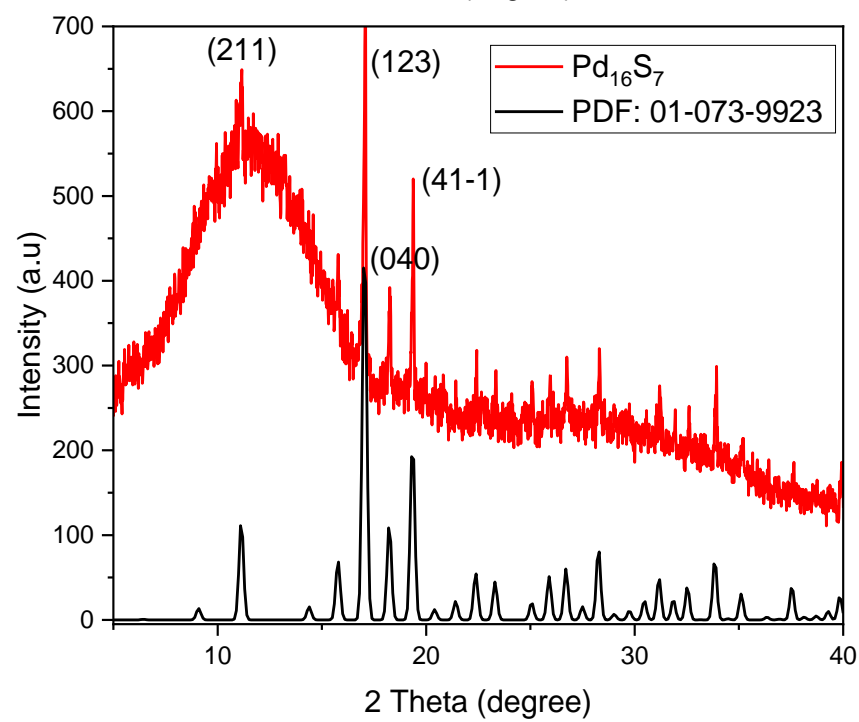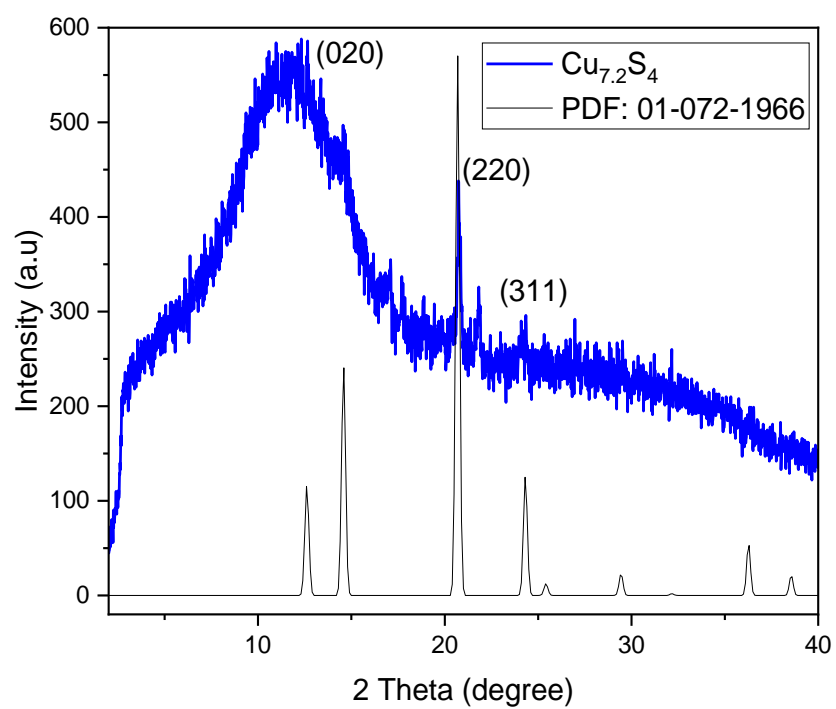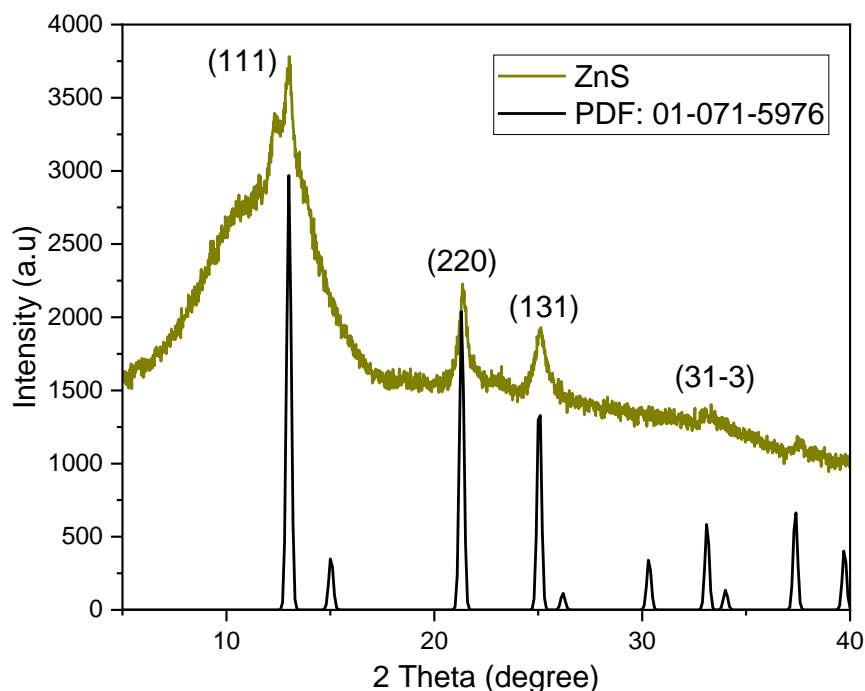
Fig. 43. Powder–XRD pattern of $Cu_{7.2}S_4$, $Pd_{16}S_7$ and ZnS NPs.

2.2.10.3 SEM and EDX Investigation of Metal Sulfides NPs

The $Cu_{7.2}S_4$ NPs are polydisperse irregular agglomerated particles with rough edges. The average particle size was determined to be 88 nm. The EDX analysis revealed copper and sulfur as prominent peaks with atomic percentages of 24.79 and 11.80%, highlighting the purity of the $Cu_{7.2}S_4$ NPs. $Pd_{16}S_7$ NPs appeared spherical with an average particle size of 78 nm. The prominent peaks are palladium and sulfur, with 58.33 and 32.00% atomic percentages. ZnS appeared to be irregular, with rough edges and polydisperse. The main atoms are Zn (22.02%) and S (17.18%), suggesting that ZnS was obtained pure. C and O atoms are impurities from the device (**Fig. 44 – 46**). The atomic percentage of the metal sulfide NPs is consistent with the PXRD phase.
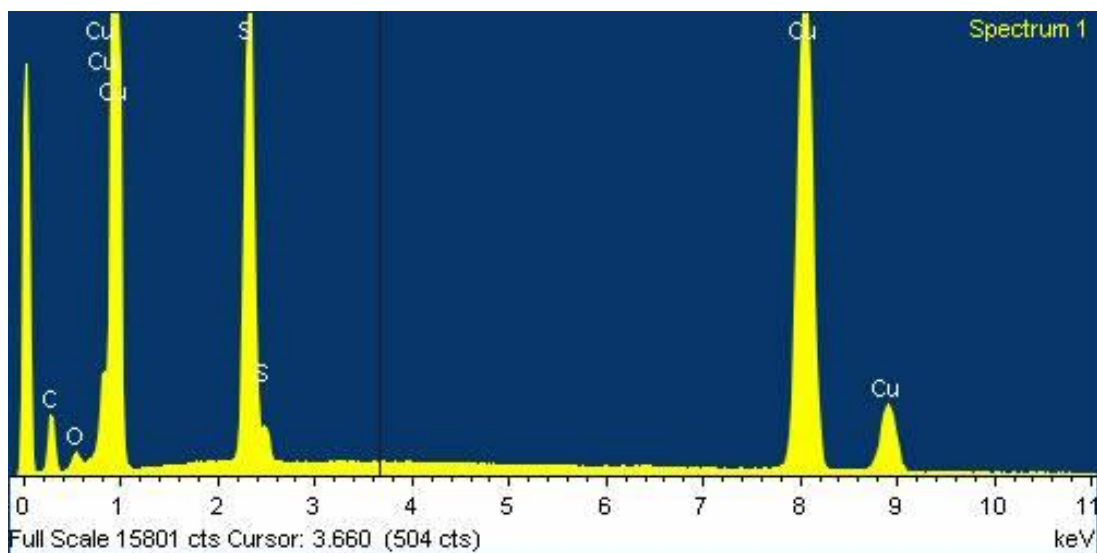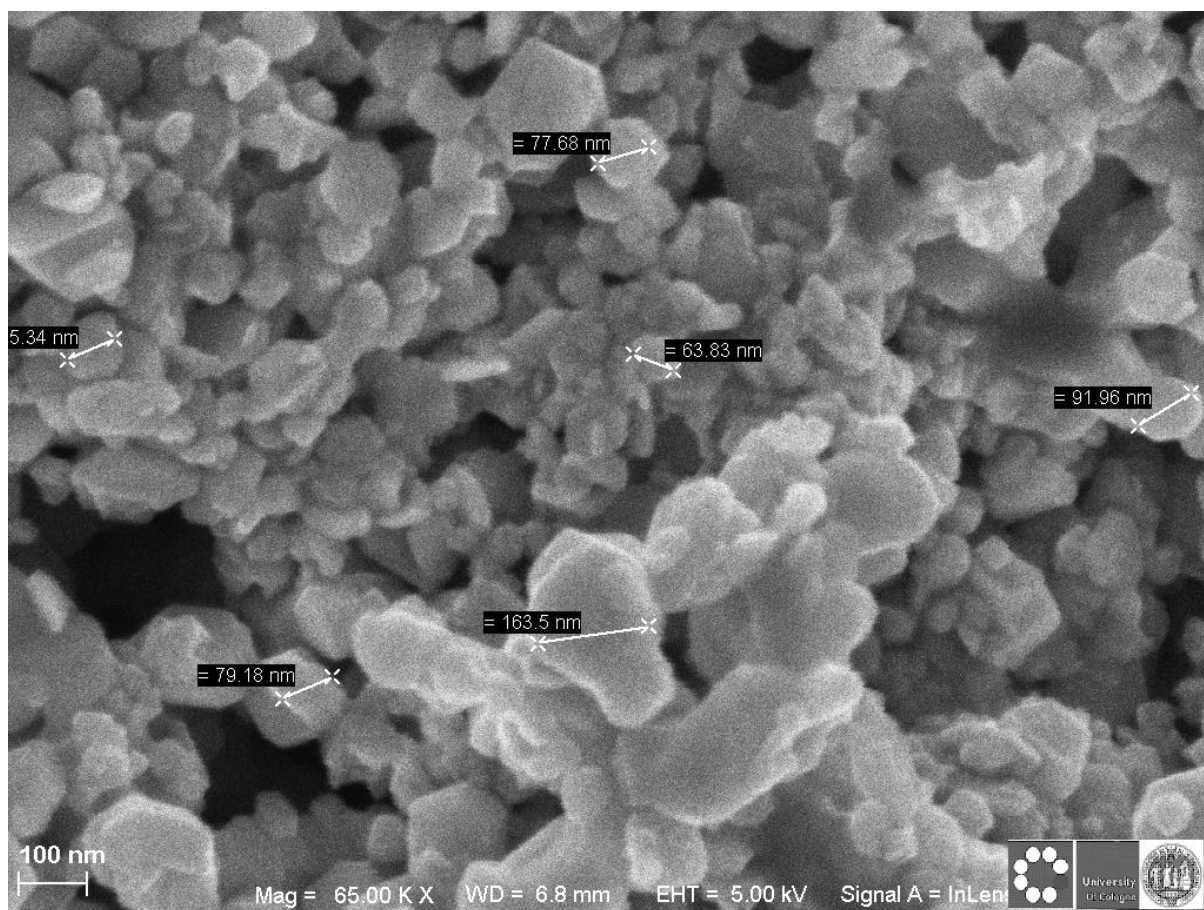
Fig. 44. SEM image and EDX analysis of Cu$_{7.2}$S$_4$ NP
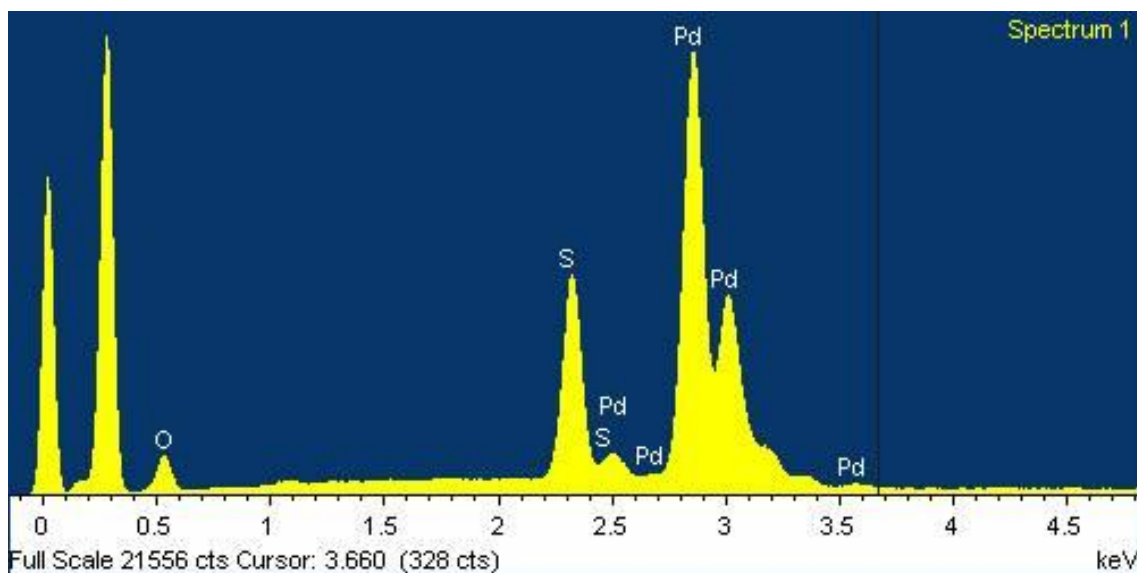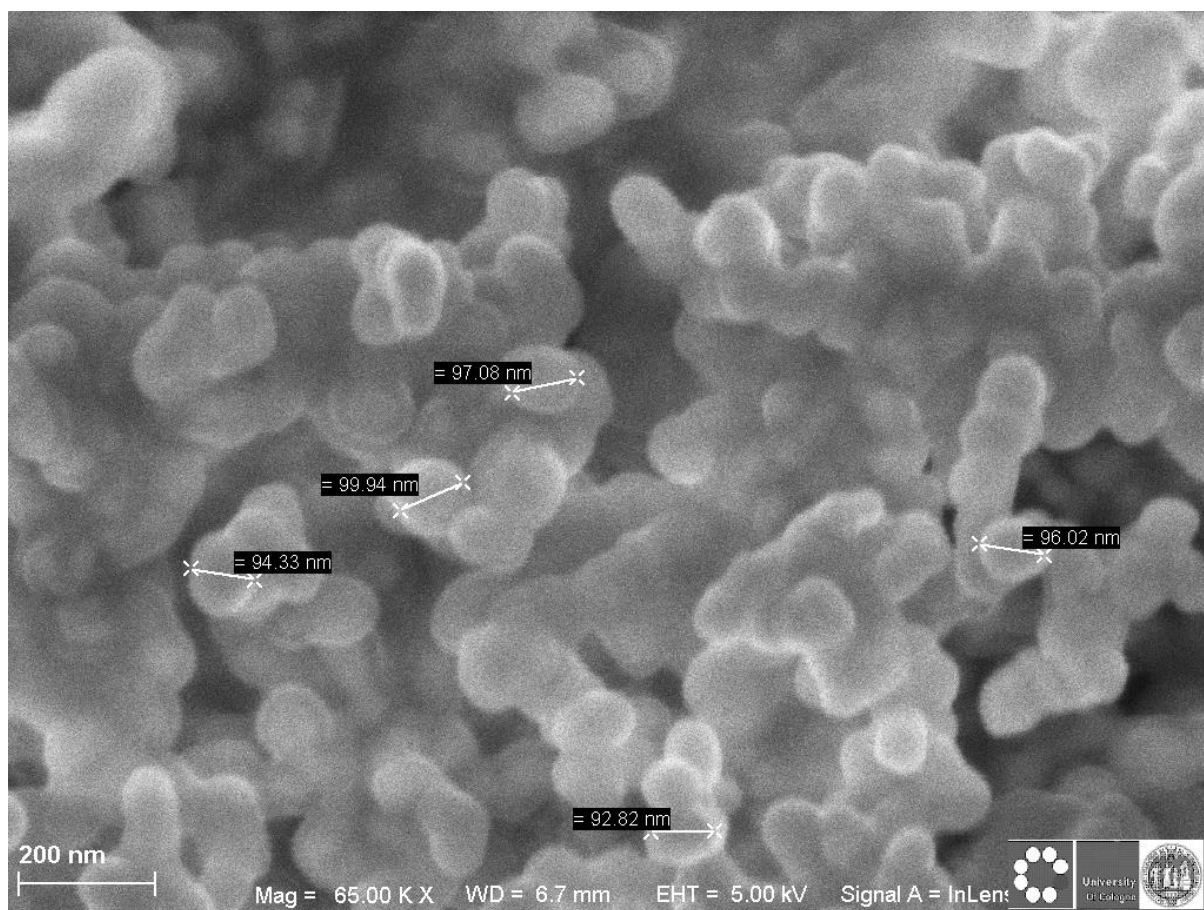
Fig. 45. SEM image and EDX analysis of $Pd_{16}S_7$ NP
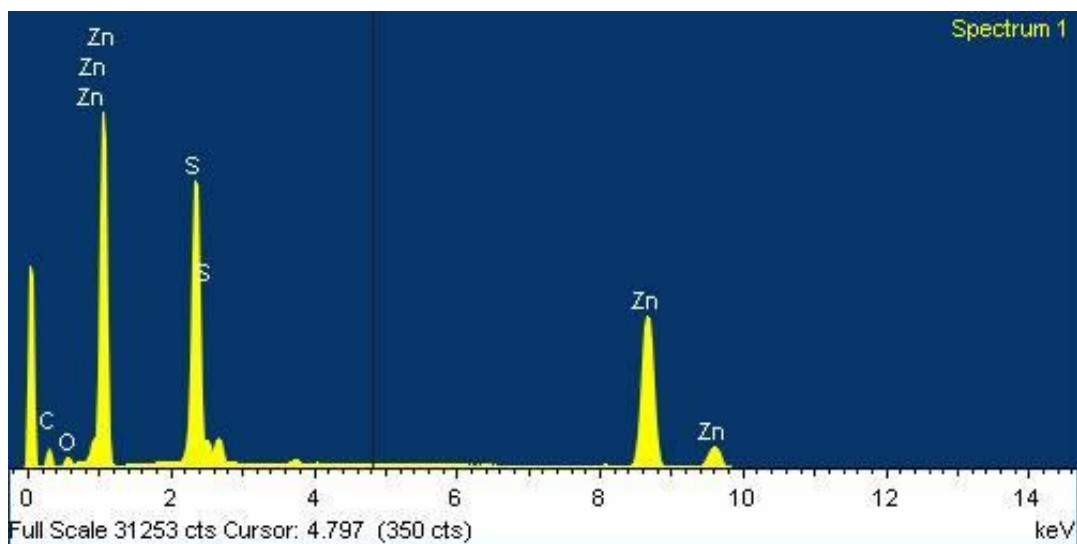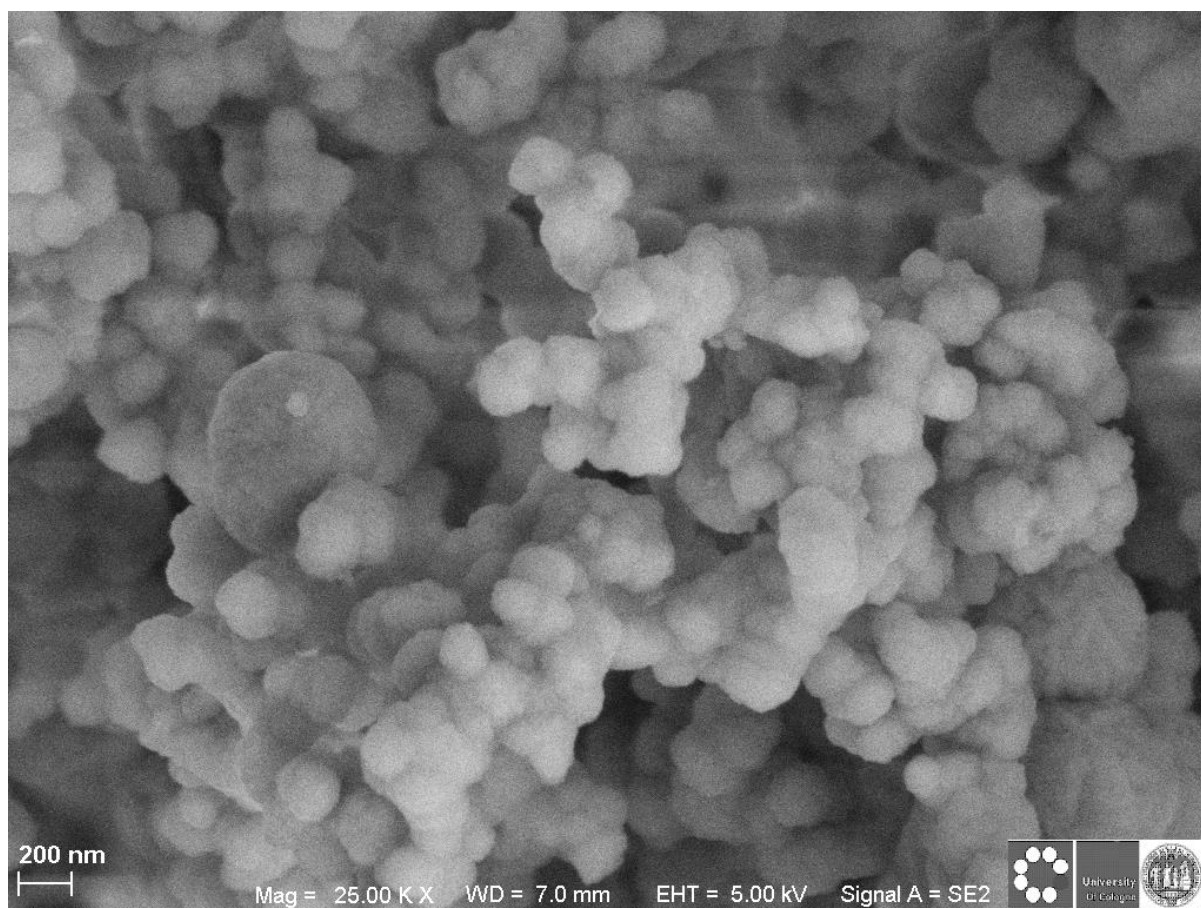
Fig. 46. SEM image and EDX analysis of ZnS NPs

2.3 Conclusion

This chapter discussed the synthesis of several new pentadentate BTSC ligands by the condensation reaction between thiosemicarbazide and dicarbonyl in acetic acid solution. The condensation reaction

in MeOH did not achieve the desired products, implying the importance of an acidic solution to drive the reaction. The primary focus was to synthesize pentadentate BTSC, which bears an additional functional group, either at the carbonyl backbone or the diamine tails. This was achieved by derivatizing the dicarbonyl backbone or the parent thiosemicarbazide. Complexation of BTSC with Zn^{2+} and Pd^{2+} indicates that the two metal ions bond differently. [Zn(BTSC)] complex is symmetrical while [Pd(BTSC)] complex is asymmetry.

The main goal of this thesis is to conjugate BTSC with different NPs covalently. Therefore, a reaction pathway was first established to confirm the condition necessary for the reaction of BTSC with different linkers. Thus, BTSC covalently conjugated dopamine and (3-aminopropyl)-triethoxysilane (APTES). The covalent conjugation of BTSC with APTES in THF achieved the desired products. However, due to solubility concerns, other BTSC derivatives were conjugated with dopamine in DMF. The hydrolysis of APTES was noticeable in DMF, thus causing the loss of at least one ethyl in one arm of the desired product.

EDC/NHS coupling chemistry was initially relied on to conjugate amine pre-functionalized Fe_3O_4, which was covalently anchored with BTSC. Subsequently, a new condition established in this thesis was relied upon for the covalent anchoring of BTSC with amine pre-functionalized SiO_2 and dopamine pre-functionalized Fe_2O_3. The chapter concluded with the microwave-assisted decomposition of [Cu(BTSC)], [Pd(BTSC)] and [Zn(BTSC)]. The result indicates that high-quality metal sulfides can be synthesized within 10 minutes. An attempt to make bimetallic Pd_2S NP was also successful.

CHAPTER 3. Results and Discussion

3.1 Fe$_3$O$_4$@SiO$_2$–APTES–BTSC Nanoparticles in Binding Pd^{2+} ions

Fe$_3$O$_4$@SiO$_2$–APTES–BTSC was used to adsorb Pd^{2+} ions in an aqueous solution. The two UV absorption bands at 210 and 240 nm were used to monitor the absorbance change of Pd^{2+} removal from HCl solutions. The calibration curve is presented in **Fig. 48**. The adsorption of Pd^{2+} with non-functionalized Fe$_3$O$_4$@SiO$_2$–APTES was also monitored for comparison (**Fig. 48**). The maximum adsorption was achieved after 25 min for Fe$_3$O$_4$@SiO$_2$–APTES–BTSC, while the blank experiment using Fe$_3$O$_4$@SiO$_2$–APTES showed saturation after 15 min. The time concentration profile, as monitored by UV-vis spectroscopy, showed that the conjugation of Fe$_3$O$_4$@SiO$_2$–APTES–BTSC with BTSC enhances the affinity for Pd^{2+}.
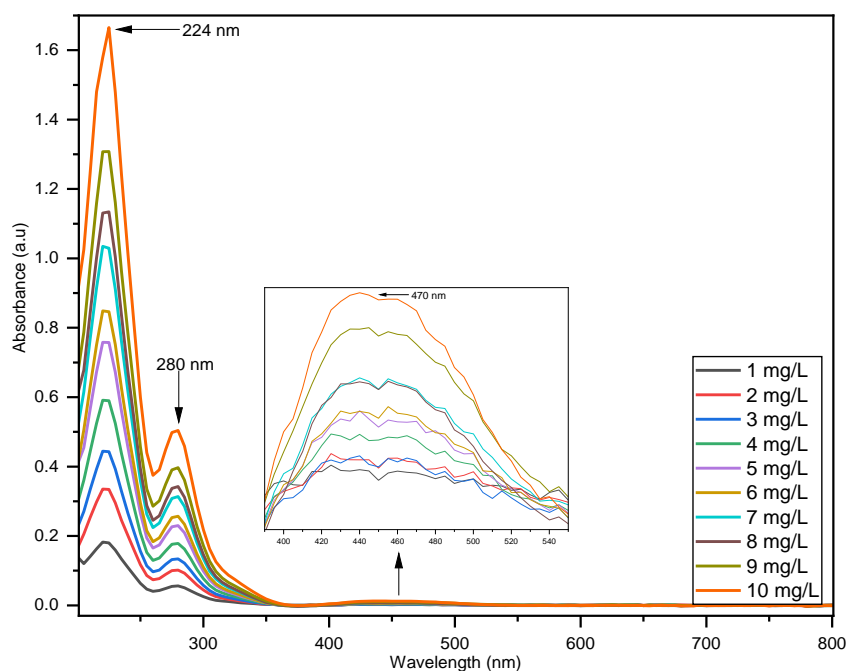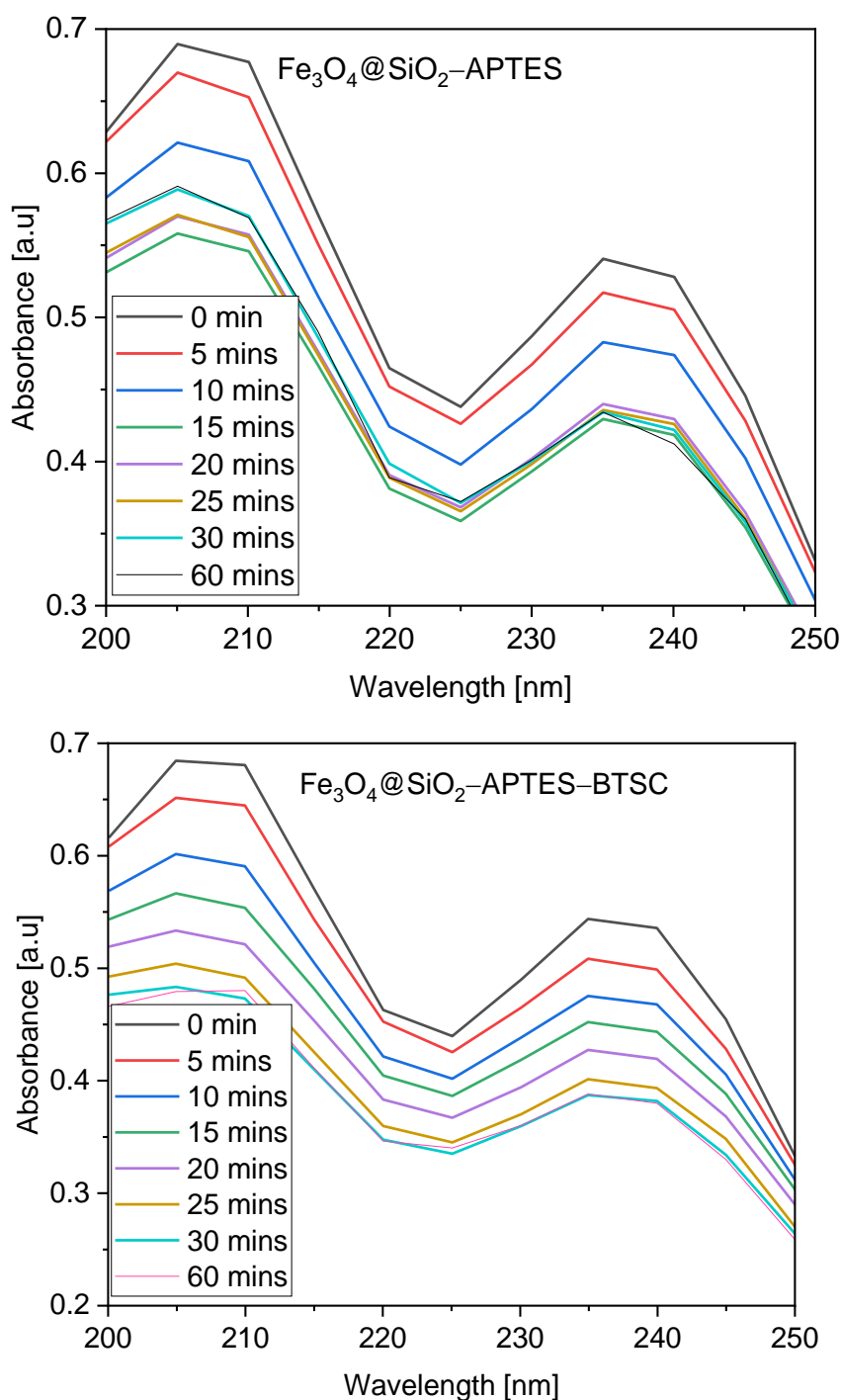
Fig. 48. UV-vis absorption spectra for the calibration curve used to investigate Pd^{2+} absorbance change (**top**). Time-concentration profile for the adsorption of Pd^{2+} ions using $Fe_3O_4@SiO_2$–APTES (**middle**) and $Fe_3O_4@SiO_2$–APTES–BTSC (**bottom**) adsorbents.

The adsorption isotherm data were fitted into non-linear Langmuir and Freundlich adsorption equations. The adsorption isotherm data is presented in **Table 6**. The adsorption capacity increased with increasing initial $K_2Pd_2Cl_4$ concentration (**Fig. 49**). The Freundlich isotherm is in keeping with an

adsorption process occurring on a heterogenous surface, it is reversible and non-uniform, while the Langmuir model is best suited for monolayer adsorption.[132,133] Furthermore, the calculated Freundlich parameters K_F = 0.4712 (mg/g)/(mg/L) and n = 1 suggest that the adsorption follows a cooperative mechanism, which is in line with multidentate binding of Pd^{2+} in the BTSC pocket. The maximum adsorption capacity for $Fe_3O_4@SiO_2$–APTES–BTSC was 793.44 mg/g. For the blank $Fe_3O_4@SiO_2$–APTES, the adsorption capacity was 270.2 mg/g, an indication that the major adsorption contribution was from the functionalized BTSC unit. Initial solution pH does not have a severe impact on the adsorption capacity. Thus, the $Fe_3O_4@SiO_2$–APTES–BTSC can function at a wide pH range. This is attributed to the N^S donor atoms of BTSC that can function at opposing pH ranges.[20]

Table 6. Equilibrium adsorption isotherm data. [a]

Initial Conc (Co) (mg/L)	q_e (mg/g)	Langmuir isotherm parameters		
1	38.56	q_{max} (mg/g)	K_L (L/mg)	R^2
5	197.16	813.008	0.124	0.9365
10	396.704	Freundlich isotherm parameters		
15	595.88	n	K_F (mg/g)/(mg/L)	R^2
20	793.44	1	0.4712	1
Effect of pH				
Initial pH	2.2	4	6.1	8.2
Final pH	2.2	4.1	6.5	7.4
q_e (mg/g)	322.96	394.12	397.68	316

[a] C_o and C_e are the initial and final concentration, q_e and q_{max} are the adsorption capacity, while K_L and K_F are the Langmuir and Freundlich constants.
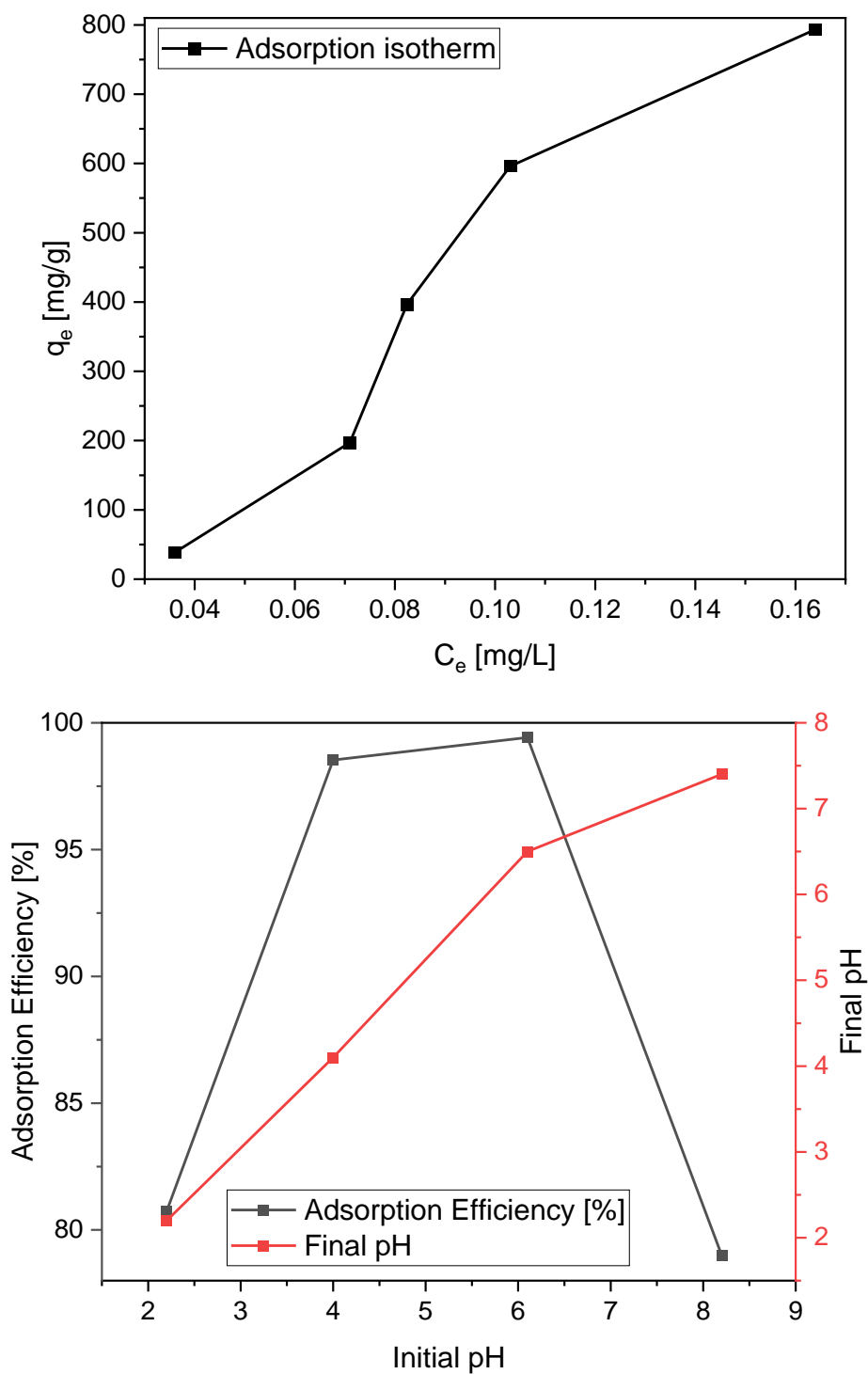
Fig. 49. Adsorption isotherm and effect of pH in removing Pd²⁺ ions from an aqueous solution using Fe₃O₄@SiO₂–APTES–BTSC.

3.1.1 Fe₃O₄@SiO₂–APTES–BTSC Nanoparticles Mechanism in Binding Pd²⁺ ions – (Adsorbed Species). To gain an insight into the adsorption mechanism, a combination of characterization techniques and modelling was employed. 2,6-diacetylpyridine-bis-(4-*N*-2-pyridyl)-BTSC ([Pd(BTSC)]) was

coordinated with Pd^{2+}. The single-crystal XRD (**Fig. 50**) showed a $S_{thiolate}$^N_{immine}^N_{Py}^N_{amide} coordination and the packing clearly showed a Pd–Pd interaction with a distance of 3.323 Å, while the DFT-calculated optimized geometries confirm that this is the most stable species (-60,661.75 eV).
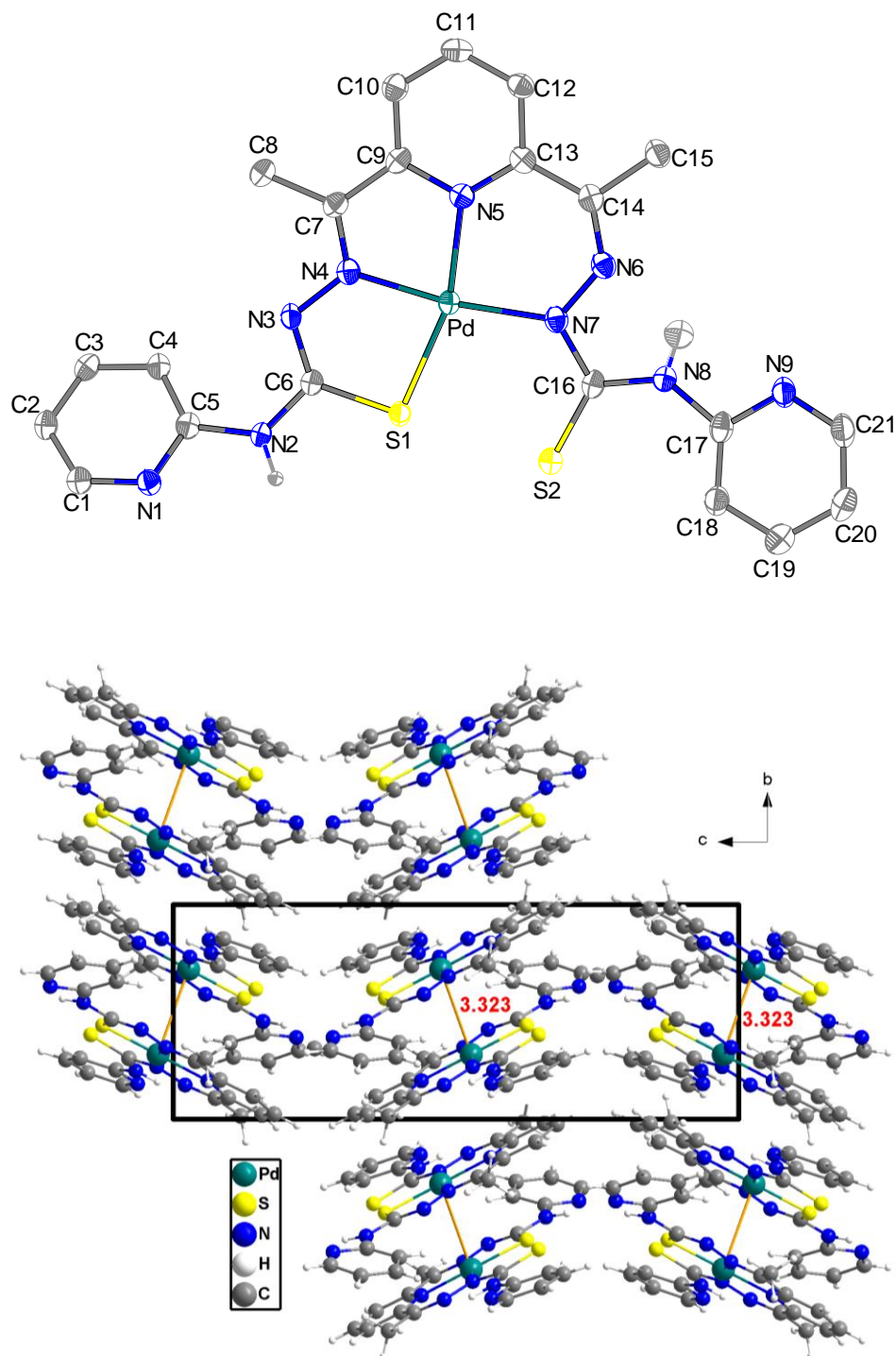
Fig. 50 Molecular structure (**Top**) and packing (**bottom**) of Pd complex of 2,6-diacetylpyridine-bis-(4-*N*-2-pyridyl)-BTSC, projected along the *a*-axis.

However, other calculated configurations, including S^N^N^S coordination (60,664.61 eV) and Pd–Cl-containing complex species (-73,206.17 eV), are very close in energy (**Fig. 51**). These species have the $S_{thiolate}$^N_{imine} chelate coordination in common (**Table 7**). Thus, it is assumed that, sooner or later, any initially present thione is deprotonated upon S_{thione}^N_{imine} chelate coordination. This thione-thiolate transformation is in agreement with a strong increase in softness [10,11,69] and is probably driven by the soft but also electrophilic Pd(II).[10,65,134]
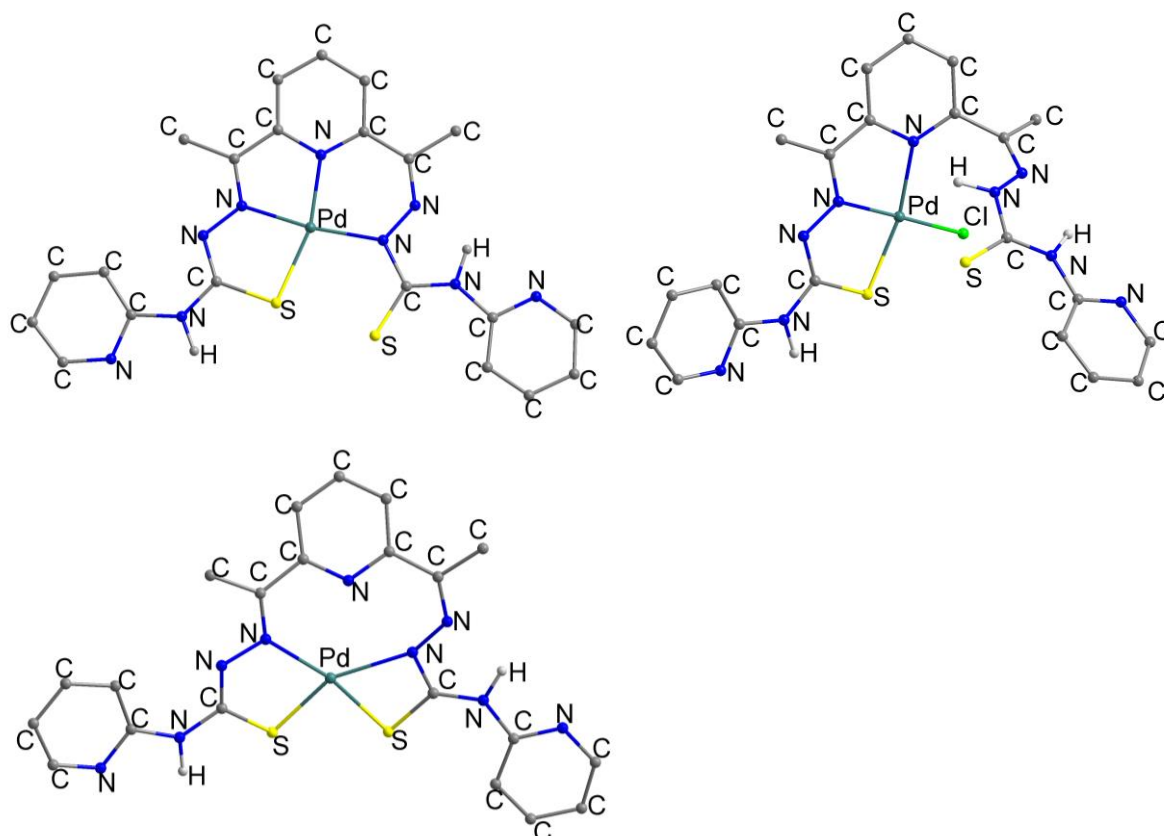
Fig. 51. DFT calculated possible isomers configuration for Pd complex of 2,6-diacetylpyridine-bis-(4-*N*-2-pyridyl)-BTSC.

The geometry of the Cl-containing structure [Pd(BTSC)Cl] with a $S_{thiolate}$^N_{imine}^N_{Py}/Cl bonding motive, shows the same preference for pyridine N binding as the experimental and the calculated structure derivative [Pd(BTSC)] but it does not include a six-ring N^N chelate motive. Therefore, it is assumed that the overall chemical preference of Pd(II) to the central pyridine N atom, while the electronically favorable six-ring N^N chelate found in the experimental and calculated structure [Pd(BTSC)] might govern the formation of this structure, but seems not to be a very important feature in binding Pd(II).

Table 6. Selected metrics in experimental and DFT-calculated [Pd(BTSC)] and [Pd(BTSC)Cl] structures.

	[Pd(BTSC)] [a]	[Pd(BTSC)] [b]	[Pd(BTSC)Cl] [b]	[Pd(BTSC)] [b,c]
	Exp.	Calc.	Calc.	Calc.
Bond length (Å)				
Pd–S(1)	2.2971(9)	2.304	2.257	2.238
Pd–N(4) (TSC-*N*1)	1.981(3)	1.991	1.966	2.171
Pd–N(5)$_{Py}$	2.035(3)	2.043	2.117	–
Pd–N(7) (TSC-*N*2)	2.044(3)	2.041	–	2.327
Pd–S(2)	–	–	–	2.294
Pd–Cl(1)	–	–	2.297	–
Angles (°)				
S(1)–Pd–N(4)	82.87(8)	83.51	84.99	82.37
N(4)–Pd–N(5)	80.32(11)	80.43	79.83	–
N(5)–Pd–N(7)	91.61(11)	91.97	–	–
N(7)–Pd–S(1)	105.12(8)	104.09	–	153.44
N(4)–Pd–N(7)	171.87(11)	172.38	–	123.87
N(5)–Pd–S(1)	162.91(8)	163.93	164.59	–
N(4)–Pd–N(6)	–	–	–	–
N(6)–Pd–(N(2)	–	–	–	–
N(6)–Pd–S(1)	–	–	–	–
N(7)-Pd-S(2)	–	–	–	66.65
S(1)–Pd–S(2)	–	–	–	86.92
N(4)–Pd–S(2)	–	–	–	169.00
S(1)–Pd–Cl(1)	–	–	93.27	–
N(5)–Pd–Cl(1)	–	–	102.13	–
N(4)–Pd–Cl(1)	–	–	171.97	–
Σ angles Pd	360.71	360.00	360.23	359.81

[a] From single crystal X-ray diffraction on [Pd(BTSC)]. [b] From DFT geometry optimization using def2-TZVP basis sets and BP86 functionals including Grimme's D3 dispersion parameterized for gas-phase. [c] Pd coordinated with two imine.

In agreement with the EDX analysis (**Fig. 52**), the XPS survey scan (**Fig. 53**) showed that Pd–Cl species play a role in final Pd-binding. The adsorption isotherm results are in line with a cooperative adsorption. This agrees with the idea of more than one Pd binding mode contributing to the overall adsorption process. This also agrees with the Pd-BTSC binding models above (**Fig. 50**).
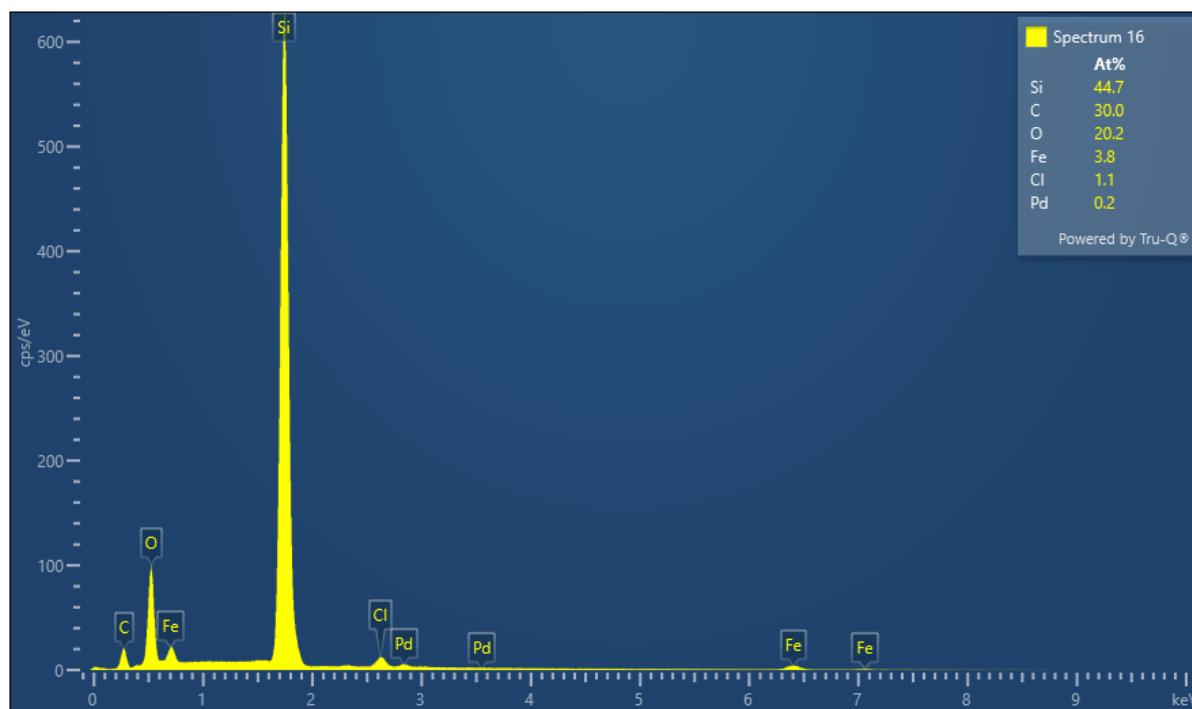
Fig. 52. EDX analysis of $Fe_3O_4@SiO_2$–APTES–BTSC–Pd NP

The XPS survey spectrum of the $Fe_3O_4@SiO_2$–APTES–BTSC–Pd spent-adsorbent showed signals for O, C, N, Cl, Si, S and Pd at binding energies of 532.72, 285.22, 400.22, 199.22, 103.39, 288.22 and 338.72 eV, respectively.[93] This is in agreement with the Cl atom found in the EDX analysis (**Fig. 52**). The high-resolution N 1s signals of $Fe_3O_4@SiO_2$–APTES–BTSC–Pd at 400.1, 402.1 and 405.1 eV (**Fig. 53**) are related to pyridine N, amide N, and imine N atoms.[104,135,136] These binding energy values increase significantly by 0.89, 3.16 and 1.53 eV compared to the XPS values N1s of $Fe_3O_4@SiO_2$–APTES. The Pd 3d peaks centred at 338.40, and 343.71 eV suggests that Pd is predominately Pd^{2+} and was not partially reduced to Pd^0. Compared with the standard spectra of $PdCl_2$ (*ca*. 337.9 eV), the binding energy decreased by 0.8 eV.[98] Together with the finding of Cl, the Pd-binding energy at 343.71 eV suggests a chlorido–Pd(II) complex such as [Pd(BTSC)Cl] (**Fig. 51**) as "extracted species". Similar Pd–binding energies have been reported for [$PdCl_2(PPh_3)_3$] (343.1 eV) and Pd_2F_6 (343.7 eV).[99,137]
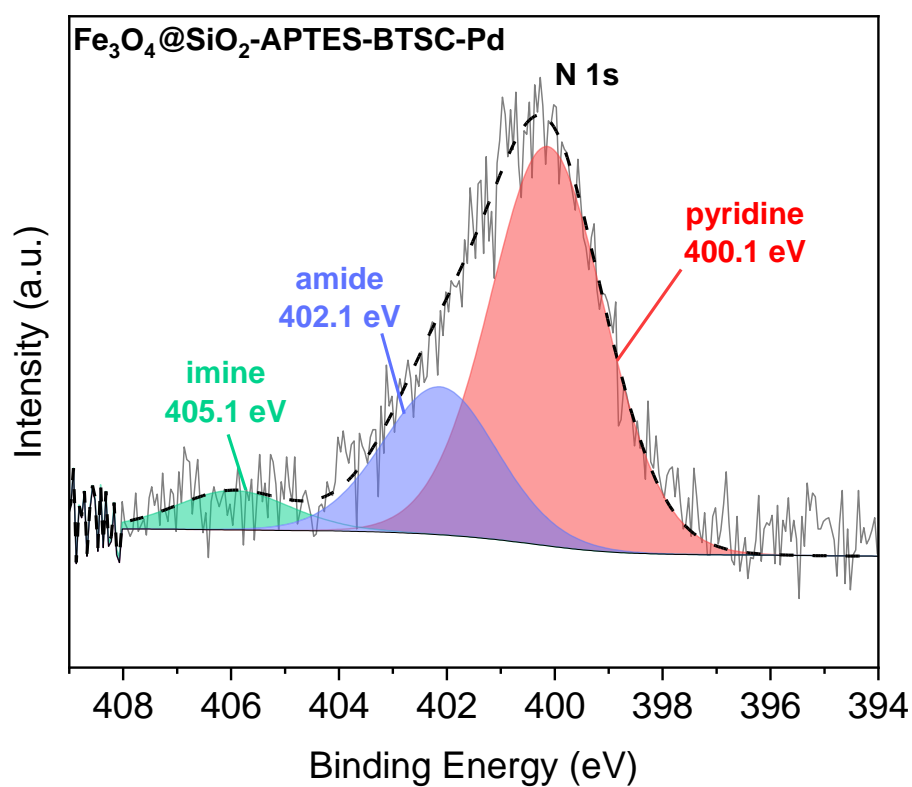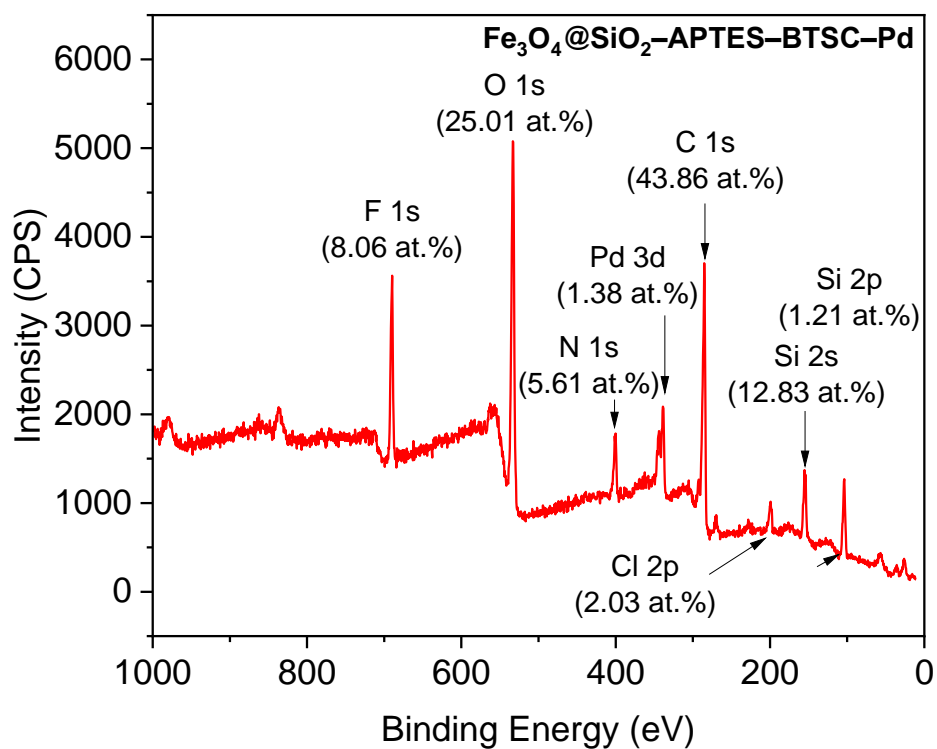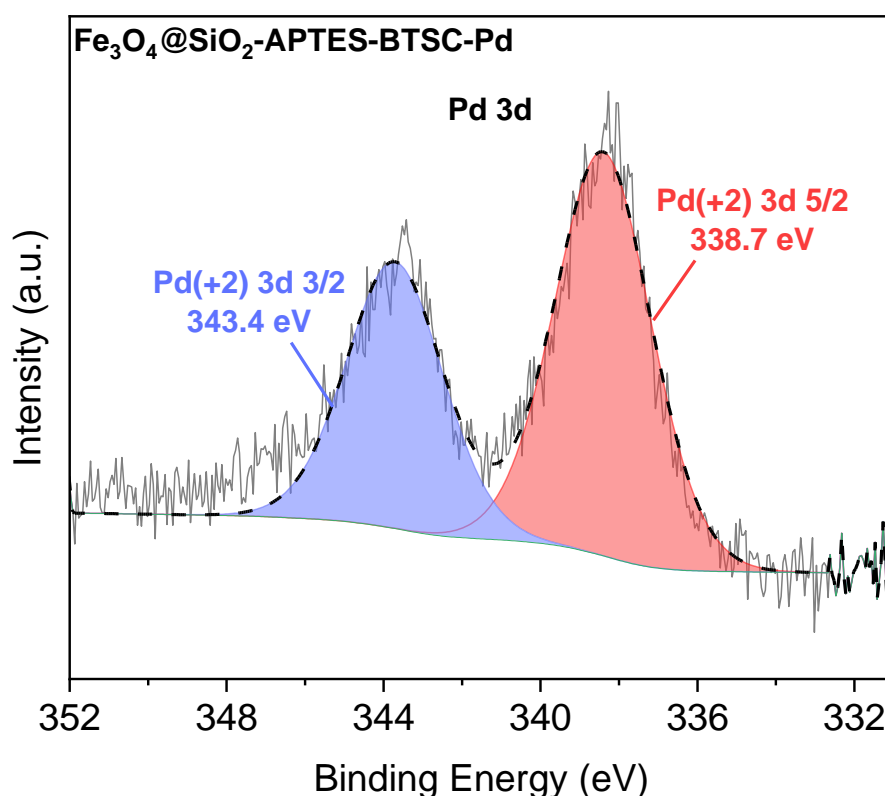
Fig. 53. XPS survey scan and high resolution XPS analysis of Fe₃O₄@SiO₂–APTES–BTSC–Pd NP

Alternatively, the isotherm adsorption results can also mean that different species are involved in the initial Pd-binding, as shown in **Fig. 54**. This also highlights the potential function of the pending 4-*N*-(2-pyridyl) groups in the Fe₃O₄@SiO₂–APTES–BTSC adsorbent. Assuming that in an aqueous HCl solution the complex [PdCl₄]²⁻ is the dominating species, the assumed *initial species* **A** show [PdCl₃]⁻ ion binding to N_{Py} or S_{thione} after cleaving one Cl⁻.[138,139] Very rapidly either an N_{Py}^S_{thione} (**B**) or N_{Py}^NH_{amine} (**C**) chelate binding might force another Cl⁻ cleavage. The initial N_{Py} coordination of the peripheral 4-*N*-(2-pyridyl) group will then be replaced by the typical TSC-type N_{imine}^S bonding, presumably including deprotonation and formation of $S_{thiolate}$⁻ (**D**). This will lead to another Cl⁻ cleavage forming the assumed final minor species **E**. The last Cl⁻ cleavage is forced by another deprotonation and formation of the final (major) product **F**. However, these initial species remain speculative and species such as [PdCl₃(H₂O)]⁻ or [PdCl(H₂O)₃]⁺ resulting from de-chlorination of the [PdCl₄]²⁻ in the test solutions,[28,29] might be the first to coordinate to the BTSC ligand.[138,139]
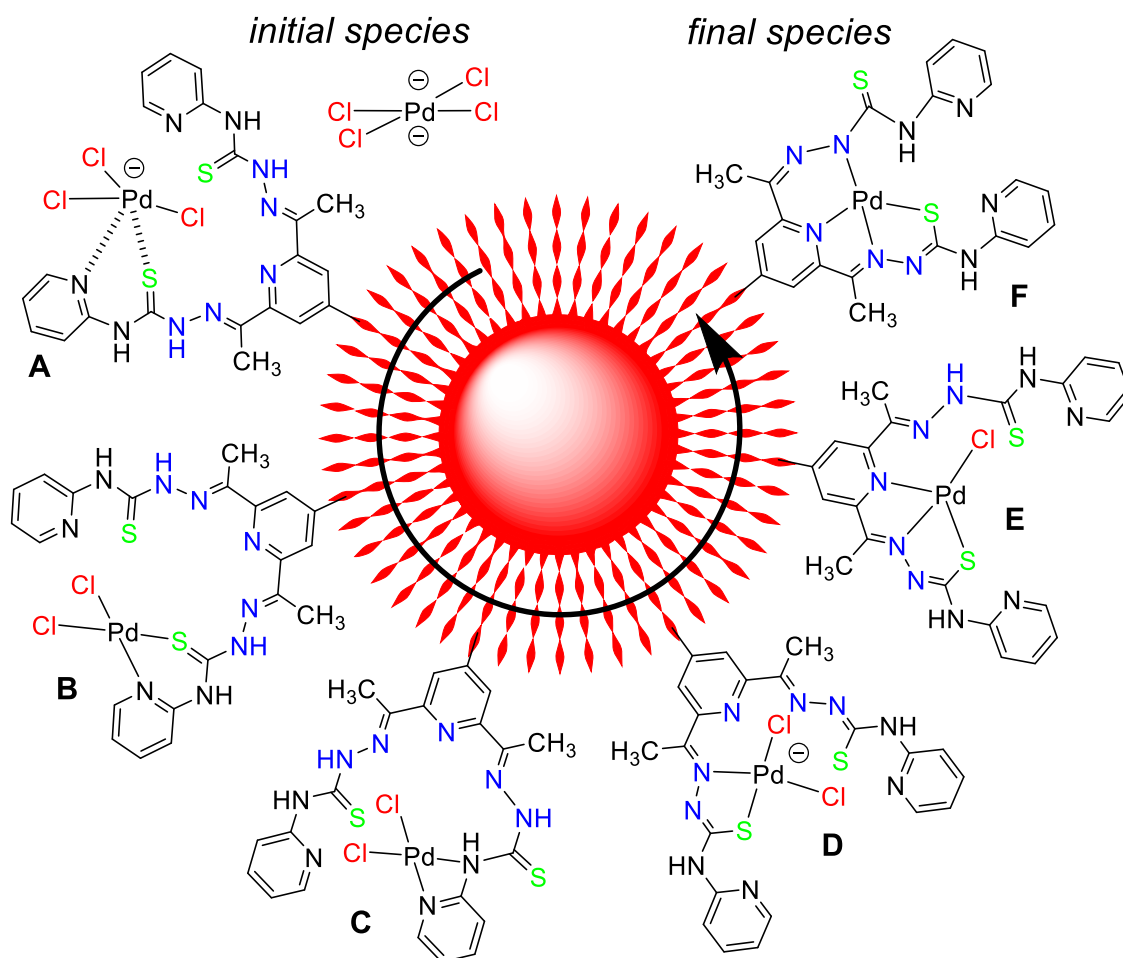
Fig. 54. Proposed adsorbed Pd-BTSC species.

Table **3.2** compared the adsorption capacity of some reported adsorbents with Fe₃O₄@SiO₂–APTES–BTSC. Fe₃O₄@SiO₂–APTES–BTSC have outperformed other adsorbents in removing Pd^{2+} from an aqueous solution (**Table 7**). This is attributed to the BTSC covering the large non-uniform surface area of the Fe₃O₄@SiO₂–APTES–BTSC, as revealed by the SEM image (**Fig. 54**).

Table 7. Comparison of Fe₃O₄@SiO₂–APTES–BTSC NPs with other absorbents used for the removal of Pd(II) ions.

Adsorbent	Initial conc (mg/L)	pH	Adsorbent dosage (g)	Adsorption capacity (mg/g)	Ref.
PMMA/PEO/DTE EFs [a]	80	1.0	4	37	[138]
TN modified PAN EFs [b]	100	1.0	0.02	348.4	[139]
Activated carbon	–	1.0	–	42.20	[137]

TAA-PP beads [c]	10	0.1	0.01	206.93	[140]
AHPP-MOF [d]	500	4.0	0.01	283.5	[141]
Zr(MOF)-pyromellitic acid	300	2.0	0.01	226.1	[142]
Glycine@chitosan	50	2.0	0.1	120.39	[143]
MOF-poly(propylene imine)	110	4.0	0.125	291	[144]
Thiourea@chitosan	400	2.0	0.1	112.4	[145]
Dispersive SPE [e]	30	6.0	0.02	24.6	[146]
Pd-Fe_3O_4@SiO_2-EGDMA/HEMA/AIBN [f]	300	4.0	1	65.75	[147]
SiO_2@THTB-TSC [g]	5	3.5	0.01	171.65	[148]
mGO@SiO_2@PPy-PTh [h]	–	4.8	0.02	45	[149]
Fe_3O_4@SiO_2@PT [i]	700	3	0.5	191.47	[150]
Fe_3O_4@SiO_2–APTES–BTSC	20	4.0	0.0005	793.44	This study

[a] Poly(methyl methacylat) (PMMA), poly(ethylene oxide) (PEO) electrospun fibers doped with 2-cyano-2-propyl benzodithioate (DTE). [b] Thionicotinic acid-modified polyacrylonitrile (PAN) electrospun fibers. [c] AHPP = 4-amino-3-hydroxybenzoic acid and *p*-phthalaldehyde. [d] Tris(2-aminoethyl)amine polystyrene polymer beads. [e] SPE = Solid Phase Extraction. [f] EGDMA = ethylene glycol dimethacrylate, HEMA = 2-hydroxyl methacrylate, AIBN = α-α'-azoisobisbutyronitrile. [g] THTB = hydroxybenzaldehyde. [h] PPy-PTh = polypyrrole-polythiophene. [i] PT = Plant Tannin.
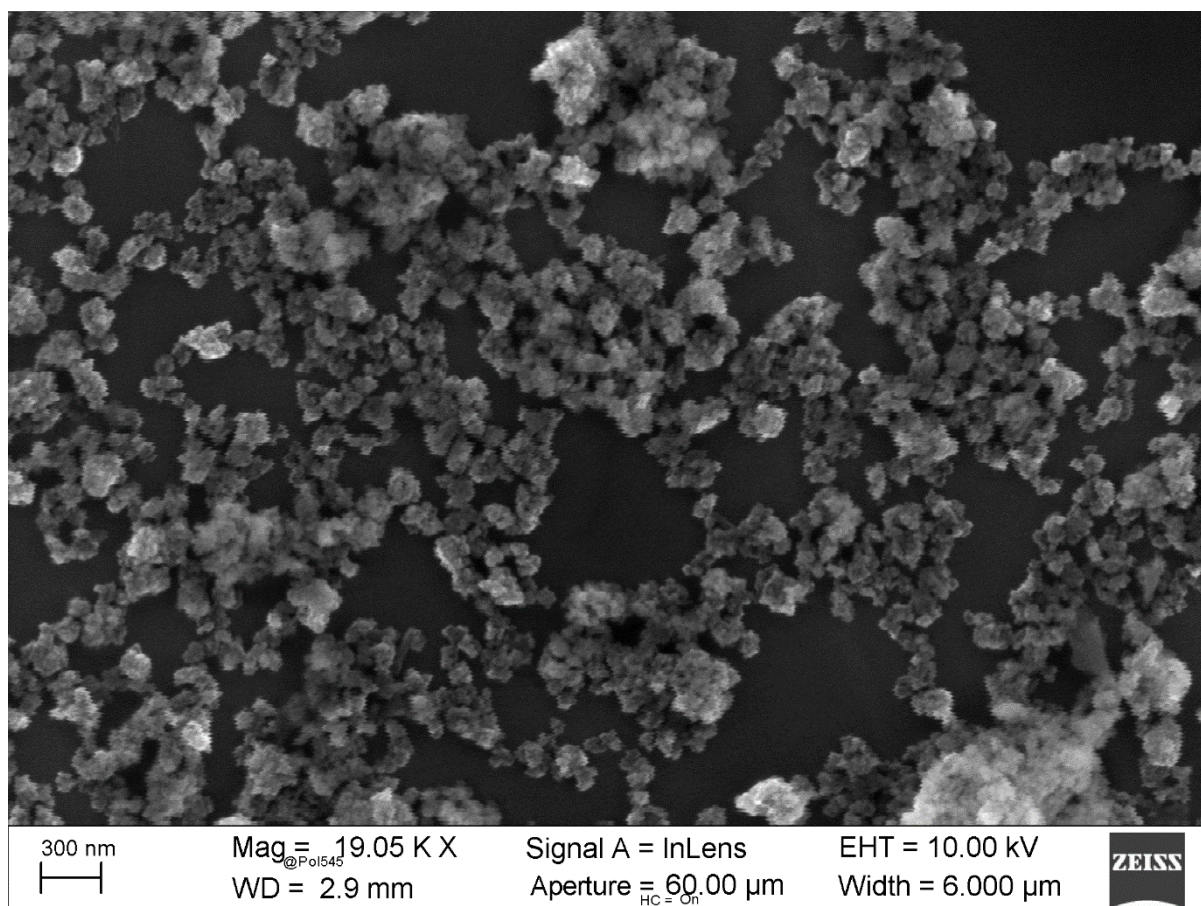
Fig. 54. SEM image of Fe$_3$O$_4$@SiO$_2$–APTES–BTSC–Pd

3.2 SiO$_2$–APTES–BTSC Nanoparticles in Suzuki-Miyaura sp2 – sp2 Cross-Coupling Reaction

The SiO$_2$–APTES–BTSC–Pd catalyst was investigated for the Suzuki cross-coupling reaction. Bromophenyl and phenylboronic acid were selected for optimization conditions (**Table 8**). The coupling reactions were carried out using different solvents (THF, EtOH and H$_2$O). EtOH gives the best results (70 %). K$_2$CO$_3$ gives the best results among the tested bases (Na$_2$CO$_3$ and Et$_3$N). The catalytic dosage was also varied between 2, 4, and 6 mol%. Increasing the catalytic dosage from 2 to 6 mol% enhanced the formation of biphenyl. However, increasing the reaction temperature from 60 to 100°C did not significantly change the isolated yield. Therefore, the 80°C was selected as the optimal dosage.

Table 8. Optimization of the reaction condition for Suzuki-Miyaura cross-coupling reactions between 1 equivalent bromobenzene and 1.2 equivalent of phenylboronic acid.

Entry	Solvent	Base	SiO$_2$–APTES–BTSC–Pd (g)	Temp. (^{o}C)	Isolated Yield
1	THF	K$_2$CO$_3$	0.4	80	54
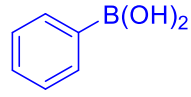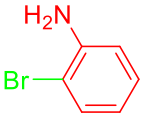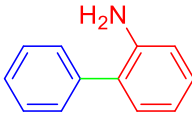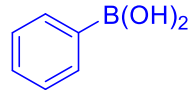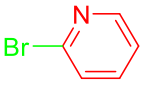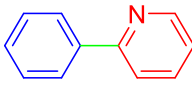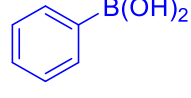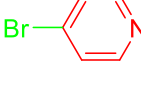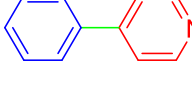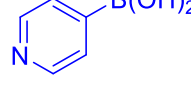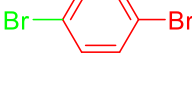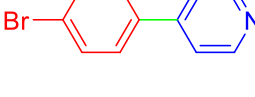
2	EtOH	K_2CO_3	0.4	80	70
3	H_2O	K_2CO_3	0.4	80	Traces
4	EtOH	Na_2CO_3	0.4	80	50
5	EtOH	Et_3N	0.4	80	45
6	EtOH	K_2CO_3	0.6	80	72
7	EtOH	K_2CO_3	0.8	80	80
8	EtOH	K_2CO_3	0.8	60	66
9	EtOH	K_2CO_3	0.8	100	81

Reaction conditions: phenylboronic acid (1.2 mmol), bromobenzene (1 mmol), base (6 mmol), 15 mL solvent, 20 hours, inert conditions.

The optimal condition was applied for the synthesis of different bi-aryl compounds. The coupling reaction gave a satisfactory result (**Table 9**). Table 2 shows that substrates with electron-donating groups are isolated in higher yield compared to substrates with electron-withdrawing groups. The highest yield was obtained for diphenyl and 2-methyl-diphenyl. Other authors have reported similar results for TSC complexes used in the Suzuki-Miyaura cross-coupling reactions.[151,152] The SiO2–APTES–BTSC–Pd can be recycled up to three times without a significant loss in catalytic activities, highlighting the catalyst stability (**Fig. 3.8**).

Table 9. Suzuki-Miyaura cross-coupling reaction of different aryl halides with phenylboronic acids.

Entry Substrate	Entry Substrate	Product	Isolated Yield (%)
			80
			70
			77

Phenyl-B(OH)$_2$	2-Bromoaniline (H$_2$N, Br)	2-Aminobiphenyl (H$_2$N)	75
Phenyl-B(OH)$_2$	2-Bromopyridine (N, Br)	2-Phenylpyridine (N)	73
Phenyl-B(OH)$_2$	4-Bromopyridine (Br, N)	4-Phenylpyridine (N)	66
Pyridin-4-yl-B(OH)$_2$ (N)	1,4-Dibromobenzene (Br–, –Br)	4-(4-Bromophenyl)pyridine (Br–, N)	70

Reaction condition: 15 mL solvents, SiO$_2$–APTES–BTSC–Pd (0.4 g), inert condition, K$_2$CO$_3$ (6 mmol), aryl-halid (1 mmol), aryl-boronic-acid (1.2 mmol).
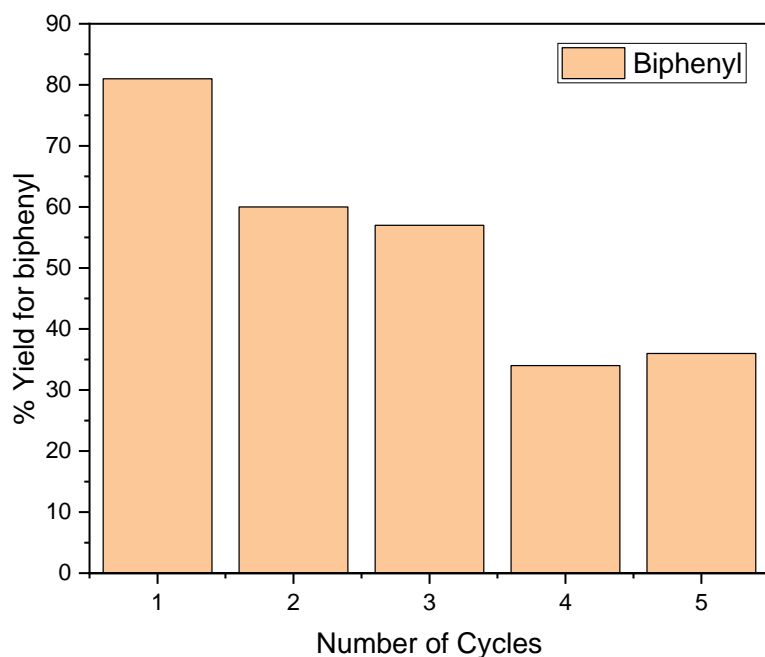
Fig. 55. Recyclability of SiO$_2$–APTES–BTSC–Pd for Suzuki-Miyaura coupling of biphenyl.

3.3 Conclusion

Chapter **3** described the adsorption of Pd^{2+} with Fe$_3$O$_4$–APTES–BTSC NP in an aqueous solution. Due to solubility concerns of the Pd source (K$_2$PdCl$_4$), Pd^{2+} was accessible in HCl solution. Fe$_3$O$_4$–APTES–BTSC exhibits a high adsorption capacity in a wide pH range. The parent BTSC was also coordinated with Pd^{2+} ions. The molecular structure revealed non-symmetric S$_{thiolate}^{N}_{imine}^{N}_{pyridine}^{N}_{amide}$ binding modes, and the crystal packing showed Pd–Pd interaction. The fitted isotherm adsorption data showed that the Freundlich isotherm adsorption model best described the adsorption process, which

suggests cooperative adsorption. In lieu, DFT calculation reveals that other binding motifs could be involved in the adsorption process and the EDX and XPS investigations supported this claim.

Chapter **3** concluded by using SiO_2–APTES–BTSC–Pd conjugate as a heterogeneous catalyst in the Suzuki-Miyaura cross-coupling reaction of aryls. SiO_2–APTES–BTSC–Pd conjugate coupled a wide range of aryl in moderate yields and SiO_2–APTES–BTSC–Pd conjugate can be regenerated upto 4 cycle with slight loss in catalytic performance. XPS investigation showed that Pd in SiO_2–APTES–BTSC–Pd catalyst is predominantly Pd^0, a vital characteristic of the catalyst in the Suzuki-Miyaura cross-coupling reaction.

Chapter 4 Conclusion and Outlook

Bis-thiosemicarbazones (BTSCs) and their metal complexes are known for their biological properties in treatment or imaging. The uncoordinated BTSCs have also been used to probe or sense metal ions in food and beverages. BTSC metal complexes have also found application in homogeneous catalysis. The main drawback to BTSC, which has limited the activities of BTSC as a biological agent, is the challenge of targeting a specific cell. Similarly, unrecovered BTSC employed in sensing metal ions in food and beverages is secondary contamination and potential food and beverage poisoning. Also, additional costs are incurred in homogenous catalysis due to the recovery of spent BTSC catalysts. These shortcomings may be addressed by the covalent anchoring of BTSC onto solid supports (NPs). The large specific surface area characterized by NPs is unique for transporting ligands to target specific cells. Other NPs properties, such as magnetism, would allow for easy recovery of NP–BTSC conjugates.

Therefore, the first objective of the study was achieved by the synthesis of BTSC bearing a carboxylate or chlorido functional group at the diketone backbone or by derivatization of thiosemicarbazide, so that the resulting BTSC bear chlorido functional group at the diamine tail. The functionalized/derivatized BTSC was first reacted with bifunctional linkers, namely, APTES and dopamine, to establish the reaction conditions. The first study involved the synthesis of ester-functionalized BTSC. The hydrolysis of the ester group affords a carboxylate functionalized BTSC. The carboxylate functionalized BTSC was reacted with amine pre-functionalized $Fe_3O_4@SiO_2$–APTES via the well-established EDC/NHS coupling chemistry to afford $Fe_3O_4@SiO_2$–APTES–BTSC conjugated. The $Fe_3O_4@SiO_2$–APTES–BTSC NP was used to adsorb Pd^{2+} ions from an aqueous solution. The $Fe_3O_4@SiO_2$–APTES–BTSC NP was characterized by high adsorption capacity (734 mg/g) and can function at a broad pH range (2 – 8). The high adsorption capacity of the $Fe_3O_4@SiO_2$–APTES–BTSC NP was attributed to the pentadentate N^S donor atoms, which bind via the S_{thiol}^N_{imine}^$N_{pyridinic}$^N_{amide} coordination and the cooperative adsorption arises from the combination of minor coordination.

SiO_2–APTES–BTSC–Pd was synthesized by reacting amine pre-functionalized SiO_2–APTES with Cl-functionalized BTSC in dry THF. SiO_2–APTES–BTSC was subsequently coordinated with Pd^{2+} ions. The SEM image of the uncoordinated SiO_2–APTES–BTSC NP showed monodispersed NPs, and the EDX analysis and XPS survey scan showed the expected elements (Si, O, N and S). The SEM image of the coordinated SiO_2–APTES–BTSC–Pd showed monodispersed NPs with unevenly dispersed Pd^{2+}

particles attached to the surface of the SiO$_2$–APTES–BTSC NPs. Si, O, N, S, Pd and Cl peaks were identified in SiO$_2$–APTES–H$_2$L–Pd and the EDX analysis revealed that Pd and Cl were present in ratio 1:1, suggesting that in addition to the S$_{thiol}^{N}_{imine}^{N}_{pyridinic}^{N}_{amide}$ coordination as revealed by single crystal XRD, minor S$_{thiol}^{N}_{imine}^{N}_{pyridinic}$^Cl coordination was also present. High–resolution X-ray photoelectron spectroscopy (XPS) analysis of N 1s, C 1s and S 2p were characterized by a shift to a lower binding energy after coordinating with Pd^{2+}, suggesting that these functional groups (C=N, C=S, N–H, pyridinic–N) are responsible for Pd^{2+} coordination. The SiO$_2$–APTES–H$_2$L–Pd NPs were used in the Suzuki-Miyaura sp2 – sp2 cross-coupling reaction. The SiO$_2$–APTES–H$_2$L–Pd catalyst performed reasonably well up to the third catalytic cycle.

The metal complex of thiosemicarbazones has been used as precursors for the synthesis of metal sulfides. The metal sulfide NPs are synthesized via pyrolysis, hydrothermal or thermal decomposition of metal complexes of thiosemicarbazone. These methods require a high amount of energy and a long reaction time. Therefore, an alternate method, such as microwave-assisted decomposition, is preferred due to low energy requirement and short reaction time. Thus, the final study involved the synthesis of copper sulfide, palladium sulfide and zinc sulfide NPs via microwave-assisted decomposition. The BTSC metal complexes (Cu, Pd and Zn) were dissolved in *N*-methyl-2-pyrrolidone and heated for 10 minutes under a microwave. Cu$_{7.2}$S$_4$ NPs were obtained in the *Fm—3m* space group, Pd$_{16}$S$_7$ NPs were obtained in the *I—43m* space group, and ZnS NPs were obtained in the *F -4 3 m*. All NPs appeared in the cubic phase. The EDX spectra showed the expected peaks, Cu, Pd and Zn, as the metal ion in addition to the S atom, and the atomic percentage agrees with the PXRD phase of the metal sulfide, which alludes to the purity of the NPs. Thus, Cu$_{7.2}$S$_4$, Pd$_{16}$S$_7$ and ZnS nanocrystals can be synthesized at reduced reaction time and energy.

Future consideration should focus on improving the solubility of the BTSC. The derivatization of the dicarbonyl backbone of the BTSC with halogen, ester, tertbutyl and phenyl did not significantly enhance the solubility. This is evident in the poor solubility of 4-bromo-2,6-diacetylpyridine-bis-(4-*N*-2-pyridyl)-TSC as compared with the unsubstituted 2,6-diacetylpyridine-bis-(4-*N*-2-pyridyl)-TSC. Similarly, the low product yield associated with the diketone backbone is also a significant concern. Thus, an alternate backbone should be considered to improve yield and solubility. The study can also be extended to a method to obtain a uniform distribution of Pd^{2+} in the conjugate by comparing pre and post-functionalization techniques. The release of coordinated metal ions (Pd^{2+}) can also be explored to extend the application of NP–BTSC conjugate to biological applications. Finally, future

consideration should be given to the facile synthesis of bimetallic and trimetallic NPs with potential applications in catalysis and as energy storage devices.

Chapter 5 Experimental Section

5.1 Instrumentation.

NMR spectra were recorded on a Bruker Avance II 300 MHz spectrometer, using a triple resonance 1H, nBB inverse probe head or a Bruker Avance III spectrometer at 499 MHz with a TCI prodigy 5 mm probe head with z–gradient (1H/^{19}F, ^{13}C, ^{15}N, ^{2}H). X-ray structure determination were carried out on a Bruker D8 Venture diffractometer, including a Bruker Photon 100 CMOS detector, Rheinhausen, Germany, at 100(2) K using Mo Kα (λ=0.71073 Å) radiation. The crystal data were collected using APEX4 v2021.10-0.[153] The structures were solved by dual-space methods using SHELXT, and the refinement was carried out with SHELXL employing the full-matrix least-squares methods on $F_O^2 < 2\sigma(F_O^2)$ as implemented in ShelXle.[154–156] The non-hydrogen atoms were refined with anisotropic displacement parameters, and hydrogen atoms were included using appropriate riding models.

Cyclic voltammetry was performed at a 100 mV/s scan rate in 0.1 M nBu$_4$NPF$_6$ solutions using a three-electrode configuration (working electrode: glassy carbon; counter electrode: Pt; reference: Ag/AgCl) and a Metrohm Autolab PG STAT 30 potentiostat with ferrocene/ferrocenium as internal reference.

The Fourier transform infrared (FTIR) spectra were recorded on a PerkinElmer–Spectrum 400 with a Universal ATR sampling accessory in the range 4000 to 400 cm^{-1}. UV–vis absorption spectra were recorded using a Varian 60 Scan spectrophotometer.

Computational studies were performed using ORCA 5.0.2, and def2–TZVP basis sets were used for all atoms.[157–159] The geometry of all compounds was optimized at the BP86 level of theory, using Grimme's Dispersion correction and the conductor-like polarizable continuum model (CPCM) parametrized for DCM and DMSO as an approximate solvation model.[160–164] The geometry optimization results were followed up with numerical frequency calculations to confirm the optimized structure's energetic minimum nature, as indicated by the absence of imaginary modes. Chemcraft software was used for visualization of DFT calculation results.[165]

Scanning Electron Microscopy (SEM) images were collected using Jeol JSM–65 10 LV QSEM advanced electron microscope with a LaB6 cathode at 20 kV. Dispersive X-ray (EDX) images of the NPs were recorded using REM Zeiss Neon 40 CrossBeam advanced electron microscope with Focused ion beam workstation and STEM detector. The Thermogravimetric analysis (DTA and DSC) of the complexes

were measured on a Perkin Elmer STA 6000, with a temperature range between 30 to 600°C and Scan Rate of 10.0 °C/min under N_2 atmosphere.

XPS measurements were carried out in an ultrahigh vacuum system (base pressure 1×10^{-9} mbar). All samples were transferred to the measurement system under nitrogen avoiding air exposure. A nonmonochromatic X-ray source (VG) with Al Kα excitation was used, having a photon energy of 1486.61 eV. The emitted photoelectrons were measured using a hemispherical analyzer (Specs Phoibos 100). The XPS data were fitted by Voight profiles using the software "XPSPEAK 4.1".

CuS, PdS and ZnS were synthesised using Anton Paar, Monowave 400 (Microwave Synthesis Reactor). The reactor was set at a temperature of 300°C and a cooling rate of 55°C, stirring at 600 rpm. The reactor's energy was set to 26 W and a pressure of 10 bar. . The powder X-ray diffractograms (PXRD) were recorded on an STOE–STADI MP diffractometer equipped with a Mo–Kα1 radiation (λ = 0.7093 Å) source and operating in transmission mode. Scanning Electron Microscopy (SEM) coupled with Energy

5.2 Synthesis

5.2.1 Synthesis of thiosemicarbazide (Method 1)

N-4-(2-pyridyl)-thiosemicarbazide (**1**)

1.25 g (16.4 mmol) CS_2 at –20 °C was added to a solution of 9.47 g (100.6 mmol) 2-aminopyridine dissolved in 25 mL ice-cold water at 0 °C. Then a solution of KOH (110.58 mmol) dissolved 25 mL H_2O at 10 °C was added to the reaction mixture. The reaction mixture was stirred for 24 h in a water bath at 10 °C until the colorless solution turned red. The solution was heated at 80 °C for 2 h until all starting materials are consumed. Then 7.0 g (140 mmol) hydrazine monohydrate was slowly added to the hot solution. The solution immediately turned colorless, and heating was continued for 2 h. Colorless needles of 2-pyridyl thiosemicarbazide began to form after cooling. The solid was filtered off, washed with water and diethyl ether, yielding 680 mg (4.04 mmol, 3.8%) colorless needles. Elemental analysis, found (calc. for $C_6H_8N_4S$, Mw = 168.05 g mol^{-1}), C, 42.91 (42.84), H, 4.18 (4.78), N, 33.73 (33.31), S, 18.68 (19.06). 1H NMR (300 MHz, DMSO-d$_6$): δ 12.59 (s, 1H), 10.58 (s, 1H), 8.22 (dd, *J* = 5.3, 1.8 Hz, 1H), 7.76 (ddd, *J* = 8.9, 7.4, 1.9 Hz, 1H), 7.13 (d, *J* = 8.4 Hz, 1H), 7.07–6.97 (m, 1H), 5.23 (d, *J* = 4.3 Hz, 6H), 2.08 (s, 2H).
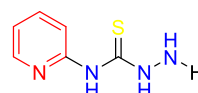
N-4–(2–ethylaniline)–thiosemicarbazide (**2**) (Method **2**)

1.28 g (10.6 mmol) 2–ethylaniline was dissolved in 5 mL deionized water, and the temperature was brought to 0 °C. Thereafter, ice-cold CS₂ (16.4 mmol, 0.99mL) was added to the solution, followed by adding 5 mL cold KOH (11.58 mmol, 0.649 g) solution. The solution was left for 24 h in an ice bath and refluxed for 2 h (80 °C) until 2–ethylaniline was completely consumed. A solution of hydrazine monohydrate (14 mmol, 0.7 mL) was added, and the reaction mixture was heated under reflux for 2.5 hrs. On cooling, a white precipitate was formed. The precipitate was washed with cold water and Et₂O. Single crystals were obtained from a solution of EtOAc and cHex in 1:1 ratio. From the bulk colourless amorphous material. Yield 90%, 1870 mg (195.08 g mol⁻¹, 9.58 mmol) were obtained. Recrystallization from MeOH/DCM led to the isolation of white crystal. 1H NMR (300 MHz, CDCl₃) δ 9.04 (s, 1H), 8.22 (s, 1H), 7.61 (s, 1H), 7.28 (dd, J = 5.9, 2.6 Hz, 3H), 4.03 (s, 2H), 2.67 (q, J = 7.6 Hz, 2H), 1.25 (t, J = 7.6 Hz, 3H) . Elemental analysis for (C₉H₁₃N₃S): found C, 56.01 H, 6.80, N, 21.20 S,14.24; required C, 55.35 H, 6.71, N, 21.52 S, 16.42. HR-GC-EI/MS: [C₉H₁₃N₃S]⁺, Rention time = 22.90 min, >90%.
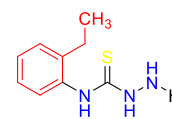
N-(3-hydroxyl-2-pyridyl)-thiosemicarbazide (**3**)

Using method **1**. From 2-amino-3-hydroxypyridine, 4.66 g, 50 mmol. Colourless crystalline solid, 2808.1 mg, (184.22 gmol⁻¹, 15.24 mmol, 36%). 1H NMR (300 MHz, DMSO-d₆): δ 12.43 (s, 1H), 8.33 (s, 1H), 7.72 (d, J = 5.1 Hz, 1H), 7.20 (d, J = 7.9 Hz, 1H), 6.94 (dd, J = 8.0, 5.0 Hz, 1H), 5.24 (s, 2H).
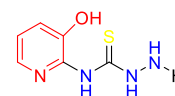
N-4-(3-pyridyl)-thiosemicarbazide (**4**)

Using method **1**. From 3-aminopyridine 4.66g, 50 mmol. Colourless solid, 3124 mg, (184.33 gmol⁻¹, 16.9 mmol, 40%). 1H NMR (300 MHz, DMSO-d₆) δ 9.28 (s, 1H), 8.69 (d, J = 2.6 Hz, 1H), 8.31 – 8.23 (m, 1H), 8.07 (d, J = 8.2 Hz, 1H), 7.33 (ddd, J = 8.2, 4.7, 0.8 Hz, 1H), 5.24 (s, 2H).
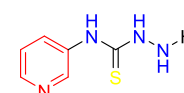
N-(5-methylpyridyl)-thiosemicarbazide (**5**)

Using method **1**. From 5-methyl-2-amino-pyridine, 50 mmol, 5.41g. Colourless solid, 4001 mg, (182.25 gmol⁻¹, 21.9 mmol, 56%). 1H NMR (300 MHz, DMSO-d₆) δ 12.65 (s, 1H), 10.48 (s, 1H), 8.08 (d, J = 5.3 Hz, 1H), 6.94 (s, 1H), 6.86 (dd, J = 5.4, 1.5 Hz, 1H), 5.21 (s, 2H), 2.26 (s, 3H).
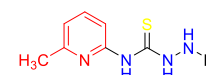
N-4(2-*tert*-butylaniline)-thiosemicarbazide (**6**)

Using method **2**. From 5-tert-butylaniline, 50 mmol, 7.46g. Colourless solid, 2459 mg, (223.34 gmol⁻¹, 11.0 mmol, 25%). 1H NMR (300 MHz, DMSO-d₆) δ 9.64 (s, 1H), 9.07 (s, 1H), 7.69 (s, 1H), 7.50 (d, J = 7.7 Hz, 1H), 7.21 (t, J = 7.9 Hz, 1H), 7.14 – 7.07 (m, 1H), 4.78 (s, 2H), 1.27 (s, 9H).
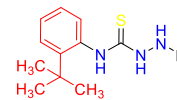
N-4(-4-aminomethyl-pyridyl)-thiosemicarbazide (**7**)

Using method **1**. From 4-amino-methyl-pyridine, 50 mmol, 5.4g. Colourless solid, 2681 mg, (182.25 gmol⁻¹, 14.7 mmol, 33%) 1H NMR (300 MHz, DMSO-d₆) δ 8.84 (s, 1H), 8.53 – 8.39 (m, 2H), 7.31 – 7.21 (m, 2H), 4.74 (d, J = 5.8 Hz, 2H), 4.64 – 4.45 (m, 2H).
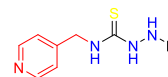
N-4-(4-chloroaniline)-thiosemicarbazide (**8**)

Using method **2**. From 4-chloroaniline, 42.4 mmol, 5.41 g. White crystalline solid, 3000.7 mg (201.67 gmol⁻¹, 1.49 mmol, 36%). 1H NMR (300 MHz, DMSO-d₆): δ 9.17 (s, 1H), 7.67 (d, *J* = 8.3 Hz, 2H), 7.38 – 7.27 (m, 2H), 4.86 (s, 2H).
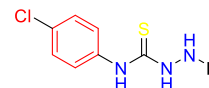
N-4-(butylamine)-thiosemicarbazide (**9**)

Using method **2**. From butylamine, 50 mmol, 3.66g. Colourless solid, 2960.9 mg (147.24 gmol⁻¹, 20 mmol, 42%) 1H NMR (300 MHz, CDCl₃) δ 7.78 (d, J = 2.8 Hz, 1H), 7.44 (s, 1H), 3.80 (s, 2H), 3.63 (td, J = 7.2, 5.7 Hz, 2H), 1.69 – 1.53 (m, 2H), 1.48 – 1.32 (m, 2H), 0.96 (t, J = 7.3 Hz, 3H).
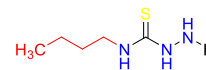
5.2.2 Synthesis of Substituted 2,6-diacetylpyridines – General Procedure

Substituted pyridine (40 mmol) was charged into 100 mL H₂SO₄ (0.4 M), then pyruvic acid (2.1 mL, 31.3 mmol), aqueous AgNO₃ (0.15 g, 0.9 mmol in 0.5 mL water) and (NH₄)₂S₂O₈ (11 g, 43.8 mmol) was added. The solution was left to stir overnight at room temperature. The mixture was filtered, and the combined organic fraction was extracted with DCM (150 mL) and dried over anhydrous Na₂SO₄. The crude product was collected via vacuum evaporation and purified using column chromatography (SiO₂, neat DCM).

4-*tert*-butyl-2,6-diacetylpyridine (**10**).

From 5.50 g (40 mmol) 4-(*tert*-butyl)pyridine. Column chromatography in CH$_2$Cl$_2$, R$_f$ = 0.70. Yield: 1.40 g (6.39 mmol, 17%) colourless amorphous solid. Elemental analysis, found (calc. for C$_{13}$H$_{17}$NO$_2$, M$_w$ = 219.125 g mol^{-1}), C, 70.98 (71.21), H, 7.65 (7.81), N, 6.39 (6.39). 1H NMR (300 MHz, CD$_2$Cl$_2$): δ = 8.20 (s, 2H), 2.75 (s, 6H), 1.36 (s, 9H) ppm.
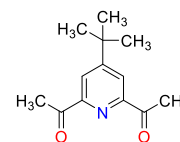
4-methyl-isonicotinate-2,6-diacetylpyridine (**11**)

From 4-methyl-2,6-diacetylisonicotinate 5.54 g (40 mmol). Column chromatography in CH$_2$Cl$_2$, R$_f$: 0.65. Yield: 1.7 g (7.68 mmol, 21%) colorless amorphous solid. Elemental analysis, found (calc. for C$_{11}$H$_{11}$NO$_4$ M$_w$ = 221.07 g mol^{-1}), C, 59.69 (59.73, H, 4.91 (5.01), N, 6.33 (6.33). 1H NMR (300 MHz, CDCl$_3$) δ 8.73 (d, *J* = 1.6 Hz, 0H), 4.01 (d, *J* = 1.5 Hz, 1H), 2.81 (d, *J* = 1.4 Hz, 1H).
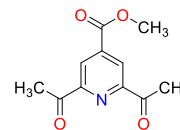
4-chloro-2,6-diacetyl-pyridine (**12**)

4-chloropyridine hydrochloric (2.3 g, 1.58 mmol) was dissolved in 5 mL deionized water and basified with saturated NaOH until pH 9. The mixture was extracted with Et$_2$O (90 mL), the combined organic fractions was dried over anhydrous Na$_2$SO$_4$ and the solvent was evaporated in a vacuum to obtain 4–chloropyridine as yellow oil. The freshly obtained 4–chloro-pyridine was discharged into 100 mL H$_2$SO$_4$ (0.4 M), then pyruvic acid (2.1 mL, 31.3 mmol), aqueous AgNO$_3$ (0.15 g, 0.9 mmol in 0.5 mL water) and (NH$_4$)$_2$S$_2$O$_8$ (11 g, 43.8 mmol) was added. The solution was left to stir overnight at RT. The mixture was filtered and the combine organic fraction was extracted with DCM (150 mL) and dried over anhydrous Na$_2$SO$_4$. The crude product was collected via vacuum evaporation and purified using column chromatography (SiO$_2$, neat DCM). Cl-DAP elute first. 1H NMR (300 MHz, CDCl$_2$) δ: 8.16 (s, 2H), 2.75 (s, 6H). Colourless solid, 690 mg (197.62 g mol^{-1}, 3.49 mmol, 22.78 %). Elemental analysis for (C$_9$H$_8$NO$_2$Cl), found: C, 53.44, 4.24, N, 6.44; required C, 54.70, H, 4.08, N, 7.09
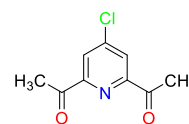
4-bromo-2,6-diacetyl-pyridine (**13**)

Using the same method above. From 4-bromo-pyridine hydrochloride. Compound **13** was obtained as a colourless solid. 1H NMR (300 MHz, CDCl$_3$) δ 1H NMR (300 MHz, CD$_2$Cl$_2$) δ 8.33 (s, 1H), 2.75 (s, 4H), 1.55 (s, 1H).
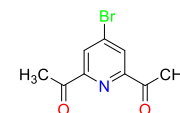
4-iodo-2,6-diacetyl-pyridine (**14**).

From 4-iodo-pyridine using general method. Compound 14 was obtained as a colourless solid. 1H NMR (300 MHz, CDCl$_3$) δ 8.55 (d, J = 0.6 Hz, 1H), 2.76 (s, 6H).
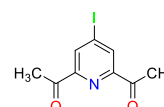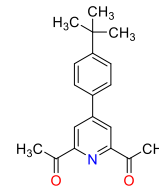
4-diethyl-phosphonate-2,6-diacetyl-pyridyl (**15**).

4-bromopyridine hydrochloride (6.22g, 32 mmol) was neutralized with saturated NaOH and extracted with diethyl-ether and dried over anhydrous Na_2SO_4, and the solvent was evaporated in a vacuum to obtain 4-bromopyridine as a yellow oil. 4-bromopyridine was reacted with diethyl-phosphite (4.8 mL, 36 mmol) in the presence of triethylamine (5 mL, 36 mmol) using $[Pd(P(C_6H_5)_3)_4]$ (1.88g, 1.62 mmol) under argon. After the coupling reaction, the mixture was extracted with ethyl acetate, and 4-diethyl-phosphonate-pyridyl was obtained by column chromatography using clean ethyl acetate. 4-diethyl-phosphonate-pyridyl was treated with pyruvic acid as described for compound **10**. 1H NMR (300 MHz, CDCl$_3$) δ 8.45 (d, J = 13.3 Hz, 0H), 4.12 (ddddd, J = 17.2, 10.1, 8.4, 7.1, 3.0 Hz, 1H), 2.72 (s, 1H), 1.28 (td, J = 7.0, 0.6 Hz, 1H).

1,1′-[4-(4-*tert*-butylphenyl)-2,6-diacetyl-pyridine (**16**)

First, 4-(4-(tertbutyl)phenyl)pyridine was synthesized by Suzuki coupling. Briefly, K_2CO_3 (4 mmol) was dissolved in a degassed solution mixture of EtOH/water (9 mL: 7 mL), followed by the addition of 4-bromopyridine (1 mmol), 4-*tert*-butyl-phenylboronic acid (1.2 mmol) and $[Pd(PPh_3)_4]$ (6 mol%). The resulting mixture was allowed to cool, and the filtrate was collected, extracted three times with EtOAc and dried in a rotary evaporator. The product was purified using column chromatography.
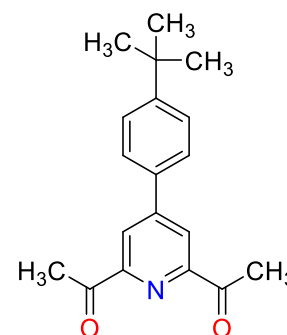
White amorphous solid. (Column chromatography, EtOAc:c-hex, 3:2), (Rf: 0.5) yield, 113 mg (211.14 g mol^{-1}, 0.535 mmol, 53.8%) 1H NMR (500 MHz, CDCl$_3$) δ 8.66 – 8.62 (m, 2H), 7.63 – 7.58 (m, 2H), 7.52 (dt, J = 6.6, 2.2 Hz, 4H), 1.37 (s, 9H). On acylation, the desired product was not obtained.

Therefore, 4-bromo-,2,6-diacetylpyridine was coupled with 4-tert-butylphenylboronic acid using Pd catalyst to obtain 1,1′-[4-(4-tert-butylphenyl)-2,6-diacetyl pyridine. White solid (column chromatography, EtoAC:Cyc, 1:1, Rf: 0.4), yield: 190 mg, (295.16 gmol^{-1}, 0.643 mmol, 66%). 1H NMR: (300 MHz, CDCl$_3$) δ 8.45 (s, 2H), 7.76 – 7.65 (m, 2H), 7.59 – 7.48 (m, 2H), 2.83 (s, 6H), 1.37 (s, 9H).

5.2.3 Synthesis of pentadentate Bis-Thiosemicarbazone

2,6-diacetylpyridine-bis-(4-*N*-2-pyridyl)-TSC (**17**)

The title compound was synthesized by dissolving compound **1** (6 mmol, 1.0 g) in 100 mL AcOH at 50°C, and 2,6-diacetyl-pyridine (2 mmol, 0.32g) was added. 0.1 mL of AcOH was added to the solution. The mixture was left in a bath sonicator for 4 hours at 50°C. A yellow precipitate was formed, which was washed with cold MeOH and acetone.
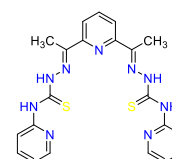
After drying, 550 mg (464.14 g mol^{-1}, 1.18 mmol, 59%) of a yellow amorphous material was obtained. 1H NMR: (500 MHz, DMSO-d$_6$) δ 15.08 (s, 2H), 11.18 (s, 2H), 8.40 (d, *J* = 5.0 Hz, 2H), 8.21 (d, *J* = 7.8 Hz, 2H), 8.01 (t, *J* = 7.9 Hz, 2H), 7.94 – 7.82 (m, 2H), 7.31 (d, *J* = 8.4 Hz, 2H), 7.15 (t, *J* = 6.3 Hz, 2H), 2.59 (s, 6H). HR-ESI-MS(+) [*m/z*] = 464.14318 ([M + H]$^+$, calc. 464.14341), 486.12513 ([M + Na]$^+$, calc. 486.12535).

4-methyl-isonicotinate 2,6-diacetylpyridine-bis-(4-*N*-2-pyridyl)-TSC (**17-1**)

Compound **1** was condensed with compound **11** in 30 mL AcOH solution and 0.5 mL of CF$_3$COOH. The yellow amorphous solid was washed as described above (EtOAc:Cy, 3:7), (Rf: 0.6), yielding a yellow solid 108 mg (521.14 g mol^{-1}, 0.207 mmol, 65.5%). 1H NMR (500 MHz, DMSO-d$_6$) δ 15.09 (s, 2H), 11.20 (s, 2H), 8.58 (s, 2H), 8.38 (d, *J* = 5.0 Hz, 2H), 7.87 (t, *J* = 8.3 Hz, 2H), 7.30 (t, 2H), 7.15 (d, *J* = 6.5 Hz, 2H), 3.97 (s, 3H), 2.60 (s, 6H). HR-ESI-MS(+) [*m/z*] = 522.14919 ([M + H]$^+$, calc. 522.14888), 544.13083 ([M + Na]$^+$, calc. 544.13119)
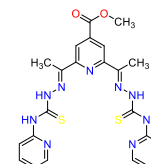
2,6-diacetylpyridine-4-carboxylic acid-bis-(4-*N*-2-pyridyl)-TSC (**17-2**)

Compound **17-1** was unprotected by hydrolyzing in an alkaline medium: 0.16g compound **17-1** (0.32 mmol) was dissolved in 80 mL DMF. The pH of the solution was then adjusted to 10 using saturated NaOH, until a yellow precipitate (the Na$^+$ salt of BTSC) began to form. The reaction was monitored for 3 days through thin-layer chromatography, till the starting material was consumed. The pH of the solution was readjusted to pH = 3 using 4N HCl solution, resulting in the disappearance of the Na$^+$ salt. A yellow precipitate was formed. This was stirred for 2 hours and was allowed to stand in the mother liquor for 24 hours in the refrigerator during which it transformed into a brick-red solid. The solid was filtered off and washed with cold water. Yield: 0.056 g (0.11 mmol, 96%) of a brick-red solid. Elemental analysis calc. for C$_{22}$H$_{21}$N$_9$O$_2$S$_2$ (M$_W$ =507.13 g mol^{-1}) (found): C, 52.06 (52.05), H, 4.17 (4.16), N, 24.84 (24.96), S, 12.63 (12.54). 1H NMR (500 MHz, DMSO-d$_6$) δ 15.06 (s, 2H), 11.15 (s, 2H), 8.58 (s, 2H), 8.40 (d, *J* = 5.0 Hz, 2H), 7.88 (ddd, *J* = 8.8, 7.3, 1.9 Hz, 2H), 7.32 (d, 2H), 7.15 (t, 2H), 2.61 (s, 6H), (Figure S14 and S15, SI). HR-ESI-MS(+) [*m/z*] = 508.1333 ([BTSC+H]$^+$, calc. 508.1333), 530.11526 ([BTSC+Na]$^+$, calc. 530.11526).
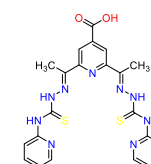
4-*tert*-butyl-2,6-diacetylpyridine-bis-(4-*N*-2-pyridyl)-TSC (**17-3**)

The condensation of compound **1** with 4-*tert*-butyl-2,6-diacetylpyridine as described above compound **17-1**. Yellow amorphous material 210 mg (519.20 g mol^{-1}, 0.404 mmol, 44.68%). 1H NMR (500 MHz, DMSO-d$_6$) δ 15.03 (s, 2H), 11.16 (s, 2H), 8.41 –
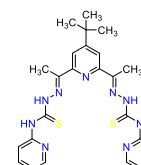
8.37 (m, 2H), 8.28 (s, 2H), 7.87 (ddd, *J* = 9.0, 7.4, 1.9 Hz, 2H), 7.30 (d, *J* = 8.3 Hz, 2H), 7.14 (t, *J* = 6.2 Hz, 2H), 2.58 (s, 6H), 1.37 (s, 9H). HR-ESI-MS(+) [*m/z*] = 520.20607 ([M + H]$^+$, calc. 520.20601), 542.18776 ([M + Na]$^+$, calc. 542.18795).

4-bromo-butyl-2,6-diacetylpyridine-bis-(4-*N*-2-pyridyl)-TSC (**17-4**)

Reaction of compound 1 with compound **13**. Yellow amorphous material 311 mg (542.48 g mol^{-1}, 1.74 mmol, 67%). 1H NMR (300 MHz, DMSO-d$_6$) δ 15.11 (s, 2H), 11.23 (s, 2H), 8.35 (d, *J* = 33.7 Hz, 4H), 7.95 – 7.83 (m, 2H), 7.24 (d, *J* = 42.3 Hz, 4H), 2.56 (s, 6H).
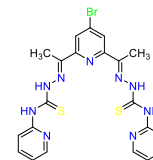
4-chloro-butyl-2,6-diacetylpyridine-bis-(4-*N*-2-pyridyl)-TSC (**17-5**)

Reaction of compound **1** with compound **12**. Yellow amorphous material 242 mg (498.02 g mol^{-1}, 2.1 mmol, 51.88%). 1H NMR (300 MHz, DMSO-d$_6$) δ 15.09 (s, 2H), 11.21 (s, 2H), 8.39 (s, 2H), 8.11 (s, 2H), 7.94 – 7.82 (m, 2H), 7.30 (s, 2H), 7.16 (s, 2H), 2.56 (s, 6H).

4-iodo-butyl-2,6-diacetylpyridine-bis-(4-*N*-2-pyridyl)-TSC (**17-6**)

Reaction of compound **1** with compound **14**. Yellow amorphous material 311 mg (589.48 g mol^{-1}, 1.9 mmol, 67.11%). 1H NMR (300 MHz, DMSO-d$_6$) δ 15.09 (s, 2H), 11.21 (s, 2H), 8.51 (d, 2H), 8.43 – 8.37 (m, 2H), 7.94 – 7.83 (m, 2H), 7.31 (d, 2H), 7.20 – 7.14 (m, 2H), 2.55 (s, 6H).
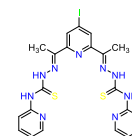
4-thiol-2,6-diacetylpyridine-bis-(4-*N*-2-pyridyl)-TSC (**17-7**)

Compound **17-4** (5.24 mmol, 2.43 g) was added to NaHS (6.28 mmol, 0.48 g) in dry DMF solution, the mixture was left to stir for 24 hours at 40°C. The mixture was allow to cool and dry under vacuum. The yellow solid was washed 4 times with water and washed thrice with cold MeOH. Yield 190 mg. 1H NMR (300 MHz, DMSO-d$_6$) δ 15.10 (s, 2H), 11.22 (s, 2H), 8.40 (s, 2H), 8.31 – 8.24 (m, 2H), 7.88 (ddd, *J* = 9.1, 7.3, 1.9 Hz, 2H), 7.30 (s, 2H), 7.17 (s, 2H), 2.55 (s, 6H).

1,1'-[4-(4-*tert*-butylphenyl)-2,6-diacetyl-pyridine-bis-(4-*N*-2-pyridyl)-TSC (**17-8**)

Reaction of compound **1** with compound **16**. Yellow amorphous material 101 mg (595.79 g mol^{-1}, 5.9 mmol, 23.3%). 1H NMR (300 MHz, DMSO-d$_6$) δ 8.36 (s, 2H), 7.81 (s, 2H), 7.75 (s, 4H), 7.62 (d, *J* = 8.0 Hz, 2H), 2.58 (s, 6H), 1.34 (s, 9H).
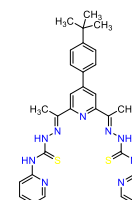
2,6–diacetyl–pyridine–bis–(4–*N*–2–ethylaniline)–thiosemicarbazone (**18**)

Compound **2** (2 mmol, 0.4 g) and 2,6-diacetyl-pyridine (0.67 mmol, 0.11 g) were dissolved in 15 mL AcOH. Then, CF₃COOH (0.1 mL) was added. The mixture was sonicated for three hours at 40 °C. A yellow precipitate was obtained, filtered and washed twice with Et₂O. 150 mg (517.21 g mol^{-1}, 0.284 mmol, 50 %). 1H NMR (500 MHz, DMSO–d_6) δ 10.67 (s, 2H), 10.10 (s, 2H), 8.58 (d, J = 7.9 Hz, 2H), 7.79 (q, J = 7.7 Hz, 1H), 7.28 (dtt, J = 11.7, 5.9, 2.4 Hz, 8H), 2.61 (q, J = 7.6 Hz, 4H), 2.54 (s, 6H), 1.22 – 1.04 (m, 6H). Elemental analysis for (C₂₇H₃₁N₇S₂): found C, 60.46, 6.24, N, 18.17, S, 10.72; required C, 62.64, H, 6.04, N, 18.94, S, 12.39. HR-ESI–MS(+) [m/z] = 518.21551 ([H¹L+H⁺]⁺, calc. 518.21551), 540.19732 ([H¹L+Na]⁺, calc. 540.19745).
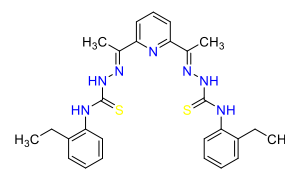
4-methyl-isonicotinate-2,6-diacetyl-pyridine-bis-(4-*N*-2-ethylaniline)-TSC (18-1)

Reaction of compound **2** with compound **11**. Yellow solid, 103 mg (575.21 g mol^{-1}, 0.18 mmol, 60.9 %). 1H NMR (499 MHz, CDCl₃) δ 9.28 (s, 2H), 8.96 (s, 2H), 8.52 (s, 2H), 7.93 – 7.85 (m, 2H), 7.34 – 7.28 (m, 6H), 3.96 (s, 3H), 2.79 – 2.70 (m, 4H), 2.56 (s, 6H), 1.32 (t, J = 7.6 Hz, 6H).
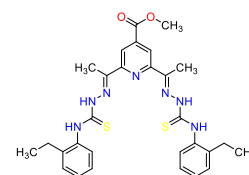
2,6-diacetyl-pyridine-4-carboxylic acid-bis-(4-*N*-2-ethylaniline)-TSC (18-2)

In a 50 mL beaker, Compound **18-1** (0.027 g, 0.04 mg) was dissolved in a mixture of CH₃Cl (2 mL) and MeOH (8 mL), and then NaOH (0.005 g, 0.12 mmol) was added. After 24 hours, the solvent was removed, and the pH of the residual substance was adjusted to 3. The yellow precipitate was filtered and washed with Et₂O, acetone and distilled water (10 mL). Yellow compound. 1H NMR (499 MHz, DMSO-d_6) δ 10.71 (d, J = 1.8 Hz, 2H), 10.19 (d, J = 3.7 Hz, 2H), 8.75 (s, 2H), 7.36 – 7.15 (m, 6H), 2.64 – 2.59 (m, 4H), 2.55 (s, 6H), 1.18 (t, J = 7.6 Hz, 6H). 15 mg (561.20 g mol^{-1}, 0.02 mmol, 57.7 %).
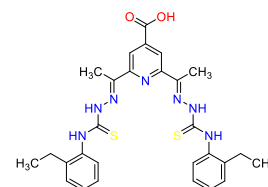
4-*tert*-butyl-2,6-diacetyl-pyridine-bis-(4-*N*-2-ethylaniline)-TSC (18-3)

Compound **2** (0.63 mmol, 0.12 g) and compound **10** (0.3 mmol, 0.065g) were dissolved in 50 mL AcOH. Then CH₃COOH (0.1 mL) was added and refluxed for 4 hours at 50 °C. The yellow precipitate obtained was filtered, washed with Et₂O. 91 mg (573.24 g mol^{-1}, 1.59 mmol, 53.5 %). 1H NMR (499 MHz, CDCl₃) δ 9.24 (s, 2H), 8.92 (s, 2H), 8.01 (s, 2H), 7.92 (dd, J = 7.8, 1.9 Hz, 2H), 7.36 – 7.27 (m, 6H), 2.73 (q, J = 7.5 Hz, 4H), 2.55 (s,61H), 1.35 (s, 9H), 1.29 (t, J = 7.6 Hz, 6H).
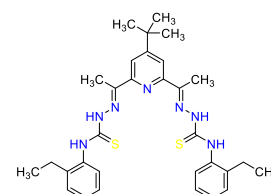
4–chloro–2,6–diacetyl–pyridine–bis–(4–*N*–2–ethylaniline)–TSC (**18-4**)

Compound **2** (1 mmol, 0.195 g) and compound **12** (0.333 mmol, 0.066 g) were dissolved in 10 mL AcOH. Then CF$_3$COOH (0.1 mL) was added and sonicated for 3 h at 40 $^\circ$C. Yellow precipitate obtained was filtered and washed with Et$_2$O. 160 mg (552.16 g mol^{-1}, 0.289 mmol, 29.1 %). 1H NMR (500 MHz, DMSO–d$_6$) δ 10.67 (s, 2H), 10.20 (s, 2H), 8.72 (s, 2H), 7.37 – 7.21 (m, 8H), 2.61 (q, J = 7.6 Hz, 4H), 2.52 (s, 6H), 1.17 (t, J = 7.6 Hz, 6H). 1H NMR (500 MHz, CDCl$_3$) δ 9.34 – 9.14 (m, 2H), 9.00 (d, J = 22.7 Hz, 2H), 7.98 (s, 2H), 7.88 – 7.70 (m, 2H), 7.37 – 7.27 (m, 6H), 2.71 (dd, J = 15.0, 7.5 Hz, 4H), 2.52 (s, 6H), 1.29 (dt, J = 10.8, 7.6 Hz, 6H). Elemental analysis for (C$_{27}$H$_{30}$ClN$_7$S$_2$): found; C, 58.74, H, 5.47, N, 17.70, S, 10.61, required; C, 58.73, H, 5.48, N, 17.76, S, 11.61. HR-ESI–MS(+) [*m/z*] = 552.17690 ([H^{1}L+H$^+$]$^+$, calc. 552.17653), 574.15889 ([H^{1}L+Na]$^+$, calc. 574.15848).
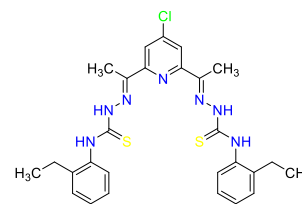
2,6-diacetylpyridine-bis-(4-*N*-3-hydroxyl-2pyridyl)-TSC (**19**)

From 2,6-diacetylpyridine (0.2 mmol, 0.03 g) and *N*-(3-hydroxyl-2-pyridiyl)-thiosemicarbazide (0.59 mmol, 0.11 g). Yield: Yellow solid, 80 mg, (495.13 gmol^{-1}, 0.16 mmol, 10%). 1H NMR (300 MHz, DMSO-d$_6$: δ 15.49 (s, 2H), 8.11 (d, *J* = 7.9 Hz, 2H), 7.97 – 7.86 (m, 1H), 7.17 (d, *J* = 4.7 Hz, 2H), 6.73 (dd, *J* = 7.9, 4.7 Hz, 2H), 6.61 (d, *J* = 7.9 Hz, 2H), 2.48 (s, 6H). Elemental analysis (C$_{21}$H$_{25}$N$_9$O$_2$S$_2$): Calcd., Exp., C (50.49, 50.49); H (5.04; 5.08); N (25.23, 25.83); S (12.83, 12.98). ESI-MS (m/z): [BTSC+H]$^+$ Calcd., 500.164, Exp., 500.303.
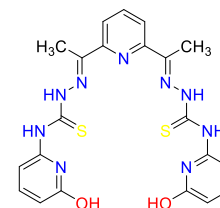
4-(*tert*-butyl)-2,6-diacetylpyridine-bis-(4-*N*-3-hydroxyl-2-pyridyl)-TSC (**19-3**)

From 4-4-(*tert*-butyl)-phenyl))-2,6-diacetylpyridine (0.05 mmol, 0.16 g) and *N*-(3-hydroxyl-2-pyridinyl)-thiosemicarbazide (0.14 mmol, 0.03 g). Yield: Yellow solid, 21 mg, (627.79 gmol^{-1}, 0.03 mmol, 21%). 1H NMR (300 MHz, DMSO-d$_6$: δ 15.44 (s, 2H), 8.30 (s, 2H), 7.75 (d, *J* = 8.0 Hz, 2H), 7.63 (d, *J* = 8.0 Hz, 2H), 6.83 – 6.58 (m, 4H), 2.53 (s, 6H), 1.26 (d, *J* = 24.5 Hz, 9H). (Fig. 5 in the Supplementary Material). Elemental analysis: (C$_{31}$H$_{37}$N$_9$O$_2$S$_2$) Calcd., Exp., C (59.31, 59.32); H (5.30; 4.99); N (20.08, 20.13); S (10.21, 10.22). ESI-MS (m/z): [BTSC+Na]$^+$ Calcd., 650.209, Exp., 659.207.
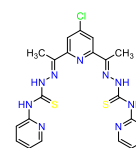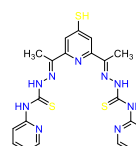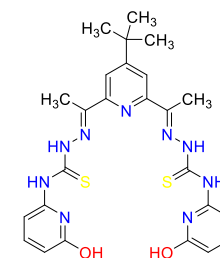
1,1'-[4-(4-*tert*-butylphenyl)-2,6-diacetyl-pyridine-bis-(4-*N*-3-hydroxyl-2-pyridyl)-TSC (**19-4**)
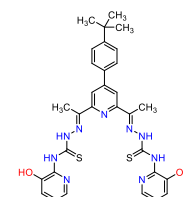
Reaction of compound 16 with compound **3**. Yellow amorphous material 298 mg (627.79 g mol^{-1}, 2.1 mmol, 50.11%). 1H NMR (300 MHz, DMSO-d$_6$) δ 15.44 (s, 2H), 8.30 (s, 2H), 7.75 (d, *J* = 8.0 Hz, 2H), 7.63 (d, *J* = 8.0 Hz, 2H), 6.83 – 6.58 (m, 4H), 2.53 (s, 6H), 1.26 (d, *J* = 24.5 Hz, 9H).

2,6-diacetylpyridine-bis-(4-*N*-3-pyridyl)-TSC (**20**)

Reaction of compound **4** with 2,6-diacetylpyridine. Yellow amorphous material 255 mg (463.58 g mol^{-1}, 1.82 mmol, 40.18%). 1H NMR (500 MHz, DMSO-d$_6$) δ 10.55 (s, 4H), 8.70 (s, 2H), 8.59 – 8.54 (m, 2H), 8.40 (s, 2H), 8.14 – 7.95 (m, 2H), 7.86 (t, *J* = 8.1 Hz, 1H), 7.45 – 7.34 (m, 2H), 2.55 (s, 6H).
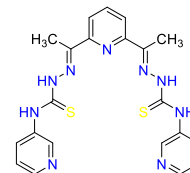
2,6-diacetylpyridine-bis-(4-*N*-5-methylpyridyl)-TSC (**21**)

Reaction of compound 5 with 2,6-diacetylpyridine. Yellow amorphous material 399 mg (491.64 g mol^{-1}, 1.23 mmol, 72.6%). 1H NMR (300 MHz, DMSO-d$_6$) δ 15.18 (s, 2H), 11.09 (s, 2H), 8.39 (d, *J* = 7.8 Hz, 2H), 8.29 – 8.15 (m, 2H), 8.09 (t, *J* = 7.8 Hz, 1H), 7.98 (d, *J* = 7.5 Hz, 2H), 7.06 (d, *J* = 32.5 Hz, 2H), 2.57 (s, 6H), 2.33 (s, 6H).
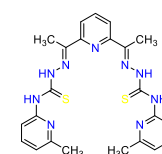
4-bromo-2,6-diacetylpyridine-bis-(4-*N*-5-methylpyridyl)-TSC (**22-1**)

Reaction of compound 5 with compound 13. Yellow amorphous material 210 mg (519.20 g mol^{-1}, 0.404 mmol, 44.68%). 1H NMR (300 MHz, DMSO-d$_6$) δ 15.19 (s, 2H), 11.13 (s, 2H), 8.25 (d, *J* = 6.6 Hz, 4H), 7.16 – 6.95 (m, 4H), 6.56 – 6.41 (m, 2H), 2.53 (s, 6H), 2.33 (s, 6H).
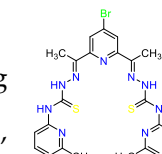
2,6–diacetyl–pyridine–bis–(4–*N*–2–tertbutylaniline)–thiosemicarbazone (**22**)

Reaction of compound **6** with compound 2,6-diacetylpyridine. Yellow amorphous material 143 mg (573.82 g mol^{-1}, 4.1 mmol, 59.91%). 1H NMR (300 MHz, CDCl$_3$) δ 8.26 – 8.17 (m, 2H), 8.05 – 7.91 (m, 1H), 7.87 – 7.79 (m, 2H), 7.38 (q, *J* = 2.1 Hz, 2H), 7.35 – 7.30 (m, 2H), 7.28 – 7.20 (m, 2H), 2.79 (s, 6H), 1.32 (s, 9H).
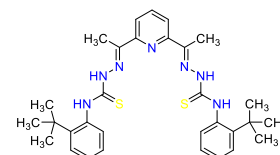
4-bromo-2,6–diacetyl–pyridine–bis–(4–*N*–methylpyridyl)–thiosemicarbazone (**23-1**).

Reaction of **7** with compound **13**. Yellow amorphous material 233 mg (570.53 g mol^{-1}, 2.45 mmol, 49.68%). 1H NMR (300 MHz, DMSO-d$_6$) δ 10.77 (s, 2H), 9.43 (t, *J* = 6.2 Hz, 2H), 8.66 (d, *J* = 5.9 Hz, 6H), 7.62 – 7.54 (m, 4H), 5.01 (d, *J* = 6.0 Hz, 4H), 2.48 (s, 6H).
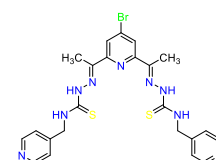
2,6-diacetylpyridine-bis-(4-*N*-chlorophenyl)-TSC (**24**)

From 2,6-diacetylpyridine (0.8 mmol, 0.13 g) and compound **8** (2.4 mmol, 0.48 g). Yield: Yellow solid, 210 mg, (530.49 gmol^{-1}, 0.39 mmol, 16.7%). 1H NMR (300 MHz, DMSO-d$_6$: 10.40 (s, 2H), 8.50 (s, 2H), 7.82 (t, J = 7.9 Hz, 1H), 7.60 (d, J = 8.3 Hz, 2H), 7.40 (d, J = 8.3 Hz, 2H), 2.06 (s, 6H). Elemental analysis (C$_{23}$H$_{25}$Cl$_2$N$_7$S$_2$): Calcd., Exp., C (52.08, 53.09); H (3.99; 3.99); N (18.48, 18.51); S (12.09, 11.99). ESI-MS (m/z): [BTSC+H]$^+$ Calcd., 530.074, Exp., 530.074.
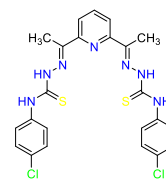
2,6-diacetylpyridine-bis-(4-*N*-butyl)-TSC (25)

Reaction of compound 9 with 2,6-diacetylpyridine. Yellow amorphous material 201 mg (421.63 g mol^{-1}, 2.1 mmol, 51%). 1H NMR (500 MHz, DMSO-d$_6$) δ 10.26 (s, 2H), 8.67 (t, J = 6.0 Hz, 2H), 8.39 (d, J = 7.9 Hz, 2H), 7.86 (t, J = 7.9 Hz, 1H), 3.64 – 3.53 (m, 4H), 2.44 (s, 6H), 1.64 – 1.55 (m, 4H), 1.33 (h, J = 7.4 Hz, 4H), 0.92 (t, J = 7.4 Hz, 6H).
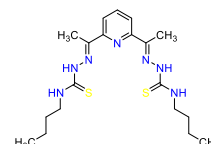
4-bromo-2,6-diacetylpyridine-bis-(4-*N*-butyl)-TSC (25-1)

Reaction of compound **9** with compound **13**. Yellow amorphous material 255 mg (500.52 g mol^{-1}, 1.96 mmol, 44.68%). 1H NMR (300 MHz, DMSO-d$_6$) δ 10.26 (s, 1H), 8.84 (t, J = 6.0 Hz, 1H), 8.61 (s, 1H), 3.61 (q, J = 6.9 Hz, 2H), 2.41 (s, 3H), 1.61 (p, J = 7.6 Hz, 2H), 1.33 (q, J = 7.5 Hz, 2H), 0.93 (t, J = 7.4 Hz, 4H).
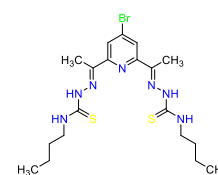
4-thiol-2,6-diacetylpyridine-bis-(4-*N*-butyl)-TSC (25-2)

Using the method for compound 17-7. Yellow amorphous material 133 mg (453.69 g mol^{-1}, 3.41 mmol, 38.18%). 1H NMR (500 MHz, DMSO-d$_6$) δ 10.26 (s, 2H), 8.84 (t, J = 6.0 Hz, 2H), 8.61 (s, 2H), 3.66 – 3.58 (m, 4H), 2.41 (s, 6H), 1.65 – 1.55 (m, 4H), 1.33 (h, J = 7.6 Hz, 4H), 0.93 (t, J = 7.4 Hz, 6H).
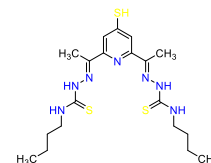
4-*tert*-butyl-2,6-diacetylpyridine-bis-(4-*N*-butyl)-TSC (25-3)

Reaction of compound **9** with compound **10**. Yellow amorphous material 251 mg (477.73 g mol^{-1}, 1,9 mmol, 47.77%). 1H NMR (300 MHz, DMSO-d$_6$) δ 10.31 (s, 2H), 8.48 (t, J = 5.8 Hz, 2H), 8.14 (s, 2H), 3.60 (p, J = 7.1 Hz, 4H), 3.32 (s, 4H), 2.44 (s, 6H), 1.67 – 1.54 (m, 4H), 1.54 – 1.17 (m, 9H), 0.90 (dt, J = 15.9, 7.3 Hz, 6H).
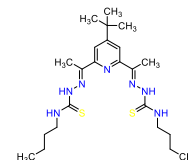
5.2.4 Anchoring Pentadentate Bis-Thiosemicarbazone with Linker

Compound **18-4**–APTES

Compound **18-4** (0.1 g, 0.19 mmol) was dissolved in THF (200 mL), and Et₃N (0.38 mmol, 53 µL) was added. The mixture was allowed to stand for 2 hours. (3-aminopropyl)triethoxysilane (APTES) (0.37 mmol, 87 µL) was added to the mixture, stirred for 4 days at room temperature, and dried under vaccum. Yellow powder 100.1 mg (736.34 g mol⁻¹, 73.78 mmol, 62.5 %). 1H NMR (300 MHz, CDCl₃) δ 9.19 (s, 2H), 8.92 (s, 2H), 7.98 (s, 2H), 7.87 – 7.78 (m, 2H), 7.36 – 7.27 (m, 6H), 5.66 (s, 1H), 3.87 – 3.77 (m, 2H), 3.64 (q, J = 7.3 Hz, 2H), 2.73 (q, J = 7.6 Hz, 4H), 2.52 (s, 6H), 1.58 (s, 9H), 1.48 (t, J = 7.3 Hz, 6H), 1.31 (t, J = 7.6 Hz, 6H), 1.27 – 1.18 (m, 2H). HR-ESI–MS(+) [*m/z*] = 737.344 ([H³L+H⁺]⁺, calc. 737.344).
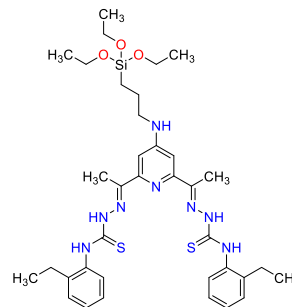
Compound **19**–Dopamine

Compound **19** (0.04g, 0.075 mmol) was dissolved in 10 mL hot DMF; then, the solution was allowed to cool to room temperature. Et₃N (35 uL, 0.25 mmol) was added, followed by the addition of dopamine hydrochloride (0.05g, 0.26 mmol). The mixture was allowed to stir for 4 days at room temperature. Cold water was added to the mixture, and the precipitate was obtained by vacuum filtration. Yellow amorphous material 313 mg (763.27 g mol⁻¹, 2.43 mmol, 62.11%). 1H NMR (500 MHz, DMSO) δ 10.81 (s, 2H), 10.24 (s, 2H), 8.84 – 8.79 (m, 2H), 8.56 (d, *J* = 7.9 Hz, 2H), 7.86 (t, *J* = 7.8 Hz, 1H), 7.61 (d, *J* = 8.0 Hz, 4H), 7.45 (d, *J* = 8.2 Hz, 4H), 7.39 – 7.32 (m, 2H), 6.69 (s, 2H), 6.56 (s, 2H), 2.79 – 2.59 (m, 4H), 2.55 (s, 6H), 2.44 – 2.30 (m, 4H).
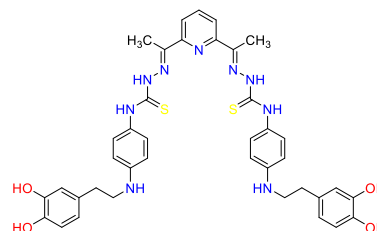
Compound **24**–APTES

Compound **24** (0.1 g, 0.19 mmol) was dissolved in THF (200 mL), and Et₃N (0.38 mmol, 53 µL) was added. The mixture was allowed to stand for 2 hours. (3-aminopropyl)-triethoxysilane (APTES) (0.37 mmol, 87 µL) was added to the mixture and stirred for 4 days at room temperature. 1H NMR (500 MHz, DMSO-d₆) δ 8.52 (s, *J* = 7.8 Hz, 2H), 7.85 (t, *J* = 7.9 Hz, 1H), 7.71 – 7.68 (m, 2H), 7.63 (d, *J* = 8.3 Hz, 4H), 7.43 (dd, *J* = 8.8, 4.4 Hz, 4H), 6.87 (s, 6H), 3.74 (q, *J* = 7.0 Hz, 2H), 3.44 (q, *J* = 7.0 Hz, 6H), 2.53 (s, 6H), 1.48 – 1.38 (m, 2H), 1.35 (s, 8H), 1.14 (t, *J* = 6.9 Hz, 4H), 1.05 (t, *J* = 7.0 Hz, 4H), 0.59 – 0.51 (m, 2H).
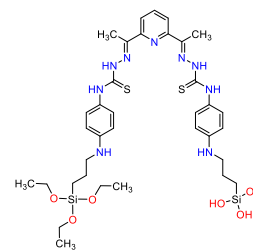
Compound **19**–**CPTES** (3-chloropropyltrimethoxysilane)

1H NMR (300 MHz, DMSO-d$_6$) δ 8.53 (d, J = 7.9 Hz, 2H), 7.85 (t, J = 7.9 Hz, 1H), 7.75 – 7.57 (m, 4H), 7.50 – 7.37 (m, 4H), 7.29 – 7.09 (m, 2H), 3.74 (qd, J = 7.0, 2.8 Hz, 8H), 3.44 (q, J = 7.0 Hz, 2H), 2.53 (s, 6H), 1.44 (p, J = 7.6 Hz, 2H), 1.21 – 1.09 (m, 6H), 1.05 (t, J = 7.0 Hz, 2H), 0.62 – 0.47 (m, 2H).
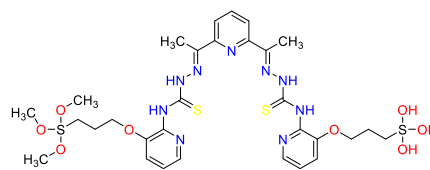
5.2.5 Synthesis of metal complexes – general procedure

A stock solution of BTSC (10 mmol) was prepared in hot DMF. 10 mL of the BTSC stock was taken, 5 mmol (70 µL) of Et$_3$N was added, followed by the addition of 10 mL (10 mmol) of metal salt (CuCl$_2$.2H$_2$O, K$_2$PdCl$_4$ or ZnCl$_2$). After stirring for an hour at room temperature, the solvent was removed, washed with DMF, and dried under a vacuum.

[Cu(BTSC)] for compound **17**. The product was isolated as a dark-blue solid. Yield: 32.00 mg. (C$_{21}$H$_{19}$N$_9$CuS$_2$, 524.05 g mol^{-1}, 0.06 mmol, 81%). HR-ESI-MS(+) [m/z] = 525.03945 ([M + H]$^+$, calc. 525.05736).
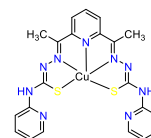
[Pd(BTSC)] for compound **17**. The product was isolated as a brick-red solid. Yield: 44.08 mg. (C$_{21}$H$_{19}$N$_9$PdS$_2$, 567.02.g mol^{-1}, 0.07 mmol, 80 %). 1H NMR (500 MHz, DMSO) δ 10.30 (s, 1H), 8.87 (d, J = 6.4 Hz, 1H), 8.32 (dt, J = 4.9, 1.4 Hz, 1H), 8.11 (ddd, J = 8.5, 7.2, 1.5 Hz, 1H), 7.99 (d, J = 7.9 Hz, 1H), 7.94 (d, J = 7.8 Hz, 1H), 7.88 (t, J = 7.9 Hz, 1H), 7.67 – 7.59 (m, 2H), 7.38 – 7.28 (m, 2H), 7.09 – 6.96 (m, 1H), 2.52 (s, 3H), 2.40 (s, 3H). . HR-ESI-MS(+) [m/z] = 568.03162 ([M + H]$^+$, calc. 568.03125.
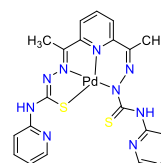
[Zn(BTSC)] for compound **17**. The product was isolated as a yellow solid. Yield: 40.00 mg. (C$_{21}$H$_{19}$N$_9$ZnS$_2$, 525.05 g mol^{-1}, 76.00 mg, 0.07 mmol, 77 %). 1H NMR (500 MHz, DMSO-d$_6$) δ 15.06 (s, 2H), 11.15 (s, 2H), 8.58 (s, 2H), 8.40 (d, J = 5.0 Hz, 2H), 7.88 (ddd, J = 8.8, 7.3, 1.9 Hz, 2H), 7.32 (d, 2H), 7.15 (t, 2H), 2.61 (s, 6H). HR-ESI-MS(+) [m/z] = 526.05341 ([M + H]$^+$, calc. 526.08513), 550.03545 ([M + Na]$^+$, calc. 550.06707).
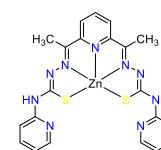
Compound **18** (0.1g, 0.2 mmol) dissolved in THF (10 mL) and Et$_3$N (0.1 mmol, 14 µL) was added, followed by the addition of the aqueous salts of CuCl$_2$.2H$_2$O, K$_2$PdCl$_4$ or ZnCl$_2$.2H$_2$O. After stirring for 60 minutes at room temperature, the solvent was removed, and the crude product was purified by column chromatography.

[Cu(BTSC)] for compound **18**. From 0.03g, 0.2 mmol CuCl$_2$.2H$_2$O. The product was isolated as a blue solid. The solid was purified by column chromatography Yield: (silica, DCM: MeOH, v:v = 97:3). 70 mg (578.21 g mol^{-1}, 0.120 mmol, 70 %). Elemental analysis for (C$_{27}$H$_{29}$N$_7$S$_2$Cu): found C, 55.56, H, 5.01, N, 15.32, S, 10.27; required C, 55.99, H, 5.05, N, 16.93, S, 11.07. HR-ESI–MS(+) [*m/z*] = 579.1639 ([H^{1}L+H$^+$]$^+$, calc. 579.2470).
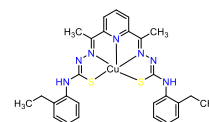
[Pd(BTSC)] for compound **18**. From 0.07g, 0.2 mmol K$_2$PdCl$_4$. The product was isolated as a red solid. Yield: (silica, DCM: MeOH, v:v = 97:3). The precipitate was recovered, washed with cold THF, and air-dried. Brick red solid 81 mg (622.12 g mol^{-1}, 0.072 mmol, 74.58 %). 81 mg (621.10 g mol^{-1}, 0.130 mmol, 65 %). 1H NMR (500 MHz, DMSO–d$_6$) δ 10.67 (s, 2H), 10.10 (s, 2H), 8.58 (d, *J* = 7.9 Hz, 2H), 7.79 (q, *J* = 7.7 Hz, 1H), 7.28 (dtt, *J* = 11.7, 5.9, 2.4 Hz, 8H), 2.61 (q, *J* = 7.6 Hz, 4H), 2.54 (s, 6H), 1.22 − 1.04 (m, 6H). Elemental analysis for (C$_{27}$H$_{29}$N$_7$S$_2$): found; C, 53.36, H, 5.30, N, 16.12, S, 10.48, required; C, 52.13, H, 4.70, N, 15.76, S, 10.31. HR-ESI–MS(+) [*m/z*] = 622.1044 ([H^{1}L+H$^+$]$^+$, calc. 622.1043)).
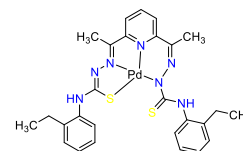
[Zn(BTSC)] for compound **18**. From 0.03g, 0.2 mmol K$_2$PdCl$_4$. The product was isolated as a red solid. Yield: (silica, DCM: MeOH, v:v = 97:3). 78 mg (578.12 g mol^{-1}, 0.134 mmol, 78 %). 1H NMR (500 MHz, DMSO–d$_6$) δ 1H NMR: (500 MHz, DMSO) δ 9.82 (s, 2H), 8.38 (t, 1H), 8.14 (d, J = 7.9 Hz, 0H), 7.41 − 7.11 (m, 1H), 2.74 − 2.58 (m, 0H), 2.57 (s, 0H), 1.15 (dt, J = 19.5, 7.4 Hz, 1H). Elemental analysis for (C$_{27}$H$_{29}$N$_7$S$_2$Zn): found C, 55.80, H, 5.00, N, 15.88, S, 10.97; required C, 55.81, H, 5.03, N, 16.87, S, 11.03. HR-ESI–MS(+) [*m/z*] = 579.1217 ([H^{1}L+H$^+$]$^+$, calc. 579.1217).
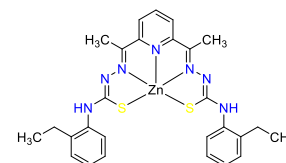
[Zn(BTSC)] from compound **21**

1H NMR (300 MHz, DMSO–d$_6$) δ 8.98 (s, 2H), 8.17 (d, *J* = 7.9 Hz, 1H), 8.13 (d, *J* = 5.1 Hz, 2H), 8.06 (d, *J* = 1.4 Hz, 2H), 7.87 (d, *J* = 7.8 Hz, 2H), 6.91 − 6.83 (m, 6H), 2.38 (s, 1H), 2.21 (s, 6H).
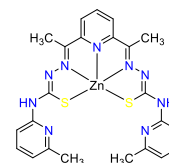
Zn(BTSC)] from compound **25-1**

1H NMR (300 MHz, DMSO–d$_6$)) δ 10.66 (s, 2H), 9.40 (t, *J* = 6.2 Hz, 2H), 8.67 (s, 2H), 8.52 (d, *J* = 5.0 Hz, 4H), 7.32 (d, *J* = 5.1 Hz, 4H), 4.92 (d, *J* = 6.1 Hz, 4H), 2.47 (s, 6H).
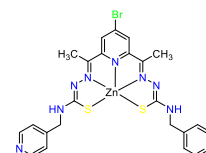
[Pd(BTSC)] from compound **24**

1H NMR (500 MHz, DMSO–d6) δ 9.56 (s, 2H), 8.35 (t, *J* = 7.8 Hz, 1H), 8.15 (d, *J* = 7.9 Hz, 2H), 7.74 – 7.68 (m, 4H), 7.39 – 7.29 (m, 4H), 2.37 (s, 6H).
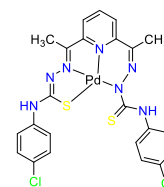
[Pd(BTSC)] from compound **25**.

1H NMR (300 MHz, CDCl3) δ 8.61 (d, *J* = 56.6 Hz, 0H), 8.11 (t, *J* = 8.4 Hz, 0H), 7.94 (d, *J* = 7.8 Hz, 0H), 7.79 (dt, *J* = 25.1, 7.5 Hz, 0H), 7.63 – 7.49 (m, 0H), 5.06 (d, *J* = 78.8 Hz, 0H), 3.93 – 3.22 (m, 0H), 2.85 – 2.07 (m, 1H), 1.82 – 1.18 (m, 1H), 1.05 – 0.76 (m, 1H).
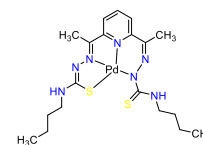
[Zn(BTSC)] from compound **25**

1H NMR (300 MHz, CDCl3) δ 7.80 (t, *J* = 7.8 Hz, 1H), 7.43 (d, *J* = 7.8 Hz, 2H), 3.63 – 3.12 (m, 4H), 2.48 (d, *J* = 5.7 Hz, 6H), 1.58 – 1.44 (m, 4H), 1.35 (q, *J* = 7.3 Hz, 4H), 0.92 (t, *J* = 7.2 Hz, 6H).
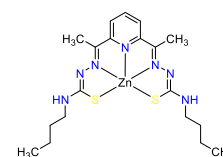
5.2.6 Synthesis of Bis-Thiosemicarbazone Nanoparticles Conjugates

Fe3O4@SiO2–APTES–BTSC

In the first part, Fe3O4 was prepared via co-precipitation and was subsequently coated with SiO2 to obtain Fe3O4@SiO2–APTES. In a separate reaction, a thoroughly dispersed Fe3O4@SiO2–APTES (0.2 g, in 15 mL MeOH) was added to a solution of compound **18-2** ligand (0.063 mmol, 0.032 g in 4 mL DMF) and *N,N″*–dicyclohexylcarbodiimide (DCC) (0.08 mmol, 0.016 g) was added as a coupling agent. The reaction was left for 24 hours at 60 °C, and the resulting precipitate (Fe3O4@SiO2–APTES–BTSC) was collected using a magnetic field and was thoroughly washed with MeOH and acetone, dried in an oven at 60 ºC.

SiO2-APTES

Monodispersed SiO2, and SiO2–(3–aminopropyl)triethoxysilane = APTES, (SiO2–APTES*)*, NP were synthesized by dispersing SiO2 (2g) in dry MeOH (100 mL) and (3–aminopropyl)triethoxysilane (2mL) was added. The mixture was allowed to stir for 24 hours and allowed to age for 24 hours. SiO2–APTES was collected by vacuum filtration. Elemental analysis for (SiO2–APTES): C, 12.24, H, 2.86, N, 4.08.

SiO2–APTES–Compound **18**

To synthesize SiO2–APTES–BTSC, compound **18-4** (0.2 g) was dissolved in dry THF (20 mL), degassed for two minutes and Et3N (100 μL) was added to the solution. SiO2–APTES (0.5 g) was sonicated in THF (20 mL) solution and added to the mixture. The mixture was allowed to react for four days at room temperature. The mixture was filtered and washed thrice in THF solution. The SiO2–APTES–H2L NPs were oven-dried at 40 C for 24 hours. Elemental analysis: C, 4.77, H, 1.37), N, (1.44), S, (0.33).

SiO2–APTES–Compound **24**–Pd

SiO2–APTES–BTSC (0.1 g) was dissolved in 50 mL by sonicating for an hour. The sonicated SiO2–APTES–BTSC was transferred onto a magnetic stirrer, and 5 mL K2PdCl4 (1 mmol, 0.32 g) in THF solution was added. The mixture was allowed to stir for an hour. SiO2–APTES–H2L–Pd was collected by vacuum filtration and washed with 20 mL of water, THF (20 mL) and acetone (20 mL) and dried in an oven (40 °C) for 24 hours.

Fe2O3 NPs

Fe2O3 nanoparticles were synthesised by dissolving 0.42 g FeSO4.H2O and 4.2 g polyvinylpyrrolidone in 120 mL DMF. The solution was heated to 40 °C and 1.6 mL of hydrazine monohydrate was added dropwise. The temperature was raised to 160 °C and maintained for 3 h. Brown precipitates were collected, centrifuged and washed with acetone and distilled water and then dried in an oven.[127] The dried brown particles were placed in a muffle furnace heated at 500 °C at a heating rate of 10 °C/min for 3 h. Brick-red products were collected.

Fe2O3–Dop NPs

Fe2O3 (500 mg) was added to 60 mL distilled water. The mixture was sonicated for 40 min, stirred for 24 h [46], and allowed to age overnight. The Fe2O3-Dop samples were collected by centrifuging and washed with distilled water and acetone. Dried dark samples were collected after drying.

Fe2O3–Dop–Compound **18** NP

Fe2O3-Dop (100 mg) was added to 150 mL DMF. The mixture was sonicated for 30 minutes, and then Et3N (0.16 mmol, 25 μL) was added and stirred for 2 h. BTSC (0.16 mmol, 0.084 g) was added and left stirring for 4 days at room temperature. The sample was collected by filtration and washed 4 times, separately with THF, MeOH, distilled water and acetone to remove unreacted BTSC and Et3N. The sample was oven-dried at 40 °C. [Elemental analysis: C = 12.65, H = 2.44, S = 1.33, N = 1.78].

5.2.7 Applications of Pentadentate Bis-Thiosemicarbazone in Metal Binding and Catalysis

5.2.7.1 Fe$_3$O$_4$–APTES–BTSC Nanoparticles for Binding Pd^{2+} Ions

K$_2$PdCl$_4$ was used as the Pd(II) source and prepared in a 0.1 M HCl solution to improve solubility. The final pH of the working solution was 4.0. The time-concentration profile study was conducted as follows: 30 mL (3.6 mg/L) of Pd(II) solution was contacted with 0.002 g of the Fe$_3$O$_4$@SiO$_2$–APTES–BTSC adsorbent stirred at 600 rpm. Samples were collected at intervals until 60 mins. The Fe$_3$O$_4$@SiO$_2$-APTES–BTSC was removed using a magnetic field, and the absorbance spectra were recorded. Similar experiment was repeated for the Fe$_3$O$_4$@SiO$_2$–APTES.

The equilibrium isotherm studies were conducted by contacting 5 x 10^{-4} g of the Fe$_3$O$_4$@SiO$_2$–APTES–BTSC with 20 mL of K$_2$PdCl$_4$ solution of varying Pd(II) ions initial concentration (mg/L) (i.e., 1, 5, 10, 15 and 20) for 20 hours. The adsorption performance of Fe$_3$O$_4$@SiO$_2$–APTES–BTSC was compared with Fe$_3$O$_4$@SiO$_2$–APTES at 10 mg/L initial concentration. The initial pH of all solutions was 4.3. The effect of pH on the adsorption of Pd(II) was studied by varying solution pH (2.2, 4, 6.1 and 8.2) at 10 mg/L initial concentration. Samples were collected after 20 hours and separated using a magnetic field. Residual Pd(II) ions were analyzed using ICP-MS. The adsorption efficiency (%) and adsorption capacity (q$_e$) were calculated using Equation 1 and 2, respectively. The obtained equilibrium isotherm data were fitted into the Langmuir (Eq. 3) and the Freundlich (Eq. 4) isotherm Equations. Where C$_o$ and C$_e$ are the initial and final concentration (mg/L), V and m are adsorbate volume (mL) and adsorbent weight (g). K$_L$ (L/mg) and K$_F$ (mg/g)/(mg/L)^n are the Langmuir and Freundlich constant, respectively, and n (dimensionless) is the Freundlich intensity parameter [48].

$$\% \ Removal = \frac{C_o - C_e}{C_o} \ X \ 100 \tag{1}$$

$$q_e = \frac{V}{m} X (C_o - C_e) \tag{2}$$

$$\frac{1}{q_e} = \frac{1}{q_{max}} + \frac{1}{q_{max} \cdot C_e \cdot K_L} \tag{3}$$

$$log \ q_e = \frac{1}{n} \ log \ C_e + log \ K_F \tag{4}$$

5.2.7.2 SiO$_2$–APTES–BTSC Nanoparticles in Suzuki-Miyaura Cross-Coupling Reaction

The coupling of phenylboronic acid and bromobenzene was used as the model experiment. In a typical experiment, 15 mL of solvent THF was degassed for 5 minutes, then K$_2$CO$_3$ (6 mmol, 0.55 g), bromobenzene (1 mmol, 106 μL), phenylboronic acid (1.2 mmol, 0.146 g) and SiO$_2$–APTES–BTSC–Pd (0.2 g) were added. The reaction was refluxed at 80°C for 20 hours. For the optimum catalytic dosage, the amount of SiO$_2$–APTES–BTSC–Pd was varied (0.4, 0.6, 0.8 g) for 20 hours at 80°C. Relying on the optimum catalytic dosage, the reaction solvents (THF, EtOH and H$_2$O), temperature (60, 80 and 100 °C) and base (K$_2$CO$_3$ or Na$_2$CO$_3$ or K$_2$CO$_3$) were also varied. The resulting mixture was allowed to cool to room temperature, extracted twice using ethyl acetate (20 mL) and dried over anhydrous Na$_2$SO$_4$. The crude product was purified using column chromatography (eluent: DCM/MeOH) to calculate the isolated yield of the individual reactions.

SiO$_2$–APTES–BTSC–Pd was tested for reuse by recovering the spent catalyst in a centrifuge tube, washed twice with 20 mL of water to remove the base and THF (20 mL) to remove the unreacted substrate and left to dry in the fumehood overnight. The recovered catalyst was used as described above.

5.2.7.3 Microwave Assisted Decomposition of Bis-Thiosemicarbazone Complexes

In a glass tube, 10 mg of BTSC complexes (Cu^{2+}, Pd^{2+} and Zn^{2+}) of compound **18** was dissolved in 5 mL N–methyl–2–pyrrolidone. The lid was tightly closed, and the mixture was placed in a microwave for 10 minutes. The particles formed were filtered and centrifuged thrice in MeOH solution. The particles were air-dried overnight in fumehood. Cu$_{7.2}$S$_4$ and Pd$_{16}$S$_7$ were black solids, while ZnS was yellow solids.

6. REFERENCE

(1)   Butler, M. S.; Blaskovich, M. A. T.; Cooper, M. A. Antibiotics in the Clinical Pipeline at the End of 2015. *J. Antibiot. (Tokyo).* **2017**, *70* (1), 3–24. https://doi.org/10.1038/ja.2016.72.

(2)   Neuberg, C.; Neimann, W. Eine Methode Zur Isolirung von Aldehyden Und Ketonen. *Berichte der Dtsch. Chem. Gesellschaft* **1902**, *35* (2), 2049–2056. https://doi.org/10.1002/cber.190203502156.

(3)   Singh, R. B.; Ishii, H. Analytical Potentialities of Thiosemicarbazones and Semicarbazones. *Crit. Rev. Anal. Chem.* **1991**, *22* (5), 381–409. https://doi.org/10.1080/10408349108051640.

(4)   Garg, B. S.; Jain, V. K. Analytical Applications of Thiosemicarbazones and Semicarbazones. *Microchem. J.* **1988**, *38* (2), 144–169. https://doi.org/10.1016/0026-265X(88)90017-3.

(5)   Kostas, I. D.; Steele, B. R. Thiosemicarbazone Complexes of Transition Metals as Catalysts for Cross-Coupling Reactions. *Catalysts*. 2020, pp 1–40. https://doi.org/10.3390/catal10101107.

(6)   Priyarega, S.; Haribabu, J.; Karvembu, R. Development of Thiosemicarbazone-Based Transition Metal Complexes as Homogeneous Catalysts for Various Organic Transformations. *Inorganica Chim. Acta* **2022**, *532*, 120742. https://doi.org/10.1016/j.ica.2021.120742.

(7)   Paterson, B. M.; Donnelly, P. S. Copper Complexes of Bis(Thiosemicarbazones): From Chemotherapeutics to Diagnostic and Therapeutic Radiopharmaceuticals. *Chem. Soc. Rev.* **2011**, *40* (5), 3005–3018. https://doi.org/10.1039/c0cs00215a.

(8)   Aguirre, A. R.; Beraldo, H. The Pharmacological Profile of Metal Complexes with Bis(Thiosemicarbazones) and Bis(Hydrazone)-Derived Ligands. *Polyhedron* **2024**, *256*, 116993. https://doi.org/10.1016/j.poly.2024.116993.

(9)   Hohnsen, J.; Rryci, L.; Obretenova, D.; Friedel, J.; Jouchaghani, S.; Klein, A. Functionalizing Thiosemicarbazones for Covalent Conjugation. *Molecules*. 2024. https://doi.org/10.3390/molecules29153680.

(10)   Prajapati, N. P.; Patel, H. D. Novel Thiosemicarbazone Derivatives and Their Metal Complexes: Recent Development. *Synth. Commun.* **2019**, *49* (21), 2767–2804. https://doi.org/10.1080/00397911.2019.1649432.

(11)   Andres, S. A.; Bajaj, K.; Vishnosky, N. S.; Peterson, M. A.; Mashuta, M. S.; Buchanan, R. M.; Bates, P. J.; Grapperhaus, C. A. Synthesis, Characterization, and Biological Activity of Hybrid Thiosemicarbazone–Alkylthiocarbamate Metal Complexes. *Inorg. Chem.* **2020**, *59* (7), 4924–4935. https://doi.org/10.1021/acs.inorgchem.0c00182.

(12)   Batha, S.; Arman, H.; Larionov, O. V; Musie, G. T. Zinc(II) Complexes of a Versatile Heptadentate Ligand as Phosphohydrolase Structural and Functional Mimics. *Inorganica Chim. Acta* **2019**, *497*, 119077. https://doi.org/10.1016/j.ica.2019.119077.

(13)   Lange, J. L.; Davey, P. R. W. J.; Ma, M. T.; White, J. M.; Morgenstern, A.; Bruchertseifer, F.;

Blower, P. J.; Paterson, B. M. An Octadentate Bis(Semicarbazone) Macrocycle: A Potential Chelator for Lead and Bismuth Radiopharmaceuticals. *Dalt. Trans.* **2020**, *49* (42), 14962–14974. https://doi.org/10.1039/D0DT02673E.

(14)   Shafiei, I.; Tavassoli, S. P.; Rahmatollahi, H. R.; Ghasemian, R.; Salehzadeh, A. A Novel Copper Oxide Nanoparticle Conjugated by Thiosemicarbazone Promote Apoptosis in Human Breast Cancer Cell Line. *J. Clust. Sci.* **2022**, *33* (6), 2697–2706. https://doi.org/10.1007/s10876-021-02187-1.

(15)   Veg, E.; Joshi, S.; Khan, T. Design and Fabrication of Heterojunctions of Thiosemicarbazones and Metallic Nanoparticles in Search of Their Medicinal Activity. *Engineering Proceedings*. 2024, p 50. https://doi.org/10.3390/proceedings2024105050.

(16)   Brown, C. A.; Kaminsky, W.; Claborn, K. A.; Goldberg, K. I.; West, D. X. Structural Studies of 2,6-Diacetyl- and 2,6-Diformylpyridine Bis(Thiosemicarbazones). *J. Braz. Chem. Soc.* **2002**, *13* (1), 10–18. https://doi.org/10.1590/S0103-50532002000100003.

(17)   Özbek, O.; Berkel, C. Sensor Properties of Thiosemicarbazones in Different Analytical Methods. *Polyhedron* **2023**, *238*, 116426. https://doi.org/10.1016/j.poly.2023.116426.

(18)   Reddy, S. A.; Reddy, K. J.; Narayana, S. L.; Reddy, A. V. Analytical Applications of 2,6-Diacetylpyridine Bis-4-Phenyl-3-Thiosemicarbazone and Determination of Cu(II) in Food Samples. *Food Chem.* **2008**, *109* (3), 654–659. https://doi.org/10.1016/j.foodchem.2007.12.073.

(19)   Khanna, S. Analysis of Thiosemicarbazones as an Effective Spectrophotometric Chemosensor. *Phosphorus, Sulfur Silicon Relat. Elem.* **2024**, 1–9. https://doi.org/10.1080/10426507.2024.2444665.

(20)   Jahangiri, M.; Kiani, F.; Tahermansouri, H.; Rajabalinezhad, A. The Removal of Lead Ions from Aqueous Solutions by Modified Multi-Walled Carbon Nanotubes with 1-Isatin-3-Thiosemicarbazone. *J. Mol. Liq.* **2015**, *212*, 219–226. https://doi.org/10.1016/j.molliq.2015.09.010.

(21)   Tadjarodi, A.; Moazen Ferdowsi, S.; Zare-Dorabei, R.; Barzin, A. Highly Efficient Ultrasonic-Assisted Removal of Hg(II) Ions on Graphene Oxide Modified with 2-Pyridinecarboxaldehyde Thiosemicarbazone: Adsorption Isotherms and Kinetics Studies. *Ultrason. Sonochem.* **2016**, *33*, 118–128. https://doi.org/10.1016/j.ultsonch.2016.04.030.

(22)   Nguyen, T. A.; Nguyen, T. A.; Tran, D. B.; Le, H. D. C.; Nguyen, Q. L.; Pham, V. Thiosemicarbazone-Modified Cellulose: Synthesis, Characterization, and Adsorption Studies on Cu(II) Removal. *ACS Omega* **2020**, *5* (24), 14481–14493. https://doi.org/10.1021/acsomega.0c01129.

(23)   Jaafar, A.; Platas-Iglesias, C.; Bilbeisi, R. A. Thiosemicarbazone Modified Zeolitic Imidazolate Framework (TSC-ZIF) for Mercury(II) Removal from Water. *RSC Adv.* **2021**, *11* (27), 16192–16199. https://doi.org/10.1039/d1ra02025k.

(24)   Selander, N.; Szabó, K. J. Catalysis by Palladium Pincer Complexes. *Chem. Rev.* **2011**, *111* (3), 2048–2076. https://doi.org/10.1021/cr1002112.

(25)   Kovala-Demertzi, D.; Yadav, P. N.; Demertzis, M. A.; Jasiski, J. P.; Andreadaki, F. J.; Kostas, I. D. First Use of a Palladium Complex with a Thiosemicarbazone Ligand as Catalyst Precursor for the Heck Reaction. *Tetrahedron Lett.* **2004**, *45* (14), 2923–2926. https://doi.org/10.1016/j.tetlet.2004.02.062.

(26)   Fassbach, T. A.; Ji, J.-M.; Vorholt, A. J.; Leitner, W. Recycling of Homogeneous Catalysts—Basic Principles, Industrial Practice, and Guidelines for Experiments and Evaluation. *ACS Catal.* **2024**, *14* (9), 7289–7298. https://doi.org/10.1021/acscatal.4c01006.

(27)   Sivadasan Chettiar, K.; Sreekumar, K. Polystyrene-Supported Thiosemicarbazone–Transition Metal Complexes: Synthesis and Application as Heterogeneous Catalysts. *Polym. Int.* **1999**, *48* (6), 455–460. https://doi.org/10.1002/(SICI)1097-0126(199906)48:6<455::AID-PI166>3.0.CO;2-F.

(28)   Islam, M.; Hossain, D.; Mondal, P.; Tuhina, K.; Roy, A. S.; Mondal, S.; Mobarak, M. Synthesis, Characterization, and Catalytic Activity of a Polymer-Supported Copper(II) Complex with a Thiosemicarbazone Ligand. *Transit. Met. Chem.* **2011**, *36* (2), 223–230. https://doi.org/10.1007/s11243-011-9459-1.

(29)   Bade, B. P.; Garje, S. S.; Niwate, Y. S.; Afzaal, M.; O'Brien, P. Tribenzyltin(IV)Chloride Thiosemicarbazones: Novel Single Source Precursors for Growth of SnS Thin Films. *Chem. Vap. Depos.* **2008**, *14* (9–10), 292–295. https://doi.org/10.1002/cvde.200806687.

(30)   Yepseu, A. P.; Girardet, T.; Nyamen, L. D.; Fleutot, S.; Ketchemen, K. I. Y.; Kun, W. N.; Cleymand, F.; Ndifon, P. T. Synthesis and Photocatalytic Activity of High-Quality Lead(II) Sulfide Nanoparticles from Lead(II) Thiosemicarbazone Complexes as Single Source Precursors. *J. Nanomater.* **2024**, *2024* (1), 9932000. https://doi.org/10.1155/2024/9932000.

(31)   Pearson, R. G. Hard and Soft Acids and Bases. *J. Am. Chem. Soc.* **1963**, *85* (22), 3533–3539. https://doi.org/10.1021/ja00905a001.

(32)   Nazimunnisa, S.; Veeranna, V.; Venkatalakshmi, V.; Yallappa, S. Estimation of Magnesium and Titanium Using 3-Aminopyridine-2-Carbaxaldehyde Thiosemicarbazone (Triapine) by Second-Order Derivative Spectrophotometry. *Results Chem.* **2022**, *4*, 100564. https://doi.org/10.1016/j.rechem.2022.100564.

(33)   GANGADHARAN, R.; AMRITHA, C.; Anto, R.; Cheryan, V. Synthesis, Thermal and Antitumour Studies of Th(IV) Complexes with Furan-2-Aldehyde-N-Phenyl Thiosemicarbazone. *J. Serbian Chem. Soc.* **2010**, *75*. https://doi.org/10.2298/JSC090729048R.

(34)   Grödler, D.; Haseloer, A.; Tobeck, C.; Bulut, Y.; Neudörfl, J. M.; Mathur, S.; Ruschewitz, U.; Klein, A.; Wickleder, M. S.; Zegke, M. Thiosemicarbazone Complexes of Uranium(IV). *Eur. J.*

Inorg. Chem. **2021**, *2021* (12), 1137–1139. https://doi.org/10.1002/ejic.202001118.

(35)   Yepseu, A. P.; Girardet, T.; Nyamen, L. D.; Fleutot, S.; Ketchemen, K. I. Y.; Cleymand, F.; Ndifon, P. T. Copper (II) Heterocyclic Thiosemicarbazone Complexes as Single-Source Precursors for the Preparation of Cu_9S_5 Nanoparticles: Application in Photocatalytic Degradation of Methylene Blue. *Catalysts*. 2022. https://doi.org/10.3390/catal12010061.

(36)   Disale, S. D.; Garje, S. S. Preparation of Ternary Metal Chalcogenide (M1-XFe$_x$S, M = Cd and Zn) Nanocrystallites Using Single Source Precursors. *J. Organomet. Chem.* **2011**, *696* (21), 3328–3336. https://doi.org/10.1016/j.jorganchem.2011.07.001.

(37)   Kelly, S. N.; Russo, D. R.; Ouellette, E. T.; Roy, D.; Swift, A. J.; Boreen, M. A.; Smith, P. W.; Moreau, L. M.; Arnold, J.; Minasian, S. G. Formation of Uranium Disulfide from a Uranium Thioamidate Single-Source Precursor. *Chem. Sci.* **2024**, *15* (33), 13325–13332. https://doi.org/10.1039/D4SC03422H.

(38)   Ain, Q. U.; Sharma, R. Structure and Bonding Trends of Bisthiosemicarbazones: An Overview. *Appl. Organomet. Chem.* **2023**, *37* (6), e7100. https://doi.org/https://doi.org/10.1002/aoc.7100.

(39)   Ain, Q. U.; Singh, I.; Carmieli, R.; Savci, A.; Paul, K.; Sharma, R. Substituted 2,5 Thiophene Dicarboxaldehyde Bisthiosemicarbazones and Their Copper(II) Complexes: Synthesis, Structure Elucidation, HSA Binding, Biological Activities and Docking Studies. *J. Mol. Struct.* **2023**, *1291*, 135996. https://doi.org/10.1016/j.molstruc.2023.135996.

(40)   Akladios, F. N.; Andrew, S. D.; Parkinson, C. J. Cytotoxic Activity of Expanded Coordination Bis-Thiosemicarbazones and Copper Complexes Thereof. *JBIC J. Biol. Inorg. Chem.* **2016**, *21* (8), 931–944. https://doi.org/10.1007/s00775-016-1390-7.

(41)   Diaz, A.; García, I.; Cao, R.; Beraldo, H.; Salberg, M. M.; West, D. X.; González, L.; Ochoa, E. Ribose, Galactose and Glucose Bis(Thiosemicarbazone) Complexes of Copper(II) and Nickel(II). *Polyhedron* **1997**, *16* (20), 3549–3555. https://doi.org/10.1016/S0277-5387(97)00119-8.

(42)   Ayeleso, A. O.; Joseph, J. S.; Oguntibeju, O. O.; Mukwevho, E. Evaluation of Free Radical Scavenging Capacity of Methoxy Containing-Hybrids of Thiosemicarbazone-Triazole and Their Influence on Glucose Transport. *BMC Pharmacol. Toxicol.* **2018**, *19* (1), 84. https://doi.org/10.1186/s40360-018-0266-6.

(43)   Tadjarodi, A.; Moazen Ferdowsi, S.; Zare-Dorabei, R.; Barzin, A. Highly Efficient Ultrasonic-Assisted Removal of Hg(II) Ions on Graphene Oxide Modified with 2-Pyridinecarboxaldehyde Thiosemicarbazone: Adsorption Isotherms and Kinetics Studies. *Ultrason. Sonochem.* **2016**, *33*, 118–128. https://doi.org/10.1016/j.ultsonch.2016.04.030.

(44)   Juyal, V. K.; Pathak, A.; Panwar, M.; Thakuri, S. C.; Prakash, O.; Agrwal, A.; Nand, V. Schiff Base Metal Complexes as a Versatile Catalyst: A Review. *J. Organomet. Chem.* **2023**, *999*, 122825.

https://doi.org/10.1016/j.jorganchem.2023.122825.

(45) Al Zoubi, W.; Ko, Y. G. Schiff Base Complexes and Their Versatile Applications as Catalysts in Oxidation of Organic Compounds: Part I. *Appl. Organomet. Chem.* **2017**, *31* (3), e3574. https://doi.org/10.1002/aoc.3574.

(46) Lawrence, M. A. W.; Thompson, C.; Lorraine, S. C. Pincer Complexes in Photo- and Electro-Catalytic Hydrogen Evolution (HER) and Carbon Dioxide Reduction Reactions (CO2RR). *Inorganica Chim. Acta* **2024**, *560*, 121829. https://doi.org/10.1016/j.ica.2023.121829.

(47) Calvin, M.; Wilson, K. W. Stability of Chelate Compounds. *J. Am. Chem. Soc.* **1945**, *67* (11), 2003–2007. https://doi.org/10.1021/ja01227a043.

(48) Zaera, F. Designing Sites in Heterogeneous Catalysis: Are We Reaching Selectivities Competitive With Those of Homogeneous Catalysts? *Chem. Rev.* **2022**, *122* (9), 8594–8757. https://doi.org/10.1021/acs.chemrev.1c00905.

(49) King, A. K.; Brar, A.; Li, G.; Findlater, M. Homogeneous and Recyclable Palladium Catalysts: Application in Suzuki–Miyaura Cross-Coupling Reactions. *Organometallics* **2023**, *42* (17), 2353–2358. https://doi.org/10.1021/acs.organomet.3c00231.

(50) L. Budarin, V.; S. Shuttleworth, P.; H. Clark, J.; Luque, R. Industrial Applications of C-C Coupling Reactions. *Curr. Org. Synth.* **2011**, *7* (6), 614–627. https://doi.org/10.2174/157017910794328529.

(51) Miyaura, N.; Yamada, K.; Suzuki, A. A New Stereospecific Cross-Coupling by the Palladium-Catalyzed Reaction of 1-Alkenylboranes with 1-Alkenyl or 1-Alkynyl Halides. *Tetrahedron Lett.* **1979**, *20* (36), 3437–3440. https://doi.org/10.1016/S0040-4039(01)95429-2.

(52) Amatore, C.; Jutand, A. Anionic Pd(0) and Pd(II) Intermediates in Palladium-Catalyzed Heck and Cross-Coupling Reactions. *Acc. Chem. Res.* **2000**, *33* (5), 314–321. https://doi.org/10.1021/ar980063a.

(53) Ho, C. C.; Olding, A.; Smith, J. A.; Bissember, A. C. Nuances in Fundamental Suzuki–Miyaura Cross-Couplings Employing [Pd(PPh3)4]: Poor Reactivity of Aryl Iodides at Lower Temperatures. *Organometallics* **2018**, *37* (11), 1745–1750. https://doi.org/10.1021/acs.organomet.8b00189.

(54) Martin, R.; Buchwald, S. L. Palladium-Catalyzed Suzuki–Miyaura Cross-Coupling Reactions Employing Dialkylbiaryl Phosphine Ligands. *Acc. Chem. Res.* **2008**, *41* (11), 1461–1473. https://doi.org/10.1021/ar800036s.

(55) Paul, P.; Datta, S.; Halder, S.; Acharyya, R.; Basuli, F.; Butcher, R. J.; Peng, S.-M.; Lee, G.-H.; Castineiras, A.; Drew, M. G. B.; Bhattacharya, S. Syntheses, Structures and Efficient Catalysis for C–C Coupling of Some Benzaldehyde Thiosemicarbazone Complexes of Palladium. *J. Mol.*

Catal. A Chem. **2011**, *344* (1), 62–73. https://doi.org/10.1016/j.molcata.2011.05.003.

(56) Yan, H.; Chellan, P.; Li, T.; Mao, J.; Chibale, K.; Smith, G. S. Cyclometallated Pd(II) Thiosemicarbazone Complexes: New Catalyst Precursors for Suzuki-Coupling Reactions. *Tetrahedron Lett.* **2013**, *54* (2), 154–157. https://doi.org/10.1016/j.tetlet.2012.10.115.

(57) Dutta, J.; Datta, S.; Kumar Seth, D.; Bhattacharya, S. Mixed-Ligand Benzaldehyde Thiosemicarbazone Complexes of Palladium Containing N,O-Donor Ancillary Ligands. Syntheses, Structures, and Catalytic Application in C-C and C-N Coupling Reactions. *RSC Adv.* **2012**, *2* (31), 11751–11763. https://doi.org/10.1039/c2ra21078a.

(58) Kumar, A.; Rao, G. K.; Kumar, S.; Singh, A. K. Organosulphur and Related Ligands in Suzuki–Miyaura C–C Coupling. *Dalt. Trans.* **2013**, *42* (15), 5200–5223. https://doi.org/10.1039/C2DT32432F.

(59) Kostas, I. D.; Andreadaki, F. J.; Kovala-Demertzi, D.; Christos Prentjas; Demertzis, M. A. Suzuki–Miyaura Cross-Coupling Reaction of Aryl Bromides and Chlorides with Phenylboronic Acid under Aerobic Conditions Catalyzed by Palladium Complexes with Thiosemicarbazone Ligands. *Tetrahedron Lett.* **2005**, *46* (12), 1967–1970. https://doi.org/10.1016/j.tetlet.2005.02.003.

(60) Castiñeiras, A.; Fernández-Hermida, N.; García-Santos, I.; Gómez-Rodríguez, L. Neutral NiII, PdII and PtII ONS-Pincer Complexes of 5-Acetylbarbituric-4N-Dimethylthiosemicarbazone: Synthesis, Characterization and Properties. *Dalt. Trans.* **2012**, *41* (43), 13486–13495. https://doi.org/10.1039/C2DT31753B.

(61) Sharma, R. K.; Pandey, A.; Gulati, S. Silica-Supported Palladium Complex: An Efficient, Highly Selective and Reusable Organic–Inorganic Hybrid Catalyst for the Synthesis of E-Stilbenes. *Appl. Catal. A Gen.* **2012**, *431–432*, 33–41. https://doi.org/10.1016/j.apcata.2012.04.009.

(62) Verma, P. R.; Mandal, S.; Gupta, P.; Mukhopadhyay, B. Carbohydrate Derived Thiosemicarbazone and Semicarbazone Palladium Complexes: Homogeneous Catalyst for C–C Cross Coupling Reactions. *Tetrahedron Lett.* **2013**, *54* (36), 4914–4917. https://doi.org/10.1016/j.tetlet.2013.06.145.

(63) Palve, A. M.; Joshi, P. V; Puranik, V.; Garje, S. S. Synthesis and X-Ray Single Crystal Structure of a Cadmium(II) Acetophenone Thiosemicarbazone Complex and Its Use as a Single-Source Precursor for the Preparation of CdS Nanocrystallites and Thin Films. *Polyhedron* **2013**, *61*, 195–201. https://doi.org/10.1016/j.poly.2013.05.052.

(64) Nair, P. S.; Scholes, G. D. Thermal Decomposition of Single Source Precursors and the Shape Evolution of CdS and CdSe Nanocrystals. *J. Mater. Chem.* **2006**, *16* (5), 467–473. https://doi.org/10.1039/B513108A.

(65) Alfarra, A.; Frackowiak, E.; Béguin, F. The HSAB Concept as a Means to Interpret the Adsorption of Metal Ions onto Activated Carbons. *Appl. Surf. Sci.* **2004**, *228* (1–4), 84–92. https://doi.org/10.1016/j.apsusc.2003.12.033.

(66) Awual, M. R.; Hasan, M. M.; Znad, H. Organic-Inorganic Based Nano-Conjugate Adsorbent for Selective Palladium(II) Detection, Separation and Recovery. *Chem. Eng. J.* **2015**, *259*, 611–619. https://doi.org/10.1016/j.cej.2014.08.028.

(67) Awual, M. R.; Hasan, M. M.; Naushad, M.; Shiwaku, H.; Yaita, T. Preparation of New Class Composite Adsorbent for Enhanced Palladium(II) Detection and Recovery. *Sensors Actuators, B Chem.* **2015**, *209*, 790–797. https://doi.org/10.1016/j.snb.2014.12.053.

(68) Mahmoud, M. E.; Yakout, A. A.; Ahmed, S. B.; Osman, M. M. Speciation, Selective Extraction and Preconcentration of Chromium Ions via Alumina-Functionalized-Isatin-Thiosemicarbazone. *J. Hazard. Mater.* **2008**, *158* (2–3), 541–548. https://doi.org/10.1016/j.jhazmat.2008.01.114.

(69) Chamjangali, M. A.; Bagherian, G.; Mokhlesian, A.; Bahramian, B. Synthesis and Application of Chloromethylated Polystyrene Modified with 1-Phenyl-1,2-Propanedione-2-Oxime Thiosemicarbazone (PPDOT) as a New Sorbent for the on-Line Preconcentration and Determination of Copper in Water, Soil, and Food Samples by FAAS. *J. Hazard. Mater.* **2011**, *192* (3), 1641–1649. https://doi.org/10.1016/j.jhazmat.2011.06.093.

(70) Matesanz, A. I.; Leitao, I.; Souza, P. Palladium(II) and Platinum(II) Bis(Thiosemicarbazone) Complexes of the 2,6-Diacetylpyridine Series with High Cytotoxic Activity in Cisplatin Resistant A2780cisR Tumor Cells and Reduced Toxicity. *J. Inorg. Biochem.* **2013**, *125*, 26–31. https://doi.org/10.1016/j.jinorgbio.2013.04.005.

(71) Metwally, M. A.; Bondock, S.; El-Azap, H.; Kandeel, E.-E. M. Thiosemicarbazides: Synthesis and Reactions. *J. Sulfur Chem.* **2011**, *32* (5), 489–519. https://doi.org/10.1080/17415993.2011.601869.

(72) Gygi, D.; Hwang, S. J.; Nocera, D. G. Scalable Syntheses of 4-Substituted Pyridine-Diimines. *J. Org. Chem.* **2017**, *82* (23), 12933–12938. https://doi.org/10.1021/acs.joc.7b02571.

(73) Lieb, D.; Kenkell, I.; Miljković, J. L.; Moldenhauer, D.; Weber, N.; Filipović, M. R.; Gröhn, F.; Ivanović-Burmazović, I. Amphiphilic Pentaazamacrocyclic Manganese Superoxide Dismutase Mimetics. *Inorg. Chem.* **2014**, *53* (2), 1009–1020. https://doi.org/10.1021/ic402469t.

(74) Mohan, M.; Sharma, P.; Kumar, M.; Jha, N. K. Metal Complexes of 2,6-Diacetylpyridine Bis(Thiosemicarbazone): Their Preparation, Characterization and Antitumour Activity. *Inorganica Chim. Acta* **1986**, *125* (1), 9–1. https://doi.org/10.1016/S0020-1693(00)85476-6.

(75) Matesanz, A. I.; Hernández, C.; Souza, P. A New Organometallic Palladium(II) Compound

Derived of 2,6-Diacetylpyridine Mono(Thiosemicarbazone): Synthesis, Spectroscopic Properties and Crystal Structure of Two Solvatomorphic Forms. *J. Organomet. Chem.* **2014**, *751*, 374–378. https://doi.org/10.1016/j.jorganchem.2013.09.022.

(76)   Casas, J. S.; Castellano, E. E.; García-Tasende, M. S.; Sánchez, A.; Sordo, J.; Zukerman-Schpector, J. Cadmium(II) Complexes of 2,6-Diacetylpyridine Bis- and Monothiosemicarhazones. The Crystal Structure of Aquodichloro(2,6-Diacetylpyridine Monothiosemicarbazone-N,N′,O,S)Cadmium(II) Monohydrate. *Zeitschrift für Anorg. und Allg. Chemie* **1997**, *623* (1–6), 825–831. https://doi.org/10.1002/zaac.199762301130.

(77)   Pedrido, R.; González-Noya, A. M.; Romero, M. J.; Martínez-Calvo, M.; Vázquez López, M.; Gómez-Fórneas, E.; Zaragoza, G.; Bermejo, M. R. Pentadentate Thiosemicarbazones as Versatile Chelating Systems. A Comparative Structural Study of Their Metallic Complexes. *J. Chem. Soc. Dalt. Trans.* **2008**, No. 47, 6776–6787. https://doi.org/10.1039/b810601k.

(78)   Pedrido, R.; Bermejo, M. R.; Romero, M. J.; Vázquez, M.; González-Noya, A. M.; Maneiro, M.; Rodríguez, M. J.; Fernández, M. I. Syntheses and X-Ray Characterization of Metal Complexes with the Pentadentate Thiosemicarbazone Ligand Bis(4-N-Methylthiosemicarbazone)-2,6-Diacetylpyridine. the First Pentacoordinate Lead(II) Complex with a Pentagonal Geometry. *Dalt. Trans.* **2005**, No. 3, 572–579. https://doi.org/10.1039/b416296j.

(79)   Matesanz, A. I.; Souza, P. Unprecedented Pt(II) Complex of an Asymmetric 2,6-Diacetylpyridine Bis(4N-Substituted Thiosemicarbazone) Ligand. *Inorg. Chem. Commun.* **2013**, *27*, 5–8. https://doi.org/10.1016/j.inoche.2012.10.022.

(80)   Anjum, R.; Palanimuthu, D.; Kalinowski, D. S.; Lewis, W.; Park, K. C.; Kovacevic, Z.; Khan, I. U.; Richardson, D. R. Synthesis, Characterization, and in Vitro Anticancer Activity of Copper and Zinc Bis(Thiosemicarbazone) Complexes. *Inorg. Chem.* **2019**, *58* (20), 13709–13723. https://doi.org/10.1021/acs.inorgchem.9b01281.

(81)   Hosseini-Yazdi, S. A.; Hosseinpour, S.; Khandar, A. A.; Kassel, W. S.; Piro, N. A. Copper(II) and Nickel(II) Complexes with Two New Bis(Thiosemicarbazone) Ligands: Synthesis, Characterization, X-Ray Crystal Structures and Their Electrochemistry Behavior. *Inorganica Chim. Acta* **2015**, *427*, 124–130. https://doi.org/10.1016/j.ica.2014.12.011.

(82)   Hosseinpour, S.; Hosseini-Yazdi, S. A.; White, J. Binuclear Zinc(II) Complexes of N(4)-Substituted Bis(Thiosemicarbazone) Ligands Incorporating Hydroxyl Group and Their Non-Hydroxyl Analogues. *Inorganica Chim. Acta* **2017**, *461*, 150–160. https://doi.org/10.1016/j.ica.2017.02.022.

(83)   Chandra, S.; Gupta, L.; Tyagi, V. P. Co(II), Ni(II), Cu(II) and Zn(II) Complexes of Thiosemicarbazones. *Synth. React. Inorg. Met. Chem.* **1996**, *26* (1), 125–137.

https://doi.org/10.1080/00945719608004251.

(84) Al-Riyahee, A. A. A.; Horton, P. N.; Coles, S. J.; Amoroso, A. J.; J. A. Pope, S. Ni(II), Cu(II) and Zn(II) Complexes of Functionalised Thiosemicarbazone Ligands: Syntheses and Reactivity, Characterization and Structural Studies. *Polyhedron* **2022**, *225*, 116079. https://doi.org/10.1016/j.poly.2022.116079.

(85) Palanimuthu, D.; Shinde, S. V.; Somasundaram, K.; Samuelson, A. G. In Vitro and in Vivo Anticancer Activity of Copper Bis(Thiosemicarbazone) Complexes. *J. Med. Chem.* **2013**, *56* (3), 722–734. https://doi.org/10.1021/jm300938r.

(86) Matesanz, A. I.; Cuadrado, I.; Pastor, C.; Souza, P. A Novel Sulfur-Bridged Dimeric Zinc(II) Complex with 2, 6-Diacetylpyridine Bis(Thiosemicarbazone). *Zeitschrift für Anorg. und Allg. Chemie* **2005**, *631* (4), 780–784. https://doi.org/10.1002/zaac.200400428.

(87) Nartop, D.; Hasanoğlu Özkan, E.; Öğütcü, H.; Kurnaz Yetim, N.; Özdemir, İ. Novel α-N-Heterocyclic Thiosemicarbazone Complexes: Synthesis, Characterization, and Antimicrobial of Properties Investigation. *RSC Adv.* **2024**, *14* (40), 29308–29318. https://doi.org/10.1039/d4ra04002c.

(88) Al-Farraj, E. S. An Efficient Synthesis for Cd(II), Cu(II), and UO2(II) Complexes with N-Ethyl-2-(1-(Naphthalen-1-Yl)Ethylidene)Hydrazine-1-Carbothioamide under Solvent-Free Condition Using Ball Milling as Green Protocol. *J. Mol. Struct.* **2024**, *1306*, 137928. https://doi.org/10.1016/j.molstruc.2024.137928.

(89) da Costa, J. P.; Oliveira-Silva, R.; Daniel-da-Silva, A. L.; Vitorino, R. Bionanoconjugation for Proteomics Applications – An Overview. *Biotechnol. Adv.* **2014**, *32* (5), 952–970. https://doi.org/10.1016/j.biotechadv.2014.04.013.

(90) Sun, H.; Schanze, K. S. Functionalization of Water-Soluble Conjugated Polymers for Bioapplications. *ACS Appl. Mater. Interfaces* **2022**, *14* (18), 20506–20519. https://doi.org/10.1021/acsami.2c02475.

(91) Yang, L.; Zou, P.; Cao, J.; Sun, Y.; Han, D.; Yang, S.; Chen, G.; Kong, X.; Yang, J. Facile Synthesis and Paramagnetic Properties of $Fe_3O_4@SiO_2$ Core–Shell Nanoparticles. *Superlattices Microstruct.* **2014**, *76*, 205–212. https://doi.org/10.1016/j.spmi.2014.10.011.

(92) Silverstein, R. M.; Webster, F. X.; Kiemle, D. J. Spectrometric Identification of Organic Compounds 7ed 2005 - Silverstein, Webster & Kiemle.Pdf. *Microchem. J.* **2005**, *21*, 496.

(93) Singh, R. N.; Kumar, A.; Tiwari, R. K.; Rawat, P. A Combined Experimental and Theoretical (DFT and AIM) Studies on Synthesis, Molecular Structure, Spectroscopic Properties and Multiple Interactions Analysis in a Novel Ethyl-4-[2-(Thiocarbamoyl)Hydrazinylidene]-3,5-Dimethyl-1H-Pyrrole-2-Carboxylate and It. *Spectrochim. Acta Part A Mol. Biomol. Spectrosc.*

2013, *112*, 182–190. https://doi.org/10.1016/j.saa.2013.04.002.

(94)   Chen, L.; Xu, Z.; Dai, H.; Zhang, S. Facile Synthesis and Magnetic Properties of Monodisperse Fe_3O_4/Silica Nanocomposite Microspheres with Embedded Structures via a Direct Solution-Based Route. *J. Alloys Compd.* **2010**, *497* (1), 221–227. https://doi.org/10.1016/j.jallcom.2010.03.016.

(95)   Ding, H. L.; Zhang, Y. X.; Wang, S.; Xu, J. M.; Xu, S. C.; Li, G. H. $Fe_3O_4@SiO_2$ Core/Shell Nanoparticles: The Silica Coating Regulations with a Single Core for Different Core Sizes and Shell Thicknesses. *Chem. Mater.* **2012**, *24* (23), 4572–4580. https://doi.org/10.1021/cm302828d.

(96)   Wiles, D. M.; Gingras, B. A.; Suprunchuk, T. The C=S Stretching Vibration in the Infrared Spectra of Some Thiosemicarbazones. *Can. J. Chem.* **1967**, *45* (5), 469–473. https://doi.org/10.1139/v67-081.

(97)   Karimzadeh, I.; Aghazadeh, M.; Ganjali, M. R.; Doroudi, T.; Kolivand, P. H. Preparation and Characterization of Iron Oxide (Fe_3O_4) Nanoparticles Coated with Polyvinylpyrrolidone/Polyethylenimine through a Facile One-Pot Deposition Route. *J. Magn. Magn. Mater.* **2017**, *433*, 148–154. https://doi.org/10.1016/j.jmmm.2017.02.048.

(98)   NIST. *X-ray Photoelectron Spectroscopy Database (SRD 20)*. https://srdata.nist.gov/xps/.

(99)   Kohzadi, H.; Soleiman-Beigi, M. XPS and Structural Studies of Fe_3O_4-PTMS-NAS@Cu as a Novel Magnetic Natural Asphalt Base Network and Recoverable Nanocatalyst for the Synthesis of Biaryl Compounds. *Sci. Rep.* **2021**, *11* (1), 24508. https://doi.org/10.1038/s41598-021-04111-z.

(100)   Artyushkova, K. Misconceptions in Interpretation of Nitrogen Chemistry from X-Ray Photoelectron Spectra. *J. Vac. Sci. Technol. A* **2020**, *38* (3), 31002. https://doi.org/10.1116/1.5135923.

(101)   Matanovic, I.; Artyushkova, K.; Strand, M. B.; Dzara, M. J.; Pylypenko, S.; Atanassov, P. Core Level Shifts of Hydrogenated Pyridinic and Pyrrolic Nitrogen in the Nitrogen-Containing Graphene-Based Electrocatalysts: In-Plane vs Edge Defects. *J. Phys. Chem. C* **2016**, *120* (51), 29225–29232. https://doi.org/10.1021/acs.jpcc.6b09778.

(102)   Titantah, J. T.; Lamoen, D. Carbon and Nitrogen 1s Energy Levels in Amorphous Carbon Nitride Systems: XPS Interpretation Using First-Principles. *Diam. Relat. Mater.* **2007**, *16* (3), 581–588. https://doi.org/10.1016/j.diamond.2006.11.048.

(103)   Fang, J.; Fan, H.; Li, M.; Long, C. Nitrogen Self-Doped Graphitic Carbon Nitride as Efficient Visible Light Photocatalyst for Hydrogen Evolution. *J. Mater. Chem. A* **2015**, *3* (26), 13819–13826. https://doi.org/10.1039/C5TA02257F.

(104)   Basri, R.; Khalid, M.; Shafiq, Z.; Tahir, M. S.; Khan, M. U.; Tahir, M. N.; Naseer, M. M.; Braga,

A. A. C. Exploration of Chromone-Based Thiosemicarbazone Derivatives: SC-XRD/DFT, Spectral (IR, UV–Vis) Characterization, and Quantum Chemical Analysis. *ACS Omega* **2020**, *5* (46), 30176–30188. https://doi.org/10.1021/acsomega.0c04653.

(105) Moorthy, N.; Prabakar, P. C. J.; Ramalingam, S.; Pandian, G. V; Anbusrinivasan, P. Vibrational, NMR and UV–Visible Spectroscopic Investigation and NLO Studies on Benzaldehyde Thiosemicarbazone Using Computational Calculations. *J. Phys. Chem. Solids* **2016**, *91*, 55–68. https://doi.org/10.1016/j.jpcs.2015.11.021.

(106) Feifel, S. C.; Lisdat, F. Silica Nanoparticles for the Layer-by-Layer Assembly of Fully Electro-Active Cytochrome c Multilayers. *J. Nanobiotechnology* **2011**, *9* (1), 59. https://doi.org/10.1186/1477-3155-9-59.

(107) Durig, J. R.; Layton, R.; Sink, D. W.; Mitchell, B. R. Far Infrared Spectra of Palladium Compounds–I. The Influence of Ligands upon the Palladium Chloride Stretching Frequency. *Spectrochim. Acta* **1965**, *21* (8), 1367–1378. https://doi.org/10.1016/0371-1951(65)80046-7.

(108) Xiao, S.; Xu, P.; Peng, Q.; Chen, J.; Huang, J.; Wang, F.; Noor, N. Layer-by-Layer Assembly of Polyelectrolyte Multilayer onto PET Fabric for Highly Tunable Dyeing with Water Soluble Dyestuffs. *Polymers*. 2017. https://doi.org/10.3390/polym9120735.

(109) Xingbin Yan; Tao Xu; Gang Chen; Shengrong Yang; Huiwen Liu; Qunji Xue. Preparation and Characterization of Electrochemically Deposited Carbon Nitride Films on Silicon Substrate. *J. Phys. D. Appl. Phys.* **2004**, *37* (6), 907. https://doi.org/10.1088/0022-3727/37/6/015.

(110) Zhang, C.; Li, X.; Jiang, Z.; Zhang, Y.; Wen, T.; Fang, M.; Tan, X.; Alsaedi, A.; Hayat, T.; Wang, X. Selective Immobilization of Highly Valent Radionuclides by Carboxyl Functionalized Mesoporous Silica Microspheres: Batch, XPS, and EXAFS Analyses. *ACS Sustain. Chem. Eng.* **2018**, *6* (11), 15644–15652. https://doi.org/10.1021/acssuschemeng.8b04146.

(111) Thi, Q. H.; Man, P.; Huang, L.; Chen, X.; Zhao, J.; Ly, T. H. Superhydrophilic 2D Carbon Nitrides Prepared by Direct Chemical Vapor Deposition. *Small Sci.* **2023**, *3* (4), 2200099. https://doi.org/10.1002/smsc.202200099.

(112) He, Y.; Shan, Z.; Tan, T.; Chen, Z.; Zhang, Y. Ternary Sulfur/Polyacrylonitrile/SiO2 Composite Cathodes for High-Performance Sulfur/Lithium Ion Full Batteries. *Polymers*. 2018. https://doi.org/10.3390/polym10080930.

(113) Huang, R.; Tang, M.; Kan, W.; Xu, H.; Wu, K.; Wang, Z.; Li, H. Single-Crystalline LiNbO$_3$ Integrated onto Si-Based Substrates via Ar Plasma-Activated Low-Temperature Direct Bonding. *J. Phys. D. Appl. Phys.* **2024**, *57* (1), 15102. https://doi.org/10.1088/1361-6463/acff05.

(114) Criado, J. J.; Fernandez, I.; Macias, B.; Salas, J. M.; Medarde, M. Novel Chelates of Pd(II) Dithiocarbamates. Spectroscopic Studies and Thermal Behaviour. *Inorganica Chim. Acta* **1990**,

174 (1), 67–75. https://doi.org/10.1016/S0020-1693(00)80280-7.

(115) Zhuangyu, Z.; Hongwen, H.; Tsi-Yu, K. [Poly(Styryl)Phenanthroline]Palladium Catalyst. Synthesis and Some of Its Applications in Vinylic Substitution Reactions with Organic Halides. *React. Polym. Ion Exch. Sorbents* **1988**, *9* (3), 249–255. https://doi.org/10.1016/0167-6989(88)90250-4.

(116) Kim, K. S.; Gossmann, A. F.; Winograd, N. X-Ray Photoelectron Spectroscopic Studies of Palladium Oxides and the Palladium-Oxygen Electrode. *Anal. Chem.* **1974**, *46* (2), 197–200. https://doi.org/10.1021/ac60338a037.

(117) Zemlyanov, D.; Aszalos-Kiss, B.; Kleimenov, E.; Teschner, D.; Zafeiratos, S.; Hävecker, M.; Knop-Gericke, A.; Schlögl, R.; Gabasch, H.; Unterberger, W.; Hayek, K.; Klötzer, B. In Situ XPS Study of Pd(111) Oxidation. Part 1: 2D Oxide Formation in 10−3mbar O_2. *Surf. Sci.* **2006**, *600* (5), 983–994. https://doi.org/10.1016/j.susc.2005.12.020.

(118) Guerrero-Ortega, L. P. A.; Ramírez-Meneses, E.; Cabrera-Sierra, R.; Palacios-Romero, L. M.; Philippot, K.; Santiago-Ramírez, C. R.; Lartundo-Rojas, L.; Manzo-Robledo, A. Pd and Pd@PdO Core–Shell Nanoparticles Supported on Vulcan Carbon XC-72R: Comparison of Electroactivity for Methanol Electro-Oxidation Reaction. *J. Mater. Sci.* **2019**, *54* (21), 13694–13714. https://doi.org/10.1007/s10853-019-03843-8.

(119) Anbarasu, G.; Malathy, M.; Rajavel, R. Synthesis and Catalytic Properties of Copper(II) Schiff-Base Complex Immobilized Silica Materials. *J. Porous Mater.* **2017**, *24* (5), 1253–1261. https://doi.org/10.1007/s10934-017-0366-5.

(120) Zhang, H.; Li, C.; Guo, J.; Zang, L.; Luo, J. In Situ Synthesis of Poly(Methyl Methacrylate)/SiO2 Hybrid Nanocomposites via "Grafting Onto" Strategy Based on UV Irradiation in the Presence of Iron Aqueous Solution. *J. Nanomater.* **2012**, *2012* (1), 217412. https://doi.org/10.1155/2012/217412.

(121) Sun, G.-D.; Zhang, G.-H.; Chou, K.-C.; Dong, A.-P. Preparation of SiS and SiO_2 Nanospheres. *Ind. Eng. Chem. Res.* **2017**, *56* (43), 12362–12368. https://doi.org/10.1021/acs.iecr.7b03292.

(122) Stöber, W.; Fink, A.; Bohn, E. Controlled Growth of Monodisperse Silica Spheres in the Micron Size Range. *J. Colloid Interface Sci.* **1968**, *26* (1), 62–69. https://doi.org/10.1016/0021-9797(68)90272-5.

(123) Gholami, T.; Salavati-Niasari, M.; Bazarganipour, M.; Noori, E. Synthesis and Characterization of Spherical Silica Nanoparticles by Modified Stöber Process Assisted by Organic Ligand. *Superlattices Microstruct.* **2013**, *61*, 33–41. https://doi.org/10.1016/j.spmi.2013.06.004.

(124) Sharma, R. K.; Sharma, S.; Gulati, S.; Pandey, A. Fabrication of a Novel Nano-Composite Carbon Paste Sensor Based on Silica-Nanospheres Functionalized with Isatin

Thiosemicarbazone for Potentiometric Monitoring of Cu^{2+} Ions in Real Samples. *Anal. Methods* **2013**, *5* (6), 1414–1426. https://doi.org/10.1039/C3AY26319C.

(125) Schneider, C. A.; Rasband, W. S.; Eliceiri, K. W. NIH Image to ImageJ: 25 Years of Image Analysis. *Nat. Methods* **2012**, *9* (7), 671–675. https://doi.org/10.1038/nmeth.2089.

(126) Ma, J.; Lian, J.; Duan, X.; Liu, X.; Zheng, W. α-Fe_2O_3: Hydrothermal Synthesis, Magnetic and Electrochemical Properties. *J. Phys. Chem. C* **2010**, *114* (24), 10671–10676. https://doi.org/10.1021/jp102243g.

(127) Zhong, J.; Cao, C. Nearly Monodisperse Hollow Fe_2O_3 Nanoovals: Synthesis, Magnetic Property and Applications in Photocatalysis and Gas Sensors. *Sensors Actuators B Chem.* **2010**, *145* (2), 651–656. https://doi.org/10.1016/j.snb.2010.01.016.

(128) Abbas, M.; Islam, M. N.; Rao, B. P.; Abdel-Hamed, M. O.; Kim, C. Facile One-Pot Chemical Approach for Synthesis of Monodisperse Chain-like Superparamagnetic Maghemite (γ-Fe_2O_3) Nanoparticles. *J. Ind. Eng. Chem.* **2015**, *31*, 43–46. https://doi.org/10.1016/j.jiec.2015.06.025.

(129) Lemine, O. M.; Madkhali, N.; Alshammari, M.; Algessair, S.; Gismelseed, A.; El Mir, L.; Hjiri, M.; Yousif, A. A.; El-Boubbou, K. Maghemite (γ-Fe_2O_3) and γ-Fe_2O_3-TiO_2 Nanoparticles for Magnetic Hyperthermia Applications: Synthesis, Characterization and Heating Efficiency. *Materials*. 2021. https://doi.org/10.3390/ma14195691.

(130) Wiles, D. M.; Gingras, B. A.; Suprunchuk, T. The C=S Stretching Vibration in the Infrared Spectra of Some Thiosemicarbazones. *Can. J. Chem.* **1967**, *45* (5), 469–473. https://doi.org/10.1139/v67-081.

(131) Guru, S.; Mishra, D.; Amritphale, S. S.; Joshi, S. Influence of Glycols in Microwave Assisted Synthesis of Ironoxide Nanoparticles. *Colloid Polym. Sci.* **2016**, *294* (1), 207–213. https://doi.org/10.1007/s00396-015-3755-9.

(132) Foo, K. Y.; Hameed, B. H. Insights into the Modeling of Adsorption Isotherm Systems. *Chem. Eng. J.* **2010**, *156* (1), 2–10. https://doi.org/10.1016/j.cej.2009.09.013.

(133) Tran, H. N.; You, S. J.; Hosseini-Bandegharaei, A.; Chao, H. P. Mistakes and Inconsistencies Regarding Adsorption of Contaminants from Aqueous Solutions: A Critical Review. *Water Res.* **2017**, *120*, 88–116. https://doi.org/10.1016/j.watres.2017.04.014.

(134) Aly, A. A.; Abdallah, E. M.; Ahmed, S. A.; Rabee, M. M.; Bräse, S. Transition Metal Complexes of Thiosemicarbazides, Thiocarbohydrazides, and Their Corresponding Carbazones with Cu(I), Cu(II), Co(II), Ni(II), Pd(II), and Ag(I)–A Review. *Molecules*. 2023. https://doi.org/10.3390/molecules28041808.

(135) Bayat, A.; Shakourian-Fard, M.; Ehyaei, N.; Hashemi, M. M. A Magnetic Supported Iron Complex for Selective Oxidation of Sulfides to Sulfoxides Using 30% Hydrogen Peroxide at

Room Temperature. *RSC Adv.* **2014**, *4* (83), 44274–44281. https://doi.org/10.1039/C4RA07356H.

(136) Aghapour, A. A.; Nemati, S.; Mohammadi, A.; Nourmoradi, H.; Karimzadeh, S. Nitrate Removal from Water Using Alum and Ferric Chloride: A Comparative Study of Alum and Ferric Chloride Efficiency. *Environ. Heal. Eng. Manag.* **2016**, *3* (2), 69–73. https://doi.org/10.15171/ehem.2016.03.

(137) Wojnicki, M.; Socha, R. P.; Pędzich, Z.; Mech, K.; Tokarski, T.; Fitzner, K. Palladium(II) Chloride Complex Ion Recovery from Aqueous Solutions Using Adsorption on Activated Carbon. *J. Chem. Eng. Data* **2018**, *63* (3), 702–711. https://doi.org/10.1021/acs.jced.7b00885.

(138) Di Bonito, L. P.; Kyriacou, P.; Di Colandrea, A.; Di Natale, F.; Ruoppolo, G.; Krasia-Christoforou, T. Design and Production of Functionalized Electrospun Fibers for Palladium Recovery. *ACS Appl. Polym. Mater.* **2024**, *6* (16), 9406–9419. https://doi.org/10.1021/acsapm.4c00324.

(139) Cheng, N.; Zhang, L.; Wang, M.; Shu, J.; Shao, P.; Yang, L.; Meng, X.; Fan, Y.; Li, M. Highly Effective Recovery of Palladium from a Spent Catalyst by an Acid- and Oxidation-Resistant Electrospun Fibers as a Sorbent. *Chem. Eng. J.* **2023**, *466*, 143171. https://doi.org/10.1016/j.cej.2023.143171.

(140) Sayın, M.; Can, M.; İmamoğlu, M. Adsorption of Pd(II) and Au(III) Ions by Commercial Tris(2-Aminoethyl) Amine Polystyrene Polymer Beads. *J. Chem. Eng. Data* **2021**, *66* (2), 1132–1143. https://doi.org/10.1021/acs.jced.0c00920.

(141) Huang, Z.; Wang, C.; Zhao, J.; Wang, S.; Zhou, Y.; Zhang, L. Adsorption Behavior of Pd(II) Ions from Aqueous Solution onto Pyromellitic Acid Modified-UiO-66-NH$_2$. *Arab. J. Chem.* **2020**, *13* (9), 7007–7019. https://doi.org/10.1016/j.arabjc.2020.07.007.

(142) Tang, J.; Zhao, J.; Wang, S.; Zhang, L.; Zhao, M.; Huang, Z.; Hu, Y. Pre-Modification Strategy to Prepare a Novel Zr-Based MOF for Selective Adsorption of Palladium(II) from Solution. *Chem. Eng. J.* **2021**, *407*, 127223. https://doi.org/10.1016/j.cej.2020.127223.

(143) Ramesh, A.; Hasegawa, H.; Sugimoto, W.; Maki, T.; Ueda, K. Adsorption of Gold(III), Platinum(IV) and Palladium(II) onto Glycine Modified Crosslinked Chitosan Resin. *Bioresour. Technol.* **2008**, *99* (9), 3801–3809. https://doi.org/10.1016/j.biortech.2007.07.008.

(144) Far, H. S.; Hasanzadeh, M.; Nashtaei, M. S.; Rabbani, M. Fast and Efficient Adsorption of Palladium from Aqueous Solution by Magnetic Metal–Organic Framework Nanocomposite Modified with Poly(Propylene Imine) Dendrimer. *Environ. Sci. Pollut. Res.* **2021**, *28* (44), 62474–62486. https://doi.org/10.1007/s11356-021-15144-2.

(145) Zhou, L.; Liu, J.; Liu, Z. Adsorption of Platinum(IV) and Palladium(II) from Aqueous Solution by Thiourea-Modified Chitosan Microspheres. *J. Hazard. Mater.* **2009**, *172* (1), 439–446.

https://doi.org/10.1016/j.jhazmat.2009.07.030.

(146) Davudabadi Farahani, M.; Shemirani, F.; Gharehbaghi, M. Ferrofluid-Based Dispersive Solid Phase Extraction of Palladium. *Talanta* **2013**, *109*, 121–127. https://doi.org/10.1016/j.talanta.2013.01.061.

(147) Shafizadeh, F.; Taghizadeh, M.; Hassanpour, S. Preparation of a Novel Magnetic Pd(II) Ion-Imprinted Polymer for the Fast and Selective Adsorption of Palladium Ions from Aqueous Solutions. *Environ. Sci. Pollut. Res.* **2019**, *26* (18), 18493–18508. https://doi.org/10.1007/s11356-019-05233-8.

(148) Awual, M. R. Novel Nanocomposite Materials for Efficient and Selective Mercury Ions Capturing from Wastewater. *Chem. Eng. J.* **2017**, *307*, 456–465. https://doi.org/10.1016/j.cej.2016.08.108.

(149) Jalilian, N.; Ebrahimzadeh, H.; Asgharinezhad, A. A.; Molaei, K. Extraction and Determination of Trace Amounts of Gold(III), Palladium(II), Platinum(II) and Silver(I) with the Aid of a Magnetic Nanosorbent Made from Fe_3O_4-Decorated and Silica-Coated Graphene Oxide Modified with a Polypyrrole-Polythiophene Copolymer. *Microchim. Acta* **2017**, *184* (7), 2191–2200. https://doi.org/10.1007/s00604-017-2170-y.

(150) Fan, R.; Min, H.; Hong, X.; Yi, Q.; Liu, W.; Zhang, Q.; Luo, Z. Plant Tannin Immobilized Fe3O4@SiO2 Microspheres: A Novel and Green Magnetic Bio-Sorbent with Superior Adsorption Capacities for Gold and Palladium. *J. Hazard. Mater.* **2019**, *364*, 780–790. https://doi.org/10.1016/j.jhazmat.2018.05.061.

(151) Tenchiu, A.-C.; Ventouri, I.-K.; Ntasi, G.; Palles, D.; Kokotos, G.; Kovala-Demertzi, D.; Kostas, I. D. Synthesis of a Palladium Complex with a β-d-Glucopyranosyl-Thiosemicarbazone and Its Application in the Suzuki–Miyaura Coupling of Aryl Bromides with Phenylboronic Acid. *Inorganica Chim. Acta* **2015**, *435*, 142–146. https://doi.org/10.1016/j.ica.2015.06.019.

(152) Bera, B.; Jana, P.; Mandal, S.; Kundu, S.; Das, A.; Chattopadhyay, K.; Mondal, T. K. Fabrication of Thiosemicarbazone-Based Pd(II) Complexes: Structural Elucidations, Catalytic Activity towards Suzuki–Miyaura Coupling Reaction and Antitumor Activity against TNBC Cells. *Dalt. Trans.* **2024**, *53* (28), 11914–11927. https://doi.org/10.1039/D4DT00950A.

(153) APEX4-Software Suite for Crystallographic Programs Bruker, A. APEX4-Software Suite for Crystallographic Programs. Inc.: Madison: WI, USA 2021.

(154) Hübschle, C. B.; Sheldrick, G. M.; Dittrich, B. ShelXle: A Qt Graphical User Interface for SHELXL. *J. Appl. Crystallogr.* **2011**, *44* (6), 1281–1284. https://doi.org/10.1107/S0021889811043202.

(155) Sheldrick, G. A Short History of ShelX. *Acta Crystallogr. A.* **2008**, *64*, 112–122.

https://doi.org/10.1107/S0108767307043930.

(156) Sheldrick, G. M. Crystal Structure Refinement with SHELXL. *Acta Crystallogr. Sect. C Struct. Chem.* **2015**, *71*, 3–8. https://doi.org/10.1107/S2053229614024218.

(157) Neese, F. Software Update: The ORCA Program System–Version 5.0. *WIREs Comput. Mol. Sci.* **2022**, *12* (5), e1606. https://doi.org/https://doi.org/10.1002/wcms.1606.

(158) Neese, F. The ORCA Program System. *WIREs Comput. Mol. Sci.* **2012**, *2* (1), 73–78. https://doi.org/https://doi.org/10.1002/wcms.81.

(159) Nkungli, N. K.; Aponglen, G. A.; Tasheh, S. N.; Hassan, A. U.; Ghogomu, J. N. A Quantum Mechanics and Molecular Mechanics Study of Bis-Thiosemicarbazones with Strong Antiplasmodial Properties as Fe(III)-Selective Chelators and Inhibitors of Hemozoin Formation. *New J. Chem.* **2024**, *48* (13), 5636–5648. https://doi.org/10.1039/D3NJ05347D.

(160) Grimme, S.; Antony, J.; Ehrlich, S.; Krieg, H. A Consistent and Accurate Ab Initio Parametrization of Density Functional Dispersion Correction (DFT-D) for the 94 Elements H-Pu. *J. Chem. Phys.* **2010**, *132* (15), 154104. https://doi.org/10.1063/1.3382344.

(161) Grimme, S.; Ehrlich, S.; Goerigk, L. Effect of the Damping Function in Dispersion Corrected Density Functional Theory. *J. Comput. Chem.* **2011**, *32* (7), 1456–1465. https://doi.org/10.1002/jcc.21759.

(162) Becke, A. D. Density-Functional Exchange-Energy Approximation with Correct Asymptotic Behavior. *Phys. Rev. A* **1988**, *38* (6), 3098–3100. https://doi.org/10.1103/PhysRevA.38.3098.

(163) Perdew, J. P.; Yue, W. Accurate and Simple Density Functional for the Electronic Exchange Energy: Generalized Gradient Approximation. *Phys. Rev. B* **1986**, *33* (12), 8800–8802. https://doi.org/10.1103/PhysRevB.33.8800.

(164) Barone, V.; Cossi, M. Quantum Calculation of Molecular Energies and Energy Gradients in Solution by a Conductor Solvent Model. *J. Phys. Chem. A* **1998**, *102* (11), 1995–2001. https://doi.org/10.1021/jp9716997.

(165) Chemcraft. Chemcraft - Graphical Software for Visualization of Quantum Chemistry Computations.

APPENDIX
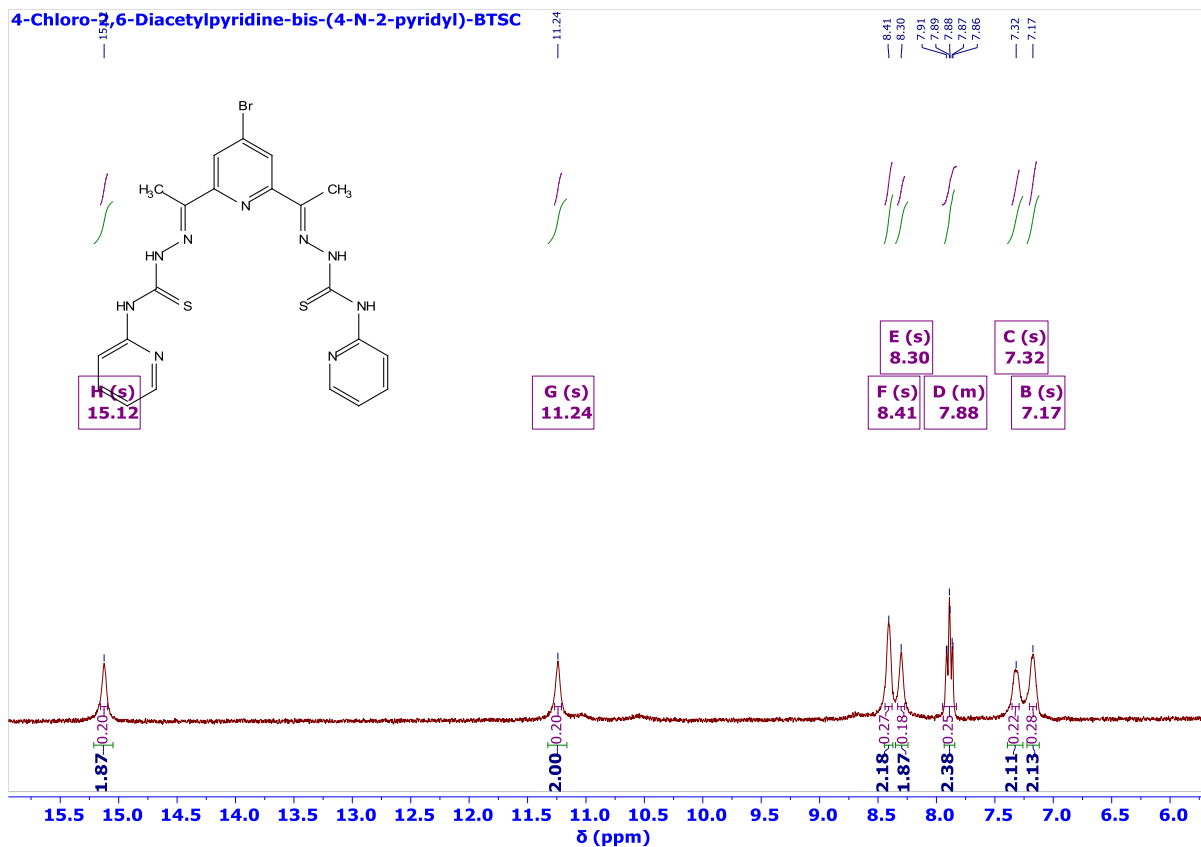
Appendix A. NMR spectra of synthesized compounds
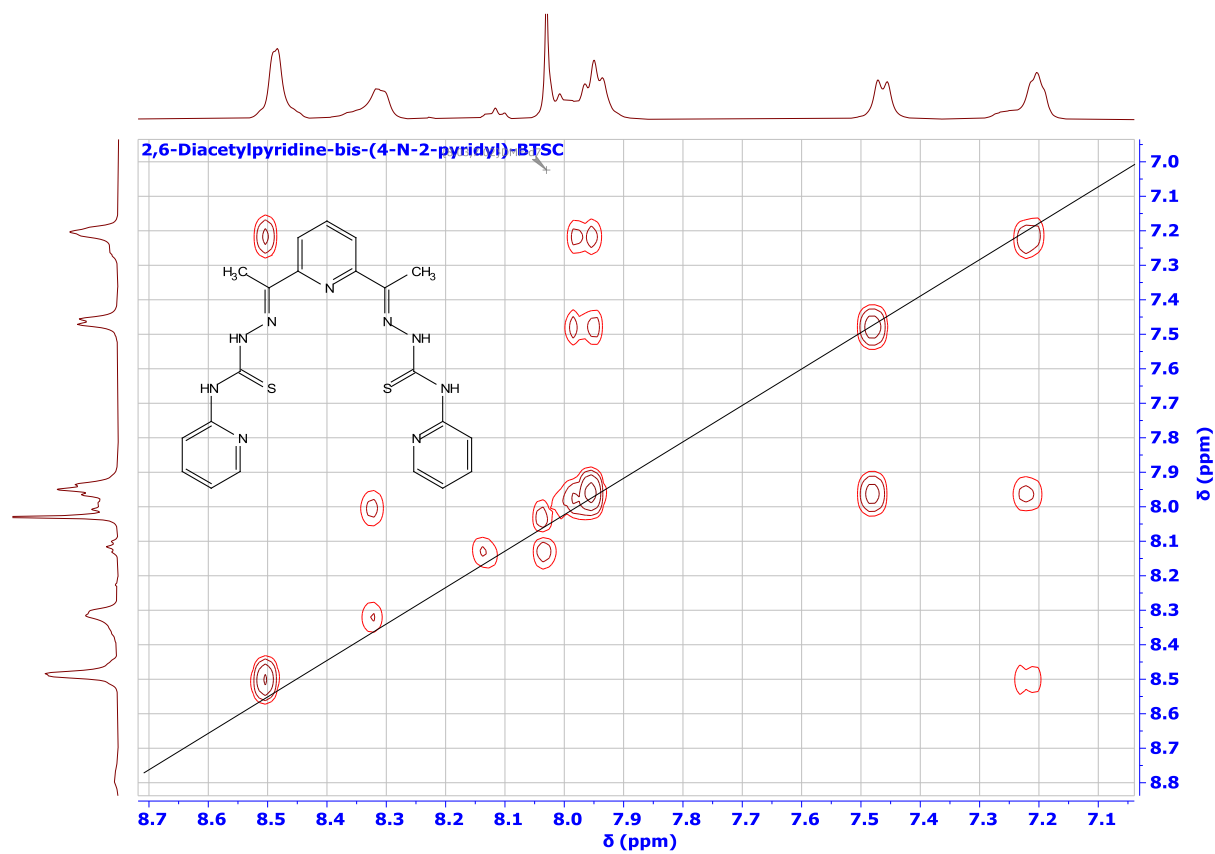
2,6-Diacetylpyridine-bis-(4-N-2-pyridyl)-BTSC

4-tert-butyl-2,6-diacetylpyridine-bis-(4-N-2-pyridyl)-TSC

| B (s) | C (s) | E (s) | H (t) |
| 15.03 | 11.16 | 8.28 | 7.14 |

| | | D (m) | F (ddd) | G (d) |
| | | 8.39 | 7.87 | 7.30 |

15.5 15.0 14.5 14.0 13.5 13.0 12.5 12.0 11.5 11.0 10.5 10.0 9.5 9.0 8.5 8.0 7.5 7.0
δ (ppm)

1.46 1.77 1.89 1.69 1.94 1.55 1.65

4-tert-butyl-2,6-diacetylpyridine-bis-(4-N-2-pyridyl)-TSC

4-thiol-2,6-diacetylpyridine-bis-(4-N-2-pyridyl)-TSC

H (s) 15.10

G (s) 11.22

E (m) 8.28
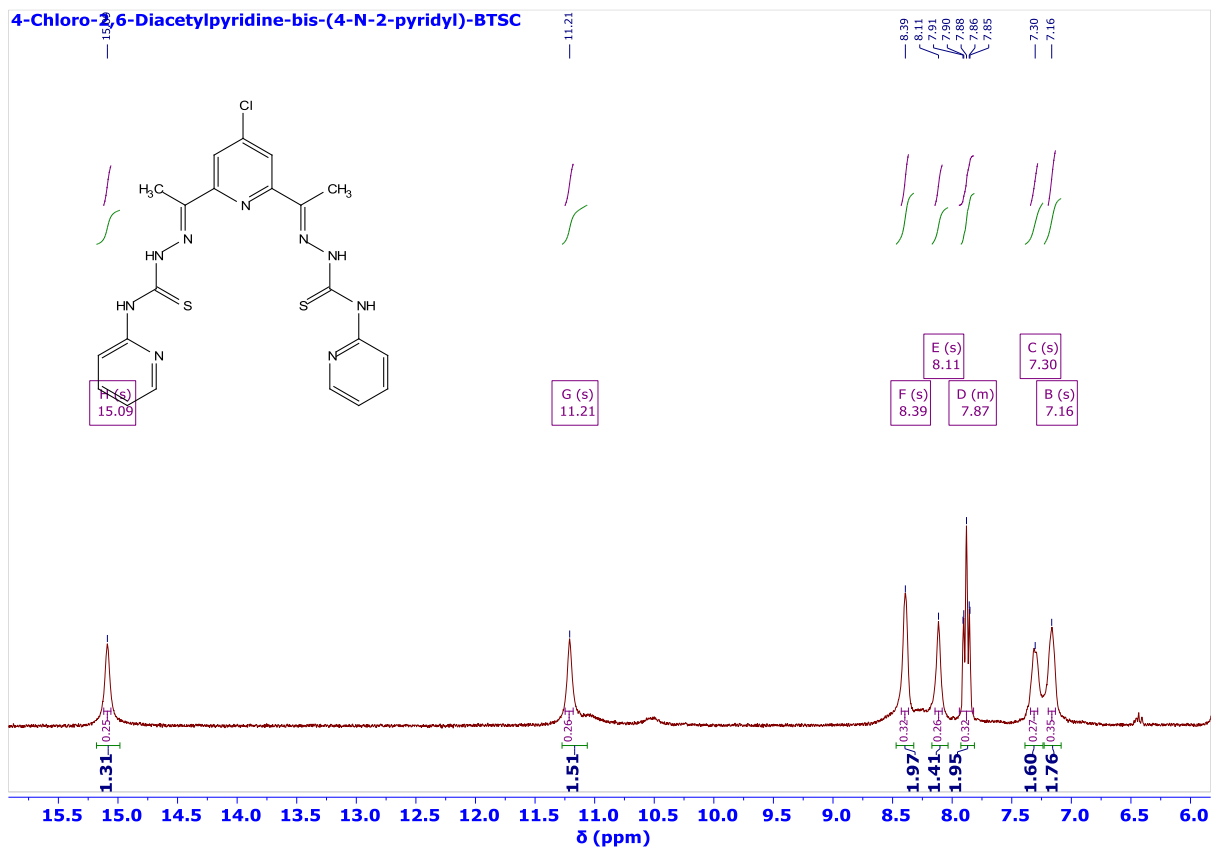
F (s) 8.40
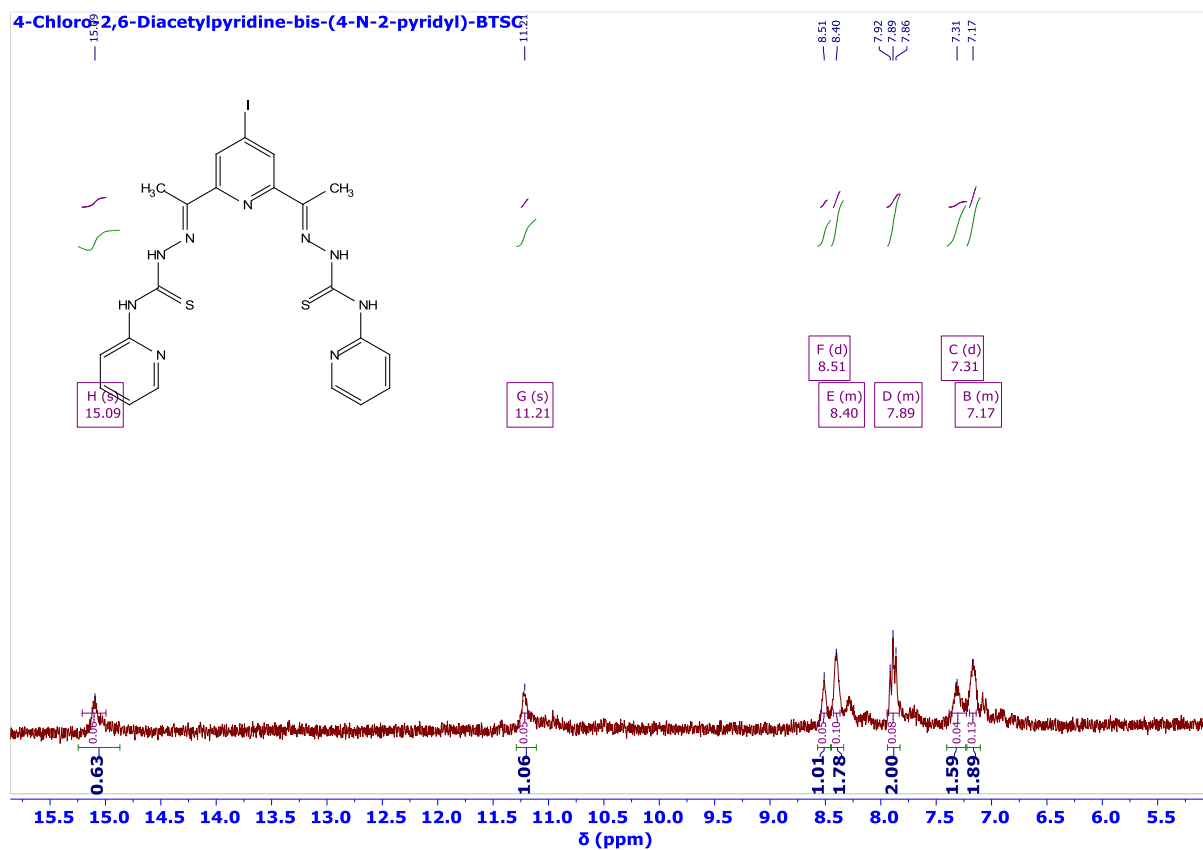
D (ddd) 7.88

C (s) 7.30

B (s) 7.17
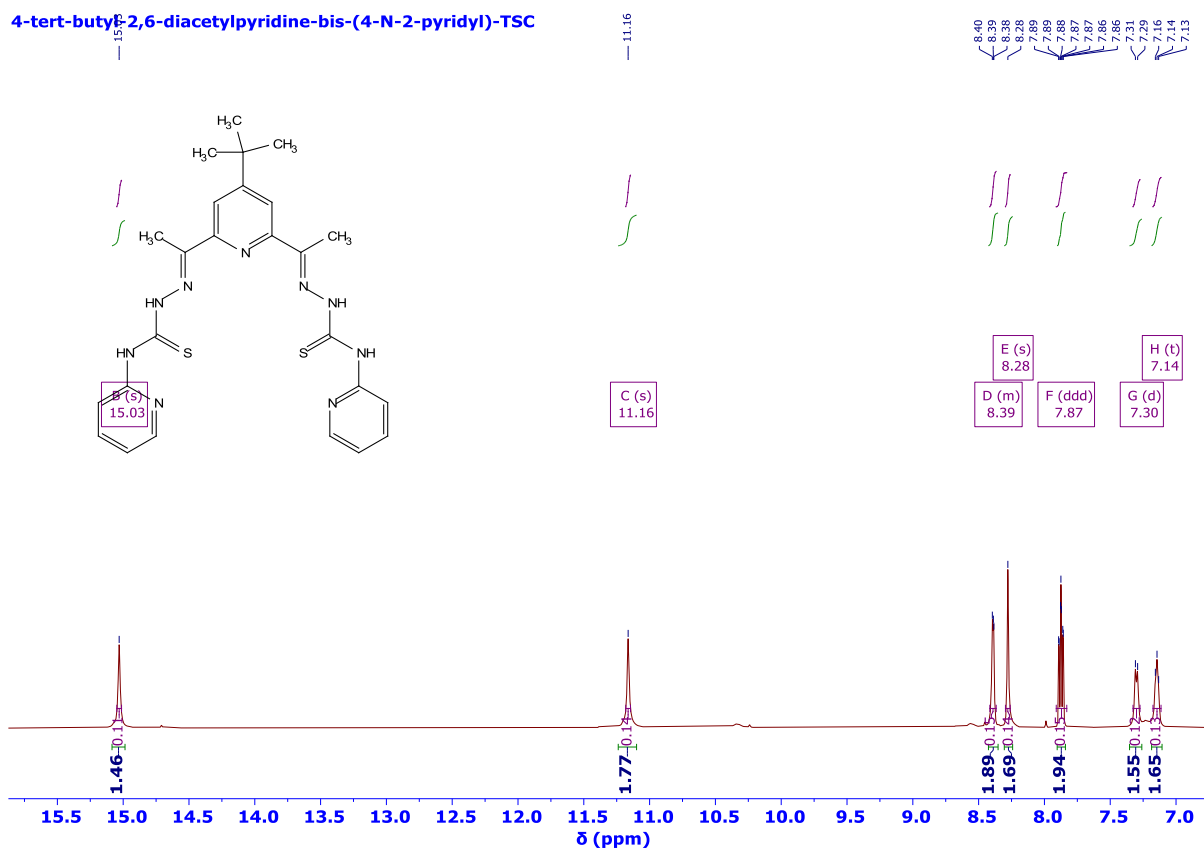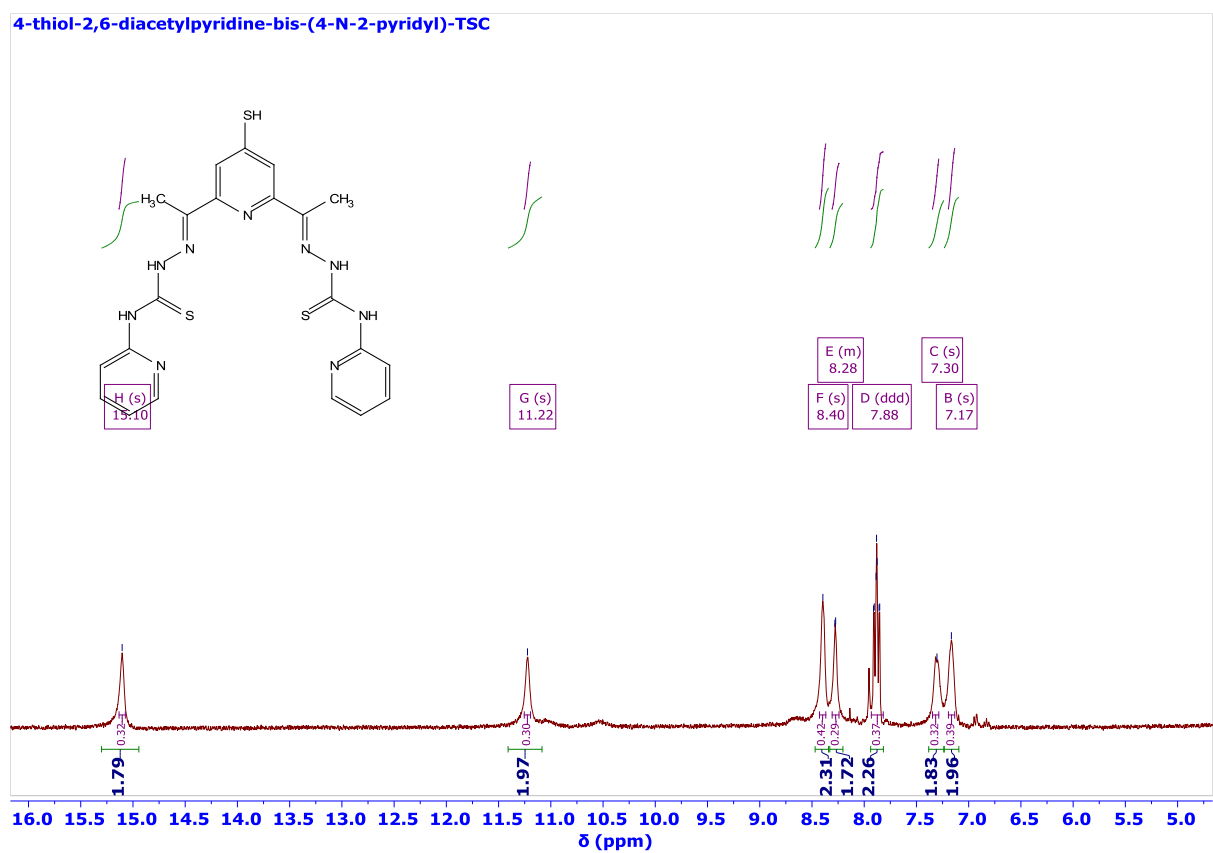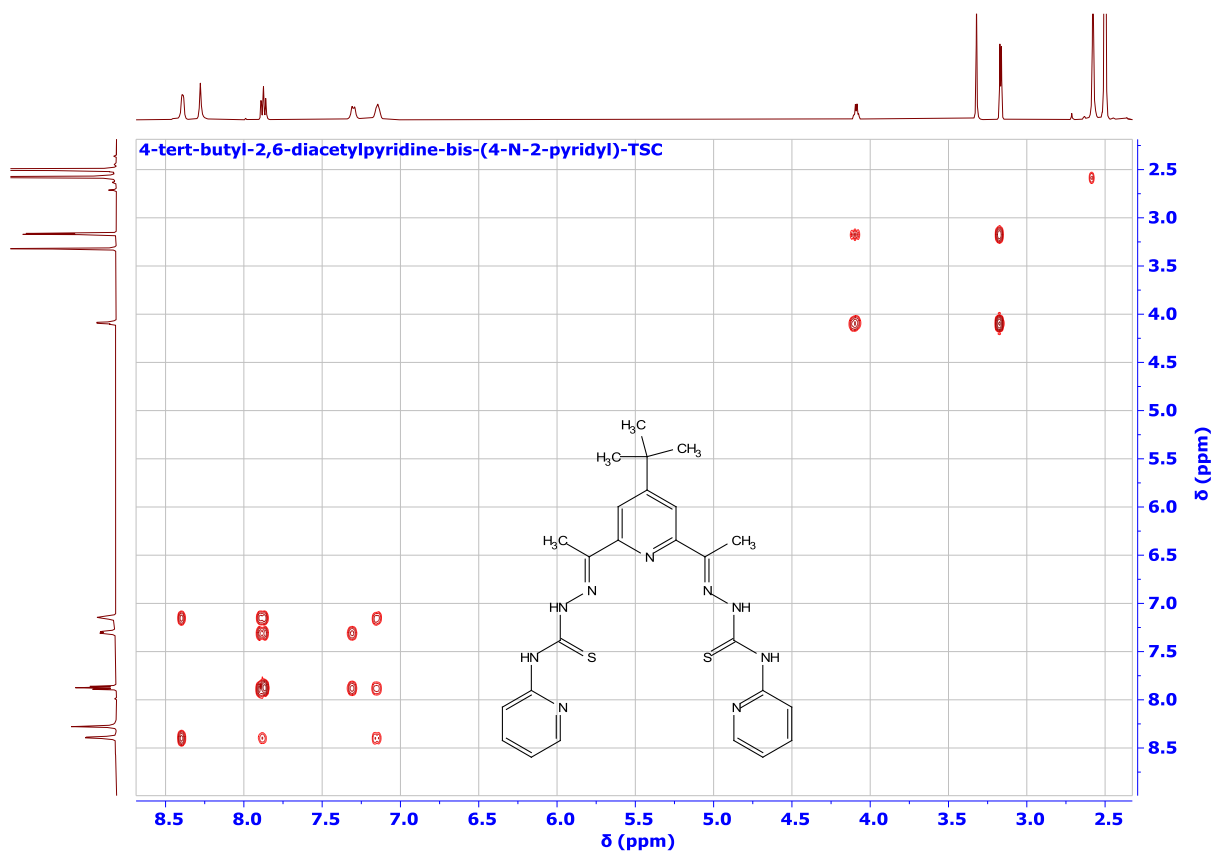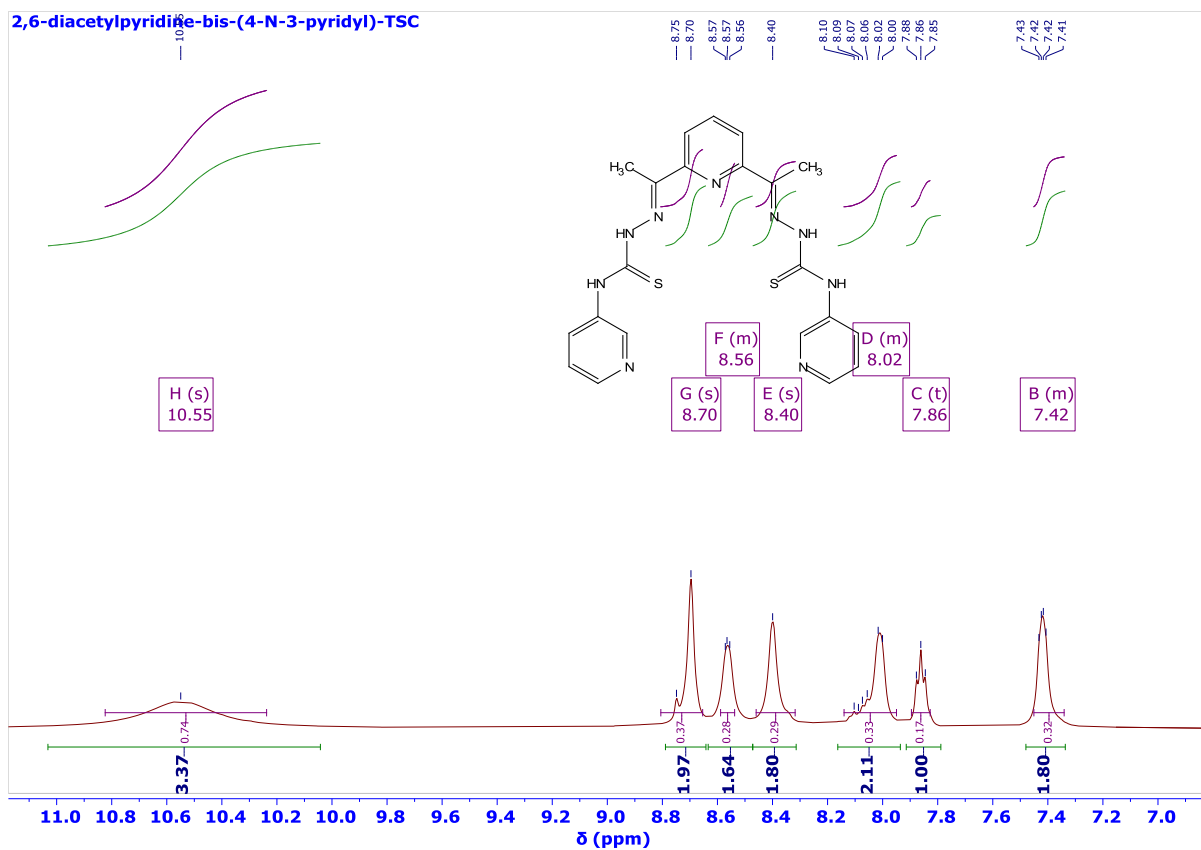
4-Chloro-2,6-Diacetylpyridine-bis-(4-N-2-pyridyl)-BTSC

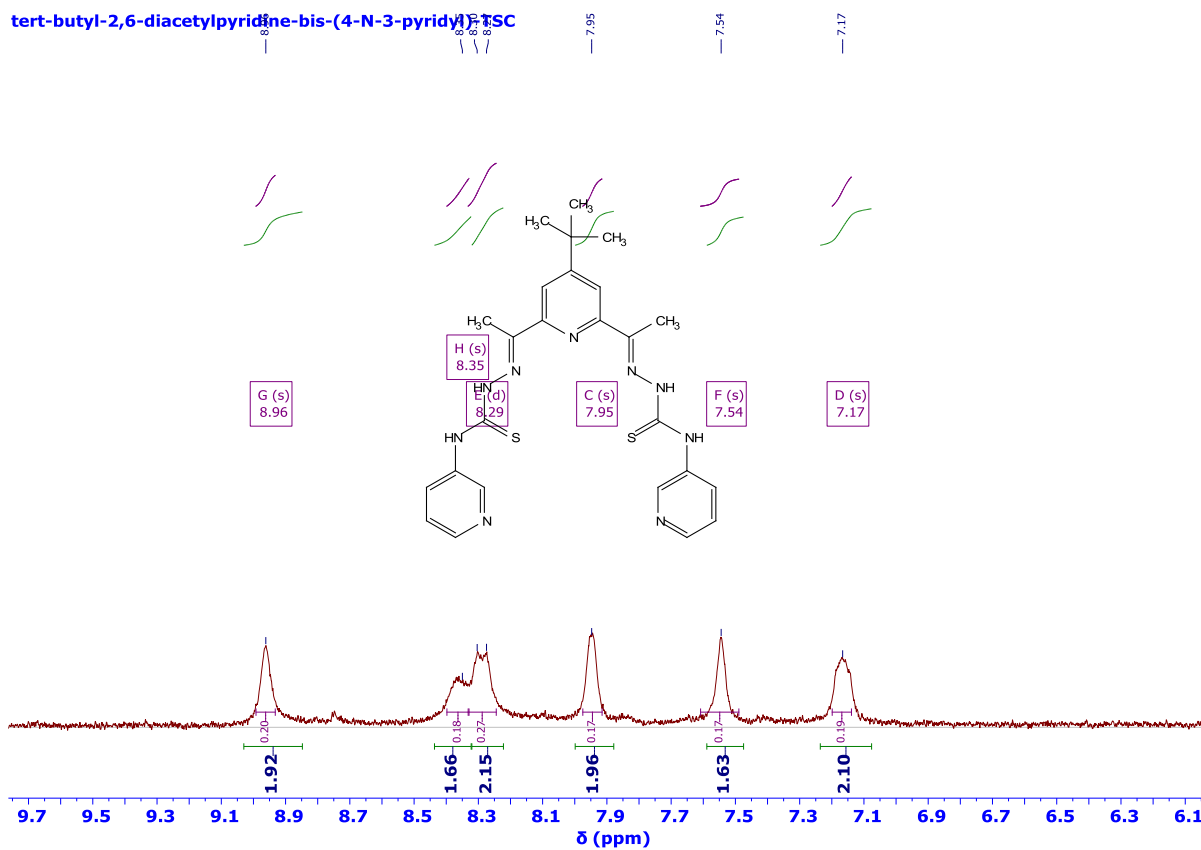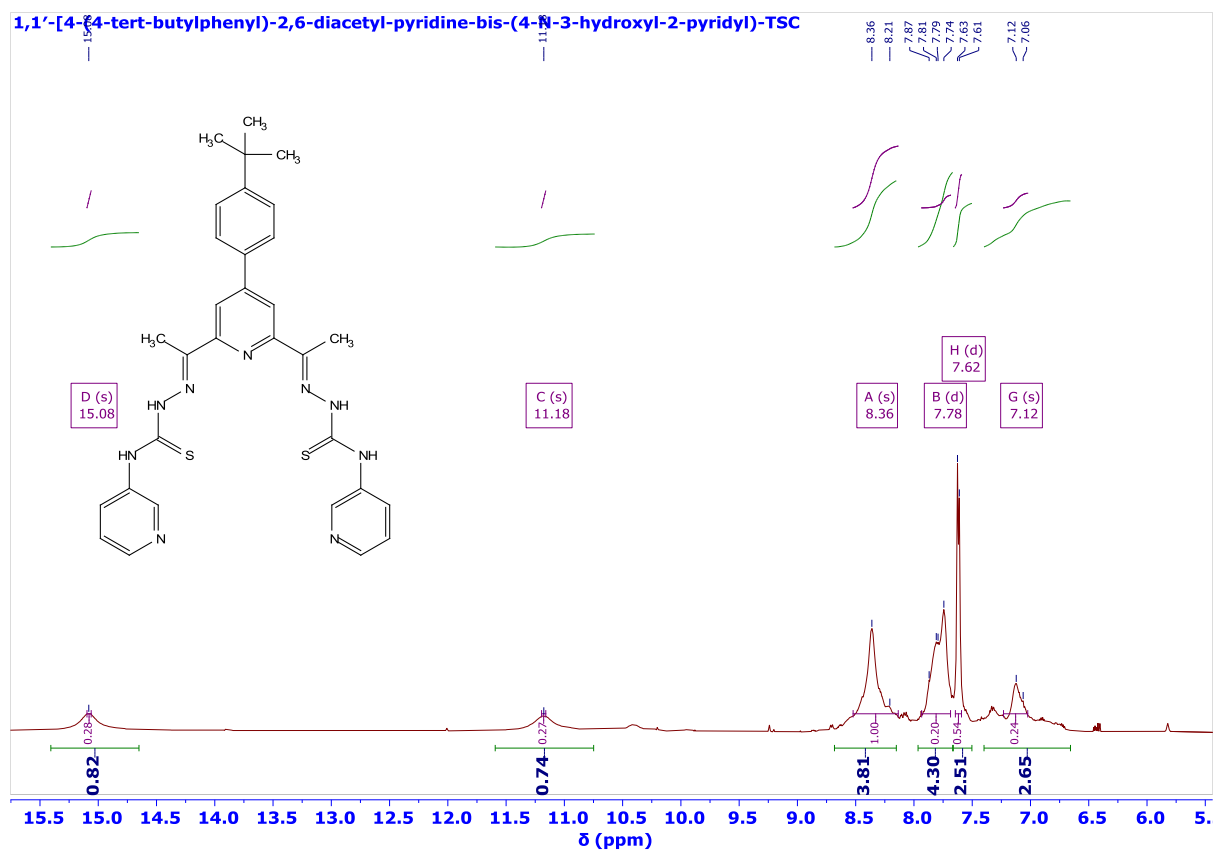**4-Chloro-2,6-Diacetylpyridine-bis-(4-N-2-pyridyl)-BTSC**
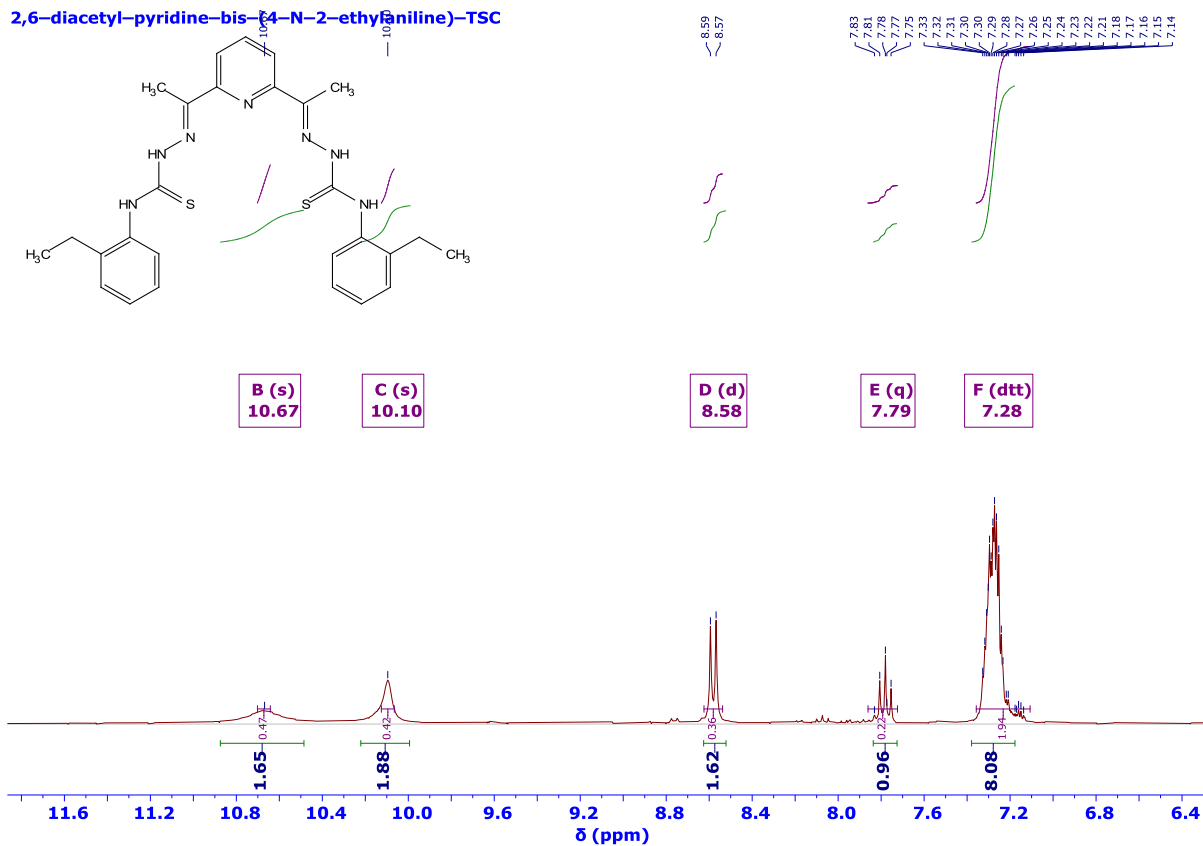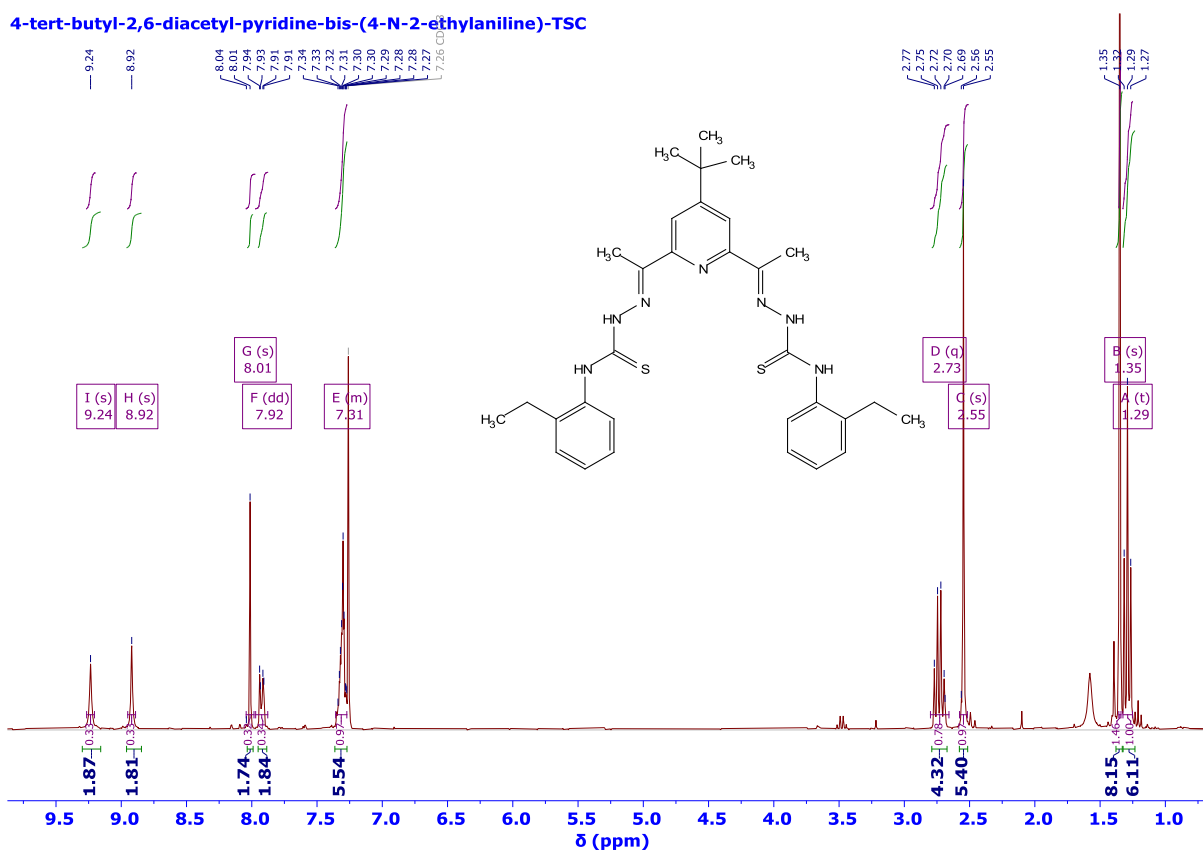
2,6-diacetylpyridine-bis-(4-N-3-pyridyl)-TSC

8.75
8.70
8.57
8.56
8.40
8.10
8.09
8.07
8.06
8.02
8.00
7.88
7.86
7.85
7.43
7.42
7.41

H₃C · · · CH₃

F (m)
8.56

D (m)
8.02

H (s)
10.55

G (s)
8.70

E (s)
8.40

C (t)
7.86

B (m)
7.42

3.37
0.74
1.97 0.37
1.64 0.28
1.80 0.29
2.11 0.33
1.00 0.17
1.80 0.32

11.0 10.8 10.6 10.4 10.2 10.0 9.8 9.6 9.4 9.2 9.0 8.8 8.6 8.4 8.2 8.0 7.8 7.6 7.4 7.2 7.0

δ (ppm)

---

tert-butyl-2,6-diacetylpyridine-bis-(4-N-3-pyridyl)-TSC

7.95
7.54
7.17

H₃C · · · CH₃

H₃C · CH₃

H (s)
8.35

G (s)
8.96

E (d)
8.29

C (s)
7.95

F (s)
7.54

D (s)
7.17

1.92 0.20
1.66 0.18
2.15 0.27
1.96 0.17
1.63 0.17
2.10 0.19

9.7 9.5 9.3 9.1 8.9 8.7 8.5 8.3 8.1 7.9 7.7 7.5 7.3 7.1 6.9 6.7 6.5 6.3 6.1

δ (ppm)

2,6–diacetyl–pyridine–bis–(4–N–2–ethylaniline)–TSC

B (s)	C (s)	D (d)	E (q)	F (dtt)
10.67	10.10	8.58	7.79	7.28

4-tert-butyl-2,6-diacetyl-pyridine-bis-(4-N-2-ethylaniline)-TSC

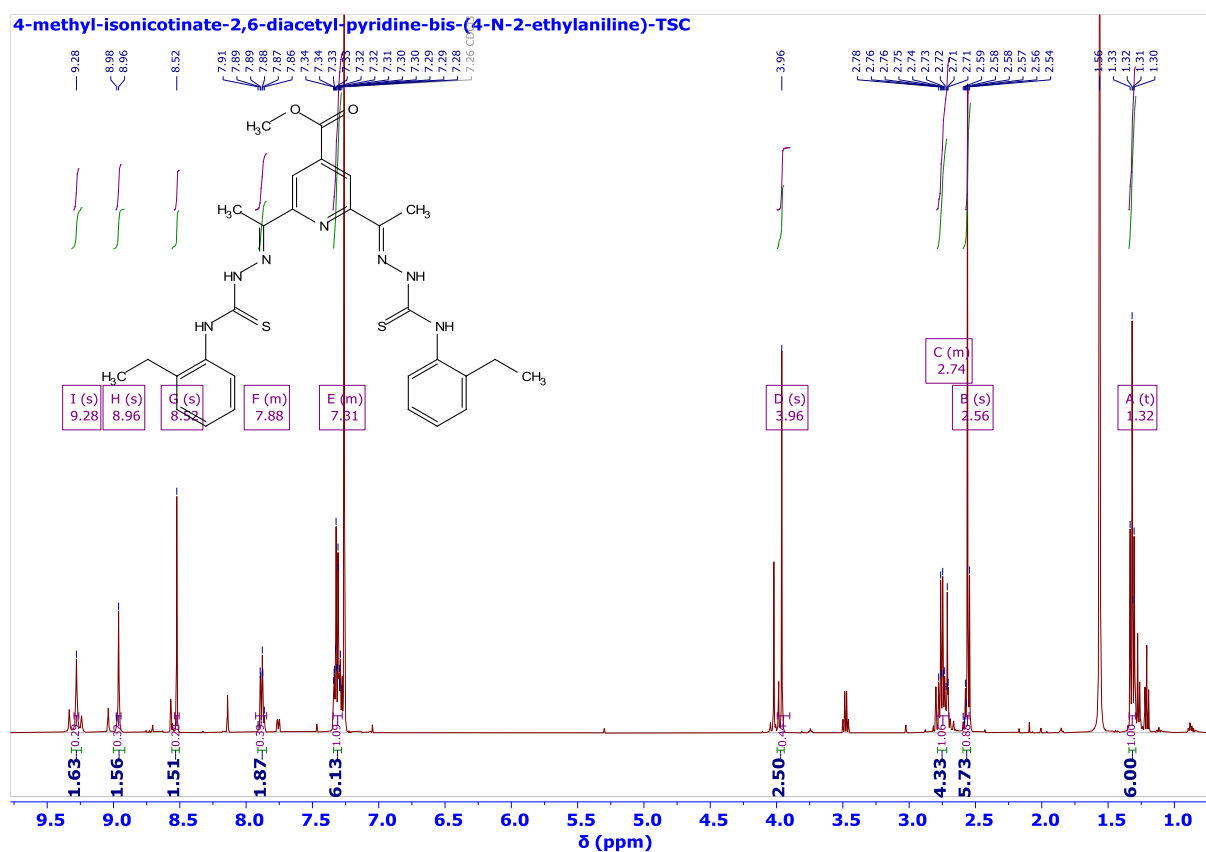| I (s)	H (s)	G (s)	F (dd)	E (m)	D (q)	C (s)	B (s)	A (t)
9.24	8.92	8.01	7.92	7.31	2.73	2.55	1.35	1.29

4-methyl-isonicotinate-2,6-diacetyl-pyridine-bis-(4-N-2-ethylaniline)-TSC

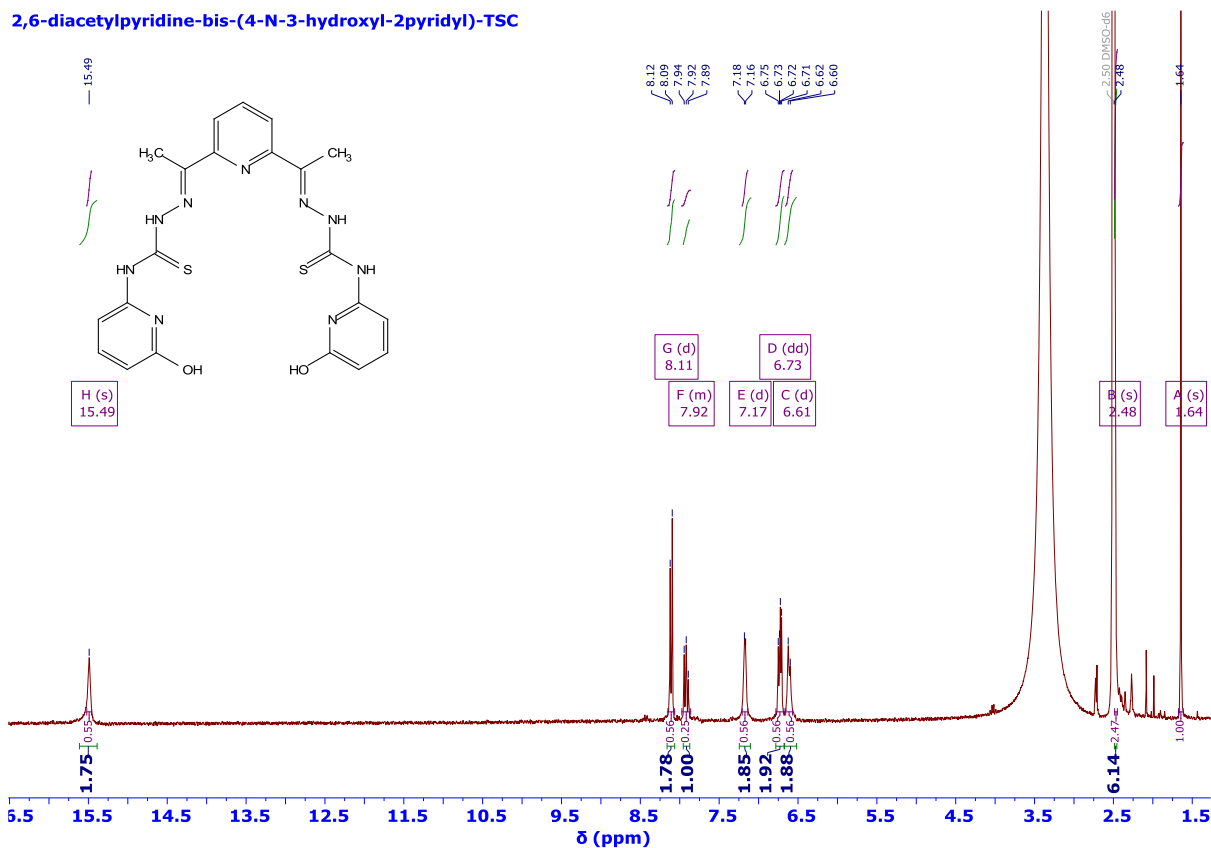:ylic acid-bis-(4-N-2-ethylaniline)-TSC

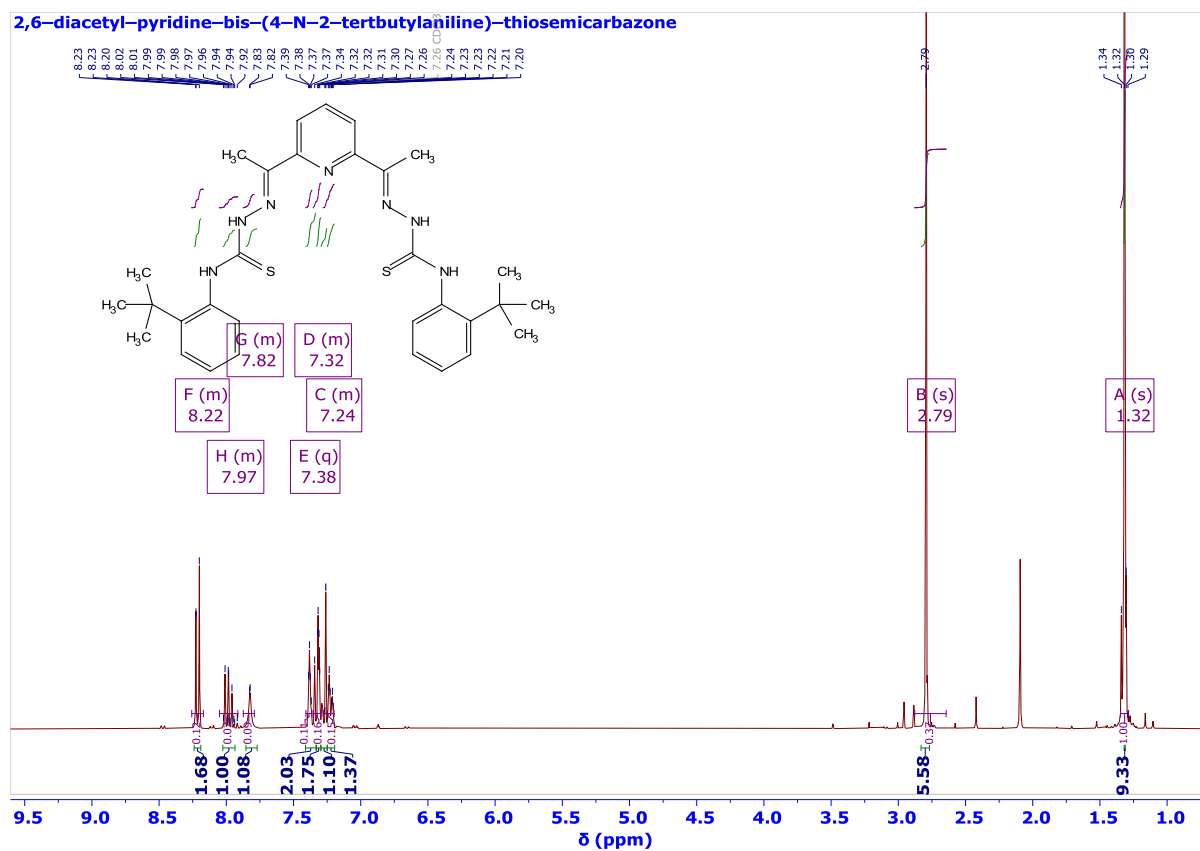2,6-diacetyl-pyridine-4-carboxylic acid-bis-(4-N-2-ethylaniline)-TSC

10.70　10.18　8.75　7.39 7.37 7.36 7.33 7.32 7.31 7.30 7.28 7.27 7.26 7.25 7.24 7.21　2.70 2.69 2.67 2.64 2.62 2.59 2.57 2.55 2.51 2.50 DMSO-d6　1.26 1.24 1.23 1.22 1.21 1.20 1.18 1.16 1.15 1.14 1.10

G (s) 10.70　F (s) 10.18　E (s) 8.75　D (m) 7.30　C (m) 2.63　B (s) 2.55　A (m) 1.19

1.94　1.95　1.78　6.09　1.71　4.34　6.00　6.39

δ (ppm)

11.5 11.0 10.5 10.0 9.5 9.0 8.5 8.0 7.5 7.0 6.5 6.0 5.5 5.0 4.5 4.0 3.5 3.0 2.5 2.0 1.5 1.0 0.5

2,6-diacetylpyridine-bis-(4-N-3-hydroxyl-2pyridyl)-TSC

15.49　8.12 8.09 7.94 7.92 7.89　7.18 7.16 6.75 6.73 6.72 6.71 6.62 6.60　2.50 DMSO-d6 2.48　1.64

H (s) 15.49　G (d) 8.11　F (m) 7.92　E (d) 7.17　D (dd) 6.73　C (d) 6.61　B (s) 2.48　A (s) 1.64

1.75　1.78　1.00　1.85　1.92　1.88　6.14　1.00

δ (ppm)

5.5 15.5 14.5 13.5 12.5 11.5 10.5 9.5 8.5 7.5 6.5 5.5 4.5 3.5 2.5 1.5

2,6–diacetyl–pyridine–bis–(4–N–2–tertbutylaniline)–thiosemicarbazone

G (m) 7.82

D (m) 7.32

F (m) 8.22

C (m) 7.24

H (m) 7.97

E (q) 7.38
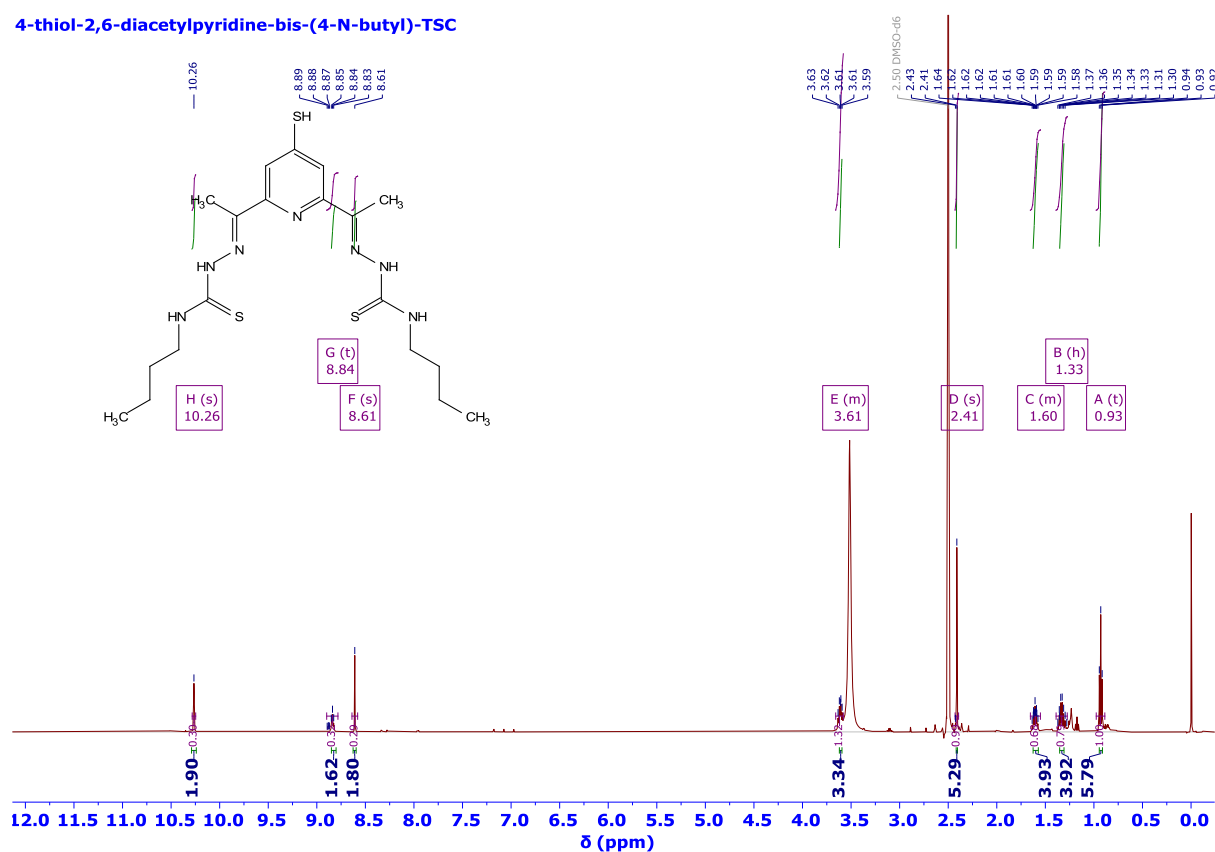
B (s) 2.79

A (s) 1.32

4-tert-butyl-2,6-diacetylpyridine-bis-(4-N-butyl)-TSC
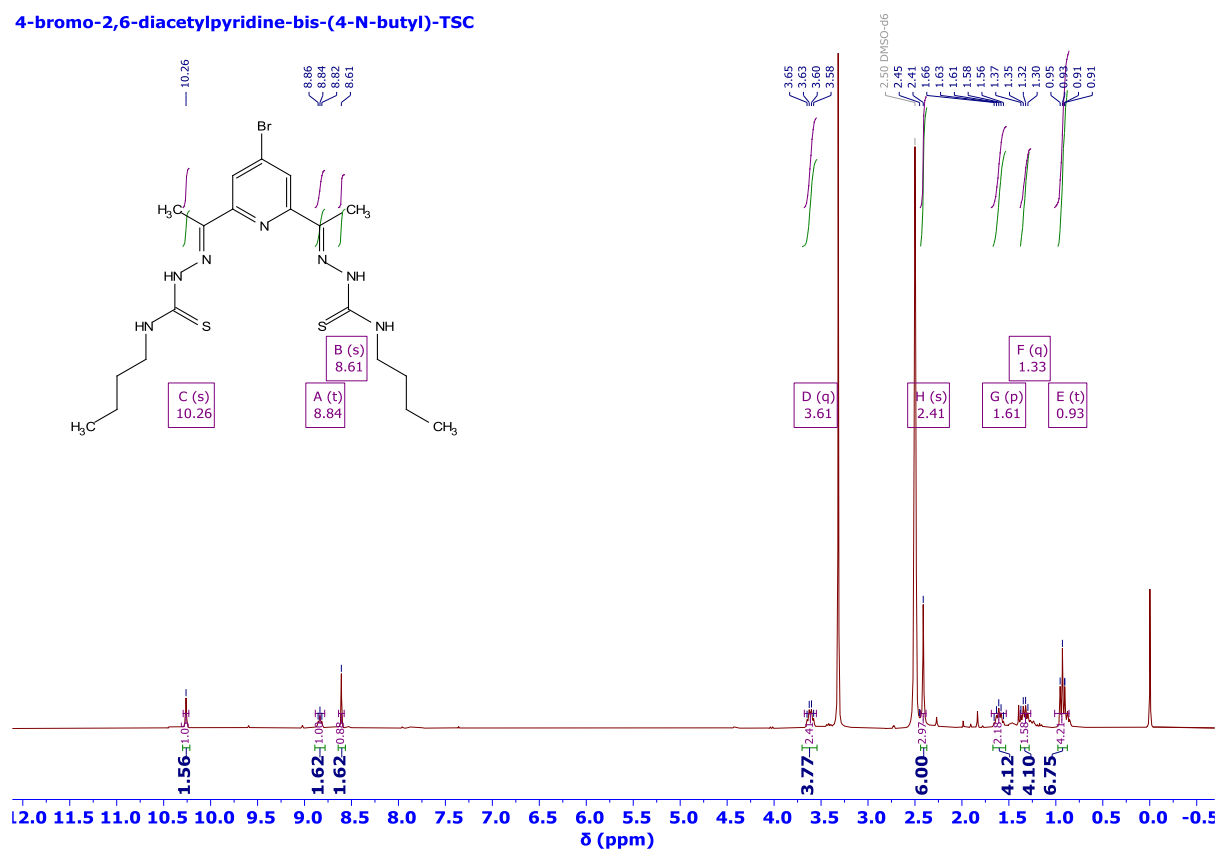

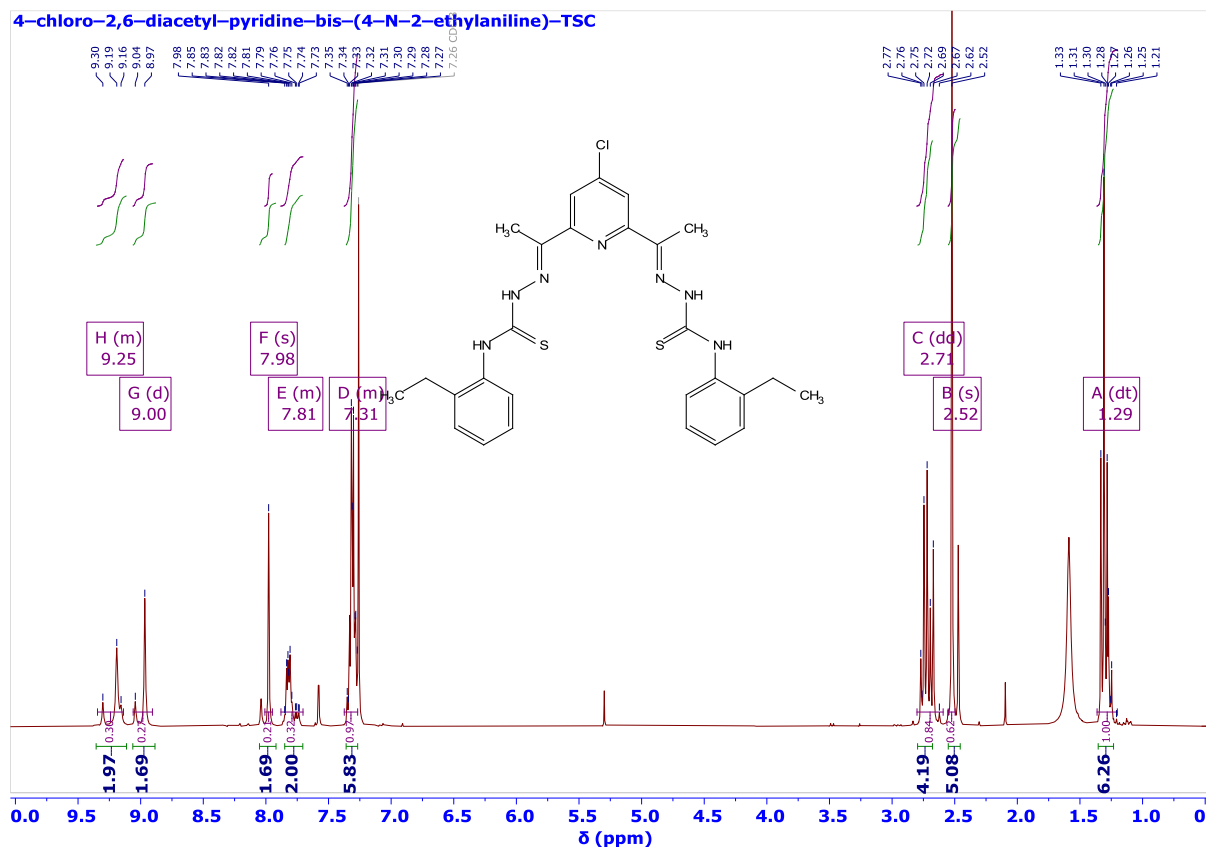**4-(tert-butyl)-2,6-diacetylpyridine-bis-(4-N-butyl)-TSC**
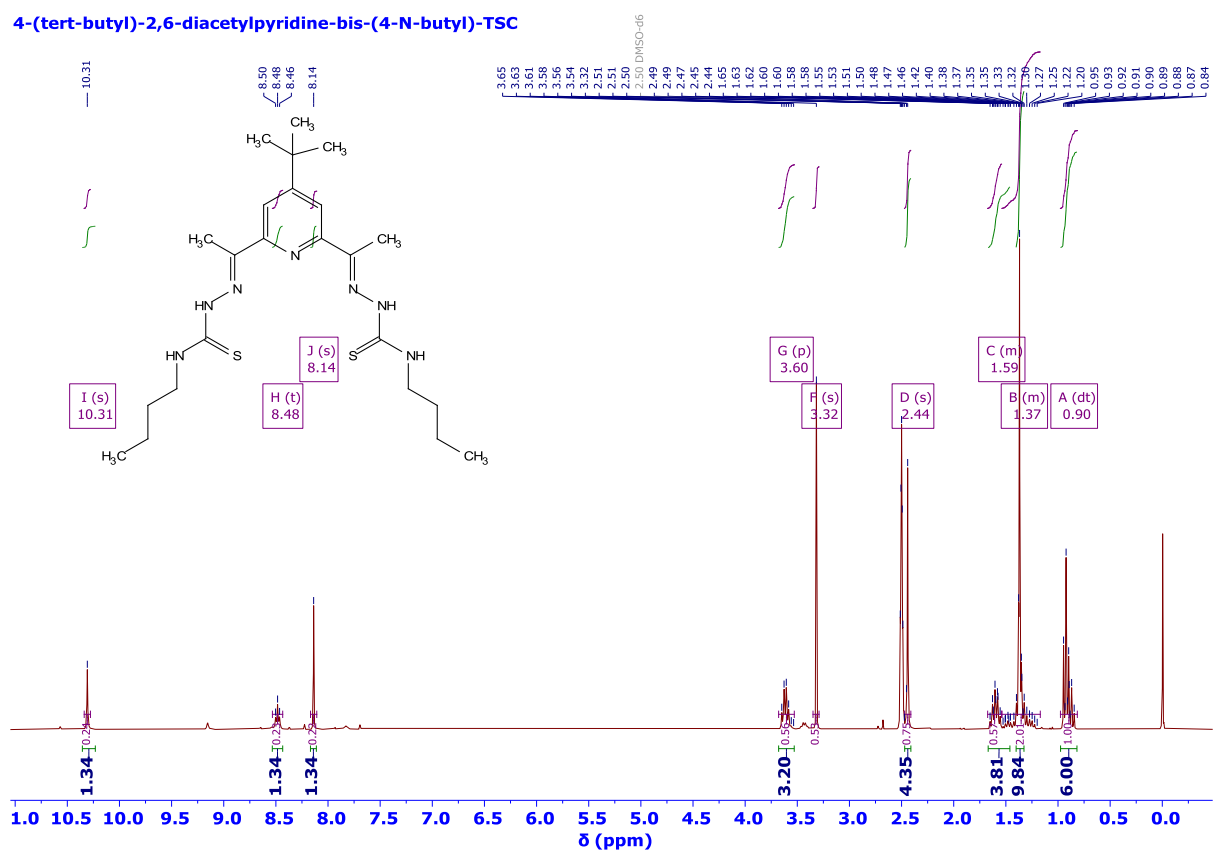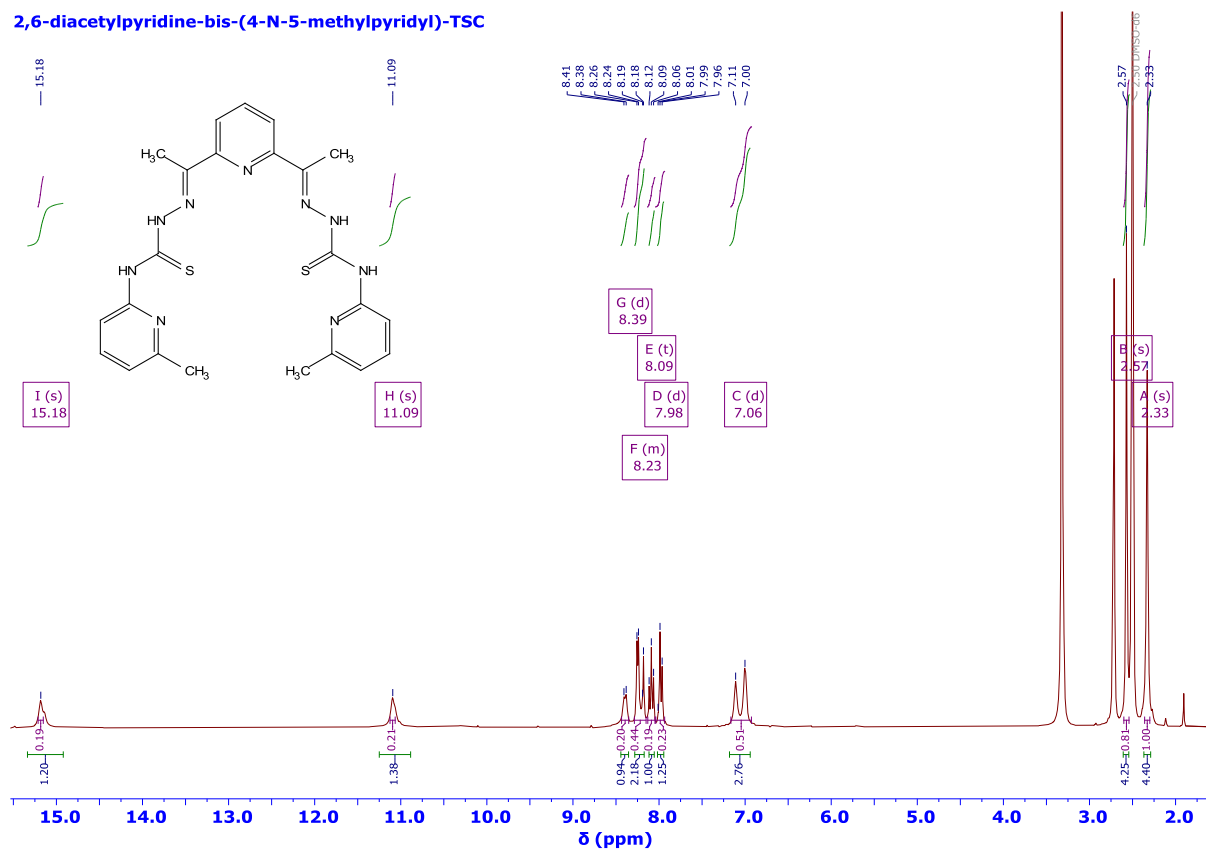
4-thiol-2,6-diacetylpyridine-bis-(4-N-butyl)-TSC
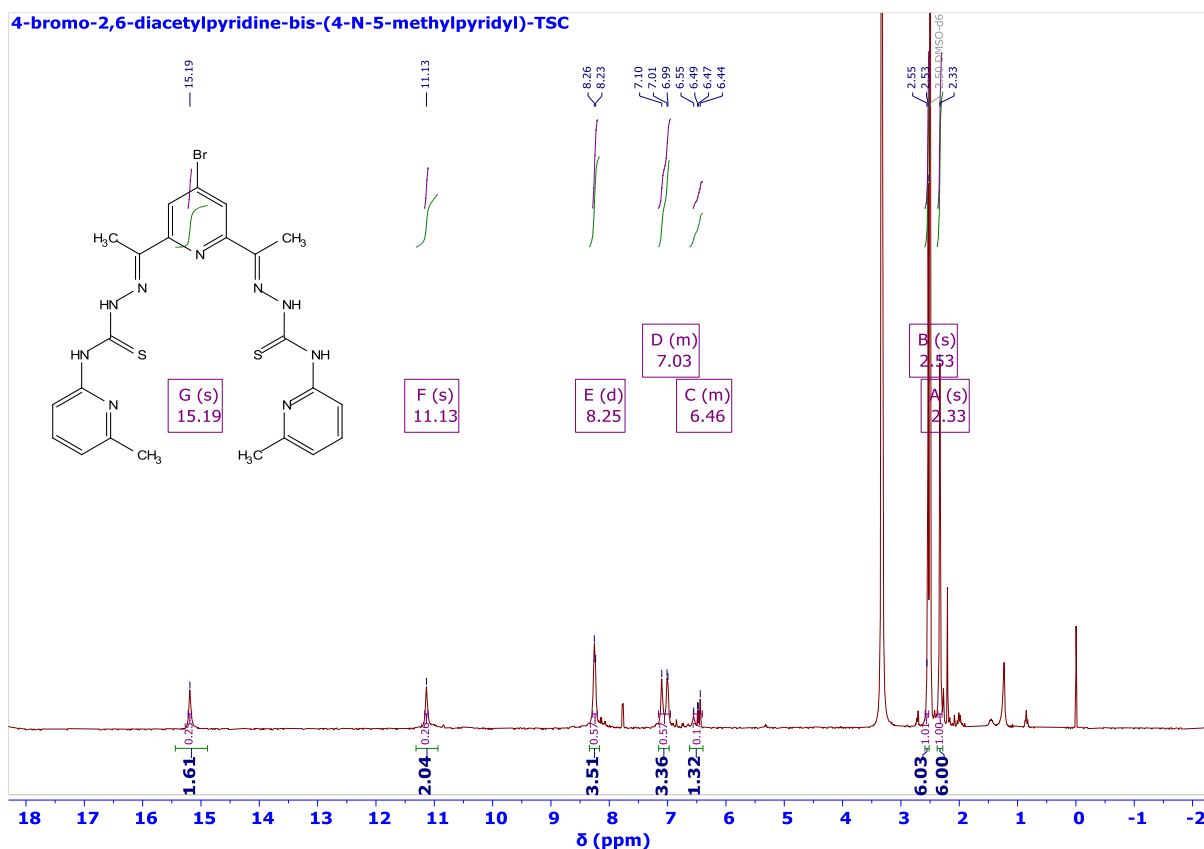

4-bromo-2,6-diacetylpyridine-bis-(4-N-butyl)-TSC

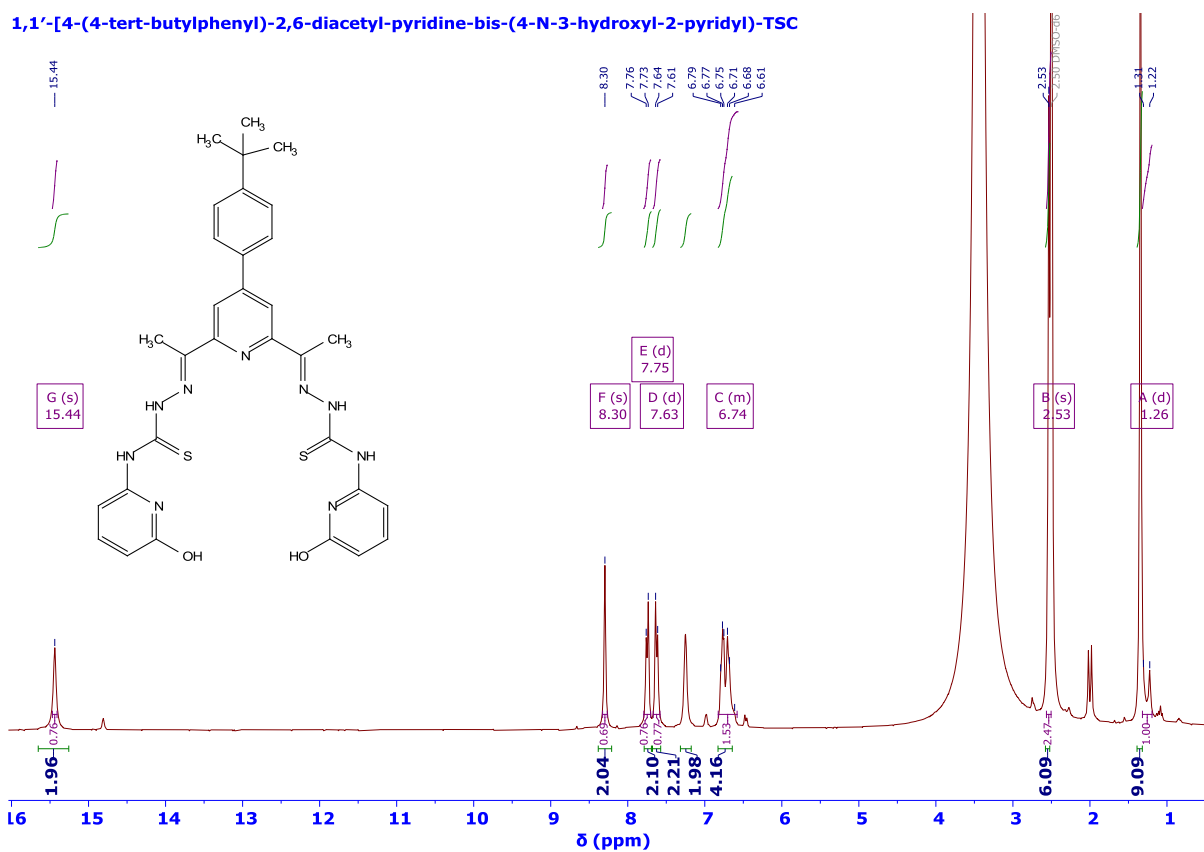**4–chloro–2,6–diacetyl–pyridine–bis–(4–N–2–ethylaniline)–TSC**

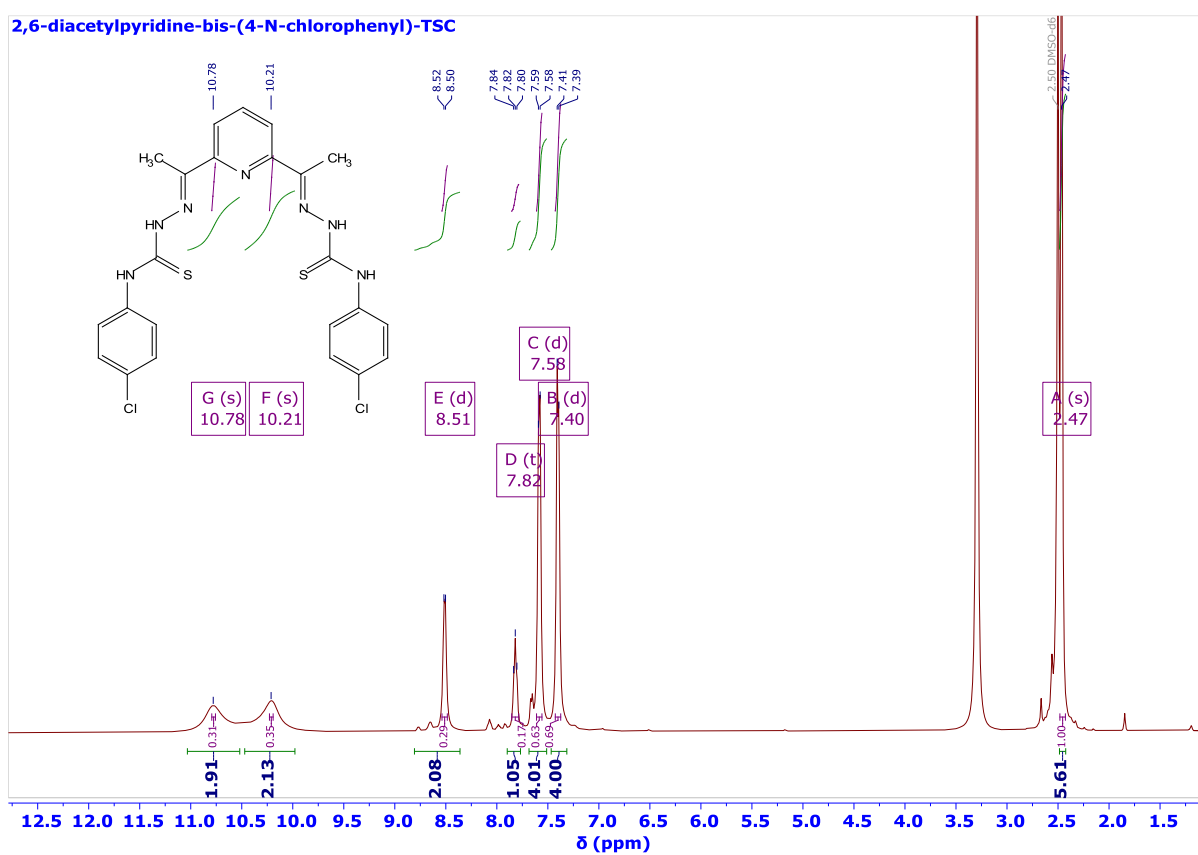**2,6-diacetylpyridine-bis-(4-N-5-methylpyridyl)-TSC**

4-bromo-2,6-diacetylpyridine-bis-(4-N-5-methylpyridyl)-TSC
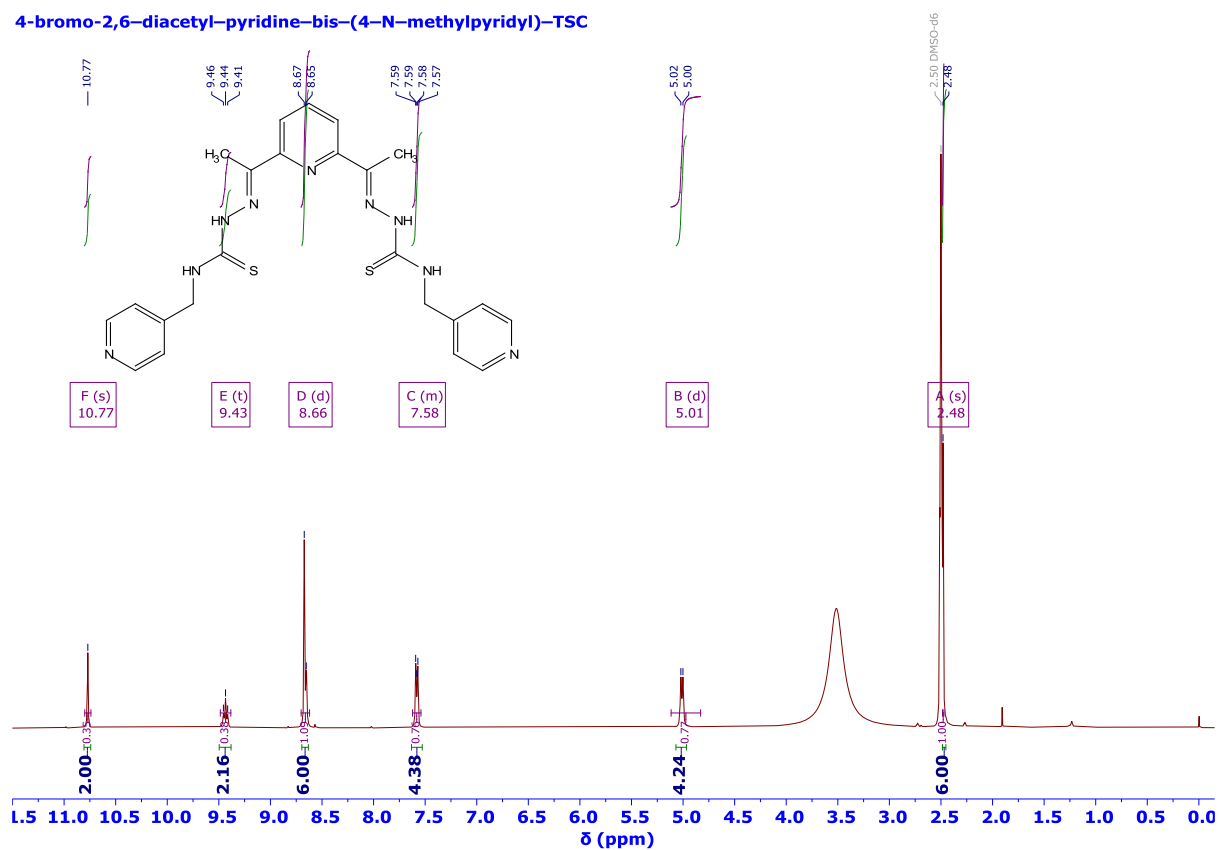

1,1'-[4-(4-tert-butylphenyl)-2,6-diacetyl-pyridine-bis-(4-N-3-hydroxyl-2-pyridyl)-TSC
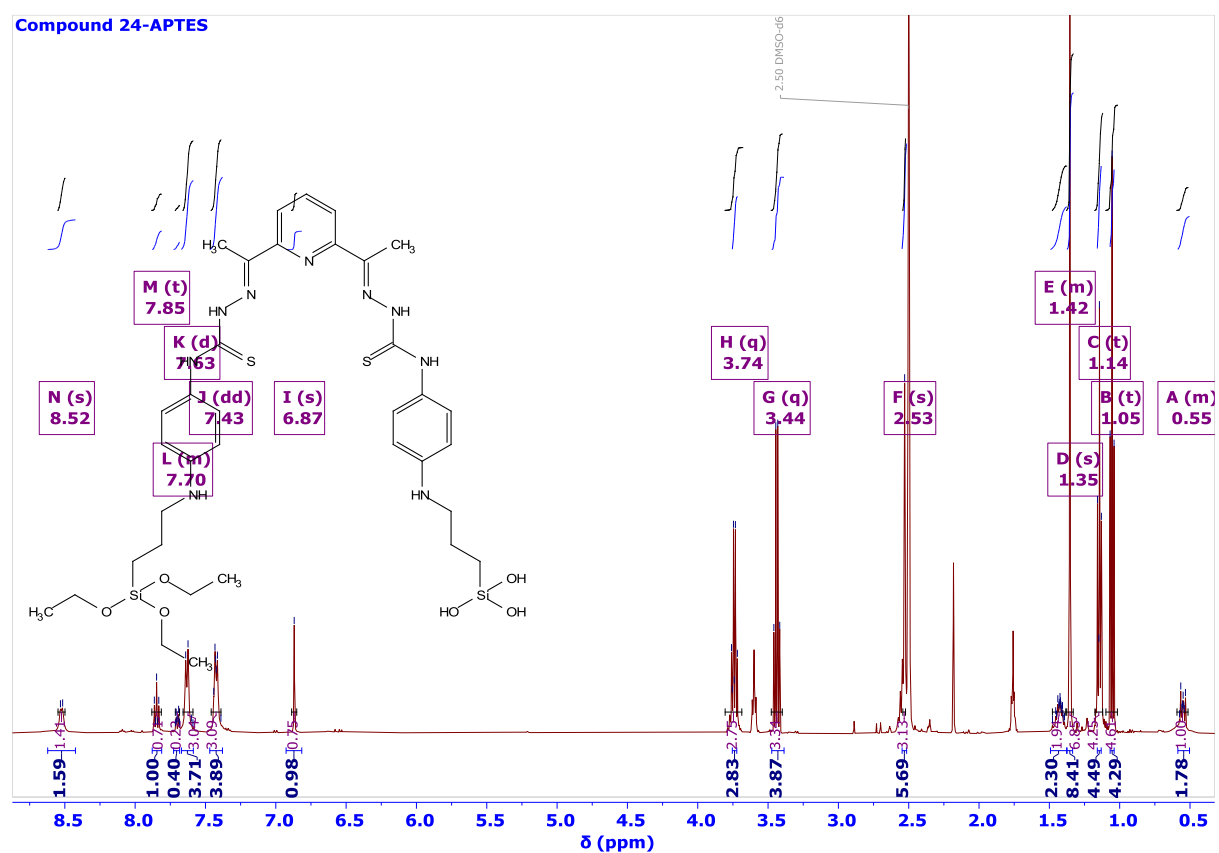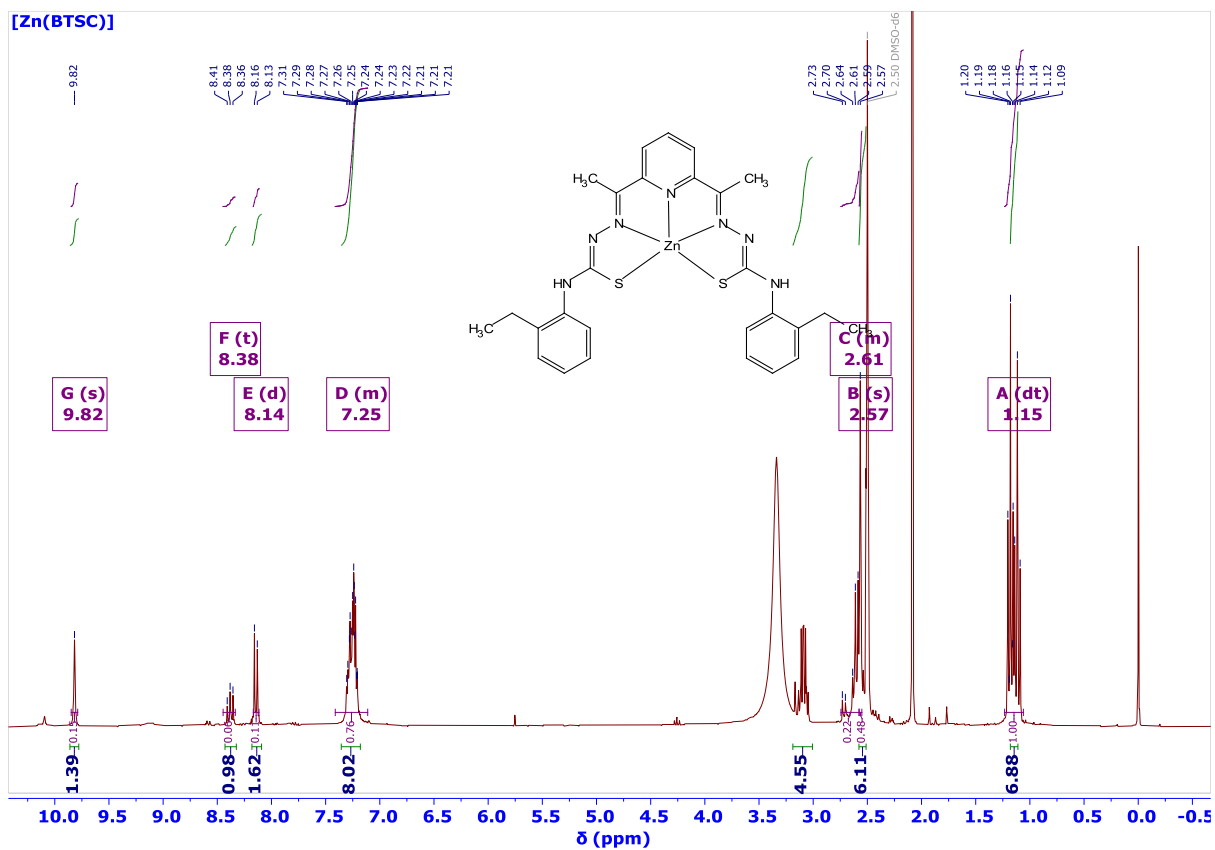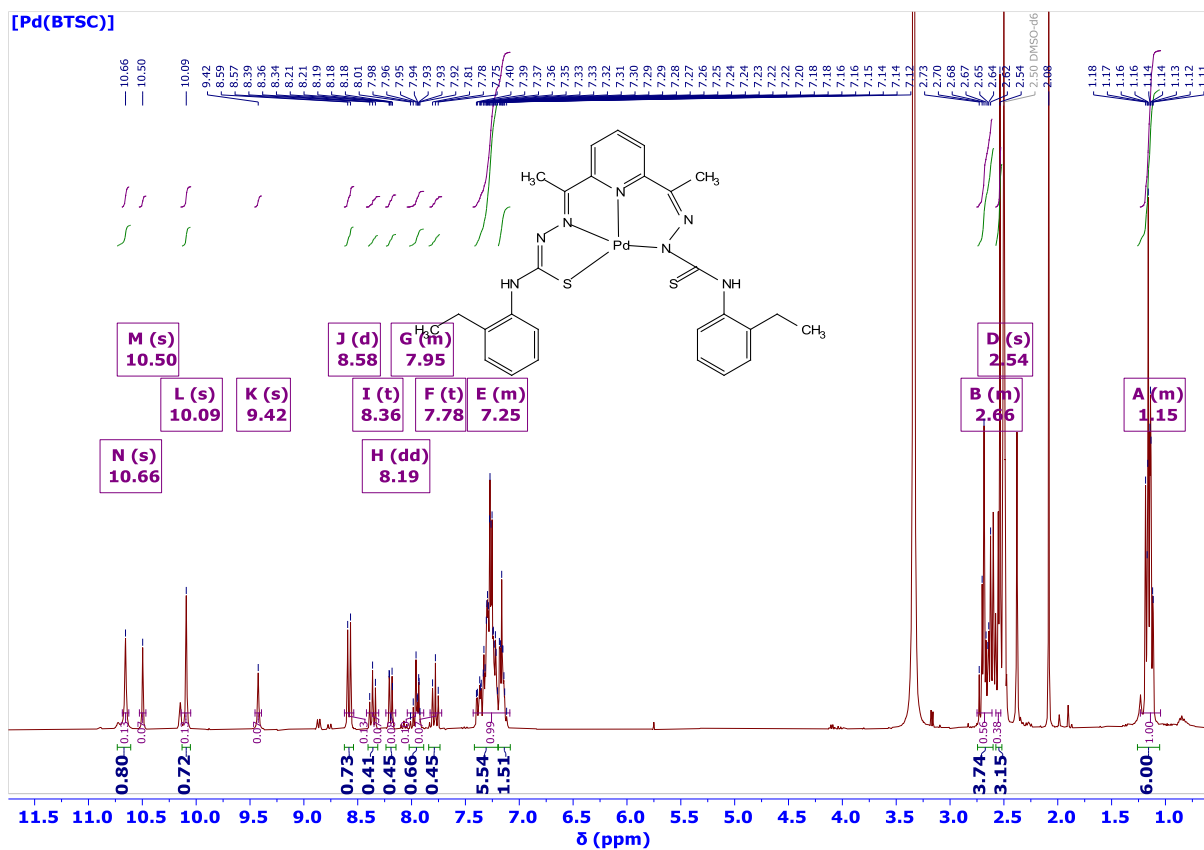
2,6-diacetylpyridine-bis-(4-N-chlorophenyl)-TSC

Label	Type	δ (ppm)
G	(s)	10.78
F	(s)	10.21
E	(d)	8.51
D	(t)	7.82
C	(d)	7.58
B	(d)	7.40
A	(s)	2.47

10.77

9.46
9.44
9.41

8.67
8.65

7.59
7.59
7.58
7.57

5.02
5.00

2.50 DMSO-d6
2.48

F (s)	E (t)	D (d)	C (m)	B (d)	A (s)
10.77	9.43	8.66	7.58	5.01	2.48

H₃C | CH₃
HN | NH
NH | NH
S | S

2.00   2.16   6.00   4.38   4.24   6.00

δ (ppm)

Compound 24-APTES

2.50 DMSO-d6

N (s)	M (t)	K (d)	L (m)	J (dd)	I (s)	H (q)	G (q)	F (s)	E (m)	D (s)	C (t)	B (t)	A (m)
8.52	7.85	7.63	7.70	7.43	6.87	3.74	3.44	2.53	1.42	1.35	1.14	1.05	0.55

H₃C | CH₃
HN | NH
S | S
NH | NH

H₃C—O—Si—O—CH₃
O
CH₃

OH
HO—Si—OH

1.59   1.00   0.40   3.71   3.89   0.98   2.83   3.87   5.69   2.30   8.41   4.49   4.29   1.78

δ (ppm)

[Pd(BTSC)]

M (s)
10.50

L (s)
10.09

K (s)
9.42

N (s)
10.66

J (d)
8.58

I (t)
8.36

H (dd)
8.19

G (m)
7.95

F (t)
7.78

E (m)
7.25

D (s)
2.54

B (m)
2.66

A (m)
1.15

[Zn(BTSC)]

G (s)
9.82

F (t)
8.38

E (d)
8.14

D (m)
7.25

C (m)
2.61

B (s)
2.57

A (dt)
1.15

	[Pd(BTSC)]
Empirical formula	$C_{25}H_{27}N_9S_2Pd$
Formula weight (g/mol)	624.07
Crystal system	Triclinic
Space group	*P-1*
a (Å)	9.5573(15)
b (Å)	11.6598(17)
c (Å)	15.040(2)
α (°)	107.717(5)
β (°)	98.002(5)
γ (°)	97.232(5)
Volume (Å^3) / Z	1555.6(4) / 2
ϱ_{calc} (g/cm^{-3})	1.332
μ (mm^{-1})	0.759
Limiting indices	$-11 \le h \le 11$
	$-14 \le k \le 14$
	$-18 \le l \le 18$
Reflection collected	70055
Independent reflections / R_{int}	6353 / 0.1825
Data/restraints/parameters	6353/0/339
goof on F^2	1.793
R_1, wR_2 [$I > 2\sigma(I)$]	0.1491
R_1, wR_2 (all data)	0.4403
Residual electrons and holes (e Å^{-3})	3.36/-1.44
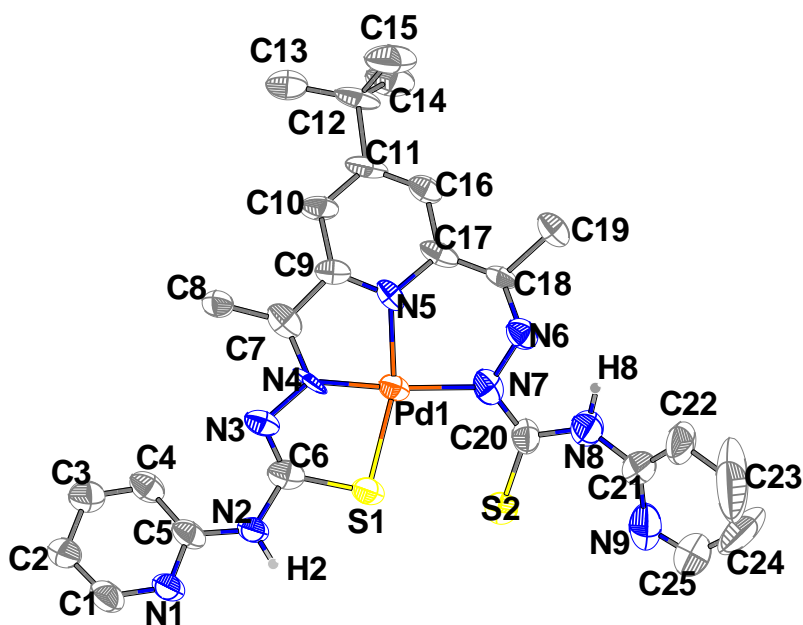
	(BTSC)
Empirical formula	$C_{29}H_{32}N_7S_2$
Formula weight (g/mol)	574.73
Crystal system	Orthorhombic
Space group	$P2_12_12_1$
a (Å)	6.7174(5)
b (Å)	18.2333(16)
c (Å)	23.8038(19)
α (°)	90
β (°)	90
γ (°)	90
Volume (Å³) / Z	2915.5(4) / 4
ϱ_{calc} (g/cm⁻³)	1.309
μ (mm⁻¹)	0.222
Limiting indices	$-8 \leq h \leq 8$
	$-23 \leq k \leq 23$
	$-30 \leq l \leq 28$
Reflection collected	31208
Independent reflections / R_{int}	6201 / 0.0888

Data/restraints/parameters	6201/0/367
goof on F^2	1.025
R_1, wR_2 [$I > 2\sigma(I)$]	0.1884
R_1, wR_2 (all data)	0.2246
Residual electrons and holes (e Å^{-3})	0.53/-0.40
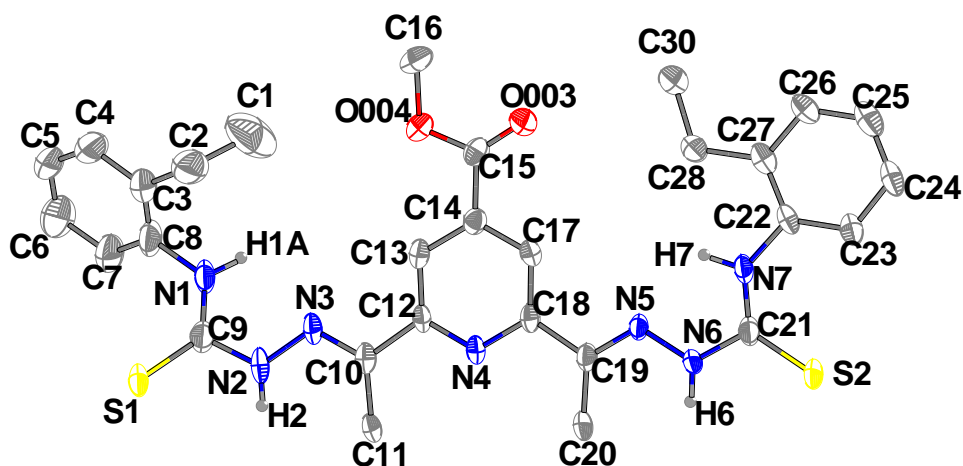
	(BTSC)
Empirical formula	$C_{19}H_{31}N_7S_2$
Formula weight (g/mol)	421.63
Crystal system	Monoclinic
Space group	$C2/c$
a (Å)	20.3700(6)
b (Å)	12.6735(4)
c (Å)	9.2550(2)
α (°)	90
β (°)	107.7470(10)
γ (°)	90
Volume (Å^3) / Z	2275.56(11) / 4
ϱ_{calc} (g/cm^{-3})	1.231
μ (mm^{-1})	0.253

Limiting indices	$-26 \leq h \leq 26$
	$-16 \leq k \leq 16$
	$-12 \leq l \leq 11$
Reflection collected	27191
Independent reflections / R_{int}	2608 / 0.186
Data/restraints/parameters	2608/0/130
goof on F^2	1.071
R_1, wR_2 [$I > 2\sigma(I)$]	0.0389
R_1, wR_2 (all data)	0.0186
Residual electrons and holes (e $Å^{-3}$)	0.43/-0.32
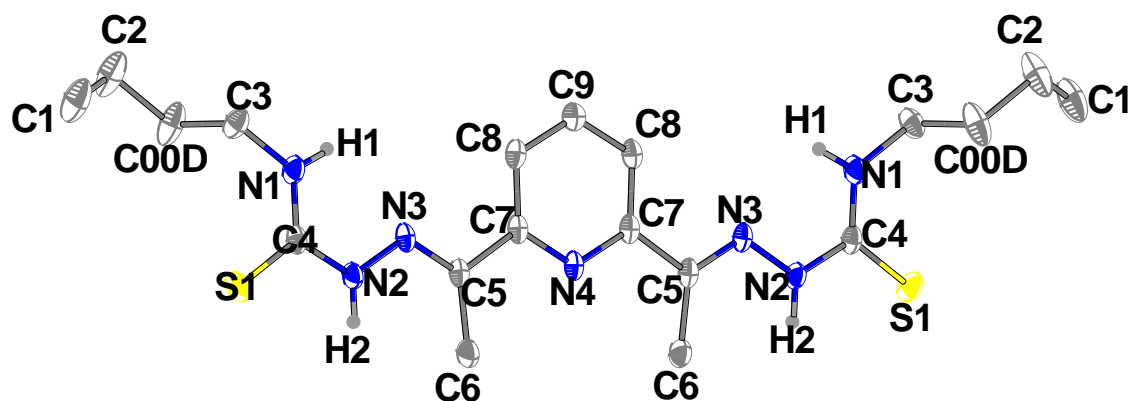
	(BTSC)
Empirical formula	$C_{25}H_{32}ClN_9S_4$
Formula weight (g/mol)	654.28
Crystal system	Monoclinic
Space group	$P2_1/n$
a (Å)	12.8177(5)
b (Å)	18.3602(6)
c (Å)	14.3460(6)
α (°)	90
β (°)	112,6830(10)
γ (°)	90

|	
Volume (Å³) / Z	3115.0(2) / 4
ϱ_{calc} (g/cm⁻³)	1.395
μ (mm⁻¹)	0.431
Limiting indices	-17 ≤ h ≤ 17
	-24 ≤ k ≤ 24
	-19 ≤ l ≤ 19
Reflection collected	27191
Independent reflections / R_{int}	7713 / 0.0207
Data/restraints/parameters	7713/0/376
goof on F^2	1.064
R_1, wR_2 [$I > 2\sigma(I)$]	0.0324
R_1, wR_2 (all data)	0.0824
Residual electrons and holes (e Å⁻³)	0.46/-0.30
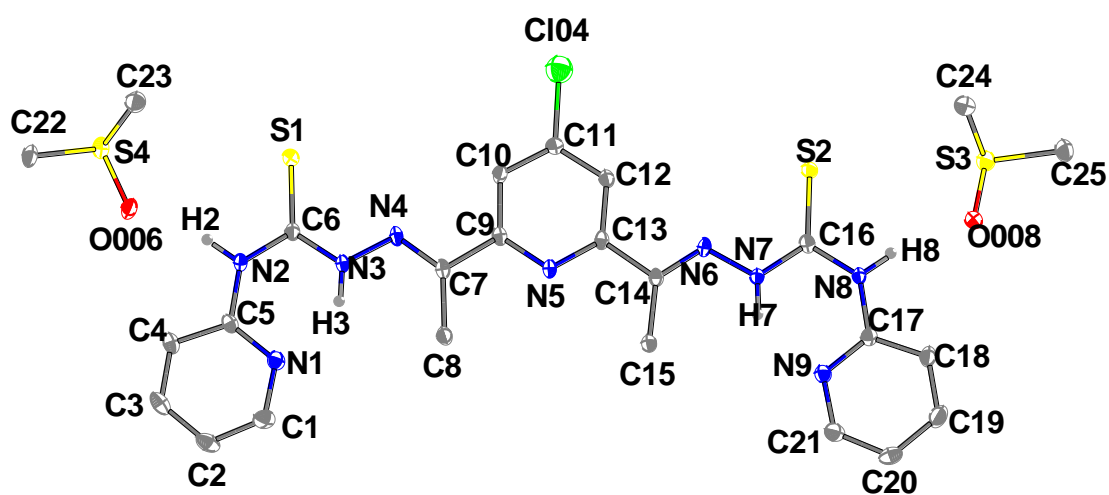
Appendix C. Cyclic Voltammetry
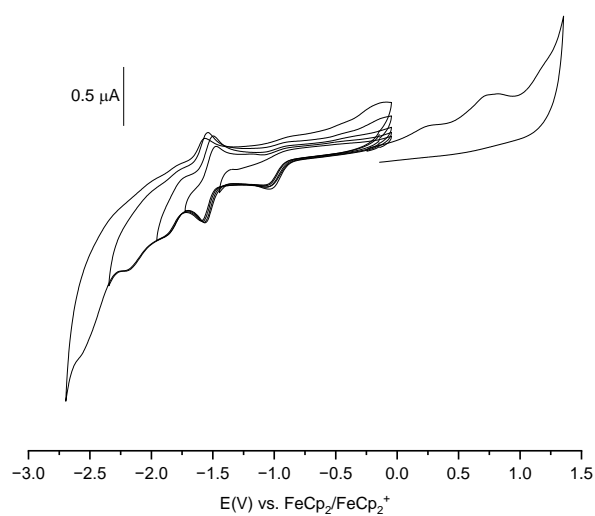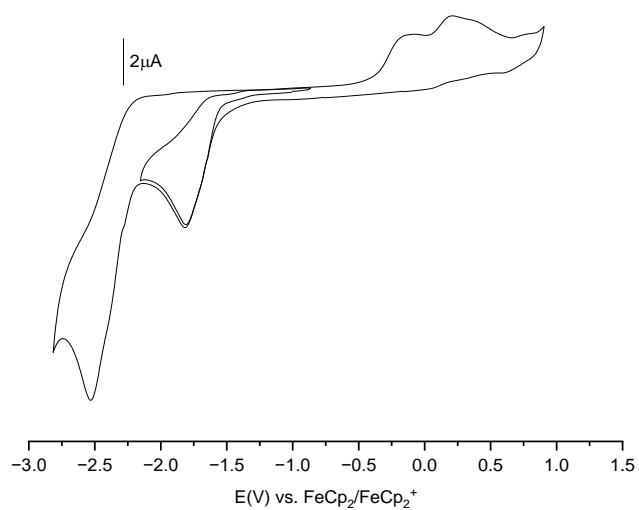
Cyclic voltammograms of Compound **17** (**top**) and its palladium complex [Pd(BTSC)] (**bottom**) measured in 0.1 M *n*-Bu₄NPF₆/THF.
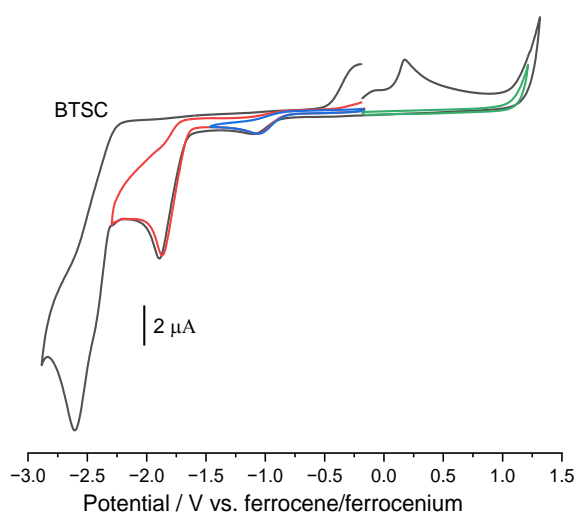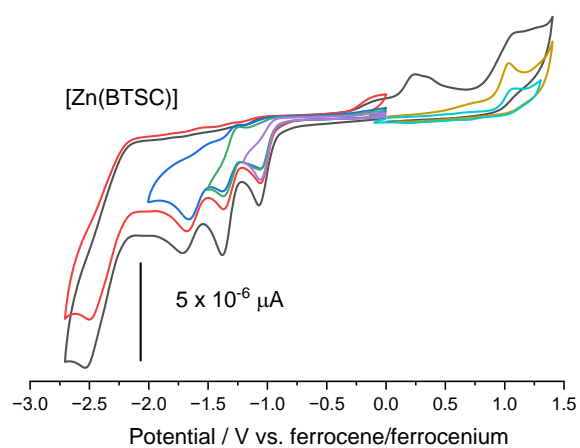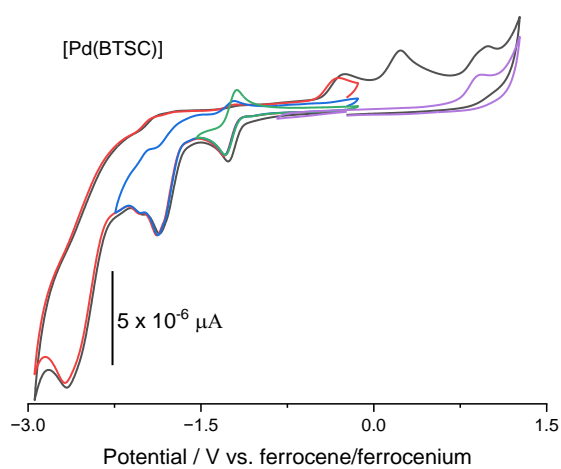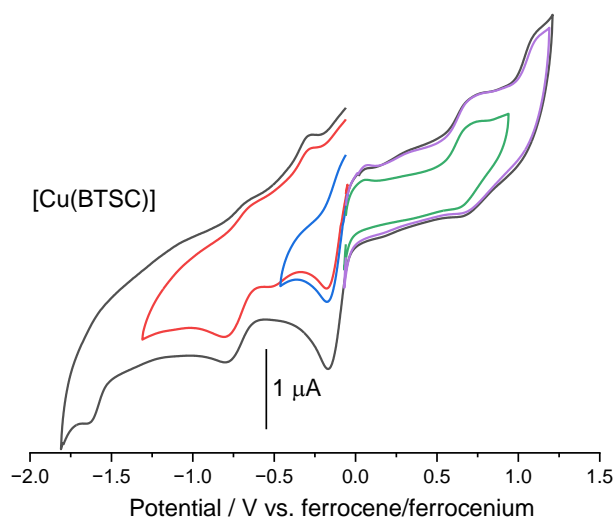
Cyclic voltammograms of Compound **18** (**top**) and its copper, palladium and zinc complex [Pd(BTSC)] (**bottom**) measured in 0.1 M *n*-Bu₄NPF₆/THF. Copper complex was measured in MeCN.

LEBENSLAUF
Anthony, Eric Tobechukwu
Ph.D. Candidate, Department of Chemistry
University of Cologne
Current Address: Olgastr. 10, 42277. Wuppertal
Phone: Email address: eanthon2@smail.uni-koeln.de

STUDIUM

Ph.D. in Chemistry, University of Cologne, Germany   2021 – Present
- Mentor: Prof. Dr. Axel Klein and Prof. Dr. Sanjay Mathur
- Research Focus: Pentadentate Bis-Thiosemicarbazones Nanoparticle Conjugates

Ph.D. in Chemistry, University of Fort Hare, South Africa   2019 – 2023
- Mentor: Prof. Omobola Okoh
- Research Focus: Adsorption of Antibiotic-Resistant Bacteria and their Cell-Free Deoxyribonucleic Acid Harbouring Resistance Genes in Drinking Water with Metal Oxides

M.Sc. in Chemistry, Adekunle Ajasin University, Nigeria   2016 – 2018
- Mentor: Prof. N. Abiola Oladoja
- Research Focus: Advanced Oxidation and Reduction Methods for the Treatment of Contaminated Wastewater

B.Sc. in Chemistry, Adekunle Ajasin University, Nigeria   2008 – 2012
- Mentor: Prof. N. Abiola Oladoja
- Research Focus: Synthesis of Nano-Sized Hydrocalumite from a Gastropod Shell for Aqua System Phosphate Removal

Secondary School Leaving Certificate   2000 – 2006

Berufliche Erfahrung

Department of Chemistry, University of Cologne, Germany
- Learning Assistant for Undergraduate Practical Organic Synthesis   2022 – 2024

Department of Chemistry, University of Fort Hare, South Africa
- Learning Assistant for Undergraduate Practical Organic Synthesis   2019 – 2021
- Teaching Assistant for First Year Chemistry Student   2019 – 2021

Department of Chemistry, Adekunle Ajasin University, Nigeria
- Teaching Assistant for Pre-Degree students.   2017 – 2019

Ehrungen und Stipendien

- German Academic Exchange Service Research Scholarship   2021 – 2025
- Supervisor Linked Bursary, University of Fort Hare   2019 – 2022

Zugehörigkeiten

- Member of the Gesellschaft Deutscher Chemiker
- Member of the American Ceramic Society
- Member of the Chemical Society of Nigeria

Fachwissen

- Ligand design and synthesis
- Synthesis of coordination complexes
- Ligand Nanoparticles Conjugates
- Air-free Schlenk Line Technique
- DNA extraction and quantification
- Water and wastewater treatment

Fertigkeiten

Instruments: Experience in operating the following instruments and interpretation of the corresponding data:

- Bruker Avance III Spectrometer 300, 400, 499 NMR
- Thermo Scientific LTQ Orbitrap XL Electrospray Ionization Mass Spectra coupled with FTMS Analyzer and (H)ESI Ion-Probe
- Perkin Elmer STA 6000 Thermogravimetric Analysis
- PerkinElmer-Spectrum 400 Fourier transform infrared Spectroscopy
- Varian 50 Scan UV spectrophotometer
- STOE-STADI MP diffractometer Powder X-ray diffractograms

Software: Advanced proficiency in: Microsoft Office, Corel Draw, EndNote X9, MNova, SciFinder, Shelxt, Olex, Mercury, Diamond, Chemdraw, ChemDoodle, WinXPow

Konferenzen und Präsentationen

- Ligand Design Workshop, Cologne, Germany – 2023
  Paper Presented: Pentadentate Thiosemicarbazones Nanoparticles Conjugates: Synthesis, Characterization and Applications in Binding of metal ions.
- Koordinationschemie-Treffen, Jena, Germany – 2022
  Paper Presented: Ligand-Nanoparticle Conjugates of Polydentate Thiosemicarbazones for Heavy Metal Binding
- Kosygin Forum, Moscow, Russia – 2022
  Paper Presented: Influence of different Ag/ZnO heterostructures on the removal efficiency of multidrug-resistant Enterococcus faecium harboring multiple resistance genes from tap water
- Akure Humboldt Kollege, Nigeria – 2017
  Paper Presented: Synthesis and Characterization of solar active nano-calcium ferrite for the reduction of Cr(VI) to Cr(III) in aqua system.

Veröffentlichungen

[1] Nurudeen Abiola Oladoja, Joseph A. Ogunniyi, Isaac A. Ololade, **Eric Tobechukwu Anthony**, Isiaka A. Lawal, Owolabi M. Bankole, Edurado A. Lopez-Maldonado, Paul D. Ojegbile, Oluwole O.

Bolawole, Olayinka S. Adanalawo. Production of redox-active reactive filter material from charcoal. *Next material*, 5 (**2024**) 100251

[2] Edurado A. Lopez-Maldonado, Youness Abdellaoui, Mahmoud H. Abu Elella, Heba M. Abdallah, Mayank Pandey, **Eric Tobechukwu Anthony**, Luminita Ghimici, Silva Alvarez-Torrellas, Veronica Pinos-Velez, Nurudeen Abiola Oladoja. Innovative biopolyelectrolytes-based technologies for wastewater treatment. *International Journals of Biological Macromolecules*, 273 (**2024**) 132895

[3] Mehdi Khalaj, Seyed-Mola Khatami, Mehdi Kalhor, Maryam Zarandi, **Eric Tobechukwu Anthony** and Axel Klein. Polyethylenimine Grafted onto Nano-$NiFe_2O_4$@SiO_2 for the Removal of CrO_4^{2-}, Ni^{2+}, and Pb^{2+} Ions from Aqueous Solutions. *Molecules, (MDPI)*, 29, (**2024**) 125

[4] Ajibola A Bayode, **Eric T Anthony**, Odunayo T Ore, Moses O Alfred, Daniel T Koko, Emmanuel I Unuabonah, Brigitte Helmreich and Martins O Omorogie. A review on the versatility of Carica papaya seed: an agrogenic waste for the removal of organic, inorganic and microbial contaminants in water. *Journal of Chemical Technology and Biotechnology* (*Springer*), 2095-2109 (**2023**) 98

[5] Nurudeen Abiola Oladoja, Joseph Adebusola Ogunniyi, **Eric Tobechukwu Anthony**, Sumit Kumar and Stephan Hofmann. Sustainable Bifunctional ZnO Composites For Synchronous Adsorption And Reduction Of Cr(VI) to Cr(III). *Environmental Science and Pollution Research* (*Springer*), 80545–80558 (**2023**) 30

[6] Garci, Fatma, Chebbi, Hammouda, Rouzbeh, Nahal, Rochels, Leonhard, Disch, Sabrina Haseloer, Alexander, Sebastian, Sean S, Ruschewitz, Uwe, **Anthony, Eric Tobechukwu**, Klein, Axel, Zid, Mohamed Faouzi. Structure, Optical and Magnetic Properties of Two Isomeric 2-Bromomethylpyridine Cu(II) Complexes [$Cu(C_6H_9NBr)_2(NO_3)_2$] with Very Different Binding Motives. *Molecules* (*MDPI*), 2 (**2023**) 28.

[7] **Anthony, Eric T**., Ojemaye, Mike O. Okoh, Omobola O. Okoh, Anthony I. Influence of different Ag/ZnO heterostructures on the removal efficiency of multidrug-resistant Enterococcus faecium harboring multiple resistance genes from tap water. *Environmental Progress and Sustainable Energy* (*Wiley*), 1-11 41 (**2022**) 6

[8] **Anthony, Eric Tobechukwu** and Oladoja, Nurudeen Abiola. Process enhancing strategies for the reduction of Cr(VI) to Cr(III) via photocatalytic pathway. *Environmental Science and Pollution Research* (*Springer*), 8026-8053 (**2022**) 29

[9] **Anthony, Eric T**. and Oladoja, Nurudeen A. Trends in the Management of Arsenic Contamination in Potable Water. *Environmental Contamination Remediation and Management* (*Springer*), 155-183 (**2021**).

[10] **Anthony, Eric T.,** Alfred, Moses O., Saliu, Toyin D., and Oladoja, Nurudeen A. One-pot thermal synthesis of Ceria/Montmorillonite composite for the removal of hexavalent chromium from aqueous system. *Surfaces and Interfaces* (*Elsevier*), 100914 (**2021**).

[11] **Anthony, Eric T**., Ojemaye, Mike O., Okoh, Anthony I., Okoh, Omobola O. Potentials of low-cost methods for the removal of antibiotic-resistant bacteria and their genes in low budget communities: A review. *Journal of Water Process Engineering* (*Elsevier*), 101919 (**2021**) 40.

[12] **Anthony, E. T.,** Lawal, I. A., Bankole, M. O., Klink, M., Ololade, I. A. and Oladoja, N. A. Solar active heterojunction of p-CaFe$_2$O$_4$/n-ZnO for photoredox reactions. *Environmental Technology and Innovation* (*Elsevier*), 101060 (**2020**) 20.

[13] **Anthony, Eric T.,** Ojemaye, Mike O., Okoh, Anthony I., and Okoh, Omobola O. Synthesis of CeO$_2$ as promising adsorbent for the management of free-DNA harboring antibiotic resistance genes from tap-water. *Chemical Engineering Journal* (*Elsevier*), 125562 (**2020**) 401.

[14] **E.T. Anthony**, O.O Okoh, A.I. Okoh and M.O. Ojemaye. A critical review on the occurrence of resistomes in the environment and their removal from wastewater using apposite treatment technologies: Limitations, successes and future improvement. *Environmental Pollution* (*Elsevier*), 113791 (**2019**).

[15] N.A. Oladoja, G.A. Bello, V. Obisesan, B. Helmreich, J.A. Ogunniyi, O.A. Daramola, H.A. Bello, **E.T. Anthony**, and T.D. Saliu, Insight into the Defluoridation Efficiency of Lateritic Soil. *Environmental Progress & Sustainable Energy (Wiley)*, 13107 (**2019**) 38.

[16] N.A. Oladoja, **E.T. Anthony**, I.A. Ololade, T.D. Saliu, G.A. Bello, Self-propagation combustion method for the synthesis of solar active nano ferrite for Cr(VI) reduction in aqua system, *Journal of Photochemistry and Photobiology A: Chemistry* (*Elsevier*), 353 (**2018**) 229–239.

[17] N.A. Oladoja, T.D. Saliu, I.A. Ololade, **E.T. Anthony**, G.A. Bello, A new indigenous green option for turbidity removal from aqueous system, *Separation and Purification Technology* (*Elsevier*), 186 (**2017**) 166 – 174.

[18] N.A. Oladoja, R.O.A. Adelagun, I.A. Ololade, **E.T. Anthony**, M.O. Alfred. Synthesis of nano-sized hydrocalumite from a Gastropod shell for aqua system phosphate removal, *Separation and Purification Technology* (*Elsevier*), 124 (**2014**) 186 – 194.